CEURS 2022

CIVIL ENGINEERING UNDERGRADUATE RESEARCH SYMPOSIUM

PROCEEDINGS

ISSN 3021-6737

PROCEEDINGS OF THE CIVIL ENGINEERING UNDERGRADUATE RESEARCH SYMPOSIUM (CEURS) - 2022

DEPARTMENT OF CIVIL ENGINEERING

FACULTY OF ENGINEERING

UNIVERSITY OF PERADENIYA

SRI LANKA

DEPARTMENT OF CIVIL ENGINEERING
FACULTY OF ENGINEERING
UNIVERSITY OF PERADENIYA
SRI LANKA

PROCEEDINGS OF THE CIVIL ENGINEERING UNDERGRADUATE RESEARCH SYMPOSIUM CEURS 2022

ISSN 3021-6737

PUBLISHED BY,
DEPARTMENT OF CIVIL ENGINEERING,
FACULTY OF ENGINEERING,
UNIVERSITY OF PERADENIYA,
SRI LANKA.

Message from the Dean, Faculty of Engineering

It is with great pleasure; I write this message to the Civil Engineering Undergraduate Research Symposium (CEURS) – 2022 to be held soon.

This is the event in which undergraduate research projects which were during a period of two semesters will be showcased to the final evaluators, staff of the faculty, engineering community visiting from the industry and other fellow students. First, I would like to thank you for all the hard work done, especially during this period of economic down turn of the Country, with all associated challengers. Even though the funding to conduct research is limited, it is good to observe that you have made use of the facilities available to the maximum extent and together with staff of your Department you have done commendable work. I notice very often that the supervising staff of the Department of Civil Engineering very often encourage and persuade their undergraduate students to carry out good quality research and publish in high indexed journals. That is a very significant contribution to the ranking of the University and development of the very essential research culture in the faculty. I congratulate and thank you for that. Further, these finding are conveyed to the industry though various seminars, workshops and CPD courses etc. That is again an essential duty from our side as a responsible institution funded by the Government. I sincerely hope at least some of the outcome from these research work will go beyond the journal papers, sale model in the lab to a prototype development, factory level manufacturing and widespread application in the industry, as this is the need of the country at this time to come out from this volatile economic situation.

I wish you a very successful day of learning and networking.

Dr. U.I. Dissanayaka
Dean / Faculty of Engineering,
University of Peradeniya.

Message from the Head, Department of Civil Engineering

It is indeed a pleasure to send this message as the Head of the Department for inclusion in the Proceedings of the Civil Engineering Undergraduate Research Symposium (CEURS) - 2022.

Final-year undergraduate research under the supervision of academic staff makes a notable contribution to the large volume of research being performed in the department at several levels and across different areas of civil engineering. Being a key component of their final year of study, the research project enables the students to acquire valuable training not only on research methods but also on reviewing literature and effective technical writing while enhancing critical thinking skills.

Clearly, publishing key findings is an essential end product of research, and as Miller said, 'If it wasn't published, it wasn't done'. Thus, the Department of Civil Engineering is pleased to compile and publish, subsequent to review, a collation of selected extended abstracts of research performed by final-year undergraduate students specializing in civil engineering during the academic year 2022/23.

Whilst congratulating the students for their research work, I would like to take this opportunity to appreciate the valuable guidance and training provided to them by the academic staff members of the department. Finally, I thank the reviewers for their important contribution and very much appreciate the editorial team for their time and effort in compiling the proceedings of the research symposium as an open-access digital publication hosted on the departmental website, thereby enabling the dissemination of the research findings to the entire world.

Prof. J. J. Wijetunge
Head / Department of Civil Engineering,
Faculty of Engineering,
University of Peradeniya.

Editorial Note

As editors, it is a great pleasure for us to release the Proceedings of the Civil Engineering Undergraduate Research Symposium (CEURS 2022), which is a compilation of peer reviewed extended abstracts of the research outcomes of final year undergraduate researches of the Department of Civil Engineering. CEURS 2022 includes 29 extended abstracts covering a wide range of research themes from diverse disciplines in Civil Engineering, including Hydraulics and Water Resources Engineering, Environmental Engineering, Materials and Structural Engineering, Transportation and Traffic Engineering, Geotechnical Engineering, and Construction Management. We believe this publication would demonstrate the research capabilities of our undergraduate students and also provide a great opportunity for them to discuss their valuable findings with a broad research community.

We are grateful to Dr. U.I. Dissanayaka, the Dean, Faculty of Engineering and Prof. J.J. Wijethunga, the Head, Department of Civil Engineering for their continuous guidance, support and encouragement throughout this process. Our grateful acknowledgement should go to the Tokyo Cement Group for their continuous financial assistance to carryout research activities in the department and holding the sponsorship of this event. Further, we should thank to Mr. H.J.S.H. Jayaweera for his contribution to design the attractive cover page and graphic designs.

Last, but not least we should pass our sincere gratitude to all the academic staff members of the Department of Civil Engineering, and all the students since this is the final outcome of their collective research efforts.

Prof. K.K. Wijesundara and Dr. M.M.G.T. De Silva
Editors of CEURS 2022
Department of Civil Engineering
Faculty of Engineering
University of Peradeniya

Table of Contents

Geotechnical and Transportation Engineering

Material and Structural Engineering

Water and Environmental Engineering

GEOTECHNICAL AND TRANSPORTATION

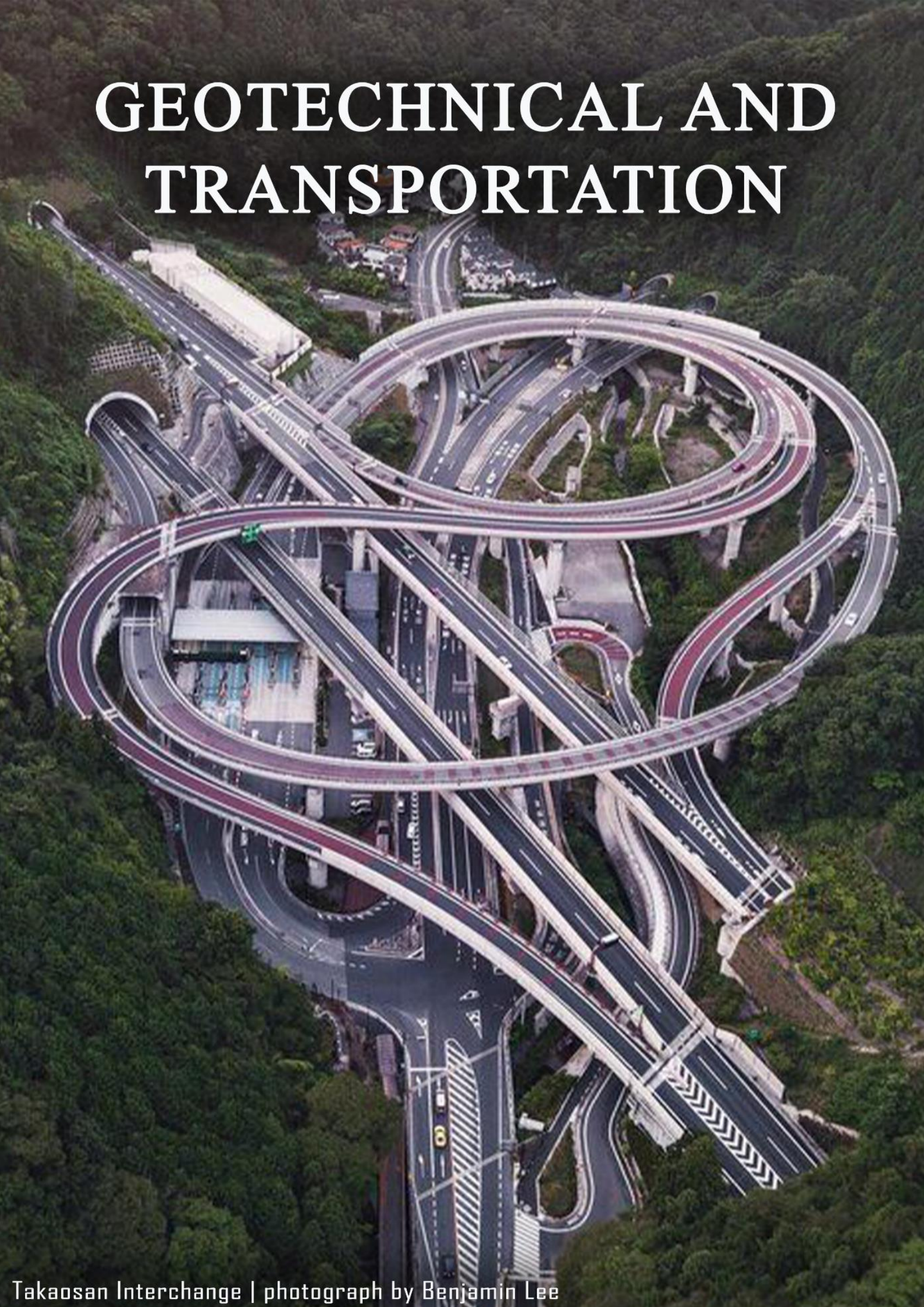

Takaosan Interchange | photograph by Benjamin Lee

Development of a Green Toolkit to Evaluate the Sustainable Urban Mobility in Small and Medium-sized Cities

Rathnayake R.M.T.S.B., Langappuli R.A., Sathyaprasad I.M.S.*

Department of Civil Engineering, University of Peradeniya, Sri Lanka

**imss@pdn.ac.lk*

Keywords: Sustainable urban mobility, Measurable indicators, Green toolkit, Framework, Benchmark

1. Introduction

Urban mobility is a critical aspect of modern city life, affecting the economic, social, and environmental well-being of individuals and communities. The rapid concentration of economic activities in urban areas has led to an increase in resource demand and environmental burdens, making sustainable urban mobility a pressing issue. A sustainable urban mobility plan is a strategic approach aimed at meeting the mobility needs of people and businesses in cities while also promoting a better quality of life. The plan should consider the three pillars of sustainability; social, economic, and environmental to achieve a balance between the present and future generations. However, evaluating the sustainability of mobility conditions is challenging, requiring the use of measurable indicators to assess progress and identify areas for improvement. This research attempts to develop a green toolkit to evaluate the sustainability of mobility conditions in small and midsized cities. The toolkit includes a comprehensive set of measurable indicators, enabling policymakers and stakeholders to quantify progress and improve sustainability in urban mobility.

2. Literature review

Sustainability is a concept that involves balancing the environment, society, and economy. The University of California, Los Angeles (UCLA) Sustainable committee defines sustainability as merging environmental health, social equity, and economic vitality to establish vibrant and robust communities for the present and future generations. This requires a comprehensive systems approach and an understanding of the interconnectedness of these issues. The transport sector plays a significant role in achieving sustainability goals, and it is essential as it seeks to change individuals' transport decisions and travel behavior in favor of a sustainable model (Sdoukopoulos & Pitsiava-Latinopoulou,2017). Any deficiencies in the design and planning of transport infrastructure could lead to low sustainability levels and result in negative social, economic, and environmental impacts.

The use of indicators is crucial in assessing sustainability, as what gets measured gets managed. Indicators are quantitative measures that simplify and convey complex phenomena, making them a common tool for tracking progress toward sustainability and they should capture the multidimensionality of sustainable transport and break down complex concepts into manageable information to facilitate comparison, benchmarking, and communication for stakeholders (Perra et al., 2017).

Perra et al. (2011) reported that large sets of indicators require a significantly high cost for data collection. The additional information gathered compared to smaller sets rarely alters the overall findings. On the other hand, simplistic sets, including inadequate indicators, often fail to illustrate the actual situation due to missing information and may mislead policymakers and stakeholders in the decision-making process (Litman, 2011; Marsden & Snell, 2009).

3. Methodology

Different literature sources refer to sustainable development indicators at different levels of geo scale as national and holistically urban levels. Therefore, the indicators developed based on the national level, and larger-sized cities were analyzed to select a set of indicators applicable to small and midsized cities. The study area is defined according to the population criteria specified by the Furman Center Analysis as small cities (between 50,000 and 99,999 residents) and mid-sized cities (between 100,000 to 499,999 residents).

3.1 Selection of an appropriate set of indicators

The selection process of the relevant indicators from the wide range of indicators found in literature is done according to the systematic

selection process defined by Karjalainen & Juhola (2021).

The first selection round provided 69 indicators which are then filtered into 21 indicators.

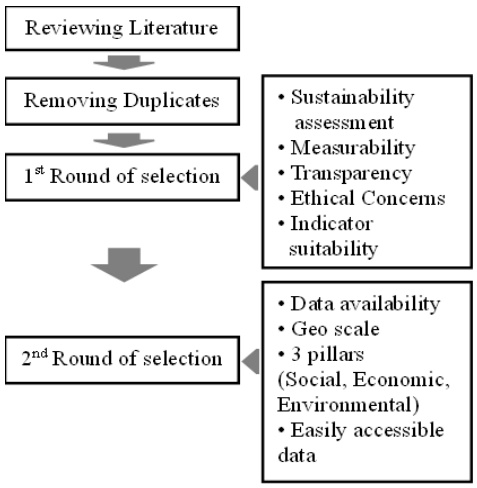

Figure 1: Systematic approach of selection

3.2 Categorization of selected indicators

The indicator set is categorized based on two aspects in order to measure sustainable urban mobility in an exhaustive and exclusive manner. Initial categorization is according to three pillars of sustainability social, economic, and environmental. The indicators are also followed by subcategorization as the choice of transport mode, energy efficiency, institutional aspects, and economic productivity, safety and security, travel efficiency and parking management, promotion of public transport, urban planning/transport planning and land use, promotion of green technologies, accessibility, and affordability, quality of travel and livable environment.

3.3 Defining indicator benchmark values

The benchmark values were carefully selected and adapted for the Sri Lankan context through a rigorous filtering process considering a range of relevant literature and global target values. This process involved a comprehensive review of available resources to ensure that the selected metrics accurately reflected the social, economic, and environmental priorities of Sri Lanka. By leveraging existing global standards and tailoring them to the specific context, the resulting benchmark values provide a robust framework for measuring progress toward sustainable urban mobility in Sri Lanka.

4. Results and discussion

Table 1: Definitions of selected indicators

Indicator	Definition
1. Modal split	% of travellers using a particular mode of transport compared to all trips made
2. Fuel efficiency of PT fleet	Average fuel consumption efficiency of PT Fleet
3. Traffic congestion delay	The percentage of extra time spent traveling due to congestion
4.Trasport Accident fatalities	Score based on the annual total number of road fatalities on the spot or within 30 days per 100,000 of the total population.
5. Cycle parking availability	Number of bicycle parking spaces per 1,000 residents
6. Road network density	The ratio of total road length and the urban area or total population
7. PT network coverage	Number of people within 500 m distance of a public transport stop as a % of the total population of the city
8. Average PT speed	Average travel speed of representative bus routes for the city
9. PT comfort	Likert scale based on seating comfort, noise levels, safety features, accessibility, cleanliness & hygiene, space and capacity, lighting, ventilation
10. PT security	Likert scale based on Crime statistics, use of surveillance cameras, Use of surveillance cameras, Emergency response protocols, Security personnel
11. PT reliability	% of PT itineraries on time
12. PT capacity in relation to population	The proportion of the population using public transportation
13. Cycling Lane density	Bicycle routes as a share of the total road network length
14. Pedestrian infrastructure density	% of the total length of pedestrian infrastructure to the total length of the urban fabric
15. Use of renewable fuels in transport	Annual total number of passenger kms ran by renewable fuel-based vehicles as a proportion of passenger kms ran for all modes
16.Affordability	Portion of household budgets devoted to transport
17.PT affordability	Cost devoted to PT as a portion of Transport cost by all means
18.Quality of transport for disadvantaged people	Likert scale based on accessibility, affordability, safety, reliability, comfort, convenience, and participation of disadvantaged people.
19.Share of vehicle fleet meeting air emission standards	Number of vehicles meeting certain air emission standards per 100 vehicles
20.Transport GHG emission	Per capita transport GHG emissions per year
21.Level of resident satisfaction	Average satisfaction score using the survey data

Table 2: Developed benchmark values and method of measurements

Index	Environmental	Social	Economic	Indicator Category	Method of Measurement
1		■	■	Choice of Transport mode	[(total number of passenger kms ran for each mode)/ (total number of passenger kms ran for all modes)]* 100
2	■		■	Energy Efficiency	[Σ(ML1)/(FC1), .., (MLi)/(FCi)]/i, where ML= kms ,FC=Fuel consumption, i= Total number of PT vehicles
3	■	■	■	Institutional aspects and Economic Productivity	{[(Average travel time of representatives routes during peak hours)- (Average travel time of representatives routes during non-peak hours)]/Average travel time of representatives routes during non-peak hours} 100%
4		■		Safety and security	(Total number of annual road fatalities on the spot or within 30 days)/(Total real population)*100000
5	■			Travel efficiency and Parking Management	[(Number of bicycle parking spaces)/(Total population)]*1000
6		■	■		(Total length of road network)/Area or (Total length of road network)/(Real population)
7		■		Promotion of Public Transport	[(Sum of population within 500m of PT Station)/(Total population of the city)]*100
8		■			[Σ(v1, v2, .., vi)]/i, where vi= Average travel speed of bus route i
9		■	■		PT comfort = (Seating comfort x A) + (Temperature control xB) + (Noise levels x C) + (Safety features x D) + (Accessibility x E) + (Cleanliness and hygiene x E)+(Space and capacity x F) + (Lighting x G) + (Ventilation x H) ; A,B,C,D,E - Weight factors
10		■	■		Public Transport Security Index = [(Crime statistics x A) + (Use of surveillance cameras x B) + (Use of surveillance cameras x C) + (Emergency response protocols x D) + (Security personnel x E) ; A,B,C,D,E - Weight factors
11		■	■		[(Number of PT itineraries on-time)/(Total number of PT itineraries)]*100
12		■	■		PT size in relation to population = (Total real population)/(Total capacity of PT vehicles)
13	■	■		Urabn Planning/ Transport planing and Land use	[(Length of bicycle network)/(Total length of road network)]*100
14	■		■		[Length of Pedestrian Infrastructure / Total Length of Urban Fabric]* 100
15			■	Promotion of Green technologies	[(Annual total number of passenger kilometers ran by renewable fuel based vehicles)/ (Annual total number of passenger kilometers ran for all modes)]* 100
16		■		Accessibility and Affordability	[(Total cost devoted to transport)/(Total household income)]*100
17		■	■		PT affordability = (public transportation expenditures / total transportation expenditures) x 100%
18		■		Quality of travel	Quality of Transport for Disadvantaged People = (Accessibility x A) + (Affordability x B) + (Safety x C) + (Reliability x D) + (Comfort x E) + (Convenience x F) + (Participation x G) ; A,B,C,D,E - Weight factors
19	■			Liveable environment	[(Number of vehicles meeting certain air emission standards)/(Total number of vehicles)]*100
20	■				[Total amount of transport GHG emissions for the city per year]/Total population
21	■				Likert Scale from 1-5. [Very Dissatisfied(1),Somewhat Dissatisfied(2),Neither Satisfied nor Dissatisfied(3),Somewhat Satisfied(4),Very Satisfied(5)]

Table 3: Developed benchmark values and ratings

Index	Benchmark Value/Range	Rating
1	Walking: 30%,Cycling: 10%,PT: 20%,Private: 40%	Walking,Cycling & PT > =60 [1] Walking,Cycling & PT<60 [0]
2	Diesel Buses: 5 km/l,Petrol Bus: 2km/l	Fuel efficiency > 5km/l(Diesel),2 km/l(Petrol) [1] Fuel efficiency< 5km/l(Diesel),2 km/l(Petrol) [0]
3	Low congestion: below 10%,Moderate congestion: between 10%-25%,High congestion: above 25%	Low congestion [1],Moderate congestion [0.5], High congestion [0]
4	Low value (less than 5 deaths per 100,000 population) Medium value (between 5 and 20 deaths per 100,000 population) High value (20 or more deaths per 100,000 population)	Low value [1],Medium value [0.5], High value [0]
5	Excellent Availability (greater than 12 per thousand population) Good Availability (between 6-12 per thousand population) Fair Availability (between 3-6 per thousand population) Poor Availability (Less than 3 per thousand population)	Excellent Availability [1],Good Availability [0.5] Fair Availability [0.25],Poor Availability [0]
6	Good: Between 1.5km/km^2 and 2.5 km/km^2	Good [1], if not [0]
7	Good: more than 90%,Fair: between 90%-70%,Poor: less than 70%	Good [1],Fair [0.5],Poor [0]
8	Good: between 15 kmph and 40 kmph	Good [1], if not [0]
9	Very Dissatisfied:1 ,Somewhat Dissatisfied: 2,Neither Satisfied nor Dissatisfied: 3,Somewhat Satisfied: 4,Very Satisfied: 5	Very Dissatisfied [0],Somewhat Dissatisfied [0.25],Neither Satisfied nor Dissatisfied [0.5],Somewhat Satisfied [0.75],Very Satisfied [1]
10	Very Dissatisfied:1 ,Somewhat Dissatisfied: 2,Neither Satisfied nor Dissatisfied: 3,Somewhat Satisfied: 4,Very Satisfied: 6	Very Dissatisfied [0],Somewhat Dissatisfied [0.25],Neither Satisfied nor Dissatisfied [0.5] Somewhat Satisfied [0.75],Very Satisfied [1]
11	Good: more than 70%,Fair: between 40%-70%,Poor: less than 40%	Good [1],Fair [0.5],Poor [0]
12	Good: more than 70%,Fair: between 40%-70%,Poor: less than 40%	Good [1],Fair [0.5],Poor [0]
13	Good: more than 20%,	Good [1], if not [0]
14	Good: between 15%-30%,Fair: between 5%-15%,Poor: less than 5%	Good [1],Fair [0.5],Poor [0]
15	Good: more than 14%,Fair: between 10%-14%,Poor: less than 10%	Good [1],Fair [0.5],Poor [0]
16	Good: less than 10%,Fair: between 10%-15%,Poor: more than 15%	Good [1],Fair [0.5],Poor [0]
17	Good: more than 10%,Fair: between 5%-10%,Poor: less than 5%	Good [1],Fair [0.5],Poor [0]
18	Very Dissatisfied:1 ,Somewhat Dissatisfied: 2,Neither Satisfied nor Dissatisfied: 3,Somewhat Satisfied: 4,Very Satisfied: 5	Very Dissatisfied [0],Somewhat Dissatisfied [0.25],Neither Satisfied nor Dissatisfied [0.5],Somewhat Satisfied [0.75],Very Satisfied [1]
19	Good: 100%	Good [1], if not [0]
20	Good: below 1.5 tonnes CO2 equivalent per capita per year	Good [1], if not [0]
21	Very Dissatisfied:1 ,Somewhat Dissatisfied: 2,Neither Satisfied nor Dissatisfied: 3,Somewhat Satisfied: 4,Very Satisfied: 5	Very Dissatisfied [0],Somewhat Dissatisfied [0.25],Neither Satisfied nor Dissatisfied [0.5],Somewhat Satisfied [0.75],Very Satisfied [1]

Following the method of measurement, the specific values for each indicator are calculated based on the city. The values for indicators, PT comfort (9), PT security (10), Affordability (16), PT affordability (17), Quality of transport for disadvantaged people (18) and Level of residents' satisfaction regarding the aesthetic and cleanliness of the public space related to transport (21) are obtained through public survey. Among those, indicator 9,10,18 and 21 are followed by a Likert scale survey. The calculated values are then compared against the

benchmark values referring to Table 3. A rating ([0]-[1]) is then awarded to each indicator and a total score is generated to evaluate the urban mobility in small and midsized cities. The degree to which sustainable mobility is achieved is measured as a score out of 21.

The toolkit is also used to identify the sustainable mobility performance of the city within each 11 subcategories defined and their effect on the three pillars of sustainability. The policymakers and urban planners can use this score to make informed decisions and set targets toward achieving more sustainable urban mobility.
The benchmark values, weight factors and the ranking system for the indicators selected are to be refine over time to reflect changing priorities and goals.

5. Conclusions

Sustainable urban mobility is essential for promoting green and sustainable transportation modes while satisfying the basic needs of society in small and mid-sized urban areas. However, data availability in small and mid-sized urban areas is challenging in developing a comprehensive toolkit for evaluating sustainable urban mobility. Despite this challenge, the green toolkit for evaluating sustainable urban mobility, consisting of 21 carefully selected and adapted indicators, was developed, which provides a robust framework for measuring progress toward sustainable development in Sri Lanka. The indicators cover all three pillars of sustainability and 11 subcategories, providing a comprehensive evaluation of sustainable urban mobility performance variables.

Given the challenge of data availability, it is recommended that policymakers and urban planners prioritize data collection and management to facilitate the development and implementation of sustainable urban mobility initiatives. It is also essential to establish collaborations between relevant stakeholders to share data and resources to fill data gaps.

References

Awasthi, A., & Omrani, H. 2018, A scenario simulation approach for sustainable mobility project evaluation based on fuzzy cognitive maps. International Journal of Modeling and Simulation, 38(4), 262–272.

Banister, D. 2008, The sustainable mobility paradigm. Transport Policy, 15(2), 73–80

Green sl rating system for sustainable cities Version 1.0 Green Building Council of Sri Lanka.

Karjalainen, L. E., & Juhola, S. 2021, Urban transportation sustainability assessments: a systematic review of literature. Transport Reviews, 41(5), 659–684

Litman, T. 2007, Developing indicators for comprehensive and sustainable transport planning. In Transportation Research Record (Issue 2017, pp. 10–15)

Mitchell, G., May, A., & McDonald, A. 1995, Picabue: A methodological framework for the development of indicators of sustainable development. International Journal of Sustainable Development and World Ecology, 2(2), 104–123.

Nicolas, J. P., Pochet, P., & Poimboeuf, H. 2003, Towards sustainable mobility indicators: Application to the Lyons conurbation. Transport Policy, 10(3), 197–208

Perra, V. M., Sdoukopoulos, A., & Pitsiava-Latinopoulou, M. 2017, Evaluation of sustainable urban mobility in the city of Thessaloniki. Transportation Research Procedia, 24, 329–336.

Sdoukopoulos, A., & Pitsiava-Latinopoulou, M. 2017, Assessing urban mobility sustainability through a system of indicators: The case of Greek cities. WIT Transactions on Ecology and the Environment, 226(1), 617–631.

Tafidis, P., Sdoukopoulos, A., & Pitsiava-Latinopoulou, M. 2017, Sustainable urban mobility indicators: Policy versus practice in the case of Greek cities. Transportation Research Procedia, 24, 304–312.

Zheng, J., Garrick, N. W., Atkinson-Palombo, C., McCahill, C., & Marshall, W. 2013, Guidelines on developing performance metrics for evaluating transportation sustainability. Research in Transportation Business and Management, 7, 4–13.

Queue Generation Due to 'U' Turn Vehicles in Divided Highways

Wijesundra H., Kulatunga P., Wickramasinghe W.M.V.S.K.*

Department of Civil Engineering, University of Peradeniya, Sri Lanka

**vskw@pdn.ac.lk*

Keywords: U-turn, Queue length, Center median openings, Time series

1. Introduction

The efficiency of a solid and methodical transportation system depends mainly on the amount of delay caused by various types of traffic conditions.

U-turn movement is such a common incident on transportation networks. To reduce the vehicle kilometre travel value, (VKT) it is very important to have sufficient U-turn locations along a highway. There are specific locations called centre median openings in divided highways for successful and safe U-turn movements. However, in most geometric designs, the safety in the vicinity of centre median openings is not considered, rather only keeps an opening for U-turn vehicles. U-turn vehicles on centre-median openings make fully or partial slowdown of flowing vehicle platoon. Therefore, the main contributors to the delays in divided highways are the disturbances caused to the traffic flow by U-turn vehicles at centre median openings.

This urges the need to analyse and model U-turn movements to predict queue generation. This research was focused on estimating queue generation at the above-selected centre median opening considering motorbikes, cars/jeeps/vans, three-wheelers, buses, and lorries as vehicle categories. A time series model was obtained using E-views software. And a successful validation process also followed arriving at the model. However, this study is only limited to present lane queue generation and for a four-lane divided highway.

2. Literature review

When considering highway engineering, not many researchers have dedicated their efforts to study queue generation due to a U-turn movement in a centre median opening in a divided highway. Some of the studies were related to finding and analysing the critical gap behaviour, waiting time, accepted gap patterns, etc. of a U-turn. These are some of the factors taken into consideration when calculating the queue generation due to a U-turn movement in a divided highway**.**

Jenjiwattanakul et. al., (2015) worked on a methodology to estimate the U-turn waiting time at a mid-block median opening. This study aimed to use field data to estimate a theoretical waiting time and compare them with the actual field data. Researchers proposed a method to estimate waiting time theoretically. Conflicting headway distribution type, mean U-turn critical headway and standard deviation were the inputs of the estimation process. This proposed simulation method was based on some assumptions. Researchers have concluded this study by stating, when the conflicting traffic is high and with the increase of conflicting flow rate waiting times also increases. The relationship obtained was exponential.

Back in 2011, the same researchers studied the effect of waiting time on the gap acceptance behaviour of U-turn vehicles at the midblock median opening. This study concluded that a waiting time of more than 30 seconds will frustrate the driver to accept an unsafe smaller gap. In both studies, the data collection method was a videography survey, and the parameters were also the same.

In 2019 another study was conducted to analyse the critical gap at a roundabout under mixed traffic conditions in Kandy, Sri Lanka. Unlike other researchers, Sandaruwanan et al., (2019) estimated the critical gap using a new proposed model. Using the data recorded from a survey, researchers carried out a gap acceptance study of each vehicle category. The researchers claimed that, due to a decrease in the number of vehicle observations in the medium bus category, newly generated equation gave high critical gap values than the modified Raff's method for all other vehicle categories.

Suman Dash et. al. (2019) also studied critical gaps of U-turns. They aimed to estimate the critical gap of U-turns at an uncontrolled opening. They used four methods for achieving their aim. Merging behaviour method were used other than in previous research, and modified

Raff's method was also used. Through their study they obtained, estimated critical gap values are varying with the category of vehicle, and variation is attributed to the wide disparity in static and dynamic features of the vehicles.
The thorough analysis revealed that many experiments on U-turning behaviour at centre median openings on divided highways have been reported. There has been no research on the generation of queue length due to U-turn vehicles on the current lane on divided highways. As a result, this research will be relevant and worthwhile for transportation engineers in the future of the country.

3. Methodology

This study's approach was divided into seven steps. These include establishing the objectives, selecting the site location, collecting the data, extracting the data, analysing the data, developing the time series model, and validating the model.

3.1 Location selection

For the analysis, a centre median opening situated in Dehiwala, Colombo (6.858168, 79.864767) was selected. For this selection, various criteria such as high vehicle flow rate, two lane divided highway, such as it should be free from gradient, curves, on street parking, pedestrian movement, and effect non-motorized vehicles.

3.2 Data collection

The data collection was done using videography survey with the aid of a stationary camera to cover the entire queue developing section. This survey was carried out using a stationary camera on top of a building overviewing the centre median.

3.3 Data extraction

Manual data extraction was done by repeatedly playing the video and TRACKER-4.11.0 was used to assess the length of the developed queue. After carrying out trial analysis, it was observed that only vehicle type, waiting time, queue length and present lane arrival flow were required for our main analysis. Rejected gaps and accepted gaps of U-turn vehicles were required for estimating critical gap.

3.4 Estimating critical gap

The critical gap is the minimum gap that a driver is willing to accept when a take U-turn to merge with the approaching traffic stream. Modified Raff's regression technique was used for estimating the critical gap acceptance. From the intersection point of Cumulative distribution function of accepted gaps F(a) and the reverse cumulative distribution function of rejected gaps F(r) is the critical gap value for the vehicle (Raffs,1950). Figure 1 shows a graph drawn for estimating critical gap for cars.

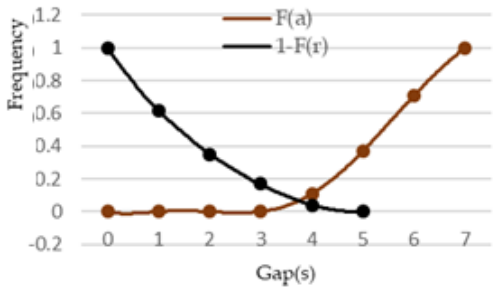

Figure 1: Modified Raff's method for estimating critical gap value for cars

Table 1 shows critical gap values that are obtained using Modified Raff's method for four types of vehicles.

Table 1: Critical gap values

Category	Critical gap(s)
Motor bike	2.8
Three-wheeler	3.0
Car	3.8
LGV	3.9

3.5 Model development

Data were analysed with respect to time. Therefore, a time series model was developed with the aid of the "EViews" student version software (Eviews 12 University Edition, 2021) to predict queue length. The VAR model was developed considering arrival flow rate (PCUs per 5 seconds), waiting time of U-turning vehicle at centre-median opening(s) and U-turning vehicle type as independent variables while queue length (meters) at the end of each 5 seconds time sequence was the dependent variable. The analysis was conducted in seven main phases. Those were stationary checking, optimal lag selection, integration checking, granger causality checking, model development, stability, and model fitting checking (validation check).

4. Results and discussion

Eighty percent of the complete set of data were used to create the model, while the remaining 20% were utilized to validate the model.

4.1 Developed VAR model

The queue length prediction model with coefficients that are related to each variable is shown below in Equation 1,

$$\begin{aligned}\text{Queue length} = {} & (0.842258\times \text{Queue length}_{t-1}) + \\ & (0.309467\times \text{Queue lengt}_{t-2}) + \\ & (0.175405\times \text{Queue length}_{t-3}) + \\ & (-0.043906\times \text{Waiting time}_{t-1}) + \\ & (-0.135645\times \text{Waiting time}_{t-2}) + \\ & (-0.652243\times \text{Waiting time}_{t3}) + \\ & (0.795822\times \text{Arrival flow}_{t-1}) + \\ & (0.172057\times \text{Arrival flow}_{t-2}) + \\ & (0.032869\times \text{Arrival flow}_{t-3}) + \\ & (2.424362\times \text{Vehicle type}_{t}) - 3.081748\end{aligned} \quad (1)$$

R-Squared 0.626319 Durbin-Watson 2.132585

Where, (t – 1) is time lag by one-time sequence and for this study it is 5s time sequence. (t – 2) is time lag by two-time sequence and it is 10s-time sequence for this study. Similarly, (t – 3) is time lag by three-time sequence and for this study it is a 15s-time sequence.

4.2 Validation of developed model

To validate the model, the stability of the developed model was obtained while checking the model fitting with residual correlation test also. Figure 2 manifest the results AR Root test. Results indicate that no points lie outside of the circle for the model. Thus, the model is in stable condition.

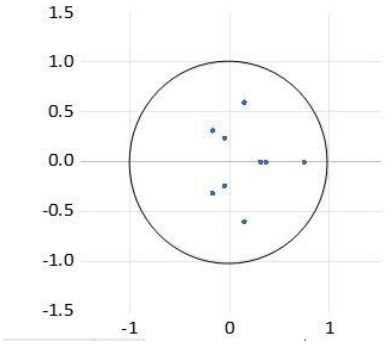

Figure 2: AR Root test results

Residual correlation test was done to check whether there is any correlation between variables under the selected lag. Obtained probability value for the developed model was 0.0002. Therefore, there is no correlation between variables for the selected lag.

4.3 Discussion

The comparison of the actual queue and the predicted queue was done after the validation and confirmation of the stability of the developed model to check the error percentages of the model. The values of Mean Average Error (MAE), Mean Average Percentage Error (MAPE), and Root Mean Square Error (RMSE) were calculated and tabulated below Table 2.

Table 2: Results of MAE, MAPE and RMSE

Actual queue vs. predicted queue	
MAE	3.453
MAPE	6.082
RMSE	5.823

Figure 3 shows the comparison results between actual queue and predicted queue.

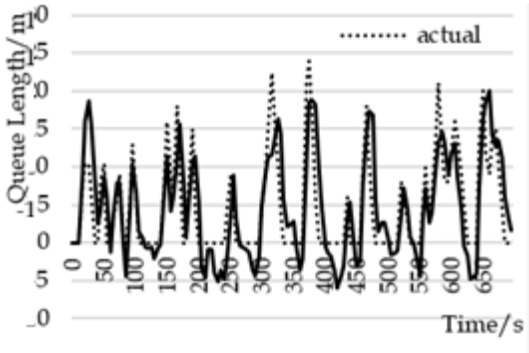

Figure 3: Actual queue vs. predicted queue

The MAE, MAPE and RMSE value comparison has been done between the developed model and the past developed models for other locations in worldwide as well as one location in Sri Lanka also.

Table 3: Results comparison with developed queue prediction models

	Dehiwala (developed model)	Weliwita Sri Lanka (Ratnayake et al., 2022)	China (Li et al., 2018)	USA (Anusha et al., 2013)
Intersection type	Un-signalized	Un-signalized	Signalized	Signalized
Method used	Time series analysis	Time series analysis	LWR shockwave	Queue polygon method
MAE	3.453	3.042	1.83	-
MAPE	6.082	5.665	11.28	-
RMSE	5.823	5.042	2.42	1.3

5. Conclusion

This study mainly focused on finding the governing parameters related to developing queue lengths at uncontrolled centre-median opening and to develop a queue length prediction model. The locations where had heterogeneous traffic conditions at uncontrolled centre-median opening location were adopted for the study. For model developing the procedure of "Box Jenkins" was followed and a time series analysis was done using the time sequence as 5 seconds with the aid of "E-views" software. It was identified that the governing parameters which cause to queue length were arrival flow rate, waiting time and U-turn vehicle type.

The assumptions made before developing the model, such as variables are stationary, the granger causality between variables, integration between variables were tested and confirmed using 80% data. After developing the model, validation and stability was checked using 20% data. The observed results manifest that the selected variables have significance influence on developing queue length.

As the summary of the project for different types of vehicles critical gaps will be different and also, they get higher when the vehicle gets higher. Queue generation has been predicted successfully. In the graph of comparing actual queue vs predicted queue, predicted queue was shifted to negative region when there is no actual queue. This issue also can be removed with high number of data sets. Actual queue was predicted with good accuracy. As this project is a transportation project which consists of vehicle movements, this range of accuracy is acceptable.

References

Dash, S., Mohapatra, S.S. and Dey, P.P. 2019, 'Estimation of critical gap of U-turns at uncontrolled median openings', Transportation Letters, 11(5), pp. 229–240.

Jenjiwattanakul, T. and Sano, K. 2011, 'Effect of Waiting Time on the Gap Acceptance Behavior of U-turning Vehicles at Midblock Median Openings, Eastern Asia Society for Transportation Studies.

Jenjiwattanakul, T., Sano, K. and Nishiuchi, H. 2015, U-turn Waiting Time Estimation at Midblock Median Opening, Eastern Asia Society for Transportation Studies.

Mohanty, M., Dey, P.P. and Panda, B. 2020, 'Assessment of traffic safety at median openings using surrogate safety measures: A case study in India', European Transport - Trasporti Europei, (80), pp. 1–12.

Omarov, M., Ismail, S., Rani, W.N.M.W.M., and Durdyev, S., 2022, 'Estimation of traffic delay due to u-turns at uncontrolled medians: Case study in phnom penh, cambodia', Sustainability (Switzerland), 14(1).

Rajashekhara, M.R. 2014, 'Characteristics of Development and Dissipation of Queue Length Under Mixed Traffic Conditions IJERTV3IS070997', International Journal of Engineering Research & Technology (IJERT).

Sandaruwana A., Karunarathne, T. and Wickramasinghe C, V. 2019, Estimating Critical Gap at Roundabout under Mixed Traffic Conditions in Sri Lanka, Eastern Asia Society for Transportation Studies.

Sharma, V.K., Mondal S., Gupta A., 2017, Analysis of U turning behavior of vehicles at mid-block median opening in six lane urban road. Traffic and Transport Engineering, 7(2): 243 - 255

Mohanty, M. and Dey, P.P. 2020, 'Modeling the lane changing behavior of major stream traffic due to U-turns', Transportation Engineering, 2(July), p.100012.

Mohanty, M. and Dey, P.P. 2019, 'Modeling the major stream delay due to U-turns', Transportation Letters, 11(9), pp. 498–505.

Davidson, Russell and James G. MacKinnon 1993, "Estimation and Inference in Econometrics". Oxford: Oxford University Press.

Li, B., Cheng, W., and Li, L., 2018, "Real-Time Prediction of Lane-Based Queue Lengths for Signalized Intersections". Journal of Advanced Transportation, 2018, pp.1-18.

Anusha, S. P., Lalitha Devi, V. and Anuj Sharma, 2013,"A Simple Method for Estimation of Queue Length". Civil Engineering Faculty Publications. 48

Rathnayake, I., Amarasinghe, N., Wickramasinghe, V., and Liyanage, K., 2022, "SLIIT International Conference on Engineering and Technology", Malabe, Sri Lanka, Vol. 01

Estimating the Delay Caused by Side Friction near 'School Zones'

Balasooriya B.M.P.M., Hewage A.H.T.A.S., Wickramasinghe W.M.V.S.K.*

Department of Civil Engineering, University of Peradeniya, Sri Lanka

**vskw@pdn.ac.lk*

Keywords: Side friction, Traffic engineering, Transportation engineering, Delay, School zones, Index, Speed, Density

1. Introduction

Smooth traffic flow in the transportation network is the expectation of all stakeholders. However, due to numerous reasons, such smooth flows cannot be achieved in road network. Accidents, junction controls, driver behavior, mixed traffic situation are some such influencing factors towards non uniform traffic flow in the road network. On top of that roadside activities also contribute significantly for the non-uniform traffic flows. Among such roadside activities, on-street parked vehicles, bus stops, walking pedestrians, pedestrian crossings, roadside vendors, left side overtaking, etc. contribute heavily on mainstream traffic characteristics. Such roadside disturbances are defined as "Side Friction". School zones are places where such side friction is very much significant. Most of the schools in major cities are located by the side of arterial roads. Due to this, a noticeable disturbance can be witnessed to the mainstream traffic within school zones. Unless this side friction is kept under some allowable limit, excessive delay will be occurred in the mainstream traffic flow and finally causing a significant reduction in Gross Domestic Product (GDP), and ultimately to the economy of the country. This research is based on quantify the delay due to the side friction near school zones. So that the outcome of this research can be used to compare delay caused due to side friction among different schools in the country and can provide sufficient measures.

2. Literature review

There are many studies available regarding the influence of roadside frictions on traffic characteristics of urban arterials. Most of them were conducted under mixed traffic conditions. Since Sri Lanka has a mixed traffic situation, this section is focused on literature related to analysis of side friction under mixed traffic situations. Although it is generally known that roadside friction activities reduce usual traffic flow speed and hence increase travel time, it is a very critical scenario to quantify that influence. There have been only few studies that attempt to quantify this influence.

Gulivindala and Mehar (2008) have performed a study to analysis the side friction with the field data collected on four-lane divided road section in India. Side friction elements such as pedestrian movements, on-street parked vehicles, entry and exit movements of vehicles and wrong movements of vehicles were identified and frequency of each element were recorded. Then relative weights were assigned to each type of the side friction element and total side friction was estimated with the help of weights multiplied by the frequency of side friction. In here, multiple linear regression analysis technique was used to estimate relative weights. Finally, authors have proposed a speed prediction model to estimate average speed under varying traffic flow rates and side friction levels by using multiple linear regression analysis. Salini et.al (2014), Singh and Kumar (2021) also developed speed models incorporating various side friction parameters by using regression analysis. In all above studies, the video recording technique was used as the data collection method.

There are few studies reported from India where attempts were made to analyze the effect of bus stops on heterogeneous traffic. Salini et.al (2014) have done research on quantitative analysis of the impact of bus bays and curbside bus stops on traffic flow characteristics of urban roads and found that reduction in capacity is more in case of curbside bus stops compared to bus bays in which the reduction is negligible. They have considered frictional parameters including dwell time of buses at bus stops, number of pedestrians walking along sides of carriage ways, number of parked vehicles, influence time of parking operations, and number of parking maneuvers for on-street parking. Other variables such as the frequency of buses stopping at bus stops, pedestrians crossing at random, and the type of parking were not included in the analysis because the variations in these variables were found to be limited and

thus regarded as relatively less significant. Then speed model was developed incorporating above side friction elements using regression analysis. Rao et.al (2016) have also done research focused on dwell time of buses and frequency of buses in addition to the accumulation of on street parked vehicles to analyze effect of the roadside friction on travel speed and capacity of urban arterials in Delhi. Video cameras were used to collect the traffic data and a number plate survey was conducted to find intensity of on-street parking. GPS was used to collect segmental speeds over the selected section using floating car technique. Then speed density models were developed using both static and dynamic PCUs. The best fitting Speed-Flow model was selected for further estimating the speed flow relationship and estimated the capacity. The study concluded that bus bays and bus stops resulted in a significant reduction in travel speed and road capacity compared to without side friction condition and, the dwell time of buses have a significant impact on capacity.

In most research, regression analysis simply considered the average speed of the traffic stream, and mode-wise speed variation was not addressed. However, the impact from side friction on speeds of various vehicle categories is important especially in Asian countries as each vehicle category exhibits different speed characteristics on urban roads. Singh and Kumar (2021) have done research on this type of mode wise speed variation due to presence of side friction.

3. Methodology

3.1 Site selection and data collection

For this research, schools in major cities located by the side of the arterial roads were selected for data collection which is having side frictional influence. According to the scope of the research, schools were selected on undivided two-lane urban arterials located away from signalized intersections, major pedestrian activity centers and such obstacles nearby to eliminate those influences. Drone surveys were employed at each section to capture the traffic flow parameters and the side friction details. Then vehicular speeds were extracted by a tracking software, called 'Tracker', and side friction parameters were counted manually.

3.2 Data analysis

In this research, on street parked vehicles, curbside bus stoppings, entry and exit vehicles, left side overtaking, pedestrians who are stationary, walking along and crossing the roads were considered as the side friction components. A special index called '*Side Friction Index (SFI)*' was created pertaining to a length along the main road of 10m stretch. For defining the side friction index, an imaginary grid was generated on the influencing area of road section and each grid cell was assigned with a weight factor which were increasing towards the road center.

3.3 Weight factors

The entire road was divided into 10m stretches along the longitudinal directions. For a one 10m stretch, it was sub divided in to 3 sections along the transverse direction namely grid 1, gride2 and grid 3. Grid 1 lies in between the end of the pedestrian sidewalk and the edge line of the road. It was inclusive with the hard and soft shoulders but exclusive with the pedestrian sidewalk. Then the lane was divided into two equal sections namely grid 2 and grid 3. When defining the weights, it was taken that negative impact occurs due to a pedestrian was directly proportional to the distance travelled from the edge of the pedestrian sidewalk. The effect created by a pedestrian stand at the center of the grid 1, was taken as 1 unit and relative weights were calculated relative to that effect.

- Weight for grid 1 = $\frac{a}{a}$ =W_1= 1
- Weight for grid 2 = $\frac{b}{a}$ = W_2
- Weight for grid 3 = $\frac{c}{a}$ = W_3

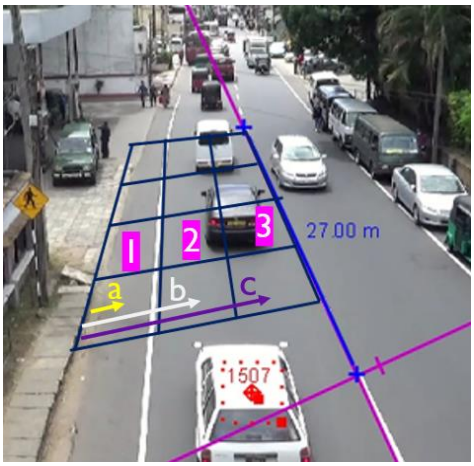

Figure 1: Grid system used in the study

3.4 Equivalent pedestrian unit (epu)

All identified side friction components were converted into equivalent pedestrian units

(EPU) which is defined to standardize the side friction unit. The EPU value gets from dividing the projected area of side friction component by standard projected area of a pedestrian and multiplied with a coefficient (C_0) which is based on static or dynamic condition of the side friction activity as shown in equation1. In here, coefficient for static activities was assumed as 1.0 and for the dynamic activities, the same coefficient was found as 1.41 from the analyzing the data.

$$EPU = \frac{\text{Projected area of the side friction componennt}}{\text{Standard projected area of a pedestrian}} \times C_0 \ldots\ldots\ldots\ldots (1)$$

3.5 Side Friction Index (SFI)

To calculate the SFI, three grid cells were selected on transverse direction as shown in figure 2 and total EPU value of each grid cell was multiplied with the relevant weight factor. Then the cumulative value of all above three values represent the side friction index for a particular transverse section which is of 10m in length. Thereby, SFI values for each transverse section along the longitudinal direction can be estimated. Equation (2) will be used to estimate the side friction index.

$$SFI = \sum_{i=1}^{3} (\sum EPU)_i \times W_i \ldots\ldots\ldots\ldots\ldots\ldots (2)$$

Where, i refers to the i^{th} grid cell in transverse direction (i=1,2,3)
$\sum EPU$ are the total equivalent pedestrian units presented in a grid cell and Wj is the weight factor of i^{th} grid cell.

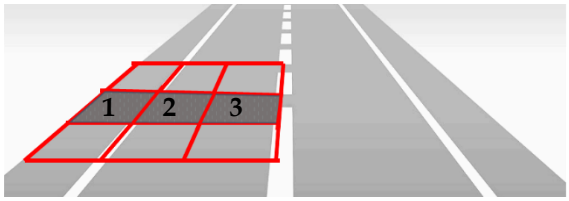

Figure 2: Selection of grid cells when estimating SFI

3.6 Data extraction

Vehicles maintaining average speeds inside 10m stretches were extracted through the tracking software and at the same time, the road densities were recorded. The side friction indices when the vehicle is at the beginning and at the halfway of the 10m stretch were recorded. Average of these represents the side friction index experiencing by the vehicle. When the side friction components presence in multiple transverse grids (mostly due to pedestrian crossing the road, wrong movement of vehicles, vehicle entry and exit), the cumulative effect of it was taken into consideration. When there are influences by nearby 10m stretches due to side friction events occurring at them, that effect also included in the side friction index.

4. Results

4.1 Speed prediction model

Multiple linear regression analysis was performed making density of the road and the SFI as the independent variables while keeping the average speed as the dependent variable.

Table 2: Regression statics

Parameter	Value
Multiple R	0.751553
R Square	0.564831
Adjusted R Square	0.561112
Standard Error	1.667266
Observations	300

Table 3: Regression outcomes

	Coefficients	*Standard Error*	*t Stat*	*P-value*	*Lower 95%*	*Upper 95%*	*Lower 95.0%*	*Upper 95.0%*
Intercept	28.92	0.7793	37.1177	4.96E-100	27.3936	30.4646	27.3936	30.4646
Density (pcu/km)	-0.1078	0.00829	-12.9995	1.915E-29	-0.1242	-0.0915	-0.12421	-0.09152
Side Friction Index	-0.08112	0.01279	-6.3379	1.185E-09	-0.10634	-0.0559	-0.10634	-0.0559

Since the p values for the independent variables are well below the significance values as shown in above tables, indicating that side friction has impact on the average speed of the vehicle.

V = - 0.1078K - 0.08112(SFI) + 28.92 ……..… (3)

V = Average vehicular speed (km/h)
K = Density on the road (PCU/km)
SFI = Side friction index

4.2 Average speed Vs density graphs

Average speed maintained inside 10m stretches were plotted against density of the road with different side friction ranges. When the side friction increases, the curves got shifted downwards and showing that side friction has some negative impact on vehicular speeds.

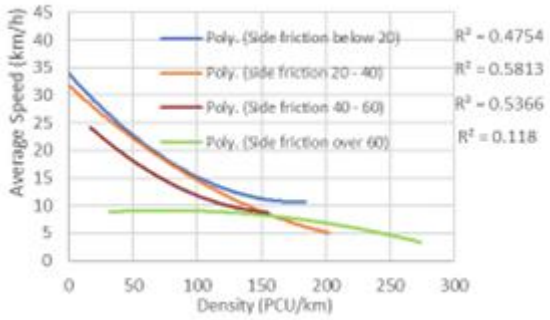

Figure 3: Average speed vs. density graph

4.3 Average speed Vs. SFI graphs

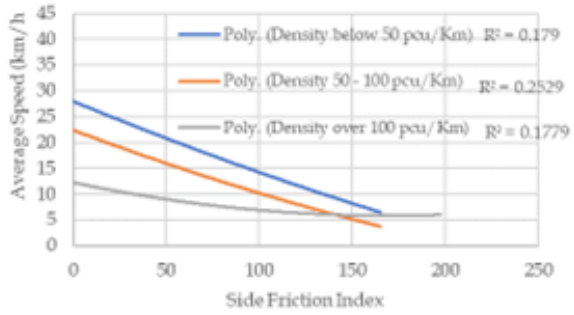

Figure 4: Average speed vs. SFI

When the road density is below 100 PCU/km, side friction has a greater influence on the mainstream vehicles. With a small increment of side friction condition on the road, a noticeable speed reduction can be expected when the road density is below 100 PCU/km. When the mainstream density goes beyond 100 PCU/km, platoon effect becomes dominant over the effect of the side friction. Therefore, large increment of side friction gives a small speed reduction on the mainstream vehicles and when after the SFI becomes 125, speed tends to be constant emphasizing that platoon effect is dominant.

5. Conclusions

By observing the results obtained, there is a significant influence on mainstream vehicular speeds due to the side friction near school zones. Further that impact increases when the prevailing side friction increases. When the density of the road exceeds a certain level (100 PCU/km), the side friction cannot make much impact on the vehicular speed as it is totally governed by the prevailing road traffic conditions. (i.e., effect of the platoon). On the other hand, when considering uncongested situations, the vehicular speeds are decided by the side friction effect. According to the resulted average speed vs. density graphs, green shields model is slightly deviating when low side friction condition presences and highly deviating when the side friction increases.

References

Biswas, S., Chandra, S. and Ghosh, I., 2021. Side friction parameters and their influences on capacity of Indian undivided urban streets. International Journal of Transportation Science and Technology.

Irawati, L., 2015. Delay Evaluation as the Impact of Side Friction on Heterogeneous Traffic Towards Road Performance with Vissim Microsimulation. Department of Civil Engineering, Faculty of Engineering Semarang University Jln. Arteri Sukarno HattaSemarang.

Gulivindala, P. and Mehar, A., 2018. Analysis of side friction on urban arterials. Transport and Telecommunication, 2018, volume 19, no. 1.

Salini, S., George, S., Ashalatha, R., 2014. Effect of Side Frictions on Traffic Characteristics of Urban Arterials. Transportation Research Procedia 17 (2016).

Singh, S. and Kumar, S., 2021. Dealing with Multicollinearity Problem in Analysis of Side Friction Characteristics Under Urban Heterogeneous Traffic Conditions. Arabian Journal for Science and Engineering.

Pal, S., Roy, S. 2015. Impact of roadside friction on Travel Speed and LOS of rural highways in India, Transportation in Developing Economics, volume 2, Issue 9.

Rao, A., Velmurugan, S. and Lakshmi, K., 2017. Evaluation of Influence of Roadside Frictions on the Capacity of Roads in Delhi, India. Transportation Research Procedia.

Hidayati, N., Sunarjono, S., Awad, S.A., Magfirona A., 2019. Different impact of side friction condition on traffic flow along Yosodipuro Street Surakarta.

Effect of Applying Area Correction in the Direct Shear Test

Chamika L.K.L., Chandima G.B.N.S., Udakara D. de S.*

Department of Civil Engineering, University of Peradeniya, Sri Lanka

**deepthiu@pdn.ac.lk*

Keyword: Direct shear test, Shear strength parameters, Cohesion, Friction angle, Corrected shear area, Circular shear box apparatus, Shear stress, Normal stress

1. Introduction

A direct shear test is a common method for measuring the shear strength parameters of various types of soil. The direct shear test is widely used because of its simple principle, convenient operation, and low cost. The accuracy of shear strength parameters is directly related to the safety and economy of engineering design and construction.

Normally, the shear area is kept constant during the direct shear test calculation. However, during the test, the lower shear box is fixed in the horizontal direction. As the experiment continues, the upper shear box is gradually moved, and the effective area of the sheared soil is dynamically reduced. When the shear displacement is large, the change in shear area is considerable. If the shear strength of the soil sample is calculated with the initial area, there will be an error.

2. Literature review

Many scholars have proposed the calculation method for effective shear area and stress. Zhan et al. studied the calculation error from the diameter of the circular box and the shear stress and proposed that the sample box should be made into a small upper box and a large lower box to eliminate the error caused by the reduction of the shear area. Xu et al. established a normal stress correction model that divides pressure by effective area. They believed that the change in the shear area should be considered in the calculation of shear stress.

Wang obtained the equation of effective shear area and shear stress by calculating the integral of the shear area. It was found that when the shear displacement reached 4 mm, the difference in shear stress before and after correction reached about 10%. Considering the change in shear area, Ge et al. studied the variation of stress and strength parameters in the rock mass structural plane. Yu et al., Dong and Wang, considered the shear surface fluctuation caused by the eccentricity of normal stress in the shear process. Based on the waveform shear surface

calculation model, the effective shear area was corrected. In summary, many scholars have reached a consensus on the issue that the change in shear area will affect shear stress and normal stress. However, due to the different simplifications of the direct shear test calculation model, the calculation models of effective shear area and stress are diverse, and the analysis of shear test results is also different. It is difficult to generalize the results of standard direct shear tests.

3. Methodology

Firstly, soil samples were collected from the Wilgamuwa and Ela Hera areas. All the samples are collected from the 1 ft depth at the existing ground level. For this study, 15 soil samples were assessed. Then a sieve analysis test was carried out according to BS 1377: Part 2 and the soil according to the British Standard Classification System (BS 5930:1981). Sieve analysis test data were presented as a size distribution curve. Then the soil samples were classified using the BSCS table. Then the dry density (Dd) of soil samples was determined by using BS 1377: Part 4. Further, the vibrating hammer method was used for the maximum dry density (Dd, max) calculation. The relative density (ID) was used at 95% in sample preparation.

$$ID = \left(\frac{Dd - Dd,min}{Dd,max - Dd,min}\right)\left(\frac{Dd,max}{Dd}\right) \quad \text{.....(1)}$$

Then the direct shear tests were carried out according to BS 1377: Part 7. First, the cohesion and friction angle values at the ultimate and peak values for each sample were identified. Then, take all those values and keep them without applying area correction for calculating stress values. This means that throughout the shear displacement, the contact area is considered constant. The same shear box

apparatus has been used for all the direct shear tests. First, the graph between horizontal shear displacement vs. shear stress values.

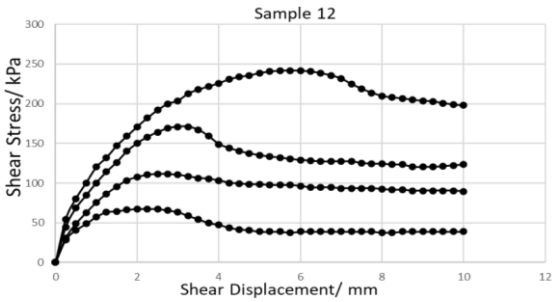

Figure 1: Variation of shear displacement vs. shear stress of sample 12

From that, identified the ultimate and peak shear stress values accordingly. Then obtained the variation between normal stress vs. shear stresses.

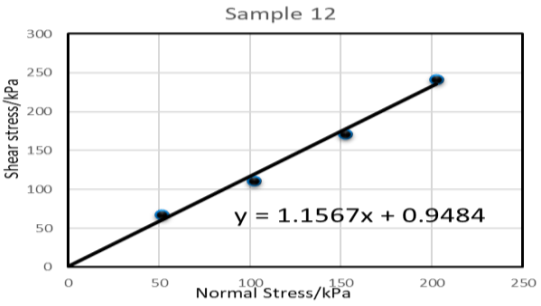

Figure 2: Variation of normal stress vs. shear stress for peak values

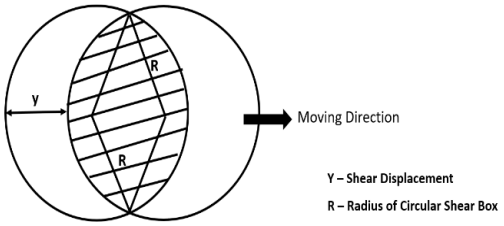

Figure 3: Shear area variation for direct shear test

For the constant normal load, by increasing the shear force, the upper shear box is moving horizontally. As a result of that, the contact area is decreasing. By considering that aspect, the correction equation was derived as

$$A_c = \frac{\cos^{-1}(\frac{y}{2R})}{360^\circ} 4\pi R^2 - y\sqrt{R^2 - \frac{y^2}{4}} \quad \ldots\ldots\ldots (2)$$

A_c = corrected shear area (mm^2),
Y = shear displacement (mm),
R = radius of circular shear box (mm).

Further, all calculations were done using an Excel sheet. Finally, compare the shear strength parameter results, considering with and without applying area correction.

Figure 4: Shear displacement Vs. shear stress for sample no.12

The error between the uncorrected shear stress and the corrected value is also related to the normal stress, which will increase with the increase of the normal stress.

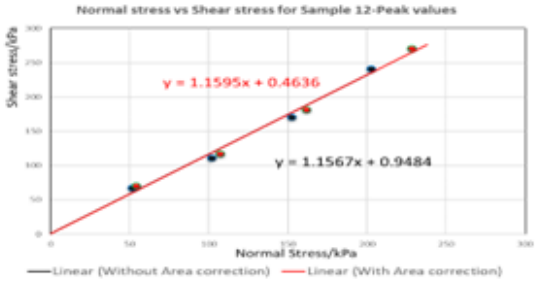

Figure 5: Variation of normal stress vs. shear stress for peak values

4. Results and discussion

Table 01: Summary of results

Soil Sample	Ultimate Shear Stress Parameters				Peak shear stress Parameters			
	Without Area Correction		With Area Correction		Without Area Correction		With Area Correction	
	C0/kPa	ϕ0/°	C0/kPa	ϕ0/°	C0/kPa	ϕ0/°	C0/kPa	ϕ0/°
1	51.11	38.48	56.59	39.82	76.97	38.06	82.90	38.25
2	7.56	46.34	10.1	46.16	16.33	49.16	19.97	48.32
4	22.01	34.75	24.37	35.18	51.85	35.88	53.64	35.95
5	38.29	44.14	45.29	43.45	56.13	41.35	63.13	41.25
6	7.85	44.99	12.35	46.98	3.96	54.63	3.42	54.78
7	2.03	46.72	12.16	45.74	27.99	44.74	30.83	44.52
8	9.41	47.42	14.15	47.55	22.14	51.69	24.78	51.46
9	8.35	44.20	7.38	44.71	18.79	47.13	19.40	47.59
10	0.54	43.08	2.42	42.05	9.28	51.24	9.89	51.26
11	5.22	47.05	4.14	47.4	15.41	48.65	16.16	48.7
15	18.51	44.69	19.84	45.07	27.38	51.26	29.53	51.35

When shear displacement increases, the effective shear area gradually decreases. Therefore, when area correction is applied, corrected values for shear stress become higher than initial shear stress values. According to Table 1, with area correction, the corrected cohesion value is increased for both the peak and ultimate stages. For small cohesion values, the correction is

small, and as the cohesion value increases, the correction value becomes significant. When the area correction is applied, there is no significant influence on friction angle values for both the peak and ultimate stages.

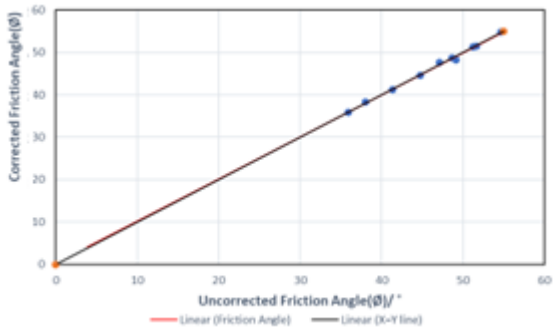

Figure 6: Variation of friction angle with and without applying area correction at peak stage

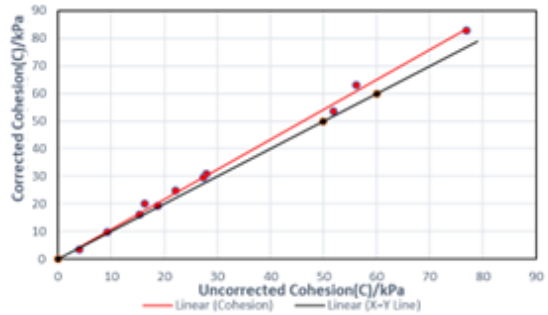

Figure 7: Variation of cohesion with and without applying area correction at peak stage

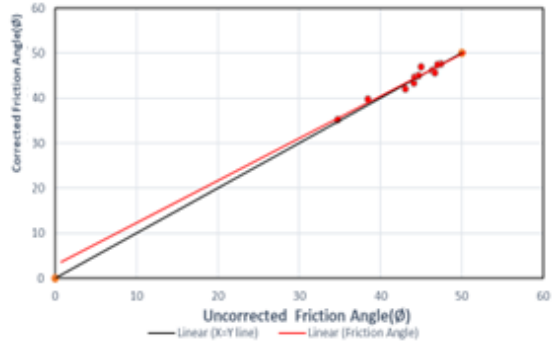

Figure 8: Variation of friction angle with and without area correction at ultimate stage

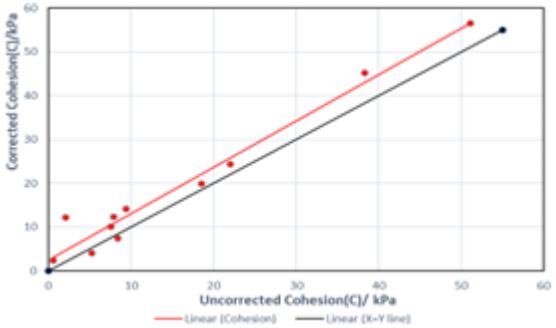

Figure 9: Variation of cohesion with and without applying area correction at ultimate stage

According to Figure 6 and Figure 8, the y = x line and the friction angle comparing line coincide. Therefore, there is no significant difference between the corrected friction angle and the uncorrected friction angle of the peak and ultimate values. According to Figure 7 and Figure 9, there are significant differences between corrected cohesion and uncorrected cohesion values for peak and ultimate values. Also, with the increase in cohesion value, the difference increases.

According to the observations, with increasing shear displacement, the effective shear area is gradually decreasing. Therefore, when area correction is applied, corrected values for shear stress become higher than initial shear stress values. Further, with area correction, the corrected cohesion value is increased for both peak and ultimate values. For small cohesion values, the correction is small, and as the cohesion value increases, the correction value becomes significant. When the area correction is applied, there is no significant influence on friction angle values for both peak and ultimate.

5. Conclusion

There is a considerable influence on the cohesion value of soil samples when area correction is applied. Therefore, area correction is recommended for the cohesion value. However, there is no considerable influence on the friction angle value of soil samples. Therefore, area correction is not needed for friction angle values.

References

Sarunas S. Tadas T.A. 2014, 'Direct shear tests with evaluation of variable shearing area' Vilnius Gediminas Technical University. Civil and transport engineering, Aviation technologies 6(5): 499-503.

Sun Z, at el. 2019, 'Direct shear test of silty clay based on corrected calculating model' International conference on oil and gas engineering and geological sciences. Shandong Agricultural University, Taiwan, China.

Wang W. 2006 'Research and application of soil-structure interface model based on energy dissipation principle'. Hohai University.

Zhan, et al. 2007 'Effect of effective shearing area on result of direct shear tests. J Journal of Hohai University (Natural Science, 35(2): 213-216.

Stability Analysis of Road Embankment Constructed by Treating Marginal Soils with Geopolymer Based Stabilizers

Tharshsany S., Shagiththiya S., Nasvi M.C.M.*

Department of Civil Engineering, University of Peradeniya, Sri Lanka

**nasvimcm@eng.pdn.ac.lk*

Keywords: Embankment, Fly ash, Rice husk ash, Stabilized soil

1. Introduction

Embankments are widely used in road construction. Embankment used in Sri Lanka should meet the specification provided in RDA guide (ICTAD SCA/5 (2009)**.** There is a shortage in suitable embankment materials in the vicinity of the construction site, and as a result, good quality embankment materials are hauled from long distances with high cost. Treating the marginal soils in the vicinity of the project site is one of the best options to reduce the energy, time and cost related to the long hauling distances. Chemical soil stabilization is becoming increasingly popular method for improving the engineering properties of soil. Additionally, chemical stabilization is often cost-effective compared to other methods. Cement and lime are commonly used stabilizers.

Power generation produces large amount of fly ash (FA) and become available as a by-product of coal-based power stations. Soil stabilization with rice husk ash (RHA) is the mostly recommended method for rice-producing regions where RHA is accessible at low cost. Muntohar, (2009) concluded that lack of cementitious properties of RHA doesn't allow it to be used solely in the soil stabilization. Geopolymer (GP) is a type of inorganic polymer which can be produced from a variety of raw materials such as fly ash, slag, clay, and other industrial by-products. It is commonly made of alkali-activated aluminosilicate materials and produce low CO_2 emission and energy consumption. Mixing of Geopolymer within the soil matrix promotes enhanced unconfined compressive strength (Phummiphan et al., 2016).

There are limited studies focusing on the stability analysis of embankments constructed by treating marginal embankment materials with GP based stabilizers. In this research, feasibility of using FA-based-GP and FA+RHA-based-GP to stabilize embankment material, which is not suitable at its natural condition, was analysed. This study contains experimental and numerical works.

2. Materials

Undisturbed and disturbed two different marginal soil samples which do not satisfy the RDA requirement for the embankment material was collected at two locations from the borrow pit of the iRoad project area, Naula, Sri Lanka. Table 1 shows liquid limit (LL), plastic limit (PL), maximum dry density (MDD) and 4 days soaked CBR at 95% MDD (CBR_4days) for location 1, 2 compared with RDA requirement.

Table 1: Properties of L1 and L2 compared with RDA requirement

Property	**RDA requirement**		**L1**	**L2**
	Type I	Type II		
LL **(%)**	≤50	≤55	50.5	39.8
PL **(%)**	≤25	≤25	23	28
MDD **(kg/m^3)**	≥1600	≥1500	1906	1785
CBR_4days **(modified) (%)**	≥7	≥5	1	2

Type of FA used for our project is ASTM class F FA and it was collected from Lakvijaya coal power plant, Norochcholai, Sri Lanka. Rice husk ash samples were collected from the rice mills in Divulapitiya, Negombo, Sri Lanka.

3. Methodology

3.1 Experimental work

Particle size analysis (BS 1377 -2:1990), Atterberg limit test (BS 1377 -2:1990), Modified Procter compaction test (BS 1377 -4:1990),) Unconfined compressive strength (UCS)test (BS 1377 -7:1990), California bearing ratio (CBR)test (BS 1377 -4:1990) and Falling head permeability test (BS 1377 -5:1990) were conducted to determine the index properties of raw soil obtained from two locations.

PL of L2 and CBR value of both locations did not meet RDA requirement according to the Table 1.

L2 was selected as the critical soil for stabilization.

It has been found that 30% Geopolymer paste, 8M NaOH, 2.5 Na_2SiO_3/NaOH and 2 FA/Alkali activators are the optimum composition of FA-GP mix (Arul et al., (2016); Mustafa et al., (2013); Dungca et al., (2017)). It has also been found that replacement of 60% FA by RHA reflects higher strength (Poltue et al., 2019; Dungca and Ephrem, 2017). Fly ash based geopolymer stabilized soil (FA-GP-SS) and fly ash rice husk ash based geopolymer stabilized soil (FA-RHA-GP-SS) were prepared in proportion mentioned above. Cohesion and friction angle values of raw soil, FA-GP-SS and FA-RHA-GP-SS were obtained from relevant literature (Kumar et al., 2014; Raj et al., 2016) and other geotechnical properties of two stabilizer systems were determined from a series of experiments.

3.2 Numerical study

Model geometry and corresponding subsoil properties were adopted from the literature (Khan and Abbas, 2014) as shown in Figure 1. Embankment with 30^0 slope and 4 m height was considered in preliminary analysis. A parametric study was conducted by changing the embankment height and slope angle and the corresponding factor of safety (FOS) values were obtained from Slope/W software and PLAXIS 2D software. Height of the embankment were changed to 6m, 8m and 10m. For each height, Slope angle was modified as 45^0 60^0 and 75^0. For the numerical study, subsoil properties obtained from literature (Chaiyaput et al.,2012) is shown in Table 2.

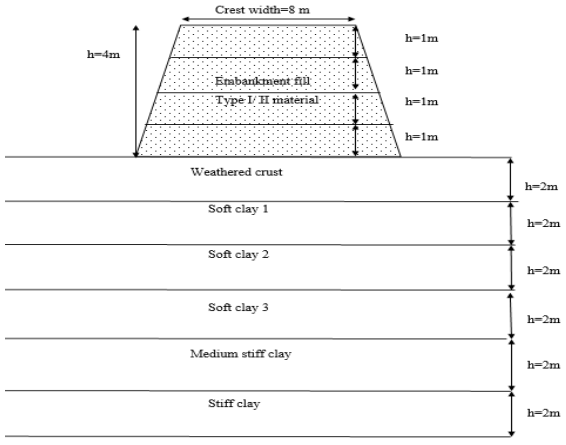

Figure 1: Embankment section with 4 m height and 30^0 slope.

In Slope/W, stability was checked using ordinary method (OM), bishop simplified method (BSM), Jambu simplified method (JSM), Spencer simplified method (SSM) and Morgenstern Price method (M-PM). PLAXIS 2D 8.6 software was utilized to conduct the Finite Element (FE) analysis. FOS was determined using the phi-c reduction method in PLAXIS 2D.

Table 2: Properties of subsoil layer (Chaiyaput et al., 2012)

	Weathered crust	Soft clay 1	Soft clay 2	Soft clay 3	Medium stiff clay	Stiff clay
Model	MCM	SSM	SSM	SSM	MCM	MCM
Material behavior	Undrained	Undrained	Undrained	Undrained	Undrained	Undrained
γ_{sat} (kN/m^3)	17	15	15	15	17	19
γ_{dry} (kN/m^3)	15	13	13	13	15	17
E (kN/m^2)	3000				5000	9000
kx (m/day)	0.002	0.0008	0.0008	0.0008	0.0004	0.004
Ky (m/day)	0.001	0.0004	0.0004	0.0004	0.0002	0.002
c (kN/m^2)	10	3	3	3	10	30
Φ (degree)	23	23	23	23	25	26
v	0.25				0.25	0.25
λ *		0.14	0.14	0.14		
K *		0.028	0.028	0.028		
OCR		1.55	1.4	1.3		

4. Results and discussion

4.1 Experimental results

Atterberg limit values of raw soil, FA-GP-SS and FA-RHA-GP-SS are shown in Table 3. Plasticity characteristics of the soil decreases with addition of FA-GP. Binding effect can decrease the liquid limit of the soil, making it less plastic.

Compaction curves for raw soil, FA-GP-SS and FA-RHA-GP-SS are shown in Figure 2. MDD decreases with addition of FA-GP due to presence of carbon content and lower specific gravity. Increase in OMC shows the need of hydration reaction for cementitious FA and to release the capillary tension from the greater exposed surface of the finer FA particle. When 60% of FA is replaced by RHA, MDD decreases further due to comparatively low specific gravity. As RHA has finer particles, more surface area needs more water to provide better lubrication. Pozzolanic reaction of RHA-GP is also attributed to an increase in OMC (Sarkar et al.,2015).

Table 3: Atterberg limits values

Property	Raw soil	FA-GP-SS	FA-RHA-GP-SS
LL (%)	39.8	32.6	27.5
PL (%)	28	24.5	22.5
PI	11.8	8.1	5

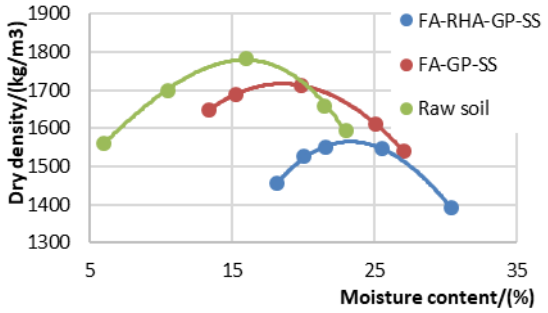

Figure 2: Compaction test results

The 4-day soaked CBR values at 95% MDD of the soil were significantly improved with the addition of FA-GP as well as with the incorporation of RHA, resulting in CBR values of 8 and 7, respectively, compared to the raw soil which had a CBR value of 2. Average Unconfined Compressive Strength (UCS) values for FA-GP-SS and FA-RHA-GP-SS were 1523 kPa and 1103 kPa, respectively whereas the average CBR for raw soil was 259 kPa as shown in Figure 3. As FA contains high silica and alumina content, it forms silica and alumina hydrates which development in the strength in the geo-polymerization. The addition of FA-GP without replacement of RHA resulted in a higher compressive strength value compared FA-RHA-GP-SS.

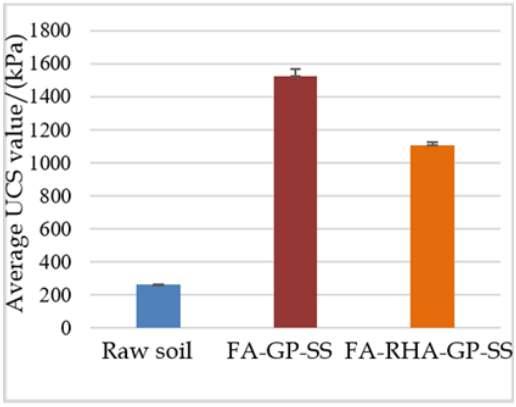

Figure 3: Average UCS values

When FA-GP and FA-RHA-GP were added to the raw soil, permeability decreased. Pozzolanic material (FA and RHA) tends to absorb the vacant space in the pore composition and significantly cuts down the permeability. Increase in cementitious content may also be a reason for the decline in permeability.

FA-GP-SS and FA-RHA-GP-SS resulted in Type I materials, as per the RDA requirement. Hence, constructing a homogeneous embankment using either FA-GP-SS or FA-RHA-GP-SS mixtures would be feasible.

4.2 Numerical results

4.2.1 Slope/W results

Critical slip surface for raw soil for a slope of height 4 m and slope of 30° is shown in Figure 4. The MPM method covers both force and moment requirements of static equilibrium. Hence it is extensively used in slope stability evaluation. MPM was used for comparison of Factor of Safety (FOS) values with PLAXIS 2D results (Ayob et al., 2019).

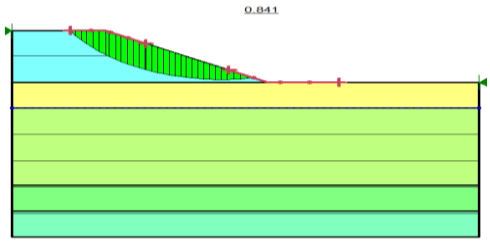

Figure 4: Critical slip surface for raw soil at height of 4 m and slope of 30^0

4.2.2 PLAXIS 2D results

The deformed mesh and critical slip surface of the embankment with FA-GP-SS (4 m height and 30° slope) are illustrated in Figures 5 and 6, respectively.

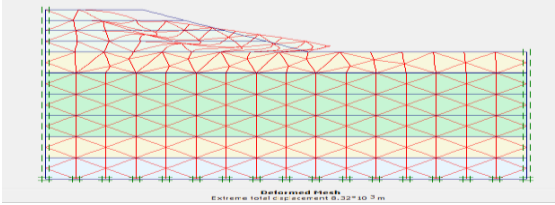

Figure 5: Deformed mesh for the embankment with FA-GP-SS (4 m height and 30^0 slope)

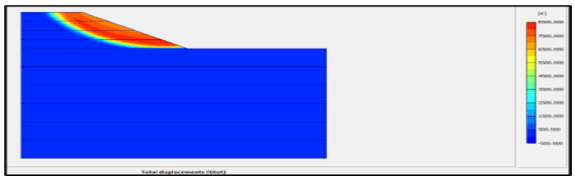

Figure 6: Critical slip surface for the embankment with FA-GP-SS (4 m height and 30^0 slope)

Table 3 presents the FOS values obtained for the raw soil, FA-GP-SS, and FA-RHA-GP-SS at a height of 4 m and different angles, as calculated using PLAXIS 2D and Slope/W.

Table 3: FOS values for raw soil, FA-GP-SS, and FA-RHA-GP-SS at a height of 4m and different angles

Slope	**For embankment height of 4 m**		
		Slope/W	PLAXIS
30^0	Raw soil	0.841	0.749
	FA-GP-SS	2.926	2.833
	FA-RHA-GP-SS	2.024	1.927
45^0	Raw soil	0.622	0.524
	FA-GP-SS	2.722	2.629
	FA-RHA-GP-SS	1.822	1.723
60^0	Raw soil	0.522	0.425
	FA-GP-SS	2.622	2.523
	FA-RHA-GP-SS	1.722	1.628
75^0	Raw soil	0.518	0.426
	FA-GP-SS	2.576	2.483
	FA-RHA-GP-SS	1.718	1.623

Table 4: FOS values from MPM method for raw soil, FA-GP-SS, and FA-RHA-GP-SS at different height and 30^0 slope

Height	**For embankment height of 30^0**		
		Slope/W	PLAXIS
4 m	Raw soil	0.841	0.749
	FA-GP-SS	2.926	2.833
	FA-RHA-GP-SS	2.024	1.927
6 m	Raw soil	0.716	0.621
	FA-GP-SS	2.816	2.723
	FA-RHA-GP-SS	1.915	1.816
8 m	Raw soil	0.630	0.535
	FA-GP-SS	2.731	2.634
	FA-RHA-GP-SS	1.832	1.737

FOS values obtained from both software were found to be consistent. Increasing the height and slope resulted in a reduction of FOS for raw soil, FA-GP-SS, and FA-RHA-GP-SS. The slope/W analysis was found to be insufficient in fully considering the stress-strain relationship of the soil. For the analysis of geotechnical problems, Plaxis2D was employed as a powerful and user-friendly finite element package (Ayob et al., 2019).

PLAXIS results were used to compare the strength improvement achieved by both mixes. Based on the FOS values obtained at different height and slopes, it can be concluded that both stabilizer mixes can be used as embankment materials since the FOS values were greater than 1. However, the FA-GP-SS performed better than FA-RHA-GP-SS.

5. Conclusions

A study was conducted to analyse the slope stability of embankments constructed using geopolymer based stabilizers using experimental and numerical techniques. Following conclusions can be drawn based on the findings.

Maximum dry density of fly ash based geopolymer stabilized soil (FA-GP-SS) and fly ash + rice husk ash based geopolymer stabilized soil (FA-RHA-GP-SS) reduced by 3.2% and 9.5% respectively compared to the raw soil and this is due to lower specific gravity of FA and RHA compared to raw soil. The moisture content (OMC) of both mixes was higher than that of raw soil.

Both unconfined compressive strength (UCS) and California bearing ratio (CBR) value of the FA-GP-SS and FA-RHA-GP-SS were higher than those of raw soil indicating an improvement in strength. This improvement may be attributed to repolymerization and the formation of cementitious compounds.

Factor of safety (FOS) values obtained from PLAXIS 2D and Slope/W software were consistent. FOS values of the embankment constructed with FA-GP-SS and FA-RHA-GP-SS were higher than the embankment made with raw soil for all height and slope angles analysed. Overall, both the FA-GP-SS and FA-RHA-GP-SS can be utilized in the construction of homogeneous embankments. Range of FOS values at considered height and slope, for FA-GP-SS and FA-RHA-GP-SS are 2.6-2.9 and 1.5-2.0 respectively. It should be noted that FA-GP-SS performed better than the FA-RHA-GP-SS.

References

Duncan JM. 1996, State of the Art: Limit Equilibrium and Finite-Element Analysis of Slopes. J Geotech Eng 1996; 122:577–96. doi:10.1061/(ASCE)0733-9410122:7(577).

Kumar, D., Kumar, N., Gupta, A. 2014. Geotechnical Properties of Fly Ash and Bottom Ash Mixtures in Different Proportions. International Journal of Science and Research (IJSR) Europe, 3(9):1487-1494

S.Chaiyaput, D.T.Bergado and S.Artidteang.2012. FEM 2D Numerical Simulations Reinforced Embankment on Soft Ground by limited life Geosynthetics (LLGS).

Novel Analytical Method to Predict the Geotechnical Engineering Properties of Clayey Soil Stabilized with Fly Ash

Jayalakshan S., Kowsikan K., Nasvi M. C. M.*

Department of Civil Engineering, University of Peradeniya, Sri Lanka

**nasvimcm@eng.pdn.ac.lk*

Keywords: Artificial neural network, Fly ash, Clay soil, Geotechnical properties

1. Introduction

Civil engineering project located in areas with inappropriate soils is one of the major problems in the world. Different methods can be selected for soil improvement such as hydraulic, mechanical, dynamical, physical, and chemical methods. Chemical soil stabilization is one of the widely used methods and this involves adding mineral additives to the clayey soil such as lime, silica, natural pozzolana, cement, slag, and fly ash. It is one of the suitable and economical methods for reducing both compressibility and plasticity but increasing both durability and strength.

Several laboratory investigations have been conducted to assess the effect of mineral additives on the geotechnical properties of soils. These laboratory studies are very beneficial for geotechnical engineers to obtain better practical results. However, laboratory tests are costly and take a long time for each study. For these reasons, analytical techniques are used to predict geotechnical properties. In addition, the analytical models have been applied as an effective approach with high performance compared with the statistical models.

There are several analytical tools and techniques are in the literature, such as artificial neural networks (ANNs) (Hanandeh et al., 2020; Leong et al., 2018), multivariable regression (MVR) (Adhikari et al., 2019; Ahmed et al., 2018), genetic programming (Hanandeh et al., 2020; Leong et al., 2018), etc. Among these techniques, ANN reflects the behaviour of the human brain, it allows computer programs to recognize patterns and solve common problems in the fields of machine learning and deep learning.

There are not any related literatures on ANN to predict soil parameters. There are very limited studies focusing on computer-based models for predicting the geotechnical properties of stabilized clayey soils whereas the previous studies showed the capacity of ANNs models in the prediction of different soil characteristics. This research used the ANN machine learning toolbox in MATLAB to develop correlations to predict the geotechnical properties of clayey soil stabilized with fly ash. The required parameters for the model including Atterberg limits, Maximum Dry Density (MDD), Optimum Moisture Content (OMC), Unconfined Compressive Strength (UCS), etc were collected from the literature. Data sets were used to develop independent model for fly ash stabilized clayey soil. The developed ANN model was validated by performing laboratory experiments for clayey samples stabilized with fly ash.

2. Methodology

2.1 Data collection and treatment

In this research, the data bases consisting of results collected from several experimental studies of different types of soil stabilized by using fly ash in the literature. Percentage of fly ash, CaO percentage, Plasticity Index (PI), MDD_n(MDD of natural soil(were chosen as input parameters for MDD model, percentage of fly ash, CaO percentage, PI (%), OMC_n(OMC of natural soil) were chosen as input parameters for OMC model and percentage of fly ash, CaO percentage, PI (%), UCS_n(UCS of natural soil) were chosen as input parameters for UCS_7d (7days UCS) and UCS_28d (28days UCS) models in fly ash stabilized clayey soil. According to the literature, these inputs affect the behaviour of the respective output. Therefore, these inputs were selected to develop respective model.

One method that is often used in regression settings is Cook's Distance Method (Gunasekera et al.,2020). Cook's distance method was used to detect and remove the outliers to improve the dataset for machine learning modeling. For MDD, OMC, UCS_7d and UCS_28d models 65, 89, 48 and 43 number of data were collected, respectively. After outlier removal 64, 86, 46 and 42 number of data were obtained, respectively.

2.2 ANN model development

The models were developed by using the Levenberg – Marquardt algorithm as training function. It was decided to use a three-layer feed forward – back propagating network with a tan-sigmoid function as the hidden layer transfer function and mean square error as the performance function. The best ANN model was determined by using trial and error method. It was preferred to use simple architecture of one hidden layer with limited number of neurons. Limited number of neurons were selected according to the better performance of the ANN model.

For this type of ANN model development needs at least 40 data sets (Gunasekara et al., 2020, Bahmed et al., 2017). The database was divided into three parts: training (70%), testing (15%) and validation (15%) (Gunasekara et al., 2020, Bahmed et al., 2017). The training data set was used to train the ANN model, the validation data set was used to stop the learning process and all testing data set was used to assess the ANN model performance after completion of the training process.

The ability of the proposed ANN models was checked using a new set of data obtained by other results from another research. Regression value R, mean square error (MSE) and mean absolute percentage error (MAPE) were used to check the efficiency of ANNs models. Mean square error is the average squared difference between output and target. Lower values are better, zero means no error. Regression R values measured the correlation between outputs and targets. R value 1 means close relationship and, 0 means random relationship.

2.3 Model validation through experiments

The model validation was done by using independent laboratory test results. Raw expansive soil was collected from Hettipola hospital site, Mahiyanganaya, Sri Lanka. The PI of raw soil is 23%. Based on the trial mixers it was found that 7% and 15% of bentonite mixed soil satisfied the required PI (25% - 50%) range for the expansive soil. 7% and 15% bentonite mixed two soil samples were prepared. According to the ranges of soil properties in the data collection, two different percentage of fly ash (15% and 25%) were mixed with the two samples. Then the natural soil samples and fly ash stabilized samples were used for the experimental procedure. Proctor compaction test was used to find the MDD and OMC. Unconfined compression test (BS1377: Part 7: 1990) was used to find the UCS of 7 days and 28 days.

3. Results and discussion

3.1 MDD model

The architecture of one hidden layer constituted of 14 neurons makes the better performance model for predicting the MDD. According to Figure 1, the training data set has high performance compared to the validation and target data sets. The regression value (R) of all data for MDD model was approximately 0.9759. The mean squared error (MSE) for training, validation and testing data set are 0.0038, 0.1927 and 0.3342 respectively.

3.2 OMC model

The architecture of one hidden layer constituted of 19 neurons makes the better performance model for predicting the OMC. As shown in Figure 2, the regression value of all data for OMC model was approximately 0.9739. The MSE for training, validation and testing data set are 0.1155, 7.0421 and 5.1819 respectively.

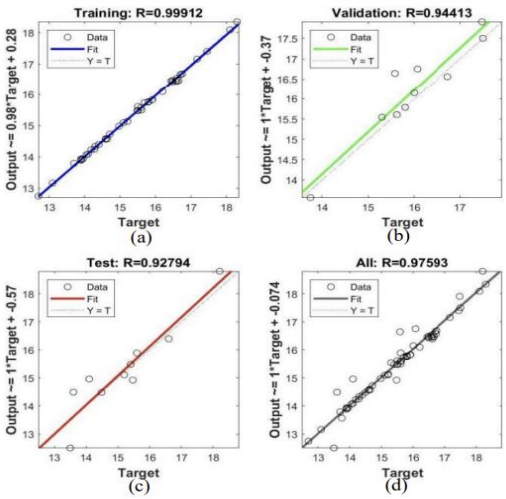

Figure 1: Regression values of MDD – ANN model (a)Training, (b) Validation, (c) Testing and (d) Overall

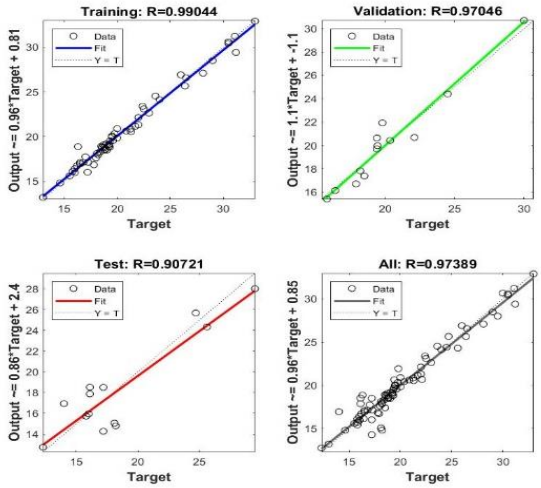

Figure 2: Regression values of OMC – ANN model (a)Training, (b) Validation, (c) Testing and (d) Overall

3.3 UCS_7days model

The architecture of one hidden layer constituted of 14 neurons makes the better performance model for predicting the UCS_7d. According to Figure 3, the training data set has high performance compared to the validation and target data sets. The regression value of all data for UCS_7d model was approximately 0.9835. The MSE for training, validation and testing data set are 28.3919, 4638.7605 and 3288.7438 respectively.

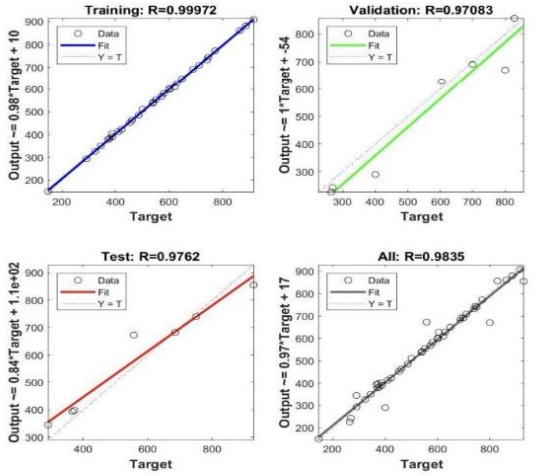

Figure 3: Regression values of UCS_7d – ANN model (a)Training, (b) Validation, (c) Testing and (d) Overall

3.4 UCS_28days model

The architecture of one hidden layer constituted of 15 neurons makes the better performance model for predicting the UCS_28d. From Figure 4, the regression value of all data for UCS_28d model was approximately 0.9888. The MSE for training, validation and testing data set are 3535.0, 10511.5 and 18201.7 respectively.

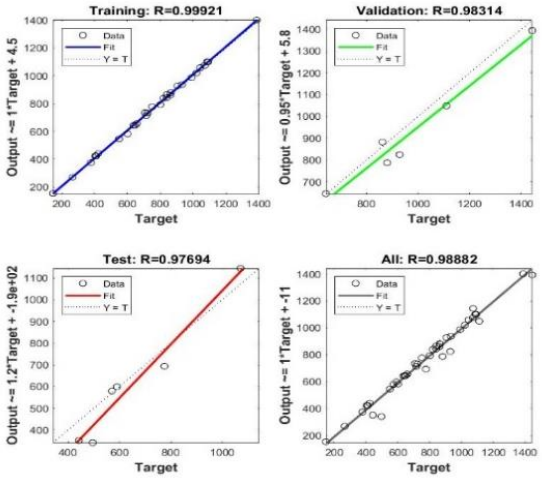

Figure 4: Regression values of UCS_28d – ANN model (a)Training, (b) Validation, (c) Testing and (d) Overall

3.5 Sensitive analysis

Connection weight approach (Leong et al., 2018) was used to find the variable contribution to the model. According to the Figure 5, the approach ranks OMC of the natural soil as the most important parameter followed by Fly ash content, PI% and CaO% for OMC model. In MDD model, MDD of the natural soil as the most important parameter followed by CaO%, PI% and Fly ash content. In UCS_7d model and UCS_28d model, fly ash % as the most important parameter followed by CaO%, PI% and UCS of the natural soil.

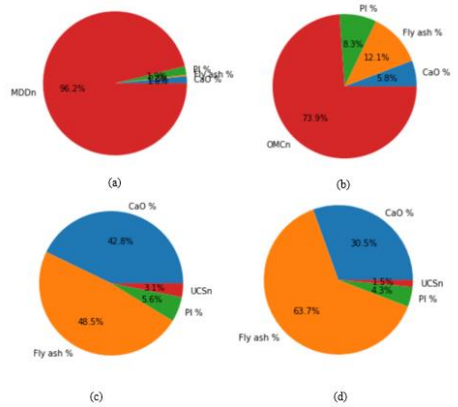

Figure 5: Sensitive analysis for (a) OMC model (b) MDD model (c) UCS_7d (d) UCS_28d

3.6 Model validation via experiment

Figure 6 shows that, comparatively OMC model has high regression value than the other three models and UCS_28d model has low regression value than the other three models. For the OMC-ANN model we used comparatively large data sets to develop the model so that the model accuracy is high for that and for UCS_28d model we used comparatively small amount of data

sets to develop the model, so that the model accuracy is low for that.

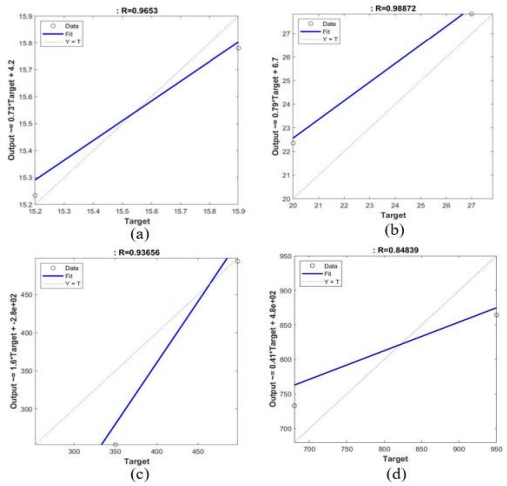

Figure 6: Regression values of (a)MDD, (b) OMC, (c) UCS_7d and (d) UCS_28d models

4. Conclusions

Artificial Neural Network (ANN) can be used to predict the unconfined compressive strength (UCS), maximum dry density (MDD) and optimum moisture content (OMC) of the expansive stabilized with fly ash.

It was verified that all proposed models were successfully trained and validated where the obtained results showed that the statistical analysis of geotechnical data is one of the most suitable techniques for developing new statistical model which can present the best understanding of problematic soils behaviour.

Sensitivity analysis shows that OMC (73.9%) and MDD (96.2%) of the natural soil most influenced the OMC model and MDD model respectively. For UCS models, fly ash content (48.5% and 63.7% for UCS_7d and UCS_28d respectively) as the most influenced parameter. The regression values of the validation studies via experiments showed a better predictability of the three constructed models for predicting the studied geotechnical properties of fly ash stabilized clayey soil. (MDD, OMC and UCS_7d).

It is recommended to use more data to develop the model to enhance the accuracy of the model outcome.

References

Ashraf, Ali, Sadek S Rahman, Omar Faruk and Abul Bashar. "Determination of Optimum Cement Content for Stabilization of Soft Soil and Durability Analysis of Soil Stabilized with Cement" Am J Civ Eng 6 (2018), 39-43.

Gunasekara, C., Lokuge, W., Keskic, M., Raj, N., Law, D.W. and Setunge, S., 2020. Design of Alkali-Activated Slag-Fly Ash Concrete Mixtures Using Machine Learning. Materials Journal, 117(5), pp.263-278.

Hossein Alavi, A., Hossein Gandomi, A., Mollahassani, A., Akbar Heshmati, A. and Rashed, A., 2010. Modeling of maximum dry density and optimum moisture content of stabilized soil using artificial neural networks. Journal of Plant Nutrition and Soil Science, 173(3), pp.368-379.

Leong, H.Y., Ong, D.E.L., Sanjayan, J.G., Nazari, A. and Kueh, S.M., 2018. Effects of significant variables on compressive strength of soil-fly ash geopolymer: Variable analytical approach based on neural networks and genetic programming. Journal of Materials in Civil Engineering, 30(7), p.04018129.

Assessment of Shear Strength Parameter of Marine Dredge Sand

Punchihewa P.L., Ranathunga R.J.K.B.C., Athapaththu A.M.R.G.*

Department of Civil Engineering, University of Peradeniya, Sri Lanka

**rasikaathapaththu@gmail.com*

Keywords: Colombo port city, Dredge sand, Direct shear test, EDEM

1. Introduction

Coastal land reclamation is more popular in densely populated and commercially developing countries. Colombo Port City Development Project (CPCDP) is the first mega coastal reclamation project in Sri Lanka. 65 million cubic meters of marine dredged sand have been used as the filling material. Dynamic compaction and Vibro-flotation methods were adopted as the deep compaction techniques. The shear strength of soils is represented mainly by cohesion and friction angle. Mohr-Coulomb envelope is the most common representation of shear strength variation of soils. The variation of the shear strength parameters of the marine dredged sand with different loading conditions and relative densities and the deviation of the linear Mohr-Coulomb envelope are studied in this research while a virtual direct shear test model was developed using DEM.

2. Literature review

2.1 Non-linearity of Mohr-Coulomb failure envelope

According to the experiments carried out by Hosseini and Jesmani, (2016) with increasing normal stress, the Mohr-Coulomb failure envelope becomes nonlinear for dense sand and this variation in the failure envelop the factors such as confining pressure, relative density, mineralogy, particle crushing, particle size distribution and fine content may be the reasons. Ranbandara, et al. (2020) have carried out experiments on Colombo port city sand for 95% relative density and had concluded the same results.

2.2 Factors affecting the variation of friction angle

According to Das (2010), the denseness of the granular materials is affected by particle size distribution, shape and relative density. Lade et al. (1998) showed that the basic attributes of granular materials are often related to the relative density (D_r) and stated an equation relating the void ratios with the relative density.

$$D_r = \frac{e_{max}-e}{e_{max}-e_{min}} . 100 \quad \text{..... (1)}$$

Where e is the void ratio in the field, e_{max} is maximum void ratio and e_{min} is the minimum void ratio.

Considering the effect of fine content Othman and Marto (2018) used a clean sand sample and categorized it into fine, medium and coarse by a sieve analysis. They concluded that e_{max} and e_{min} decreased up to 30% addition of fines for coarse sands and medium sands. But fine sand showed the minimal value of e_{max} and e_{min} at about 10% of fines addition.

2.3 Discrete element method

Grabowski and Nitka (2021) had simulated a direct shear test with a shear box size 60 x 25 x 5 mm^3 for grain sizes of d_{50} = 0.5 mm radii varying from d = 0.25 mm to 0.75 mm and have concluded that using DEM for geotechnical tests to find the friction angle, stress or volumetric change leads to having comparatively good results with the experimental data.

3. Methodology

As different compaction levels are achieved depending on the construction type the variation of shear strength parameters with the relative densities and the confining pressure should be determined. So, the laboratory experiments were carried out to identify the geotechnical properties of dredged sand in the Colombo Port City Project. Table 1 shows basic properties of dredged sand in the Colombo Port City Project. (Ranbandara, et al (2020))

Table 3: Sand parameters of dredged sand in the Colombo Port City Project (Ranbandara, et al (2020))

Parameter	Value	Units
Minimum dry density of sand	1515.15	kg/m^3
Maximum dry density of sand	1818.50	kg/m^3
Specific gravity of sand	2.68	_

3.1 Direct shear test

The standard direct shear test (BS 1377-7: 1990 clause 4) was selected to determine the shear strength parameters of the dredged sand for different relative densities. A series of direct shear test was performed for oven dried sand samples of 105 0C to 110 0C under 90% and 97% relative densities and for normal stresses of 20, 50, 100, 200, 400 and 800 kPa. For the direct shear test the square shear box of size 60mm x 60mm was used with the shearing rate of 0.5 mm/min was kept throughout the test series.

3.2 Sieve analysis test

Sieve analysis (BS 1377-2: 1990 clause 9.3) was performed before and after the direct shear test. During the direct shear test sand samples experienced shear stress as well as normal stress. Due to that shear stress and normal stress, crushing of sand particles could have occurred. So, to determine at which rate the particle crushing occurred to the sample after the direct shear test another sieve analysis test was carried out.

3.3 Development of a virtual direct shear test model using DEM

It is time-consuming to perform laboratory tests manually and there may be more errors included in the results. So, a virtual model was developed to mitigate the short comes. The virtual model was developed for direct shear test using Discrete Element Method (DEM). EDEM software was used for modeling the virtual direct shear test.

Percentage volume of the particles with different diameters were calculated based on the sieve analysis tests and input for the EDEM model as shown in Table 2. All the particles were modelled as spheres and due to the particle size is very small and causes to increase the computation time drastically. Therefore, all the particles were enlarged by 10 times.

Table 4: Particle size distribution

Particle name	Sieve size (mm)	Particle radius (mm)	Volume percentage
D1	2.00	10.00	2.06 %
D2	0.85	4.25	18.77 %
D3	0.60	3.00	20.71 %
D4	0.43	2.13	21.33 %
D5	0.25	1.25	25.01 %
D6	0.15	0.75	12.12 %

Series of virtual direct shear test simulations with applied normal stresses of 50, 100, 200, 400, and 800 kPa were carried out for different relative densities. Figure 1 shows the model after the shearing process.

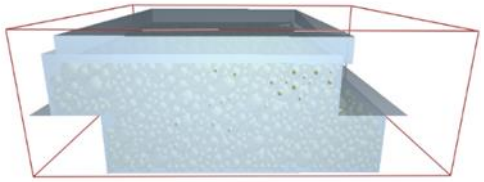

Figure 1: EDEM direct shear test model after shearing

4. Results and discussion

4.1 Direct shear test

Figure 2 and Figure 3 illustrates the variation of shear stress with shear displacements for 90% and 97% degree of compactions respectively.

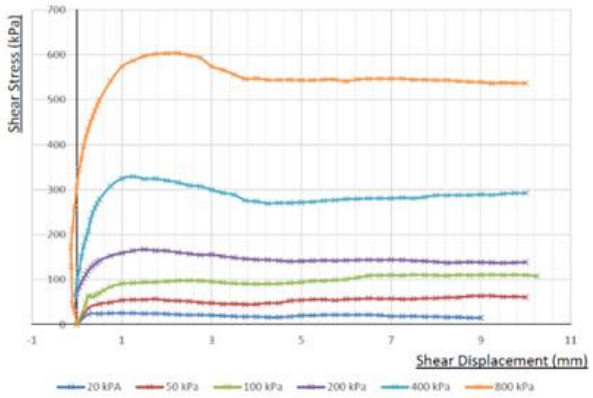

Figure 2: Variation of shear stress versus shear displacement for 90% relative density

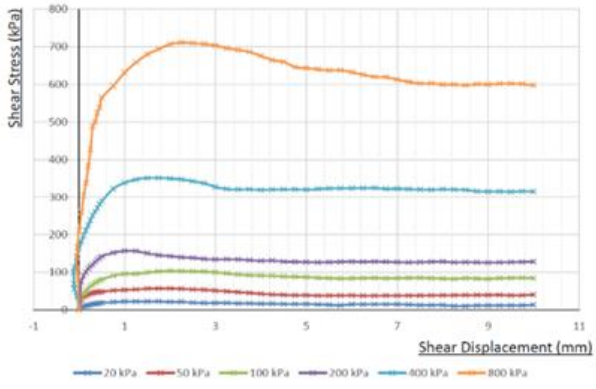

Figure 3: Variation of normal displacement versus shear displacement for 97% relative density

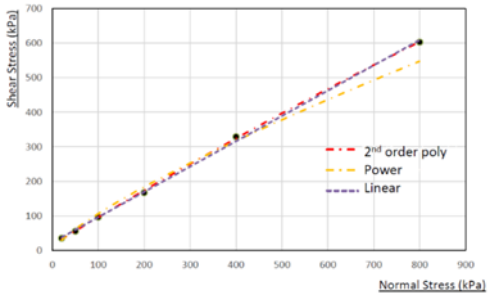

Figure 4: Linear and nonlinear failure envelopes for 90% relative density

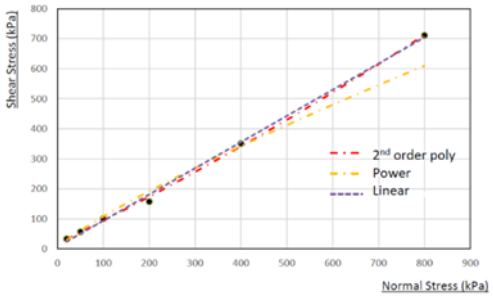

Figure 5: Linear and nonlinear failure envelopes for 97% relative density

The shear strength parameters are tending to vary linearly for low normal stresses and then become nonlinearly with the increment of applied normal stress for relative densities 90% and 97% as shown in Figure 4 and Figure 5. The linear function cannot be used to describe the shear strength variation as it shows the intercept. Therefore, power and second-order polynomial curve fit were utilized to describe the non-linear fluctuation. The sand grains from Port City may be crushed during shear and hence dilatancy reduces. Equations resulted for 90% relative density and 97% relative density can be seen in Table 3 and Table 4.

Table 5: Failure envelope equations for 90% relative density

Envelope	Equation	R^2
Linear	Y=0.7332x+22.481	0.9990
2nd order polynomial	$Y=-0.0002x^2+0.9056x$	0.9989
Power	$Y=2.8095x^{0.7888}$	0.9959

Table 6: Failure envelope equations for 97% relative density

Envelope	Equation	R^2
Linear	0.8718x+6.5781	0.9975
2nd order polynomial	$0.00004x^2+0.8575x$	0.9981
Power	$2.3128x^{0.834}$	0.9890

4.2 Sieve analysis

Upon completion of the direct shear tests, sieve analysis tests were carried out to check the degree of the particle crushing. It was noticed that the crushing has occurred for the samples with normal stresses larger than 100 kPa. Figure 6 presents the variation of particle size distribution before and after compaction process for 97% relative density.

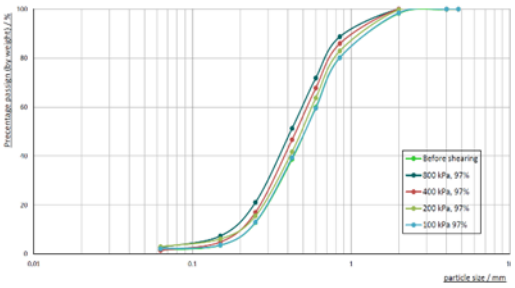

Figure 6: Variation of particle size distribution before and after the compaction process for 97% relative density

4.3 EDEM model

Since direct test results cannot be obtained from EDEM, first the total force acting on the bottom box with time was analysed and the shear stress was calculated via the total force. Figure 7 compares the variation of shear stress with the shear displacement for the EDEM results and the laboratory results without application of a correlation.

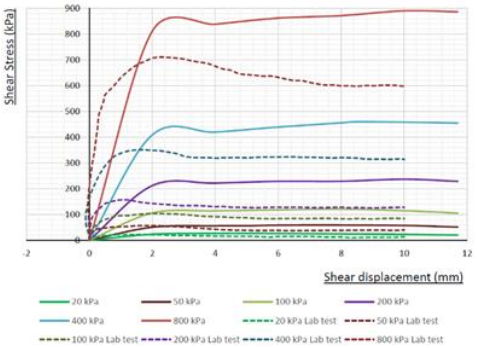

Figure 7: Variation of shear stress with the shear displacement for the EDEM results and the laboratory results

To find the correlation function, the ultimate shear stress derived from the laboratory experiments and the DEM model was plotted as a linear function. Using a linear function with zero intercept, a correlation function was obtained, and the corrected results are shown in Figure 8.

$$\tau_{corrected} = 0.6743\tau_{simulation} \quad \text{..... (2)}$$

where $\tau_{corrected}$ is the corrected ultimate shear stress and $\tau_{simulation}$ is the ultimate shear stress obtained from the EDEM simulation.

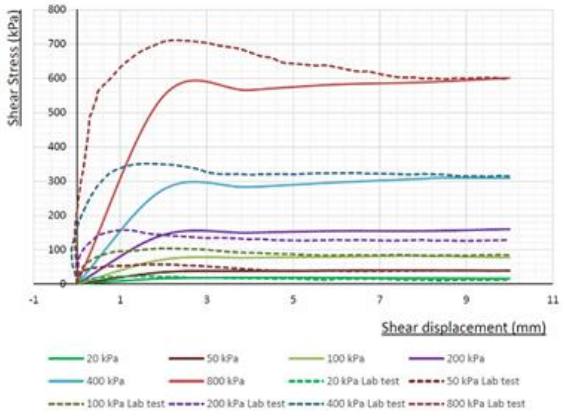

Figure 8: Variation of corrected shear stress of the DEM model and shear stress from the laboratory experiments with the shear displacement

Table 5 summarize the results secant friction angles obtained for different relative densities and from the EDEM model.

Table 5: Summarized secant friction angles

Relative Density	Avg. Peak Friction angle (°)	Ultimate Friction angle (°)
90	36.03	33.62
95	39.07	34.45
97	41.24	37.10
EDEM Model	46.47	37.16

5. Conclusions

When direct shear tests were performed for the compacted sand samples from 20 kPa to 100 kPa, there is no crushing occurred during the shearing. With the increment of normal load from 200 kPa, a significant amount of particle crushing has occurred while the shearing process has been carried out.

Shear strength increment with the increasing of normal stresses up to 100 kPa can be described as a linear variation for both the sand samples with 90% and 97% relative densities.

Linear relationships cannot be used to represent the variation of shear strength with higher normal stresses.

Secant friction angle increases with the increase of relative density.

By increasing the degree of compaction shear strength of the dredged sand can be increased.

Since the change of friction angle is nonlinear, it is more suitable to use the nonlinear variation of secant friction angle for high load carrying geotechnical designs.

Results obtained from the EDEM software are reasonably acceptable when comparing with the laboratory experimental results for low normal stresses.

Since the variation of shear stress with shear displacement has similar pattern compared to the laboratory results, a correction factor is applied for the EDEM results.

References

Bolton, M.D., 1986. The strength and dilatancy of sands. Geotechnique, 36(1), pp.65-78.

Grabowski, A. and Nitka, M. 2020. 3D DEM simulations of basic geotechnical tests with early detection of shear localization. Studia Geotechnica et Mechanica, 43(1), pp.48–64. doi:10.2478/sgem-2020-0010.

Hosseini, S.M.R. and Jesmani, M., 2016. Effect of normal stress and relative compaction on secant friction angle of sands. Turkish Journal of Engineering and Environmental Sciences, 38(3), pp.382-391.

Othman, B.A. and Marto, A. 2018. Laboratory test on maximum and minimum void ratio of tropical sand matrix soils. IOP Conference Series: Earth and Environmental Science, 140, pp.012084.doi:10.1088/17551315/140/1/012084

Ranbandara, P.G.G.M., Thilakarathne, R.U., Athapaththu, A.M.R.G., Kurukulasooriya, L.C. and Gonaduwage, B.P. 2020. Examination on Geotechnical Properties of Marine Dredge Sand of Colombo Port City.

Numerical Simulation of Load-Displacement Behaviour Under Sleeper Pad (USP) Using Hyper-Elastic Material Models for Railway Applications

Panneerselvam D., Ratnavel K., Navaratnarajah S.K.*

Department of Civil Engineering, University of Peradeniya, Sri Lanka

**navask@eng.pdn.ac.lk*

Keywords: Ballasted track, Under sleeper pad, Hyper-elastic materials, Numerical simulation

1. Introduction

Rail networks are crucial for transporting both bulk freight and commuters, but growing population, urbanization, and highway congestion have pushed the rail industry to develop faster and more robust railway corridors. To enhance efficiency, reduce maintenance costs, and improve passenger comfort, researchers have proposed the use of energy-absorbing rubber pads in rail systems. Three types of these pads are Rail Pads (RPs), Under Sleeper Pads (USPs), and Under Ballast Mats (UBMs). USPs are particularly popular globally due to their positive impact on track performance. In the realm of numerical studies for railways, the Finite Element Method (FEM) stands out. It has been effectively employed to analyze various aspects, such as ballast layer stress, deformations, and sleeper stress. However, modeling the hyper-elastic behaviour of USPs has been relatively less explored. Some studies have treated USPs as linear elastic materials in FEM simulations, but this approach doesn't capture the non-linear stress-strain behaviour typical of rubber-like materials.

To address this, recent research has incorporated hyper-elastic material models to accurately predict the non-linear behaviour of USPs. One key parameter in assessing the performance of these energy-absorbing rubber pads is the static bedding modulus, which can be determined through laboratory static load tests. This study focuses on developing numerical models using FEM to simulate the static load test of USPs while incorporating hyper-elastic material properties to accurately represent rubber's non-linear behavior. The models were validated using experimental data, and a parametric study was conducted to explore how varying the thickness of the rubber pad affects the static bedding modulus. These findings contribute to improving the design and performance of railway track systems, ensuring safer and more efficient transportation.

2. Hyper-elastic material models in Abaqus

The most attractive property of rubbers is their ability to experience large deformation under small loads and to retain initial configuration without considerable permanent deformation after the load is removed. Their stress-strain behavior is highly non-linear. Hyper-elastic materials are commonly used to capture the nonlinear stress-strain behavior of rubber when subjected to large deformations. In this study, a hyper-elastic material model is adopted to capture the behavior of the rubber pad using ABAQUS commercial FEM software. ABAQUS software has many forms of hyper-elastic material models. They are the Moony-Rivlin model, Neo-Hookean model, Yeoh model, Ogden model, Reduced Polynomial model, Full Polynomial model, and Arruda-Boyce model, among others. It is important to select the best suit hyper-elastic material model to accurately predict the behaviour of a particular rubber pad having specific material properties. To select the most appropriate material model, it is necessary to have a set of test data from at least one uniaxial test, one biaxial test, one volumetric test, and one planar test (Arachchi et al., 2021). The curve fitting approach in ABAQUS facilitates the user to evaluate these test data and determines the stable hyper-elastic material models together with corresponding coefficient values to represent each material model. An error calculation with respect to test data is done to compare the stable material models by using three selected statistical indexes; Mean Absolute Percentage Error (MAPE), Mean Absolute Deviation (MAD), and Mean Squared Deviation (MSD). Finally, the best-suited material model was selected.

$$\text{MAPE} = \frac{\sum_{t=1}^{n}\left|\frac{Y_t - \hat{Y}}{Y_t}\right|}{n} \times 100\% \quad \text{.....(1)}$$

$$\text{MAD} = \frac{\sum_{t=1}^{n}\left|Y_t - \hat{Y}\right|}{n} \quad \text{.....(2)}$$

$$MSD = \frac{\sum_{t=1}^{n}\left|Y_t - \hat{Y}\right|^2}{n} \quad \text{.....(3)}$$

In equation (1), (2) and (3), the test data values Y_t and obtained stress values ($\hat{Y}$).

3. Numerical simulation of static load test on USP

3.1 Selection of the best hyper-elastic material model

The curve-fitting approach was used to evaluate the uniaxial compression data of a rubber pad obtained from Navaratnarajah (2017). Ogden N=1, Reduced polynomial N=1, Reduced polynomial N =3 and Arruda-Boyce models were obtained as the stable material models from the curve fitting approach, and the accuracy of the models was assessed using statistical error indices. Here N is the Number of terms in the strain energy function. The statistical error index calculations of the stable models are shown in Table 1.

Table 1: Statistical index values

Error indexes	Stable hyper-elastic models			
	Ogden N=1	Reduced polynomial N=1	Reduced polynomial N=3	Arruda Boyce
MAPE	4.93	4.92	4.49	4.42
MSD	7.1×10^6	9.6×10^6	4.1×10^6	9.7×10^6
MAD	2374.0	2208.7	1744.9	2214.0

It was clear from the error measurements that the Arruda-Boyce material model obtains the minimum values for the statistical indexes and shows a good curve fit with experimental results obtained from uniaxial compression test data and volumetric test data as shown in Figure 1. Therefore, it was taken as the best-fitted material model, and material coefficients were obtained from the results of the material evaluation as shown in Table 2. In this table μ, μ_o, λ_m, and D are temperature dependent material parameters.

Table 2: Material coefficient of Arruda Boyce material model

Coefficients (Pa)	μ	μ_o	λ_m	D
Values	593558.5	600965.5	7.0	3.8

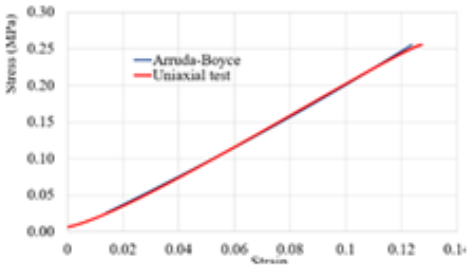

Figure 1: The comparison of the uniaxial compression test data and Arruda Boyce material model results evaluated in ABAQUS 6.14/CAE

3.2 Development of the USP model

A model of the static load test (DIN 45673-5) on USP was developed in ABAQUS 6.14/CAE. The experimental data for the validation of the numerical simulation of the static load test on the sleeper pad was taken from Navaratnarajah (2017). According to the standard, the rubber pad was placed on a strong base plate and the load was applied on top of the rubber pad using the loading plate. The load to be applied on the top loading plate is shown in Figure 2.

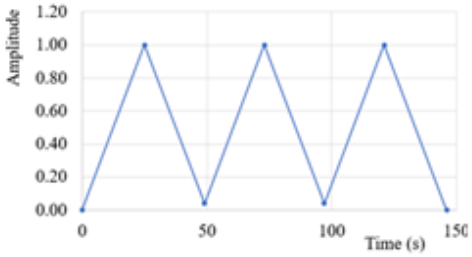

Figure 2: Amplitude curve of quasi-static loading

The USP was developed as a 3-D deformable solid element having the dimensions of 200×200×10 mm. Two 3D discrete shell planar rigid plates were introduced to the top (loading plate) and bottom (base plate) of the USP surfaces Figure. 4 shows the developed model of USP with top and bottom plates. The density of USP was used as 420 kg/m^3 (Navaratnarajah 2017). The hyper-elastic material properties given in Table 2 were assigned to USP to capture the non-linear behavior.

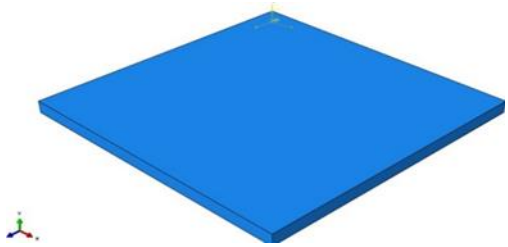

Figure 3: The modelled USP with rigid plates

The viscoelastic property of rubber material helps it to return to its original shape after deformation. Viscoelastic properties are incorporated to enhance the material model toward the real scenario. It can be analysed under the time domain or frequency domain. Here time domain, Prony series was used for the viscoelastic constants. The constants and the values used are shown in Table 3.

Table 3: Viscos elastic properties

g	k	μ
0.15	0	5.76
0.08	0	220.41

The surface-to-surface interaction with frictional penalty condition with frictional co-efficient μ = 0.85 between sleeper pad and rigid bodies was introduced in the numerical model. The model was restrained using two boundary conditions where the bottom rigid plate was fixed while the top rigid plate was only unrestrained for vertical motion. Dynamic implicit analysis was used for the quasi-static loading. The applied load is 0.25MPa as shown in Figure 3.

3.3 Meshing and mesh sensitivity analysis

The mesh was assigned from the standard element library of a family of 3D stress. The 8-node linear brick, reduced integration with hourglass control, and hybrid with constant pressure (C3D8RH) elements were adopted for modeling the sleeper pad. In contrast, the two rigid bodies have meshed with R3D4 elements, which is a 4-node 3D bilinear rigid quadrilateral from a discrete rigid element family. The appropriate meshing size of the elements should be determined since coarser elements consume lesser computation time. However, to get real results in displacements and stress distribution optimum size should be determined through a mesh convergence study (Navaratnarajah, 2017).

Variation of the maximum stress on the sleeper pad with mesh density was analysed in the mesh sensitivity analysis. The mesh density, where the results were shown to be converging was selected as the converged mesh density. The obtained converged number of elements (mesh density) was 13600 (Figure 4).

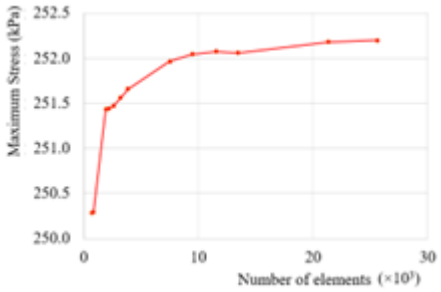

Figure 4: Variation of maximum stress in sleeper pad with mesh density

4. Results and discussion

4.1 Validation

The validation of the numerical model of the static load test on USP was done by comparing the numerical results with the experimental results from Navaratnarajah (2017). Variation of vertical stress with vertical strain was considered in the comparison process. Obtained variation of stress vs, strain for three cycles is given in Figure 5. The comparison of the experimental and numerical results for the third load cycle is shown in Figure 6.

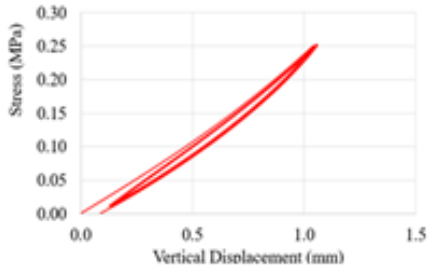

Figure 5: Variation of vertical stress with vertical displacement

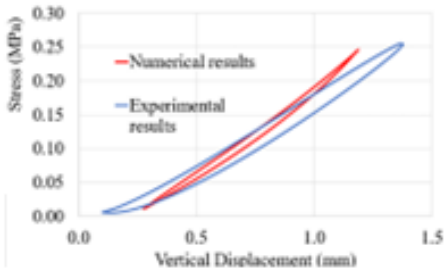

Figure 6: Comparison of FEM results and experimental results (Navaratnarajah 2017) for the 3rd cycle

4.2 Parametric study

Under the parametric study, the validated numerical model with the 10 mm thick USP was used to investigate the effect of USP thickness on its static bedding modulus values. For that, 3

different numerical models of static load test were developed with 8 mm, 12 mm, and 14 mm thick USPs. The variation of vertical stress with vertical displacement for 8 mm, 10 mm, 12 mm, and 14 mm thick USPs under the third load cycle is shown in Figure 7**.**

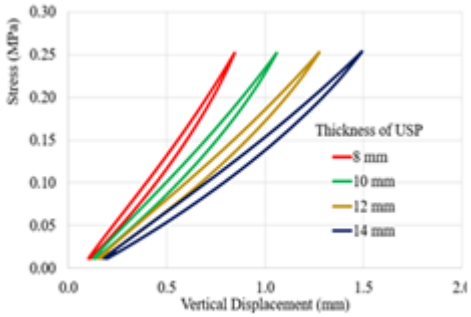

Figure 7: Variation of vertical stress with vertical displacement for the third load cycle for various thicknesses

4.3 Results

Following the DIN 45673-5 specification, for the static analysis, the calculated static bedding modulus (C_{stat}) values based on the gradients of stress-displacement curves are shown in Figure 8. The experimental and numerical bedding modulus values are 0.20N/mm^3 and 0.25N/mm^3, respectively and the variation between them is about 25%. Therefore, the developed numerical models in FEM can be successfully used for the simulation of large-scale laboratory tests involving sleeper pads, allowing for accurate analysis and prediction of their performance under various conditions.

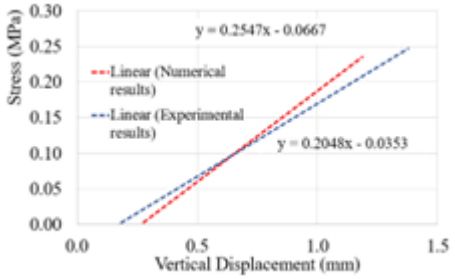

Figure 8: Gradients of stress-displacement curves and calculated static bedding modulus value

The static bedding modulus values of each thickness are obtained from the gradients of the stress displacement curve which are shown in Figure 9. Results clearly show that the static bedding modulus of the sleeper pad increases as the thickness decreases. Therefore, the developed numerical models in FEM can be successfully used for the simulation of large-scale laboratory tests where sleeper pads.

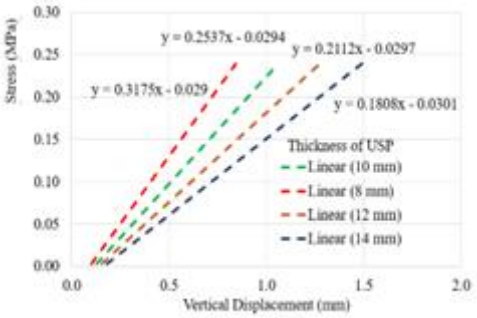

Figure 9: Gradients of stress-displacement curves and calculated static bedding modulus values

5. Conclusions

This study aims to simulate the non-linear behaviour of USPs for static responses using hyper-elastic material models in FEM. The static load test on USP was numerically modeled and validated with the experimental data from the literature. From the validated numerical model, a parametric study was conducted for different thicknesses of USP. It is identified that static stiffness is significantly varied with the thickness of the USP.

The stiffness and the bedding modulus increase when the thickness of the sleeper pad decreases. Therefore, a lower thickness (8mm – 10mm) of the sleeper pad can be used where the stiffer pad is needed.

References

Arachchi, N.M.L.W., Abegunasekara, C.D., Premarathna, W.A.A.S., Jayasinghe, J.A.S.C., Bandara, C.S. and Ranathunga, R.R.M.S.K., 2021. Finite Element Modeling and Simulation of Rubber Based Products: Application to Solid Resilient Tire. In ICSECM 2019 pp. 517-531. Springer, Singapore.

DIN 45673-5:2010-08 Mechanical vibration. Resilient elements used in railway tracks. Part 5: Laboratory test procedures for under-ballast mats.

Indraratna, B. and Nimbalkar, S., 2013. Stress-strain degradation response of railway ballast stabilized with geosynthetics. Journal of geotechnical and geoenvironmental engineering, 139(5), pp.684-700.

Mayuranga, H.G.S., Navaratnarajah, S.K., Bandara, C.S. and Jayasinghe, J.A.S.C., 2019, A State-of-The-Art Review of The Influence of Rubber Inclusions in Railway Tracks.

Testing Sensitivity and Stability of Multinomial Logit (Mnl) Modeling Approach for Travelers' Mode Choice Parameter Estimation

Akshani U.H.D., Wijesundara W.M.L.P., Dharmarathna W.R.S.S.*

Department of Civil Engineering, University of Peradeniya, Sri Lanka

**samal@eng.ac.lk*

Keywords: Multinomial logit model, Mode choice, Optimum number of trips, Sensitivity, Stability

1. Introduction

Mode choice is the selection of a travel mode to transport people and/or goods. It is influenced by factors such as level-of-service attributes, subjective factors, land use and accessibility, and personal, family features. Mode choice is a discrete choice, with individual behaviour explained by preferences and assumptions that the consumer chooses the most profitable option. Parameter estimation using the MNL model is important in making decisions in transportation planning, as it provides choice probabilities for each alternative based on the utility of all alternatives.

The main objective of this study is to understand the sensitivity and stability of the MNL modeling approach for mode choice parameter estimation. For that, trip characteristics affecting model stability were identified, and the optimum number of trips for a stable and accurate MNL modeling determined.

The study focuses on the trips that are made on Island-wide. All-purpose trips are considered. For the analysis of the data and modeling, MNL modeling approach is used, and it is performed in the R-studio platform.

2. Literature review

The MNL model is often used for mode choice model analysis due to its simplicity in parameter estimation and interpretation. The majority of the research related to mode choice used the MNL model (Elharoun M. et al. 2018).

2.1 Modeling techniques

Bernal et al. (2019) identified trip makers' characteristics that affect the transport mode choice in a comparison between two age groups, the non-elderly, and the elderly. This study was done by using MNL modeling in RStudio platform.

Obaid and Hamad (2020) investigated mode choice of travellers in Sharjah University City using a multinomial discrete logit choice model. They considered car, private bus, public bus, taxi, and active transport as modes and studied various trips and travellers' characteristics, as well as other contributing factors. A sensitivity analysis was also performed.

Al-Salih and Esztergár-Kiss (2021) conducted a study on mode choice methodology. The methodology involved three steps, including identifying activity purpose, individual and household characteristics, and travel mode, analysing mode choice using MNL and NL based on individual, household, and travel characteristics, and investigating mode choice behaviour based on the utility function. The study determined the influence of different variables on mode choice and obtained estimated coefficients, statistically significant levels, and t values from the analysis.

Wan et al. (2021) proposed an MNL model based on disaggregate theory to analyse the sensitivity of incentive situations and personal attributes to driving anger. The study mentioned that a variable is considered significant if its absolute t-value is not less than 1.96 and its sign is correct.

2.2 Sensitivity and stability analysis

Elharoun M. et al. (2018) checked the sensitivity of increasing microbus fare affects transportation mode usage in Mansoura city, Egypt, by testing different fare increases while holding other variables constant. The effect of increasing the microbus fare on modal shares of other modes was checked under different scenarios.

The study on driving anger based on MNL model introduced elasticity to test influencing factors and estimated model parameters for personal attributes. It calculated elasticity values and determined if attributes had significant sensitivity to driving anger (Wan et al. 2021).

Elharoun M. et al. (2018) tested the stability of a mode choice model in Mansoura city, Egypt, using different data sets from different time periods. The model calibrated with 2015 data predicted 84.60% of the choices of new data

collected in 2017-2018, indicating its stability and appropriateness in predicting mode choice behaviour despite changes in travel cost.

3. Methodology

In this study, trip data was collected through online and face-to-face questionnaire surveys. The population of 18 years and above was considered for the data collection. The survey covered all trip purposes.

3.1 Cross sectional analysis

A cross-sectional analysis was conducted on gathered data before moving into the deep analysis. Figure 1 shows the distribution of choosing different travel modes.

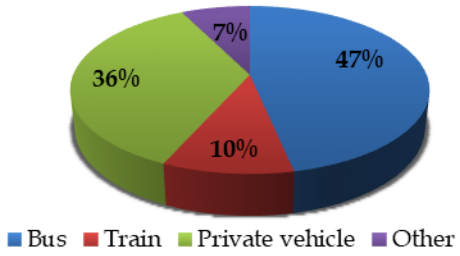

Figure 1: Distribution of trips for modes

Figure 1 indicates that 57% of respondents in Sri Lanka use public transportation and 36% use private vehicles. Walking and bicycling levels were found to be low.

Figure 2 shows the variation of trips in relation to each 30-minute intervals.

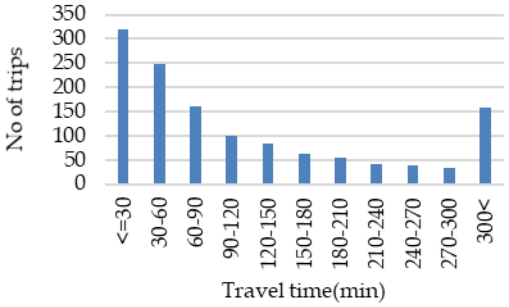

Figure 2: Histogram of total travel time

Most of the trips, as depicted in figure 2 are clearly short trips, with a significant proportion of the data having a journey time of less than half an hour. These are likely to be daily commuters. Figure 3 shows the mode choice of different income level categories.

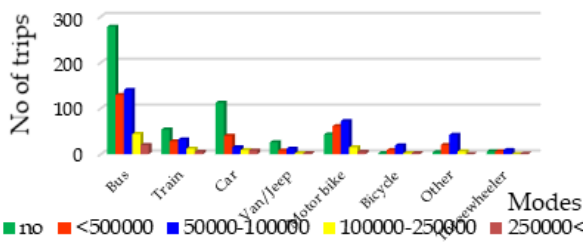

Figure 3: Mode choice of different income level categories

According to most of the respondents belong to no income category and figure confirms that low-income people are mostly chosen public transport (bus) for their travel while medium-income people are using their own vehicles.

3.2 Theoretical background

A utility function was defined based on selected parameters to express the trip makers' satisfaction for the mode choice. The utility function can be expressed as,

$$U_x = \beta_0 + \beta_1 X_1 + \beta_2 X_2 + \ldots + \varepsilon \quad \ldots\ldots(1)$$

Where,
U is the utility
X_1, $X_2 \ldots X_n$ are the attributes of alternatives
β_0, β_1, $\beta_2 \ldots \beta n$ are the respective parameters
ε is the random error term

The MNL model is used to calculate the probability of the decision-maker choosing alternative k, based on the utility maximization. It is calculated as follows.

$$P(k) = \frac{e^{Uk}}{\sum e^{Ux}} \quad \ldots\ldots(2)$$

Where,
P(k) is the probability of a passenger selecting an option k
U_k is the utility of mode k
The goodness of fit is measured by using the likelihood ratio index (ρ^2) and the significance of the estimated parameters are tested by t-statistic values. The likelihood ratio index is calculated as below.

$$\text{Likelihood ratio index, } \rho^2 = 1 - \frac{LL(\hat{\beta})}{LL\ (0)} \quad \ldots\ldots(3)$$

Where,
$(\hat{\beta})$ is the value of the log-likelihood function at the estimated parameters
LL (0) is the value when all the parameters are set equal to zero

The t distribution is used when data are approximately normally distributed. t-statistic value is calculated as below.

$$t - \text{statistic} = \frac{\hat{\beta}k - \beta*k}{Sk} \quad \text{.....(4)}$$

Where,
$\hat{\beta}_k$ is the estimate for the k^{th} parameter
β^*_k is the hypothesized value for the k^{th} parameter
S_k is the standard error of the estimate

3.3 Data categorization

Gathered data were categorized under the total travel time of the trips to check the sensitivity of the model. Categorization of the time was based on the past studies and average speed of the vehicles within the cities in Sri Lanka. Halldorsdottir et al. (2011) have done study on Modeling mode choice in short trips and trips shorter than 22 km considered for the study. Moeckel et al. (2014) have done study focused on mode choice modeling for long distance travel and trips of 50 miles or more (80 km or more) defined as the long-distance trips in their study. Based on these statements and average vehicle speed in Sri Lanka, short time trips, intermediate time trips and long-time trips were defined.
Table 1 shows the categorization of trips based on the total travel time, selected time range and sample size for each category.

Table 1: Categorization of trips based on the total travel time

Category	Time range (in minutes)	Sample Size
Short time trips	30>	320
Intermediate time trips	30-120	508
Long-time trips	120<	472

4. Results and discussion

The developed model is a discrete choice model for travellers choosing a mode of travel in the country from the available alternatives. The parameter estimation was completed using the MNL modeling approach in the RStudio platform. Total travel time and the travel cost were considered as parameters.

The model fit was measured using the likelihood ratio index and the adjusted likelihood ratio index, which were found to be 0.13 and 0.12 respectively. These values indicate a significant level of fit between the model and the data.
According to the obtained results, both the parameters are significant with 95% confident as the respective t-values are greater than 1.96.
Travel time parameter gives a higher value indicating travelers have given more priority on travel time when they are choosing a travel mode when compared to the travel cost. Therefore, total travel time was selected as base model parameter and used for further analysis. Table 2 shows the estimated results of the base model.

Table 2: Parameter estimation results of the base model

	Estimates	t value
Total travel time	-0.276	-3.17
Sample size		1300
Initial LL		-1405.32
Final LL		-1155.02
Rho-square		0.18
Adjusted rho-square		0.17

4.1 Optimum number of trips for stable modeling

To obtain a stable estimation, trips were used in decreasing order with a gap of 100 until an unstable condition was reached. This was done by generating random samples and taking five trials for each category. Travel time parameter was used for estimation. Sample size included 1000, 900, 800, 600, 500, 400, and 300 trips per sample. Table 3 shows the estimated results of five trials for sample size 1000.

Table 3: Parameter estimation results for sample size 1000

Trial no.	Estimation of total travel time	t value	Adjusted rho-square
1	-0.401	-3.83	0.16
2	-0.568	-4.79	0.16
3	-0.467	-4.06	0.18
4	-0.195	-2.05	0.17
5	-0.263	-2.68	0.18

Table 3 demonstrates that, total travel time, the base model parameter is significant with 95% confident as the respective t-values are greater than 1.96 in all the five trials. Therefore, sample size 1000 is a stable condition for the model. According to the obtained results, total travel time is significant with 95% confident as the

respective t-values are greater than 1.96 in all the five trials for sample size 900, 800 and 600. For sample size 500, the t-values exceed 1.96 in three trials out of five, for sample size 400, the t-values exceed 1.96 in four trials out of five and for sample size 300, and it was two trials out of five. Therefore, the total travel time is significant for sample size 500, 400 and 300. So, sample size 900, 800, 600, 500, 400 and 300 are stable conditions for the model. The t value of total travel time was not significant in any case where the sample size was less than 300. Therefore, the model was not able to produce accurate predictions with sample sizes less than 300.

Then, it can be concluded that a sample size of 300 is the optimal number of trips for a stable model as our key finding of the study.

4.2 Sensitivity analysis

To study how the model is sensible with the behaviour of different trip characteristics, specifically focused on the behaviour of categorized samples in relation to total travel time. Some results of this analysis are presented in Table 4.

Table 4: Parameter estimation results of five trials for short time trips, sample size 300

Trial no.	Estimation of total travel time	t- value	Adjusted Rho-square
1	-4.426	-4.51	0.31
2	-5.870	-5.12	0.31
3	-4.996	-5.04	0.31
4	-10.829	-7.88	0.38
5	-11.233	-8.25	0.40

To check how the short time trips are affected for sensible model, random samples of short time trips were generated and estimated by considering five trials. Due to the total number of short time trips are 320, only random sample size of 300 was considered for this case.

To check how the intermediate time trips are affected for sensible model, random samples of intermediate time trips were generated and estimated by taking five trials for each sample size. Due to the total number of intermediate time trips are 508, only random sample size of 300, 400, and 500 were considered for this case. The total travel time is significant with 95% confident as the respective t-values are greater than 1.96 in all the five trials for all the random sample sizes.

Therefore, it can be concluded that, both short time and intermediate time trips are sensitive to the total travel time while according to the results interpretation, short time trips are more sensitive to the total travel time as estimations and t-values are higher.

5. Conclusions

The research involved 1300 trips in Sri Lanka, collected via online and face-to-face questionnaires. The MNL model was used to estimate parameters based on utility maximization theory, with travel time and cost being found to be significant factors in mode choice. The study determined that total travel time was the most important parameter, as travellers prioritize it over travel cost when selecting a mode of transportation. The model was found to perform well with a sample size of 300 or more, and the results were statistically significant, with the model not producing accurate predictions for sample sizes less than 300. The study also found that both short and intermediate-time trips were sensitive to travel time, with short time trips being more sensitive to it. The research highlights the need to enhance time-related factors to encourage more individuals to use public transportation.

References

Al-Salih, W.Q. and Esztergár-Kiss, D. 2021, 'Linking Mode Choice with Travel Behavior by Using Logit Model Based on Utility Function', Sustainability,13(8),p.4332.doi:10.3390/su13084332.

Elharoun, M., Shahdah, U.E. and El-Badawy, S.M. 2018 'developing a mode choice model for mansoura city in egypt', International Journal for Traffic and Transport Engineering, p.15. doi: http://dx.doi.org/10.7708/ijtte.2018.8(4).10

1. Wan, P., yan, L. and lu, S. 2021. 'Sensitivity Analysis of Incentive Situations and Personal Attributes to Driving Anger Based on MNL Model: A Naturalistic Experimental Study', Tehnicki vjesnik - Technical Gazette, 28(5). doi:10.17559/TV-20210601103911.

Machine Learning Approach for Mode Choice Modeling

Lakmini W.D., Jayasena I.C.S., Dharmarathna W.R.S.S*., Jayasinghe U.

Department of Civil Engineering, University of Peradeniya, Sri Lanka

**samal@eng.ac.lk*

Keywords: Machine learning, Multinomial logit model, Support vector machine, Travel mode choice, Transportation planning

1. Introduction

The importance of understanding travel mode choice is that it affects the efficiency of travel, the space required for transportation functions, and the range of mode alternatives available for users. Different factors affect travel mode choice modeling including trip-specific data, socio-economic data, and household data associated with each trip. Thus, the Multinomial Logit (MNL) model can be indicated as the most widely used mode choice model for the discrete mode choice models (McFadden, 1973).

Machine Learning (ML) is used to define an algorithm that builds models by means of a methodical pattern in statistically significant data. The usefulness of ML models has already been demonstrated in different areas of the transportation sector. ML algorithms do not make strong assumptions about the studied data, and it was able to represent complex relationships in a non-linear and in general, data-based way (Bishop, 2006). Therefore, ML models come across as the better model for modeling travel mode choice.

The aim of this research is to estimate travellers' mode choice parameters, by using ML algorithms and compare them with the MNL approach. There are two specific objectives in this study. They are,

- To develop a method to estimate mode choice parameters by using the Support Vector Machine (SVM) and Random Forest (RF) method.
- To perform a comparative study of parameter estimation between ML and MNL approaches.

The study focused on trips related to the whole country. It was considered only the travel mode behavior of participants aged 18 and over. Trip data were collected based on trip-specific data (travel mode, trip distance, cost, time, etc.) socio-economic data (gender, age, ethnicity), and household data (income, number of cars/ bicycles, etc.). All trip purposes were considered, which included work, education, leisure, shopping trips, etc.

2. Literature review

2.1 Modeling techniques

Omrani, 2015 studied four ML methods (Artificial Neural Network Multilayer Perceptron (ANN-MLP), Artificial Neural Network Radial Basis Function (ANN-RBF), multinomial logistic regression, and SVM) that were used to predict the travel mode of households. Ali, et al., 2021 evaluated the efficacy of Neural Network (NN), RF, Decision Tree (DT), and SVM, ML models against a logistic regression in predicting travel mode choice. In addition, ML models were compared with Binary logistic regression and used to predict travel mode choice. Jaramillo & Juan, 2019 studied ANNs, DTs, and SVM models used to model travel mode choice. The SVM model was compared with several models such as NNs, Extreme Gradient Boosting (XGB), Bayesian Network, and Standard SVM model (Qian, et al., 2021). The performance of those models has been evaluated by accuracy, precision, recall, and F1 score criteria. Hagenauer & Helbich, 2017 compared the predictive performance of the MNL and the six ML classifiers (Naïve Bayes (NB), SVM, ANN, BOOST, BAG, RF) for travel mode choice analysis.

Zhao, et al., 2020 carried out a study to examine the basic differences in model development, evaluation, and behavioural interpretation between logit models and seven machine learning models for mode choice modeling. A study, by Salas, et al., 2021 compared the predictive performance of five machine learning classifiers (K-Nearest Neighbours (KNN), NN, RF, SVM, XGB) and MNL and MMNL models.

2.2 Survey methods

User's travel mode choice in Malaysia was studied by Ali, et al., 2021 using the data collected through the Revealed and Stated Preference (RPSP) surveying technique. Omrani, 2015 suggested the use of NN outer to predict

travel mode choice based on the Socio-economic Panel Survey Liewen Zu Le Tzebuerg (PSELL Survey). Richards & Zill, 2019 used the Victorian Integrated Survey of Travel and Activity (VISTA), while Qian et al., 2021 analysed the 2017 National Household Travel Survey (NHTS) - California dataset for imbalanced mode choice data. Sekhar et al., 2006 collected travel behaviour data through a traditional home-based personal interview survey, while Hagenauer & Helbich, 2017 using data from the Dutch National Travel Survey (NTS) conducted from 2010 to 2012 for their study.

2.3 Result interpretation

Ali, et al., 2021 showed that the NN model has a higher accuracy than the Binary Logistic regression model. Omrani, 2015 also, confirmed that the NN model was the best when compared to other ML models (Multinomial logistic regression and SVM). Jaramillo & Juan, 2019 pointed out the RF and DTs algorithms in the ML model as the best way to model travel mode choice.

3. Methodology

3.1 Overview

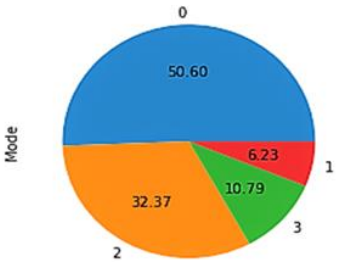

Figure 1: Cross-sectional analysis

So far, as per our understanding, no one has done a study to develop a method to estimate mode choice parameters by using the ML approach in Sri Lanka. The flow chart illustrated in Figure 2 describes the basic steps involved in the methodology.

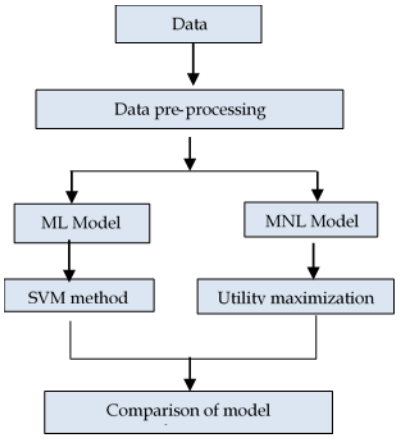

Figure 2: Flow chart of the methodology

3.2 Data collection

Raw data were obtained from online and face-to-face questionnaire surveys to identify the mode of transport used. It was focused on trips of the entire country with the aim of detecting methodical patterns in travel behaviour data scattered all over the country. Trip data were collected based on trip-specific data, socio-economic data, and household data. It was considered only the travel mode behaviour of participants aged 18 and over. For this study, 1500 raw data were collected which agreed to all the above conditions.

3.3 Data pre-processing

Data pre-processing refers to the technique of preparing (cleaning, formatting, and organizing) the raw data to make them suitable for building and training models. Refer to Figure 2 for the cross-sectional analysis of the raw data set and refer to Table 1 for a summary of the raw data set obtained from data collection. The value 0,1,2,3 stands for bus, other vehicles, train, and private vehicles respectively.

Table 1: Summary of raw data

Mode	Interpretation number	Count for each mode
Bus	0	544
Other vehicles	1	116
Train	2	348
Private vehicles	3	67

Due to the low number of responses for other vehicles and private vehicles, oversampling was done up to 544 responses. Oversampling increases the number of samples in the minority class of an imbalanced dataset to improve the model's ability to learn from and generalize to the minority class. Figure 3 shows the cross-sectional analysis of the data set after oversampling.

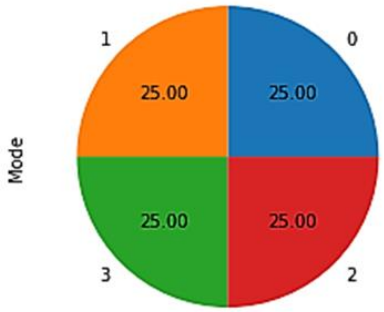

Figure 3: Cross-sectional analysis of data set after oversampling

3.4 Analysis with ML model

This analysis was carried out using SVM algorithms. After pre-processing of data, all data referred to SVM model and the outputs were obtained.

3.4.1 Cross-validation

The five-fold cross-validation technique was used to evaluate the performance of the data set. The data set was split into five different subsets. Then four subsets were used to train the data and the last subset as test data. Then the model against each of the folds and then finalized the model. Finally, the model was tested against the test set.

3.4.2 Feature selection

Here, the filter method was used as the feature selection technique. Under that, the data set ranked for each feature based on a univariate metric. Then selected the highest-ranking independent features with no constant variables, fewer quasi-constant variables, no duplicate rows, high correlation with the target variable, and low correlation with other independent variables.

3.4.3 Support Vector Method (SVM) algorithm

The goal of the SVM algorithm is to create the best line or decision boundary that can segregate n-dimensional space into classes. SVM can be of two types. They are,

- Linear SVM
  - Linear kernel
- Nonlinear SVM
  - Polynomial kernel
  - Radial Basis Function kernel
  - Sigmoid kernel

3.4.4 Model performance

This study carried out four evaluation criteria to evaluate the performance of the model developed in this study. These criteria included prediction accuracy, precision, F1 score, and recall. Furthermore, these four criteria are based on the terminology of the confusion matrix.
The terminology implemented in the confusion matrix can be explained as follows in Table 2.

Table 2: The terminology used in the confusion matrix.

		Predicted	
		N	P
Actual	N	TN	FP
	P	FN	TP

Where, TP: True Positive, these are cases predicted as yes. TN: True Negative, the cases are predicted as no. FP: False Positive, the cases are predicted as yes but users will choose the actual one. FN: False Negative, the cases are predicted as no but users will not choose the actual one.

$$Prediction\ Accuracy = \frac{(TP + TN)}{(TP + TN + FP + FN)\ \times\ 100} \quad (1)$$

$$Precision\ = \frac{TP}{(TP + FP)} \quad (2)$$

$$Recall\ = \frac{TP}{(TP + FN)} \quad (3)$$

$$F1 - score = 2 * \frac{Precision\ *\ Recall}{Precision\ +\ Recall} \quad (4)$$

3.5 Analysis with MNL model

The same data set used for the SVM model was used. But the MNL model is analysed based on the likelihood of commuters selecting travel modes. Nine available modes were considered in our study. These are bus, car, train, van/jeep, motorbike, three-wheeler, taxi, bicycle, and walking.
Initially, it was identified what modes of travel are available to commuters for each trip using a data sample. Then, if any mode is available for each trip, the available distance, available travel time, and available travel cost of each mode are considered. Thus, the data sample was rearranged according to the above three variables in relation to the modes for each trip. The following output was taken into after running the MNL model,

- Initial likelihood
- Maximum likelihood
- Rho-square
- Corrected rho-square
- Parameter estimates

4. Result and discussion

4.1 ML model

Table 3 shows the results of each kernel function under the SVM model analysis.
The values on the diagonal of the confusion matrix represented true positive values associated with each mode.

Table 3: Results of each kernel function

		Confusion Matrix				Precision	Recall	F1-Score	Accuracy
		0	1	2	3				
Polynomial Kernel	0	27	36	18	22	0.44	0.46	0.45	0.48
	1	4	89	10	9	0.73	0.85	0.78	
	2	17	26	52	18	0.62	0.58	0.60	
	3	15	22	17	54	0.65	0.56	0.60	
Radial Basis Function Kernel	0	27	36	18	22	0.43	0.26	0.33	0.61
	1	4	89	10	9	0.51	0.79	0.62	
	2	17	26	52	18	0.54	0.46	0.50	
	3	15	22	17	54	0.52	0.50	0.51	
Sigmoid Kernel	0	43	42	7	11	0.23	0.42	0.30	0.25
	1	47	45	17	3	0.25	0.40	0.30	
	2	39	48	22	4	0.45	0.19	0.27	
	3	56	47	3	2	0.10	0.02	0.03	
Linear Kernel	0	48	21	16	18	0.35	0.47	0.40	0.38
	1	30	37	28	17	0.36	0.33	0.35	
	2	24	20	53	16	0.46	0.47	0.46	
	3	37	24	19	28	0.35	0.26	0.30	

Furthermore, Precision, recall, and F1-score were obtained for each mode under different kernel functions. Prediction accuracy was taken for the each of kernel functions. There the Radial Basis Function kernel had the maximum prediction accuracy of 0.61. Precision, recall, and F1-score values were highest in other vehicle modes under the polynomial kernel function.

4.2 MNL model

Table 4 shows parameter estimation results.

Table 4: Parameter estimation values

Parameter	Result
Estimated parameter of travel time	-0.9039
Estimated parameter of travel cost	-0.0035
Estimated parameter of travel distance	-0.4266
Initial likelihood	-1114.47
Final likelihood	-958.87
Rho-square (likelihood ratio index)	0.1396
Adjusted rho-Square	0.1315

5. Discussion

The performance of two models has been compared with the probability values of each travel mode. Under the SVM model, prediction accuracy, recall, precision, and F-1 score values were taken for the each of kernel functions. There the RBF kernel had the maximum prediction accuracy corresponding to the other vehicle mode and precision, recall, and F1-score values were highest in other vehicle modes under the polynomial kernel function.

The initial likelihood, maximum likelihood, rho-square, corrected rho-square, and parameter estimates of alternative values were taken under the MNL model. According to the obtained likelihood ratio index and adjusted likelihood ratio index values, the MNL model was a good fit for the observed data. Furthermore, estimated parameter values for travel time, have the highest negative impact on the choice behavior of travelers. Therefore, travel time has a significant contribution to the utility function in choosing the mode for each trip.

6. Conclusion

According to the results obtained from the ML model and MNL model, it can be concluded that estimated parameter values for travel time have the highest negative impact on the choice behavior of travelers. Therefore, travel time has a significant contribution to the utility function in choosing the mode for each trip. RBF kernel estimates the correct mode choice method more accurately than other kernel functions.

In conclusion, though this research has been done there exists a research gap regarding the comparison between mode choice modeling by using the ML method and MNL method in Sri Lanka. Therefore, it is important to investigate mode choice modeling using other ML models and learning techniques and compare the result with the MNL model as future work.

Reference

Qian, Y, Abbasi, MA, Ali, M, Alqurashi, M, Salah, B, Zainol, R, Moeinaddini, M & Hussein, EE 2021 'Classification of imbalance travel mode choice to work data using adjustable SVM model', Applied Sciences, vol. 11, no. 24.

STRUCTURES AND MATERIALS

Shenzhen One Excellence | photograph by Eric Cheung

Wind Structure Interaction of Tall Buildings by Numerical Simulations: Large Eddy Simulation

Balasooriya L.H.S.U., Krishantha B.R.G.A., Wijesundara K.K.*

Department of Civil Engineering, University of Peradeniya, Sri Lanka

**kalmithkush@yahoo.com*

Keywords: RANSE, LES, Structured mesh, Mesh optimization

1. Introduction

The demand for high-rise buildings is increasing day by day. Due to the higher slenderness of taller buildings, they would become more sensitive to wind loading. Therefore, the prediction of wind structure interactions would become one of the major concerns in design.
The code of practices in the estimation of wind loads on structures are not reliable in economical designs of tall buildings due to the limitation and conservative predictions (Jayasundara et. al., 2018). As an alternative, wind tunnel tests are widely used to predict the wind-induced action.

2. Wind phenomena

Complicated environment is created around the building by wakes, and flow separations which results in creating different pressure zones around the building that would impose loads on the structure and its facades (Mendis et. al., 2007).

Depending on the characteristics of wind and the structure, the structure will have different modes of response. Namely along wind response, across wind response and tortional response. Heavy structures such as reinforced concrete structures can be taken as rigid and their deflections are negligibly small. But when considering the slender structures, the aero elastic behaviour cannot be omitted. The slender structures are becoming more popular due to economical requirements and various new design techniques are now being used to make reliable structures in more optimized manner. For such a complicated phenomenon, conducting a wind tunnel test requires a lot of effort in creating the scaled-down model of the prototype to have proper similitude between model and prototype [3] (Frison, Maria (2018)).
Hence a proper simulation method should be there to analyse the behaviour of wind and structural interactions and the corresponding structural responses.

3. Reynolds averaged Navier Stokes equations

By time averaging the Navier Stokes equation for incompressible fluids, an average flow representation of the actual flow is obtained by RANSE. The momentarily values are decomposed into mean and fluctuating value as shown in Figure 1 and as in Eq [1].

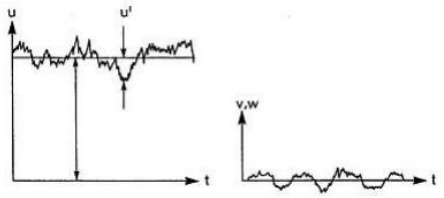

Figure 1: Turbulent velocity as a combination of mean and fluctuating components

$$u = \bar{u} + u', v = \bar{v} + v', w = \bar{w} + w' \qquad \text{Eq [1].}$$

Hence time average of fluctuating velocity should be zero as in Eq [2].

$$\overline{u'} = 0 \ , \overline{v'} = 0 \ , \overline{w'} = 0 \ , \overline{p'} = 0 \qquad \text{Eq [2].}$$

Substitute these equations to the NS equation and taking time average will result the following form as in Eq [3].

$$\overline{\rho\left(\frac{\partial(\bar{u}+u')}{\partial t} + \frac{\partial(\bar{u}+u')^2}{\partial x} + \frac{\partial(\bar{u}+u')(\bar{v}+v')}{\partial y} + \frac{\partial(\bar{u}+u')(\bar{w}+w')}{\partial z}\right)}$$

$$= \overline{F - \frac{\partial(\bar{p}+p')}{\partial x} + \mu\left(\frac{\partial^2(\bar{u}+u')}{\partial x^2} + \frac{\partial^2(\bar{u}+u\prime)}{\partial y^2} + \frac{\partial^2(\bar{u}+u\prime)}{\partial z^2}\right)} \qquad \text{Eq[3].}$$

By simplifying the above equation and final time averaged Navier Stokes equations (RANS) for all three directions (x,y,z) can be expressed as in Eq [4].

$$\rho \frac{D\overline{u_i}}{Dt} = F_i - \frac{\partial \bar{p}}{\partial x_i} + \mu \Delta \overline{u_i} - \rho\left(\frac{\partial \overline{u_i' u_j'}}{\partial x_i}\right) \qquad \text{Eq[4].}$$

This results an additional term in the NS equation is called Reynolds stress and to resolve

this term, eddy viscosity stress models are used, here k-ε model was used.

3.1 K- ε model

According to **B. E. Launder and Sharma (1974**) [4], for low Reynolds applications, damping functions are applied to the model coefficients in the transport equations. k-ω SST model is preferred for low Reynolds number applications where the buffer region is less than 5m from building walls. for high Reynolds number applications, the k-ε model is preferred when the buffer zone is within 5-30m from the building walls. This model is represented with Equations Eq [5] and Eq [6] which is used for this simulation.

$$\frac{\partial(\rho k)}{\partial t} + \nabla.(\rho U k) = \nabla.\left[(\mu + \frac{\mu_t}{\sigma_k})\nabla k\right] + P_k + P_b - \rho\epsilon + S_k \quad \text{Eq[5]}$$

$$\frac{\partial(\rho \epsilon)}{\partial t} + \nabla.(\rho U \epsilon) = \nabla.\left[(\mu + \frac{\mu_t}{\sigma_\epsilon})\nabla \epsilon\right] + C_1 \frac{\epsilon}{k}(P_k + C_3 P_b) - C_2 \rho \frac{\epsilon^2}{k} + S_\epsilon \quad \text{Eq[6]}$$

Where the C_1, C_2, C_3 are model coefficients, these are varying between models.

4. Large eddy simulation

In large eddy simulation, the cell sizes should be roughly determined prior to the formulation of the CFD grid so the mesh resolves more than 80% of turbulent kinetic energy. For this the usual practice is to have the minimum size of a cell to be at least $1/5^{th}$ of the integral length scale. Smagorinsky - lily model was used here. In this model, an additional stress term is applied to dissipate the eddies just larger than mesh size as in Equations Eq [7] and Eq [8].

$$\frac{\partial p}{\partial t} + \frac{\partial(\rho U_j)}{\partial x_j} = 0 \quad \text{Eq[7]}$$

$$\frac{\partial(\rho U_i)}{\partial t} + \frac{\partial}{\partial x_j}\left(\rho U_i U_j\right) = -\frac{\partial p}{\partial x_j} + \frac{\partial}{\partial x_j}(\tau_{ij} + \tau_{sgs}) \quad \text{Eq[8]}$$

To calculate τ_{sgs} , an eddy viscosity approach is used as shown in Eq [9].

$$\tau_{sgs} = 2\rho v_{sgs} {S_{ij}}^* - \frac{2}{3} k_{sgs} \delta_{ij} \quad \text{Eq[9]}$$

Where,

$${S_{ij}}^* = \frac{1}{2}\left(\frac{\partial U_i}{\partial x_j} + \frac{\partial U_j}{\partial x_j} - \frac{\partial U_k}{3\partial x_k}\delta_{ij}\right) \quad \text{Eq[10]}$$

Now to calculate v_{sgs}, Eq [11] can be used.

$$v_{sgs} = {l_0}^2 * \sqrt{S_{ij} S_{ij}} \quad \text{Eq[11]}$$

Where the l_0 is called the sub grid length scale. The sub grid length scale can be determined using Eq [12].

$$l_0 = C_s \Delta \quad \text{Eq[12]}$$

5. Model development

5.1 Computational domain and mesh arrangement

The dimensions of the building model used in the computational domain is the full-scale rigid model of the CAARC standard building is shown in Figure 2.

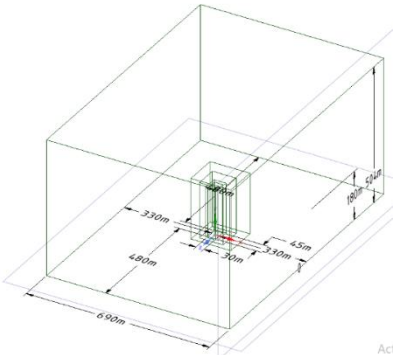

Figure 2: Computational domain

The CAARC standard tall building model which is a rectangular prismatic body with flat surfaces, without parapets as defined in Melbourne (1980) was used for the building since the same building model has been tested in wind tunnels and the results can be used to validate the CFD results. The building has the height of 180 m, the length of 30 m and the width of 45 m. For the purpose of comparison of results with some earlier simulations available in literature, blockage effect, flow obstacle effect, boundary layer development of wind tunnel walls was considered when creating the domain which has been considered by the majority of early simulations (Choi & Kwon, 1998; Huang, 2010). But it was clear that for CFD simulations the all-natural phenomena shouldn't be considered due to availability of facilities to define the desirable boundary conditions in software like ANSYS fluent. But for the for easy reference, larger domain was taken.

The structured domain with 4 regions was created by ANSYS workbench space claim. This enables the programmer to allocate desired element sizes, shapes at places of his interest which are the turbulent regions and flow

separation regions in the domain. Hence, this will facilitate modeling turbulent kinetic energy effectively. The layers were made eccentric with more shift to the leeward side since wind is more turbulent at the backside of the building after interacting with the structure. The element sizes were increased from inside to out by these layers and interconnection were made by the cut cell method using transition layer in between layers. The mesh arrangement is shown in Figure 3. The layers are of 0.5m and 0.9, 2.5, and 10m size hexahedral elements respectively. The continuity of the domain was maintained by energy coupling between contact surfaces. Inflation layers and sharp angle edges were defined for further smooth interactions between solid walls and wind. Number of elements generated in this mesh was 4.13 X 10^6.

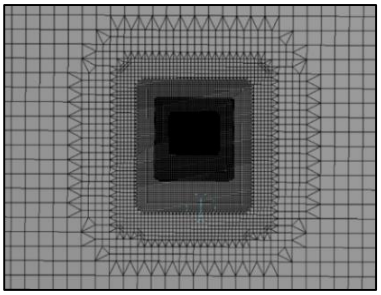

Figure 3: The cut cell assembly of layers of the mesh arrangement

5.2 Boundary conditions

The power law wind profile in NAE a, NAE b, and western (Melbourne, 1980) with exponent 0.28 has been used in the simulation. The velocity components in the y and z axis are made zero at the inlet to create the power law wind profile in the Eq [13].

$$\frac{U}{U_H} = \left(\frac{Y}{Y_H}\right)^{\alpha} \qquad \text{Eq[13]}$$

Where U is the velocity at height Y, U_H is the maximum velocity of the domain 15 m/s, Y_H is the height of the domain and α being 0.28. air was considered incompressible fluid with density 1.225 kg/m3 and Viscosity 1.79 x 10^{-5} kg/m.s at 25 □C. Zero pressure was given at the outlet face preventing any reverse flow. The ground and faces of the building are no-slip boundaries while the wind tunnel walls were defined to be slip boundaries.

6. Results

6.1 Observations

The numerical simulation produces the variation of pressure and within the domain. The pressure values around the perimeter at 2/3rd height of the building can be used to derive the non-dimensional pressure to compare with the wind tunnel test. The non-dimensional pressure is calculated by Eq [14]. For comparing RANSE and Large eddy simulation, both simulations were carried out in the same mesh at the same input parameters as explained. The results can be seen as in Figures 6, 7 and 8.

$$Normalized\ pressure\ (P') = \frac{p}{\frac{1}{2}\rho {U_H}^2} \qquad \text{Eq [14]}$$

Comparing the results with wind tunnel test and past studies, RANSE is now able to overcome the large deviations that were observed at the points of flow separation and sharp edge is shown in Figure 4. The results of RANSE are now more accurate on the windward side and leeward side of the building. This is mainly because of the structured mesh arrangement used here and it can model the shear layer of wind at flow separation point is shown in Figure 7. Due to selective mesh refinement at the edges building, effects of shearing, and flow separation has been modelled very accurately from this mesh arrangement than it was modelled using auto mesh arrangements in previous studies. It is clear now the LES is more sensitive to finer details of wind phenomenon comparing with RANSE. Hence, LES produces more accurate results in turbulent regions than RANSE. By pressure contours are shown in Figures 5 and 6, LES has solved the pressure gradient to initiate the crosswind response of a building that cannot be observed in RANSE. Hence, in further studies LES will be more reliable in predicting the response of slender structures even though this study is limited to rigid structures.

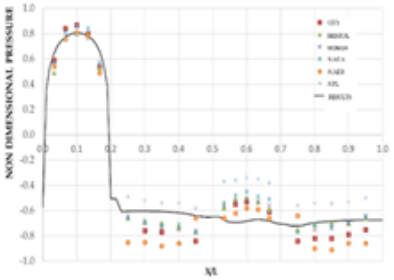

(a)

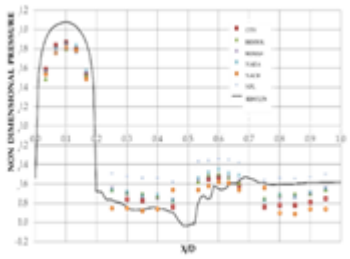

(b)

Figure 4: Normalized pressure at 120m (a)RANSE (b) LES

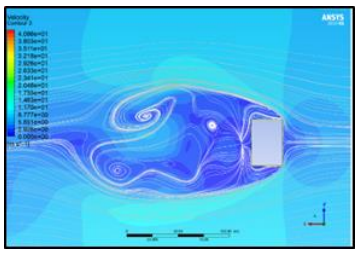

Figure 5: Pressure contours and streamlines of RANSE

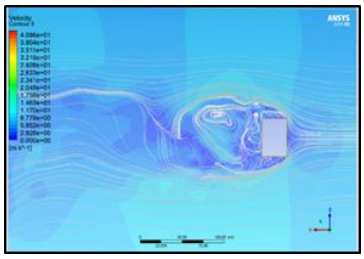

Figure 6: Pressure contours and streamlines of LES

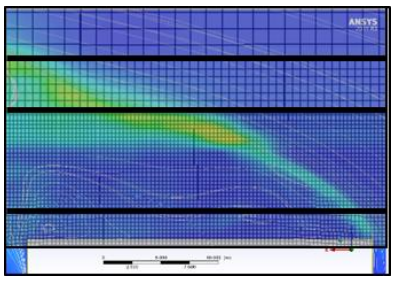

Figure 7: Accurate modeling of shear layer using structured mesh

5. Conclusions

Despite of minor discrepancies LES can provide more realistic, natural wind and structural interactions compared to RANSE. Considering the computational effort, RANSE is still economical to perform and still will be reliable for simple applications. Furthermore, it is not useful when using the theories that are there for wind-tunnels in defining the computational domain for CFD since programs like ANSYS has the ability of modeling wind tunnel walls without developing boundary layers. Hence height and width equivalent to 2 heights of the building will be sufficient as observed by this simulation for the computational domain given that no other tall buildings in the proximity of the subject. This will be helpful in reducing the number of elements in the mesh to a greater extent thereby reducing the computational power.

References

Jayasundara, Dilhara & Koliyabandara, Nipun & Wijesundara, Kushan. 2018. Wind Loads on Tall Buildings: A Comparative Study of the International Wind Codes and Numerical Simulation. Engineer: Journal of the Institution of Engineers, Sri Lanka. 51. 31. 10.4038/engineer. v51i3.7304.

Mendis P., Ngo T., Hira A., Samali B., Cheung J., Wind loading on Tall Buildings, Electronic Journal of Structural Engineering, Special Issue: Loading on Structures, 2007, 42-54.

Frison, Giovanni & Marra, Antonino & Bartoli, Gianni & Scotta, Roberto. 2019. Full-Aeroelastic Model of CAARC Building: Iterative Design Procedure and Wind Tunnel Tests: IN-VENTO 2018. 10.1007/978-3-030-12815-9_25.

Launder, B. and Spalding, D., 1974. The numerical computation of turbulent flows. Computer Methods in Applied Mechanics and Engineering, 3(2), pp.269-289

Melbourne W.H., Comparison of Measurements on The CAARC Standard tall Building Model in Simulated Model Wind Flows, Journal of Wind Engineering

Choi, C.-K. and Kwon, D.-K. 1998, "Wind tunnel blockage effects on aerodynamic behavior of Bluff Body," Wind and Structures, 1(4), pp. 351–364

Huang, S.H., Li, Q.S., Wu, J.R., A general inflow turbulence generator for large eddy simulation, Journal of Wind Engineering and Industrial Aerodynamics, 98, 600–617, 2010.

Jayathilake, S. and Wijesundara, K. 2021. Prediction of Wind Induced Response of Tall Buildings Using RANS Simulations,:Journal of the Institution of Engineers, Sri Lanka.

Koliyabandara, N.,Jayasundara, D. and Wijesundara, K. 2018. Evaluation of Different Turbulence Models in Determining Wind Loads on Tall Buildings.society of structural engineers sri lanka, annual sessions 2018.

Performance Based Design of Stiffened Extended End Plate Beam to Column Connection

Rajapaksha R.A.S.C., Premasiri S.M.C., Wijesundara K.K.*

Department of Civil Engineering, University of Peradeniya, Sri Lanka

**kalmithkush@yahoo.com*

Keywords: Performance based design, Steel connection, Stiffened extended end plate connection

1. Introduction

In steel building construction, beam and column connections are crucial elements because the connection is what holds the beam and the column together. If the connection fails, there will be nothing to hold the beam and column together, which could be a primary reason for the collapse of the entire structure. Therefore, it is essential to design the connection properly to withstand the expected load. Over the past years, numerous experiments have been conducted to determine the most secure and economical solutions for connecting two steel elements to withstand different kinds of loads without failure (Tartaglia R. et al., 2018).

In steel connections, welding two materials together was the easiest and most effective method in the past (Shi Y. et al., 2007). Welding allowed for a rigid connection that could resist moments, but it only satisfied the strength requirement and not the ductility. For this reason, during the 1994 Northridge earthquake and the 1995 Kobe earthquake, although structures appeared sound, detailed studies revealed many fractures occurring in welded connections. To address this issue, end plates were introduced. An end plate was welded to the beam web and then connected to the column flange using bolts (Nader M. et al., 1996). However, the moment resistance of this approach was not as expected. To improve it, the end plate was extended, increasing the lever arm and thus enhancing the moment-resisting capacity of the connection (Faridmehr I. et al., 2019). Despite being adequate for the job, this connection also faced challenges. Because the top part of the extended end plate is fixed to the column flange with bolts, bolt failures occurred at the edges due to prying forces. To mitigate this, a stiffener was introduced, fixed to the end plate and the beam flange to prevent bolt failures from prying forces. This not only increased the moment-resisting capacity of the connection but also improved its stability (Mokhtar R. et al., 2020).

There are various types of steel connections and different approaches to designing and constructing them. This research project focuses on the stiffened extended end plate connection, which falls under the category of rigid connections (Moncarz P. et al., 2001). While various construction codes provide methods for building typical connections, even in Eurocode, there is no specific method to design a stiffened extended end plate beam-to-column connection. While specifications for stiffened extended end plate connections exist, such as those in AISC, these methods primarily fulfill the strength requirements of the connection, neglecting its ductility. As a result, the full capacity of each connection component is not utilized (Bjorhovde R. et al., 1990). Normally, ultimate limit state design and serviceability limit state design methods are employed for designing connections (as per Eurocode), but these methods do not explicitly address the behaviour of the connection under exclusive load situations.

Typically, when designing based on existing code-based methods, structures are designed so that the resisting loads remain within the elastic range of the material (well below the yield point, usually at around 2/3 of the elastic range (Bjorhovde R. et al., 1990). This approach ensures structural safety but underutilizes the material's capacity, as it can withstand yielding without failure. Incorporating yielding into the design process allows the material to be used to its fullest capacity, resulting in greater economic efficiency compared to standard code-based methods (Tartaglia R. et al., 2017).

Therefore, this project aims to develop a design method for constructing a stiffened extended

end plate beam-to-column connection. This method will consider not only strength but also ductility, enabling the prediction of failure in excessive load situations. The objective is for the most preferable failure to occur first in such situations, preventing total structural collapse and resulting in a more effective stiffened extended end plate beam-to-column connection than existing code-based methods.

2. Literature review

We conducted a comprehensive literature review, exploring the intricate landscape of performance-based designs for stiffened extended end plate beam-to-column connections. This review not only delved into the significance of this innovative approach but also systematically unearthed the gaps within current knowledge, while concurrently highlighting its undeniable advantages when compared to the more traditional code-based methods (Raafat E. S. Ismail, 2014). Our investigation was further enriched by an exhaustive examination of numerical and experimental findings, providing crucial insights into the vulnerabilities of alternative connections, the nuances of failure patterns, and the intricacies of yield mechanisms. All these findings are of paramount importance, as they form the bedrock of our current research efforts.

Literature review primarily centred on the domain of steel connections, with an unwavering focus on the historical failures documented within such structures. We dedicated significant attention to prior experimental studies that scrutinized stiffened extended end plate connections, extending our evaluation to encompass the diverse array of yield mechanisms and failure modes that hold relevance to steel connections as a whole (Xing S. et al., 2016).

This in-depth review has, in essence, provided us with a profound understanding of the multifaceted nature of steel connections. It underscores the pressing need to address the identified gaps within current design methodologies, underscoring the urgency of transitioning to a more performance-oriented approach. By synthesizing a diverse array of sources, ranging from meticulously documented experimental results to rigorously tested theoretical insights, this review emerges as a foundational cornerstone for the subsequent development of an effective and cutting-edge performance-based design methodology for stiffened extended end plate beam-to-column connections (Zhao W. et al., 2012).

Furthermore, our exploration unveiled a clear trajectory for future research endeavours within this field. The potential applications of performance-based designs extend beyond just improved structural integrity. They have the capacity to revolutionize the way we conceive, design, and evaluate steel connections in the broader context of civil engineering. The gaps identified in the current body of knowledge serve as signposts, guiding us towards a more resilient and sustainable future in structural design.

As we continue this journey of innovation, it becomes increasingly evident that the evolution of performance-based design methodologies for stiffened extended end plate beam-to-column connections has the potential to reshape the landscape of structural engineering, where safety, efficiency, and sustainability converge seamlessly.

3. Methodology

Designing of performance based stiffened extended end plate connection has done according to main steps shown in Figure 1.

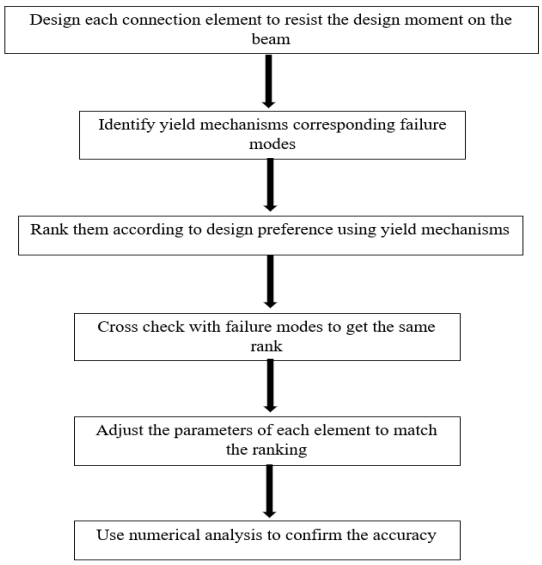

Figure 1: Main steps in methodology

Initially, the design process involves calculating the design moment on the beam and dimensioning each connection element to withstand this calculated moment. This can be

accomplished using established equations derived from Eurocode and other relevant literature sources. Once the initial design of connection elements is complete, the subsequent steps focus on assessing the yield mechanisms and corresponding failure modes present within the connection.

A pivotal aspect of this methodology entails prioritizing these yield mechanisms and failure modes. This prioritization is based on a predetermined ranking order, as preferred by the designer or engineering standards. Ensuring structural integrity without abrupt collapse due to connection failure hinges upon orchestrating the sequence of failures. Ideally, the most ductile failure mechanism should initiate the sequence, ensuring a progressive structural response. This contrasts with a scenario where the least ductile (or most brittle) failure starts the sequence, leading to rapid and potentially catastrophic failure.

To achieve the desired sequence, the yield strength of the most ductile failure mechanism should be the lowest among all potential failure modes. Conversely, the yield strength of the least ductile failure mechanism should be the highest. Adjustments to the parameters of each connection component are then made to attain the required yield strengths, aligning with the intended failure sequence.

A subsequent validation step involves cross-referencing the ultimate strengths of each component against the intended failure sequence. If the ranking is not consistent with the expected order, further parameter adjustments are warranted to reconcile the discrepancy.

Finally, to ensure the efficacy of the design, numerical simulations are conducted using tools such as MIDAS software. These simulations serve to validate the envisioned failure sequence and ascertain that the designed ranking order is upheld. This iterative and comprehensive approach not only provides a means to design robust connections but also establishes confidence in the structural integrity of the entire system.

4. Results and discussion

Initially, the validity of both the MIDAS software and the employed numerical modeling methodology was established through a rigorous validation process which used experimental data that was taken from a past experiment (Figure 2) which was done by Shi Y. et al., 2007. Same experimental setup was modeled using MIDAS software as a numerical simulation and the results are compared with experimental results to ensure the validity of the tool.

After doing the same test using numerical analysis (Figure 3), it was observed that results are very close in both experiment and numerical analysis as shown in Figure 4. This concluded that this numerical analysis method is adequate for obtaining accurate results, hence this numerical analysis is valid for using in this research.

Utilizing the previously mentioned steps and methods, models were created using MIDAS according to the preferred ranking order and the poor ranking order. Force-displacement curves for yielding and stress-strain curves were developed for each of these models. These graphs were generated by considering a specific point on the model and were employed to analyze the failure modes of the model.

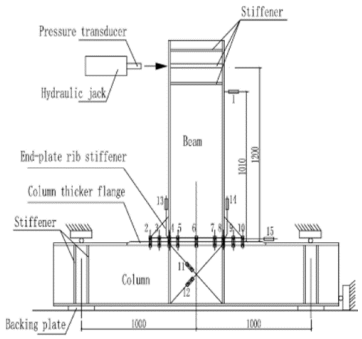

Figure 2: Loading arrangement used in experiment

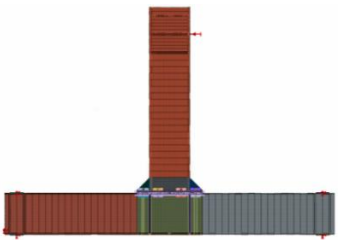

Figure 3: Validation model made using MIDAS

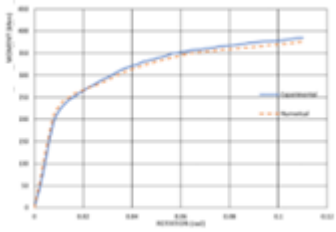

Figure 4: Comparison of experimental results and numerical results

Upon referring to the results of the preferred ranking order model, it was evident that the connection behaved in accordance with the predictions, in other words, failures occurred as per the preferred ranking order. After modeling the design for the poor ranking order, it was observed that the poor ranking model could not withstand as much stress as the preferred ranking model, and the connection would fail first (Figures 5 and 6). This demonstrates that connections designed according to the preferred ranking order are the most suitable connections for withstanding higher loads while retaining the capacity to maintain the connection without experiencing premature failure during situations of excessive load.

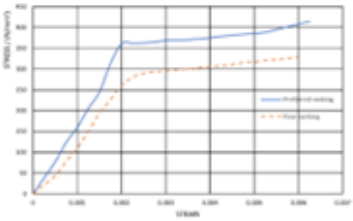

Figure 5: Comparison between preferred ranking order and poor ranking order (stress vs. strain)

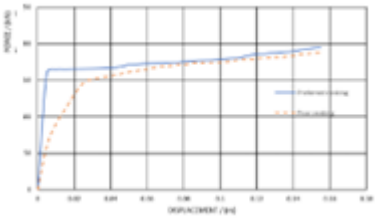

Figure 6: Comparison between preferred ranking order and poor ranking order (force vs. displacement)

5. Conclusions

By comparing preferred ranking design and poorranking design, it showed that around 5% of strength enhancement and around 5% of ductility enhancement have been achieved. Therefore, it can be concluded that both strength enhancement and ductility enhancement can be achieved by using the proposed preferred ranking order for performance-based design method, unlike in code- based methods where only the strength isconsidered.

Also in this research, it was concluded that using stiffeners connecting beam flange and end plate, have stabilized the connection even more and moment resistance capacity was higher than moment resistance capacity of connections without stiffeners.

References

Bjorhovde, R., Colson, A., & Brozzetti, J. 1990. Classification System for Beam-to-Column Connections. Journal of Structural Engineering, 116(11), 3059-3076.

Faridmehr, I., Tahir, M., Osman, M., & Azimi, M. 2019. Cyclic Behaviour of Fully Rigid and Semi-Rigid Steel Beam-to-Column Connections. International Journal of Steel Structures, 20(2), 365-385.

Mokhtar, R., Ibrahim, Z., Jumaat, M., Abd. Hamid, Z., & Abdul Rahim, A. 2020. Behaviour of semi-rigid precast beam-to-column connection determined using static and reversible load tests. Measurement, 164, 108007.

Moncarz, P., McDonald, B., & Caligiuri, R. 2001. Earthquake failures of welded building connections. International Journal of Solids and Structures, 38(10-13), 2025-2032.

Nader, M., & Astaneh-Asl, A. 1996. Shaking Table Tests of Rigid, Semirigid, and Flexible Steel Frames. Journal of Structural Engineering, 122(6), 589-596.

Özkılıç, Y. 2021. A comparative study on yield line mechanisms for four bolted extended end-plated connection. Challenge Journal of Structural Mechanics, 7(2), 93.

Raafat E. S. Ismail, 2014. Alexandria International Conference of structural and Geotechnical Engineering -(AICSGE 8), Alexandria, Egypt.

Shi, Y., Shi, G., & Wang, Y. 2007. Experimental and theoretical analysis of the moment–rotation behavior of stiffened extended end plate connections. Journal of Constructional Steel Research, 63(9), 1279-1293.

Tartaglia, R., D'Aniello, M., Rassati, G., Swanson, J., & Landolfo, R. 2018. Full strength extended stiffened end-plate joints: AISC vs. recent European design criteria. Engineering Structures, 159, 155-171.

Tartaglia, R., & D'Aniello, M. 2017. Nonlinear Performance of Extended Stiffened End Plate Bolted Beam-to-column Joints Subjected to Column Removal. The Open Civil Engineering Journal, 11(1), 369-383.

Xing, S., Dong, P., & Threstha, A. 2016. Analysis of fatigue failure mode transition in load-carrying fillet-welded connections. Marine Structures, 46, 102-126.

Zhao, W., & Tong, G. 2012. Demand on Stiffeners in Stiffened Extended End-Plate Connections. Advances in Structural Engineering, 15(8), 1455-1469.

Failure Prediction of Impaired Dapped End Beams: Analytical Approach

Abeysingha M.L.T., Padmasiri W.P.P.M., Yapa H.D.*

Department of Civil Engineering, University of Peradeniya, Sri Lanka

**hdy@eng.pdn.ac.lk*

Keywords: Dapped end, Kinematics, Failure

1. Introduction

Reinforced concrete dapped end beams, also referred to as half-joints, have a complex geometry that consists of both a locally disturbed nib region and a full depth section. Even though dapped end beams were popular in several decades ago, the unusual shape of the beam induces a severe stress concentration at the re-entrant corner which may lead to several defects due to material deterioration or improper reinforcement detailing. Still, there are a number of involvements regarding the failure analysis of dapped end beams, a research vacuum can be identified for further exploration. There is a possibility of application of analytical tools for the failure load prediction of impaired dapped end beams. Moreover, limited levels of distresses have been attempted in existing model. Therefore, the study has focused on failure prediction of structurally deficient dapped-end beam and aimed to promote load capacity prediction via analytical tools.

2. Literature review

2.1 Dapped end beams

Dapped End Beams are characterized by its geometry due to the local reductions in the overall depth of the beam at the supports achieving by recessing the supporting corbels into the depth of the beams supported. Generally dapped end beams are designed following one of two main reinforcement layouts; diagonal type and orthogonal type (Desnerck et al., 2016).

2.2 Design approaches

The geometric discontinuity of the dapped end creates a disturbance in stress flow close to the re-entrant corner and in the nib area, which is caused to form a disturbed region (D-region) where the hypothesis of Bernoulli is no longer valid. Therefore, usual design practices cannot be followed in order to design dapped end beams. By referring to the literature, strut and tie modeling, Precast/ pre-stressed Concrete Institute (PCI) Guidelines, mechanism analysis, kinematic based model and nonlinear numerical modeling have been identified as potential design approaches and techniques. Amongst, kinematics-based model which is presented by Rajapakse et al. (2022), is focused on the ability of applying the measurable data of existing dapped end connections. The model is aimed at capturing the peak resistance of dapped-end connections whose behavior is governed by the widening of a critical inclined crack at the re-entrant corner, based on first principles: kinematics, equilibrium and constitutive relationships. The existing approach has been developed to predict the peak resistance for a fixed maximum strain of 0.0035 at the top fibre of the concrete surface.

2.3 Structural deficiencies

The failure of dapped end beams may cause an immense damage with little or no warning. The investigations showed that the misalignment and reduction of reinforcing bars, improper reinforcement detailing, deterioration defects and combinations of those defects led to the collapses. In the diagonal type reinforcement arrangement, diagonal bar and U bar were identified as key elements of a half joint (Desnerck et al.,2018).

3. Methodology

3.1 Initial study

The process of failure analysis of dapped end connection can be expressed through several stages. Initially, a literature survey was carried out to identify analytical approaches and numerical simulation method under identification of design approaches. The study was extended to identify a set of critical defects too. Furthermore, kinematic based model was selected as the appropriate analytical approach for the implementation due to its applicability to

both diagonal and orthogonal reinforcement arrangements and ability to take onsite measurements for the prediction. The study focused primarily on extension of this existing kinematics-based model towards dapped end beams that are vulnerable for distinct defects.

3.2 Extension of the existing model

The major extensions included: introduction of provisions for failure due to steel yielding, association of full depth diagonal tension crack and improvement of formulation to capture local reductions of reinforcement.

A dapped end does not especially reach its peak resistance for a fixed strain equals to 0.0035, since the failure of steel reinforcement could take place before the failure of concrete. Hence, in this study the model was extended to input the strains of the post peak regime of the concrete stress strain behavior curve to the ultimate strain (0.0035) with an incremental variation. Meanwhile, failure option for steel reinforcement also was inserted by preventing the increasing of stresses of reinforcement beyond the ultimate stresses of the steel. The solution procedure for the extended kinematics-based model is illustrated in Figure 1 and the extensions are highlighted in blue colour.

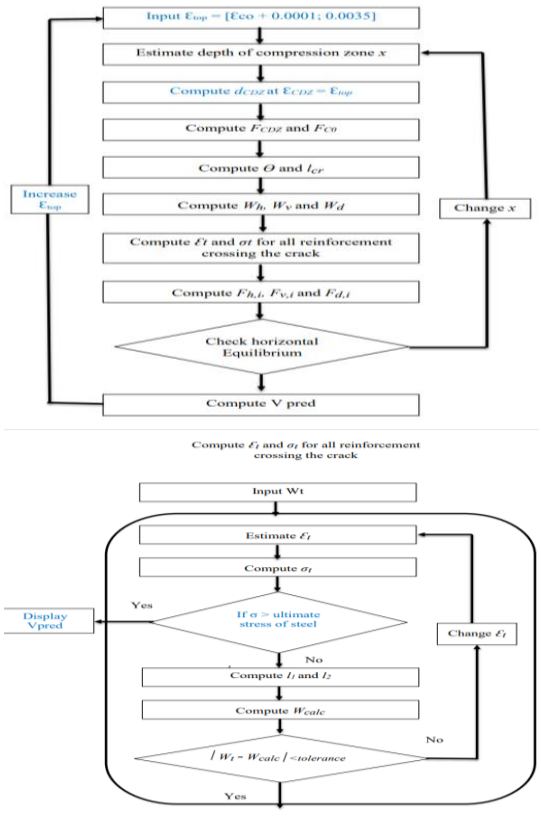

Figure 1: Solution procedure for extended model

This will lead to the failure of the beam either due to the reaching of the reinforcement stress to its ultimate stress or due to the reaching of the strain of the top fiber of concrete to its ultimate strain (Ɛtop =0.0035).

Even though the existing kinematic based model is mainly focused on the opening of re-entrant corner crack, in this study, the existing model was extended to account for full depth diagonal tension crack since it shows a flexural behaviour. A similar kinematic behaviour was assumed to model the full depth diagonal tension crack by considering the first principles for relevant reinforcing elements and concrete compression zones. In such cases, the failure load is obtained as the minimum value given by both crack patterns.

In the case of local reinforcement corrosion, the force equilibrium was developed in a same manner considering the reduced bar diameter to account for anchorage lengths and forces.

3.3 Shear capacity prediction

There were six specimens including the control beam (NS-REF), a beam with low concrete strength (LS-REF) and 4 defective beams representing the defects of elimination of diagonal bar (NS-ND), elimination of U bar (NS-NU), reduced shear links (NS-RS), and effect of local reduction due to corrosion (NS-LR) in the selected list for the shear capacity prediction. The model validation was done comparing the specimens with experimental values given in the literature. Furthermore, the extended model was used to predict the load capacity of dapped end connections impaired due to three levels of reduced shear links ($1^{st}/2^{nd}$ links, $1^{st}/3^{rd}$ links, and $2^{nd}/4^{th}$ links). All three defective specimens were modeled using non- linear numerical simulation and predicted values were compared with numerically obtained results. The validity of application of numerical model was evident with the analysis of control beam using non-linear numerical modeling.

4. Results and discussion

Figure 2 shows an overview of the variation of predicted values from the extended model with the experimentally obtained results. Predicted values shows promising results in contrast to the experimental values since the prediction offset was in a range of -24% to 7%. In most of the cases, extended model predicts failure in a

reasonable similar mode with experimental results.

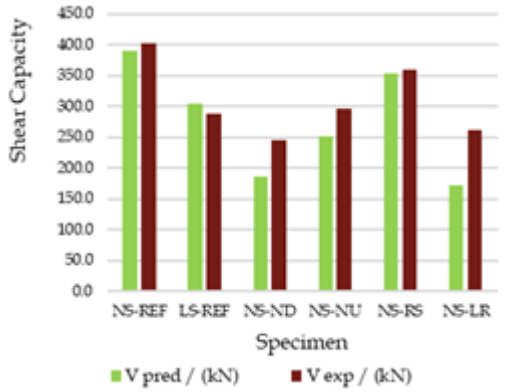

Figure 2: Comparison of predicted results with experimental results

The results obtained from the extended model were compared with the results which were extracted from the literature for the existing model. It can be observed that the precision has improved by 14% with the extended model for the control beam and in case of defects it has improved by nearly 3% (Figure 3). However, an improvement can be obtained with the extended model.

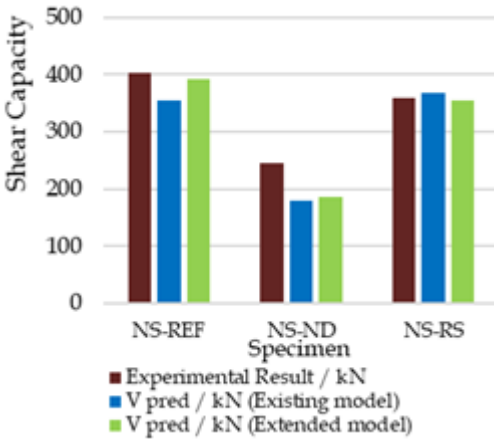

Figure 3: Comparison of extended model with existing model

A comparison between predicted results for shear capacity using different design approaches and the experimentally obtained results are illustrated in Figure 4. Extended kinematics-based model has always given a better prediction compared to the STM prediction.

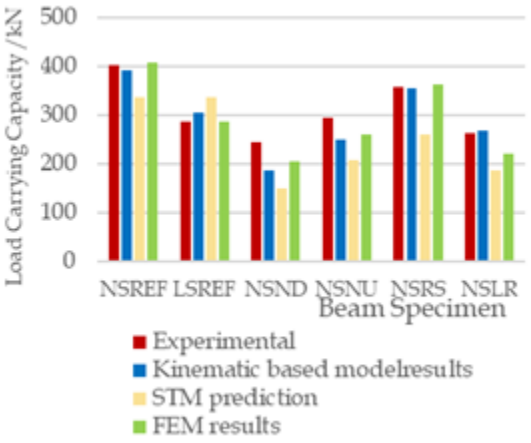

Figure 4: Comparison of results

NS-REF specimen was simulated using MIDAS FEA software and compared with the experimental results with the intention to check whether the developed numerical model will give satisfactory results for novel defects. The predicted load displacement behaviour and crack pattern are matched with experimental result as shown in Figure 5 and 6 respectively.

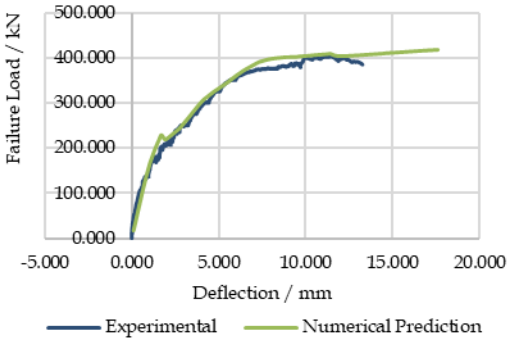

Figure 5: Comparison of numerical results and experimental results for NSREF

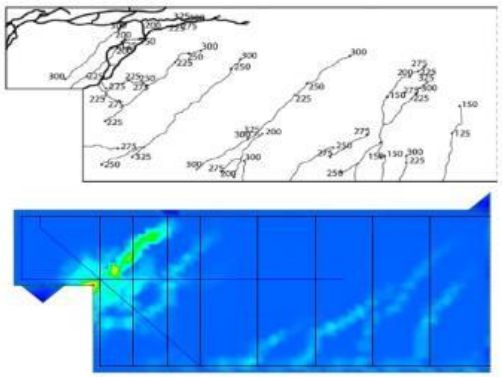

Figure 6: Experimental and numerical crack patterns of NSREF

Figure 7 shows the results obtained from numerical model and extended model for NS-RS specimens. Elimination of 1st and 2nd shear links causes the lowest shear capacity

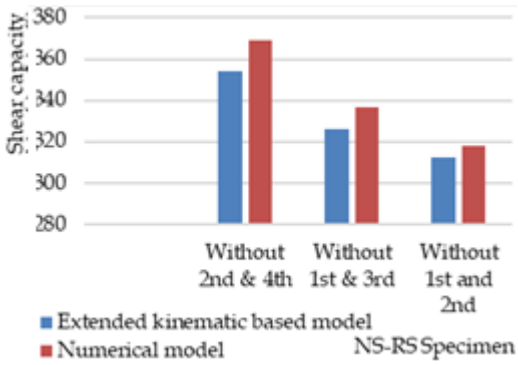

Figure 7: Comparison of results from extended model and numerical model for NSRS

5. Conclusions

The extended kinematics-based model provided better predictions for the available experimental results in contrast to the existing model. The prediction offset was in a range of -24% to 7%.

The prediction precisions of the extended model were 2.7 % and 1% for the control beam and the beam with reduced shear links respectively whereas those were 16.7% and 2.7% from the existing model respectively.

The predictions from the extended model were much superior to the traditional STM prediction.

The load capacity of dapped end connections impaired due to three levels of reduced shear links ($1^{st}/2^{nd}$ links, $1^{st}/3^{rd}$ links, and $2^{nd}/4^{th}$ links) were predicted with the extended analytical model and compared with the experimental results (only for the $2^{nd}/4^{th}$ links case) and with the non-linear Finite Element predictions. The prediction offset was under 4% across all these comparisons. All the kinematic based model predictions for these scenarios associated with the extension introduced to the full depth shear crack.

The reduction of the first two shear links was the most critical type of defect amongst the cases of reduced shear reinforcement distress. For instance, the load reduction due to $1^{st}/2^{nd}$ link elimination was 20% in contrast to the elimination of $1^{st}/ 3^{rd}$ shear 73 links (load reduction = 16.5%) and to elimination of $2^{nd}/4^{th}$ shear links (reduction = 9.4%)

In the case of local reduction of reinforcement due to corrosion, the load capacity reduced by 21%, 32% and 55% respectively for 25%, 50% and 75% of reinforcement area reductions. However, a simple correlation could not be identified between the input and the output. Further studies into the matter is identified as a matter for future work

References

Abeysinghe, S.A. and Yapa, H.D., 2022. Numerical simulation of damaged reinforced concrete half-joint beams: towards appraisal and retrofitting. Proceedings of the Institution of Civil Engineers-Structures and Buildings, pp.1-37.

ACI 318-05, Building code requirements for structural concrete and commentary, American Concrete Institute, USA, 2005.

Desnerck, P., Lees, J. and Morley, C. 2015. Bond behaviour of reinforcing bars in cracked concrete. Construction and Building Materials, 94, pp.126-136.

Desnerck, P., Lees, J. and Morley, C. 2016. Impact of the reinforcement layout on the load capacity of reinforced concrete half-joints. Engineering Structures, 127, pp.227-239.

Desnerck, P., Lees, J. and Morley, C. 2017. The effect of local reinforcing bar reductions and anchorage zone cracking on the load capacity of RC half-joints. Engineering Structures, 152, pp.865-877.

Desnerck, P., Lees, J. and Morley, C. 2018. Strut-and-tie models for deteriorated reinforced concrete half-joints. Engineering Structures, 161, pp.41-54.

Eurocode 2: Design of concrete Structures-Part 1-1: General rules and rules for buildings 1992.

Mihaylov, B., Rajapakse, C. and Berger, P.H., 2022. Effect of steel fibers on the ultimate flexural behavior of dapped-end connections. Engineering Structures, 259, p.114147.

Rajapakse, C., Degee, H. and Mihaylov, B., 2021. Assessment of Failure along Re-Entrant Corner Cracks in Existing RC Dapped-End Connections. Structural Engineering International, 31(2), pp.216-226.

Damage Detection of Post-tension Concrete Girder Bridges Using Deep Learning Approach

Sanjeewa R.D.J.P., Dammika A.J.*

Department of Civil Engineering, University of Peradeniya, Sri Lanka

**dammikaaj@gmail.com*

Keywords: PC bridges, Damage detection, Deep learning

1. Introduction

Road bridge construction using post-tension concrete girders is commonly used since its inception. During the service life of these bridges, deteriorations occur as a result of increasing traffic volume, environmental factors, and material deterioration over time. Structural damage detection, as an important part of structural health monitoring (SHM), aims to timely and accurately find out structural problems so that corresponding maintenance can be taken to ensure the safety and reliability of a structure during its service period. The development of vibration-based monitoring tools has been a key focus of SHM research in recent years as it can eliminate human errors and accessibility issues associated with a visual inspection. The theory underlying these methods is that damage-induced changes in structural parameters like mass, stiffness, and damping will alter the structure's dynamic characteristics. Because of their ability to cope with uncertainty and noise, machine learning algorithms have been widely applied in vibration-based SHM of engineering structures throughout the last two decades. The most prevalent of these strategies is feed-forward artificial neural networks (ANNs). Hence identification of the presence of damages in a post-tension concrete girder bridge using a deep learning algorithm is focusing in this research.

2. Literature review

Damage Identification is an essential requirement to ensure the safety of the structure. There are four levels of identification by considering major steps in that area. The determination that damage is present in the structure, Determination of the geometric location of the damage, Quantification of the severity of the damage, and Prediction of the remaining service life of the structure. Vibration-based structural damage detection (SDD) systems are classified as nonparametric and parametric methods depending on the extracted information from the observed signals. This study used supervised vibration-based SDD approaches based on machine learning algorithms. Machine Learning (ML) enables systems to learn and improve without being explicitly programmed. This is due to machine learning (ML) technology, which allows a computer to learn the knowledge required to accomplish a task by analysing a large amount of relevant data. Deep Learning (DL) is a subfield of machine learning that can handle complicated patterns and objects in very large datasets - (O. Avci et al, 2021). DL enables computational models made up of several processing layers to learn data representations at various levels of abstraction. The best DL architecture is usually determined by the type of application. Autoencoders and Convolutional Neural Networks (CNNs) have been the only DL tools used in vibration-based SDD applications thus far - (Pathirage et al, 2018). Unsupervised and supervised algorithms are the two types of machine learning algorithms. As an example, supervised algorithms require a dataset for training that contains human-labeled data. As a result, the major goal of supervised learning is to find the best mapping between inputs and desired (or target) outputs. Deep learning is a type of representational learning technology that allows a network architecture to learn highly abstract features from raw data autonomously to perform recognition or classification tasks. In this study, the strategy to detect damages in the post-tension concrete girder brides was based on a supervised regression machine learning (ML) approach, in which the generated data from the FE models would be employed to learn an ML model.

3. Methodology

This discusses the approaches, target outcome, and analysis techniques for a research methodology focused on numerical modeling and implementation of a deep learning model for damage detection. The finite element model

of the post-tension concrete girder bridge is created using Midas FEA. Multiple cases are created by introducing damage to the bridge through changes in the modulus of elasticity (E) value of different regions of the bridge center. Time history analyses were conducted for every case and vibration responses were generated. One set of data is used to train a deep learning model while other set is used to validate the model. The validated model is then applied to detect damages in the bridge.

3.1 Selected bridge details

Table 1: Bridge details

Name	Lewalla Bridge
Location	Lewalla
Bridge No	B 069-2/3
No of Spans	4
Span	76 ft
Width	34 ft
No of girders	5

3.2 Numerical analysis and modeling

To obtain modal parameters numerically, finite element models of the selected bridge were modeled using MIDAS FEA by referring to drawings. Solid elements were used as the element type, and structural components such as girders, diaphragms, and slab decks were considered. The support conditions include pin and roller supports. Additional nodal masses were added for the asphalt layer, foot walk, and handrails.

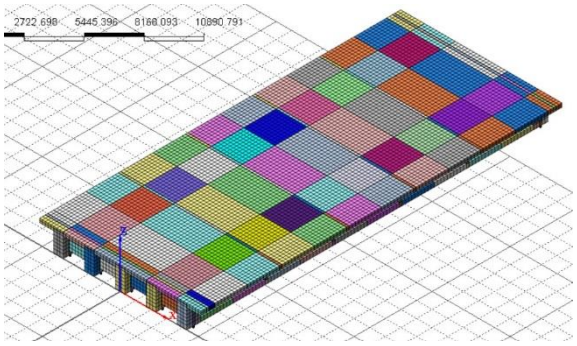

Figure 1: Bridge model

In the modeling process, the primary task involves dividing the bridge into multiple segments, primarily including girders, diaphragms, and slabs. Subsequently, one should adjust the material properties of these components based on a chosen set of criteria.

Table 2: No of divisions

Girders	100
Diaphragms	32
Slab	100

3.3 Data generation

When changing the elastic modulus of girders, diaphragms, and slab, it changes according to the selected order. Elastic modulus changes from 100% to 79% with a 1.5% reduction. In each change, time history was recorded. There are 253 cases according to the selected order and, each case has 24 data points. Time-varying load is applied for 5 seconds and the vibration response of the bridge is recorded for 15 seconds including 10 seconds of free vibration response.

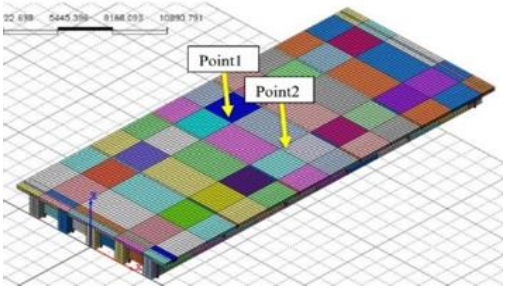

Figure 2: Load applying points

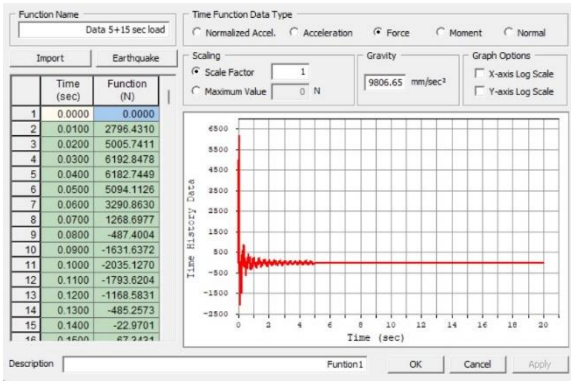

Figure 3: Applied load

3.4 Dataset preparation and training

Training datasets of vibration responses were prepared using finite element (FE) models. A Convolutional Neural Network (CNN) was utilized to train and validate a deep learning model, aiming to estimate the accuracy of damage prediction. The training process was divided into a training phase and a testing phase, where the CNN updated and reduced the error between actual and target outputs. PYTHON scripts were used to prepare the deep learning model. The prediction accuracy of damage was obtained by comparing the target and actual outputs of the network. Deep learning (also known as Deep Neural Network - DDN) is a branch of machine learning that attempts to construct a model using a deep

graph organized in many linear layers and non-linear transformations. The input layer feeds the network with the input instance, while the output is the network's result (Gulgec, Takáč and Pakzad, 2017).

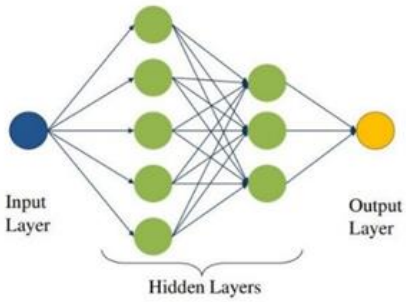

Figure 4: A DNN with two hidden layers (Gulgec, Takáč and Pakzad, 2017)

3.5 Validation and damage identification

Selected one set of data for training the deep learning model while other set of data is used to validate the model. Training datasets of vibration responses were prepared using finite element (FE) models. A Convolutional Neural Network (CNN), which is an Artificial Neural Network (ANN) model, was employed to train and validate a deep learning model for estimating the accuracy of damage prediction. The training process was divided into the training and testing phases, with CNN conducting network training to update the model and reduce the error between actual and target outputs. The accuracy of damage prediction was obtained by comparing the target and actual outputs of the network.

4. Result and discussion

4.1 Eigenvalue analysis

Eigenvalue analysis conducted for undamaged structure. In the beginning, the material properties of the girders, diaphragms, and slab are taken as specified in construction drawings. The obtained mode shapes are:
Mode 1: 5.42 Hz - Vertical bending mode and Mode 2: 7.2 Hz, - Asymmetric tortional mode.

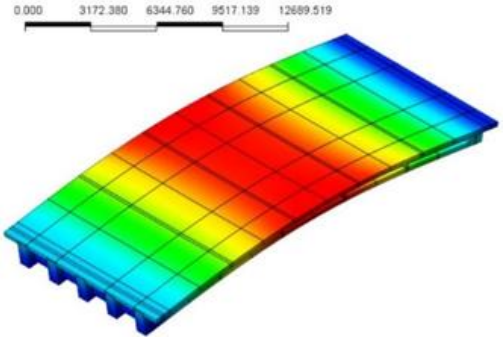

Figure 5: Vertical bending mode

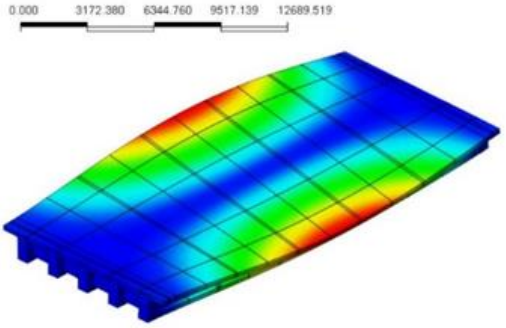

Figure 6: Asymetric torsional mode

4.2 Time history results

For one material change, there are 24-time history results, because there are 24 measurement points for one change.

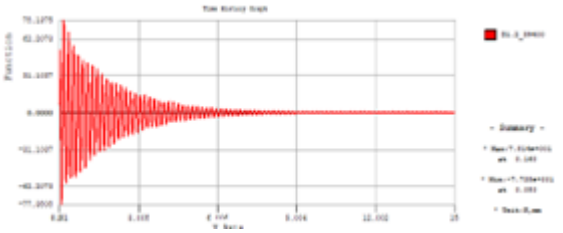

Figure 7: Sample time history result at a point

4.3 R-squared value vs. Epoch value

R-squared is usually used in linear regression models to measure the goodness of fit of the model to the data. In this case, there are two types of deep neural networks are considered. Those are convolutional neural networks and classical fully connected dense layers.

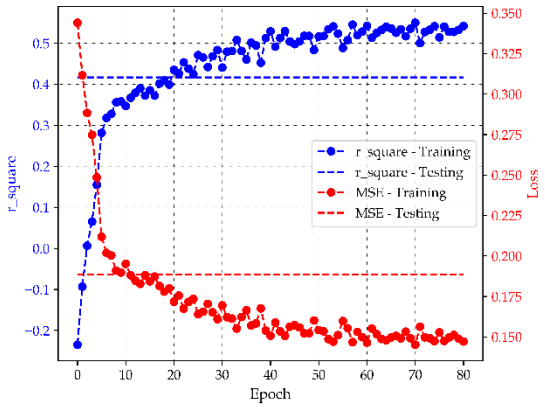

Figure 8: R-squared vs. Epoch CNN

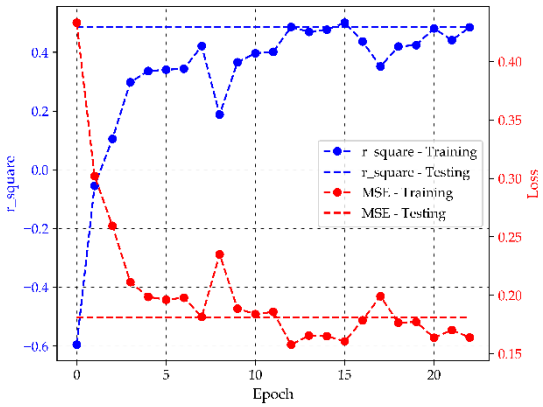

Figure 9: R squared vs. Epoch Fully Connected

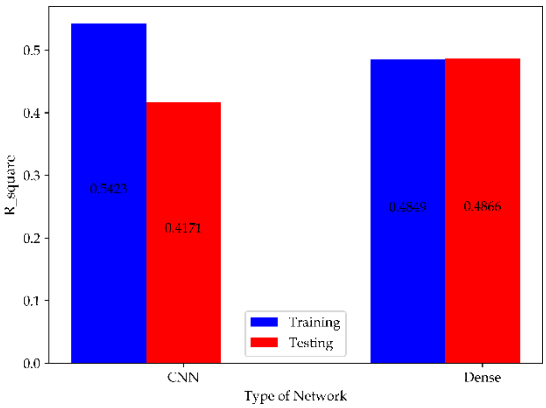

Figure 10: R squared vs. method

Comparing both methods CNN takes the higher R square value in the training phase, and the Dense method takes the higher R square value in the testing phase. Therefore, CNN has good performance in the training phase, but generalization performance is low. For the dense method, generalization performance is good compared to CNN, but training performance is low. When considering the output, R square value is very low. To increase the R square value, it is needed to consider the whole bridge for the data generation and increase the number of data generations for each part of the bridge.

6. Conclusions and recommendations

5.1 Conclusions

In this study, the R square value is 0.54 for CNN and 0.48 for the Dence method. It should be increased near to one for a good deep learning model. This assures the requirement of using huge amount of data for training the deep learning model to obtain better performance.

5.2. Recommendations

For the next step of this study, the data generation process needs to go with automation. For a deep learning model manual data generation process is not practical as huge amount of data sets are required for better performance.

References

Avci, O., Abdeljaber, O., Kiranyaz, S., Hussein, M., Gabbouj, M. and Inman, D., 2021. A review of vibration-based damage detection in civil structures: From traditional methods to Machine Learning and Deep Learning applications. Mechanical Systems and Signal Processing, 147, p.107077.

Gulgec, N., Takáč, M. and Pakzad, S., 2017. Structural Damage Detection Using Convolutional Neural Networks. Model Validation and Uncertainty Quantification, Volume 3, pp.331-337.

Pathirage, C., Li, J., Li, L., Hao, H., Liu, W. and Ni, P., 2018. Structural damage identification based on autoencoder neural networks and deep learning. Engineering Structures, 172, pp.13-28

Enhance the Lateral Performance of Partially Concrete Filled Steel Box Column: A Numerical Approach

Kokulan V., Lavanja L., Jayasinghe J.A.S.C.*

Department of Civil Engineering, University of Peradeniya, Sri Lanka

*supun0chamara@gmail.com

Keywords: Cyclic loading, Ductility, Finite element model, Low yield steel, PCFST member, Strength

1. Introduction

Nowadays, transportation plays a significant role worldwide. Especially in developed countries, highway transportation is widely used. It is essential to design and construct sustainable bridge piers to withstand seismic load, mainly in areas where earthquakes are likely to occur. Due to their structural and constructional efficiency, concrete-filled steel hollow columns are used in bridge piers. They delay buckling. Longitudinal stiffness can be welded inside or outside the steel plate to make it more effective. The partially concrete-filled steel tube (PCFST) members are easy to transport and build, relatively cheap, and the column's weight is considerably less than reinforced concrete columns.

The ability of structures to survive severe earthquakes depends on both the strength and ductility of structures. The aim of this study is to enhance the lateral performance of partially concrete-filled steel box columns. Experimental tests are found to be very expensive and the results are inadequate to make exact conclusions. Due to this reason, this study is mainly focused on the numerical procedure (Finite element model). The analytical procedure is very reliable with a good validated numerical model in predicting the seismic resisting performance of steel columns.

A numerical model of a partially concrete-filled steel box column is validated with an experimental model (Ge *et al*. (1996)) and then, significant parameters that affect the strength, ductility, and buckling position of partially concrete-filled steel box columns are identified. Then, an energy dissipation mechanism with low yield point (LYP) steel plates (to enhance the performance of partially concrete-filled steel box columns and to ease the rectification process) is introduced to the columns and evaluated for better performance and at the same time, the effect of the thickness of the steel plate and LYP plate is also identified.

2. Literature review

In general, structures or structural members such as bridge piers are designed to develop a certain amount of inelastic deformation during a severe earthquake. However, they must be able to withstand strong earthquakes without collapsing. Therefore, ductility is one of the most important considerations in designing a structure. The use of steel sections with infilled concrete has led to an improvement in the ductile behaviour of compression members (Ge *et al*., 1992). In practical designs, thin-walled steel bridge piers are partially filled with concrete in many cases, since it is important to reduce the dead weight of the structure for designing the foundations. In the past, Experimental work on the inelastic cyclic behaviour of steel bridge piers has been conducted. However, only a few experimental studies are available on the inelastic behaviour of partially concrete-filled steel bridge piers under cyclic loading. Thus, further investigations on the behaviour of such columns under severe earthquakes are necessary in order to develop a reliable earthquake-resistant design method for partial concrete-filled steel piers with thin-walled box sections (Usami *et al*., 1994).

In the study by Li *et al*. (2019), they proposed a novel steel box bridge pier with an earthquake-resilient, that is, a specific energy dissipation zone with replaceable components installed at the bottom of box-shaped steel bridge piers. This energy dissipation zone was mainly composed of low-yield-point steel energy dissipation wall plates, surrounded by constraining steel plates. After moderate earthquakes, the damaged low-yield-point steel energy dissipation wall plates and the surrounding constraining steel plates can be rapidly replaced. After rare earthquakes, the entire energy dissipation zone at the base can also be replaced, and the seismic resistance of

the steel bridge piers can be recovered rapidly. However, installing the energy dissipation zone at the base will alter the force transfer mechanism and failure mode of steel bridge piers. In this study, an energy dissipation mechanism made out of LYP steel plates is introduced just above the concrete fill and up to the next diaphragm level.

3. Methodology

A finite element model for a partially concrete-filled steel box column is created in ABAQUS and it is validated with the past experimental result by Ge and Usami, (1996). Past experimental model and validated numerical model with Von Mises stress (Pa) distribution in steel are shown in Figure 1. The properties of the model are provided in Table 1 and the cyclic loading applied for the model is shown in Figure 2. Then, a series of analyses are conducted to see the effects of (a) slenderness ratio (λ), (b) width-to-thickness ratio of flange plate (Rf), (c) load factor (P/P_y), (d) concrete height, (e) distance between diaphragms (α), (f) concrete grade on strength, ductility, and buckling position of partially concrete-filled steel box column using the established numerical model.

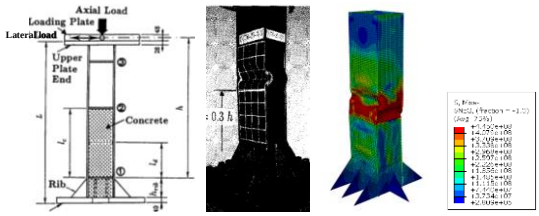

Figure 1: Past experimental setup and the validated model

Table 7: Material properties

Properties	Values
Density of concrete (tonnes/mm^3)	2.4e^{-9}
Young's modulus of concrete	25.5GPa
Poisson's ratio of concrete	0.165
Density of steel (tonnes/mm^3)	7.8e^{-9}
Young's modulus of steel	211GPa
Poisson's ratio of steel	0.3
Yield stress of steel	30MPa
Ultimate stress of steel	455MPa
Plastic strain of steel	0.01864

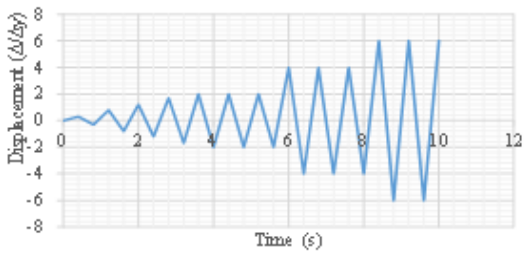

Figure 2: Displacement history (Usami and Ge, 1996)

4. Results and Discussion

4.1 Validation of the model

Figure 3, envelop curves are developed by joining the peak points of the experimental and numerical results obtained for the displacement vs. reaction force curve. It shows that the obtained result is quite similar to the experimental result, and therefore, the numerical model is reliable.

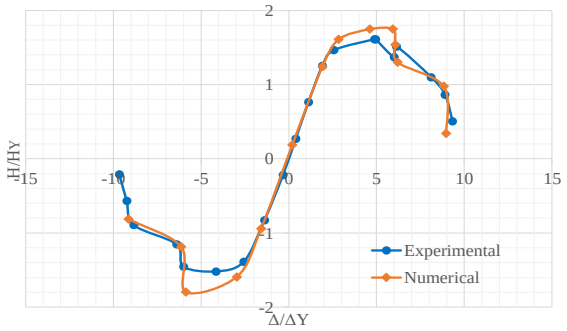

Figure 3: Comparison of experimental and numerical envelope curves

4.2 Failure modes of partially concrete-filled steel columns

Buckling can occur above the concrete filling height or within the concrete range. It is observed that the width-to-thickness ratio of the flange plate (Rf) is the main parameter that decides the place of buckling for a given concrete filling height. If the buckling occurs within the concrete range, it is very difficult to rectify the column. Because, when buckling occurs within the concrete range, at first the concrete gets crashed, and thereafter the steel column buckles. So, it is difficult to remove the crashed concrete within the column and restore the column. To overcome this problem, it is decided to transfer the occurrence of buckling above the concrete range.

By keeping the concrete infilling height at 30% and changing various Rf values, it is observed that for the 30% Rf value 0.729 and below 0.729,

the buckling occurs within the concrete range and for Rf the value 0.961 and above 0.961, buckling occurs above the concrete range. To identify the transient region, three models with Rf values 0.800, 0.845, and 0.903 were modelled (other parameters are within the usual range, 30% infilled concrete) and allowed to run. When the Rf value is 0.800, buckling occurs within the concrete range as shown in Figure 4(a). (Buckled area is denoted by oval shape) When the Rf value is 0.845, buckling tends to occur in both areas (above and within the concrete range) as shown in Figure 4(b). When the Rf value is 0.903, buckling occurs above the concrete range as shown in Figure 4(c). The comparison of failure modes (buckling within the concrete range and buckling above the concrete range) for different Rf and λ pairs are shown in Figure 5. By observing Figure 5, it can be concluded that there is a transient region between 0.800 and 0.903.

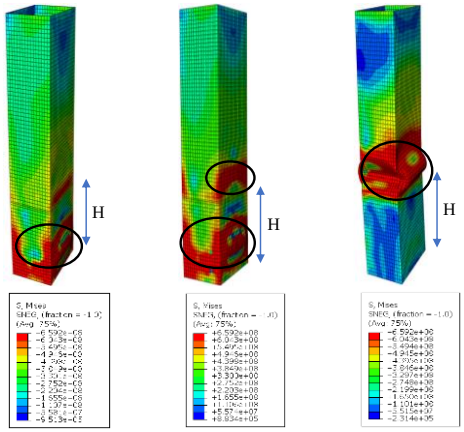

Figure 4: Von Mises stress (Pa) distribution in steel part at failure: (a) Rf= 0.800, (b) Rf= 0.845 and (c) Rf= 0.903

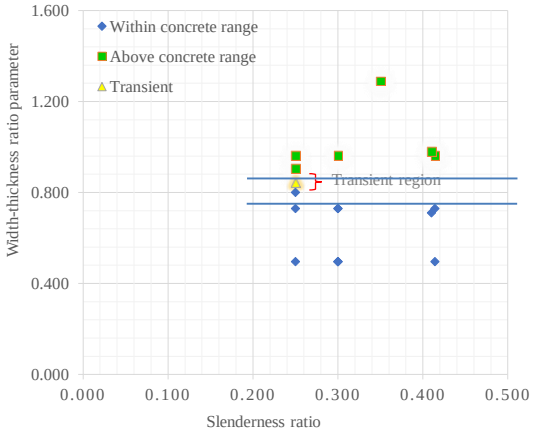

Figure 5: Comparison of failure modes

4.3 Enhance partially concrete-filled steel columns

To enhance the column and to transfer the buckling above the concrete range, 3 models (A, B, C) with random Rf and λ parameters (but within the usual range) were first created and analyzed. Then, an energy dissipation mechanism as shown in Figure 6 is introduced just above the concrete fill and up to the next diaphragm level to those three columns and evaluated for better performance (models A', B', C'.) The comparisons of the three columns and their corresponding columns with energy dissipation mechanism are shown in Figure 7. Here, U2 is the displacement in the direction of the lateral load at failure.

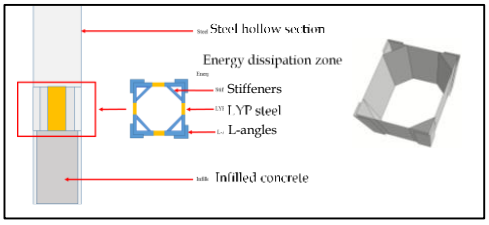

Figure 6: Introduced energy dissipation mechanism

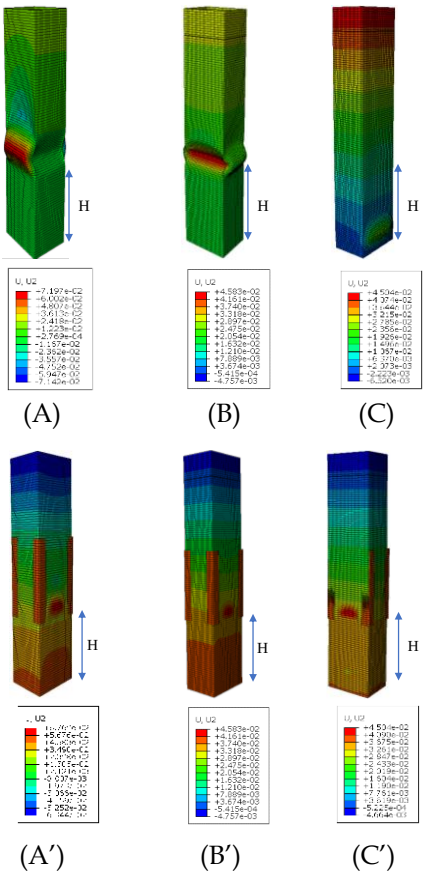

Figure 7: Deformed numerical models with U2-displacement (m) in the steel part

5. Conclusions

In this study, the effect of slenderness ratio, the width-to-thickness ratio of the flange plate, load factor, concrete height, the distance between diaphragms, and concrete grade on strength, ductility, and buckling position of partially concrete-filled steel box column were observed. Based on the results of the study, the following conclusions are made,

Failure of the PCFST can be divided into two types. The first one is the local buckling above the concrete fill and the other one is buckling within the concrete fill.

Limiting the range of designable Rf is vital to avoid buckling within the concrete filling regions. Increasing the Rf is economically viable and fails above the filling height but increases the possibility of failure by local buckling. On the other hand, reducing the Rf increases the possibility of the occurrence of buckling within the filling height, and the rectification of the CFST pier after the earthquake is difficult.

When the concrete filling height is 30% and Rf is less than 0.800, buckling occurs within the concrete fill and when Rf is greater than 0.903, buckling occurs above the concrete fill. A transient region exists when Rf values are between 0.800 and 0.903, where buckling tends to occur in both places (i.e., within and above concrete fill).

The decreasing λ increases the H/H_y , μ, and μ_{95}. However, the influence is insignificant with the R_f.

The H/H_y of PCFST increases with the decreasing P/P_y and it doesn't affect the buckling position.

An increase in concrete filling height does not affect the strength and ductility much, but when increasing the concrete filling height, buckling tends to occur within the concrete fill. So, it is practical to use 30% fill concrete.

With the concrete grade, the strength of the column increases (but no difference was observed in the failure pattern in the steel tube).

After introducing the energy dissipation mechanism, all the lateral performance indices were increased immensely. However, it was found that the proper energy dissipation mechanism should be selected (also consider the thickness of the LYP plate).

The thickness of the LYP plate to be used depends on the thickness of the steel plates of the column. Providing a thickened LYP plate leads to buckling within the concrete range. It is advisable to use the thickness of LYP plate same or less than the thickness of steel plates.

An increase in the thickness of the steel plate makes an insignificant difference in strength and ductility between the column and its enhanced column.

References

Ge, H. and Usami, T. 1996, 'Cyclic tests of concrete-filled steel box columns', Journal of structural engineering, 122(10), pp.1169-1177.

Ge, H. B., and Usami, T. 1992. 'Strength of concrete-filled steel thin-walled box columns: experiment', J. Struct. Engrg. ASCE, 118(11), 3036-3054.

H. Li, J. Luo, F. Han, and J. Luo, 'Experimental study on seismic behavior of new steel box bridge piers with embedded energy dissipation shells', International Journal of Steel Structures, vol. 19, no. 3, pp. 952–969, 2019.

Usami, T., and Ge, H. B. 1994, 'Ductility of concrete-filled steel box columns under cyclic loading', J. Struct. Engrg. ASCE, 120(7), 2021-2040.

Modification of Wind Response Caused by Shape of Structure Considering Interfering Effects

Ekanayake E.M.R., Herath H.M.A.I., Jayasinghe J.A.S.C.*

Department of Civil Engineering, University of Peradeniya, Sri Lanka

**supun0chamara@gmail.com*

Keywords: CFD simulations, Interfering effect, Turbulence model, Wind response, Wind tunnel test

1. Introduction

The response of structures to wind loads is a complex phenomenon influenced by various factors, such as the shape of the structure, its surrounding environment, and the interference effects caused by nearby buildings or terrain features. This study investigates the effects of interfering building shape, height, and angle between the principal building and the interfering building on wind response, considering the impact of the interfering effect. The study utilized base moment, base shear, and pressure fluctuation as the comparative parameters to assess the interfering effect. The commercial CFD package Midas NFX is used for numerical analysis.

2. Literature review

The most commonly used methods for analysing the wind response around a building are wind tunnel testing, computational fluid dynamics, and code-based methods. Among those methods, computational fluid dynamics (CFD) simulations have been widely used in the analysis of wind response to buildings. Wang et al. (2013) used CFD simulations to investigate the effect of building shape on wind pressure distribution, finding that the ratio of width to height and the shape of the building significantly impact wind pressure distribution. Other studies have investigated the effect of building orientation on wind response. Liu et al. (2019) found that wind pressure distribution on the surface of a building is strongly influenced by wind direction and building orientation. Previously most of the studies were done with 2D simulations or 3D simulations only considering one or two parameters from the shape, height, and angle.

3. Methodology

The general steps of the methodology of this study are shown in Figure 1.

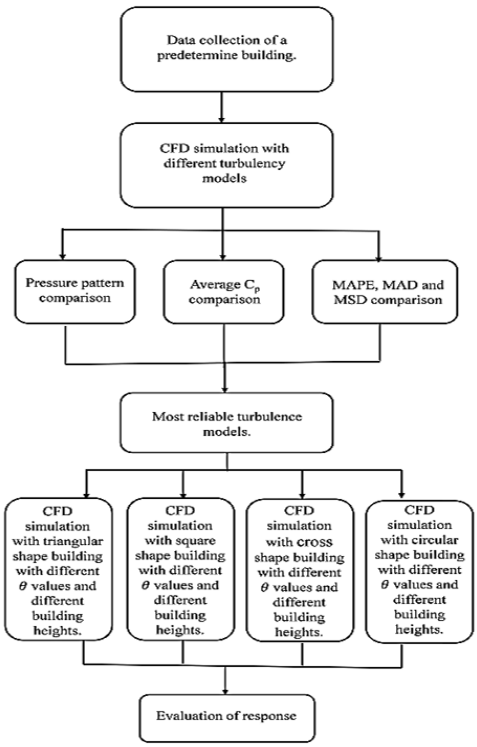

Figure 1: Flow chart of the methodology

3.1 Data collection of a predetermined building

The first step of the methodology is to compare the reliability of turbulence models with experimental data. To make this comparison, a building with reliable experimental data is needed. In this case, the Commonwealth Advisory Aeronautical Council (CAARC) standard tall building is being used as the pre-determined building for the comparison. The selected prototype building is rectangular and prismatic, with dimensions of 100 ft x 150 ft (30.48 x 45.72 m) for its sides and a height of 600 ft (182.88 m) (Melbourne W.H., 1980).

Figure 2 shows the wind tunnel test data that six different institutions, namely City University - England (City), University of Bristol -England (Bristol), Monash University-Australia (Monash) and National Aeronautical

Establishment-Canada (a & b) (NAE) are conducted on CAARC standard tall buildings.

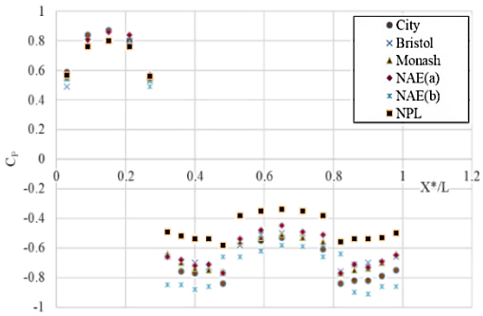

Figure 2: Wind tunnel test data of CAARC building

3.2 Development of numerical model

As shown in Figure 3, a sufficient distance from the building surface to the computational boundary should be maintained to avoid the influence of the outer boundary on surface pressure over buildings.

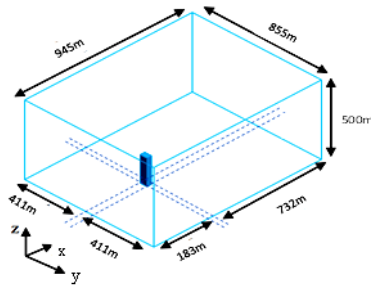

Figure 3: Computational domain of CFD model

The wind profile was developed for this study using the power law equation (1).

$$\frac{U(Z)}{U_H} = \left(\frac{Z}{Z_H}\right)^{\alpha} \quad \text{.....(1)}$$

Where $U(Z)$ is wind speed at the height of Z, U_H is the wind speed at building height of Z_H=180 m, set as 12.7 m/s, and α is wind profile coefficient, set as 0.3.

As shown in Figure 4, mesh was generated by setting the element size growth rate as 1.05 and ratio between minimum and maximum element size as 2, the density of air as 1.25 $kg\ m^{-3}$, and the viscosity of air as $1.79x10^{-5}\ kg/m.s$, turbulent intensity as 0.003.

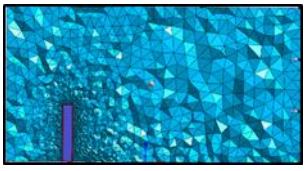

Figure 4: Sectional view of mesh

To compare the sensitivity of wind pressure coefficients to grid resolution, both the grid number and the grid size were modified. Four models with different degrees of grid resolution were established. The wind pressure coefficient was calculated using Eq. (2).

$$C_{pi} = \frac{P_i - P_\alpha}{\frac{1}{2}\rho U_\alpha^2} \quad \text{..... (2)}$$

Where C_{pi} is the mean wind pressure coefficient of a specific point i, P_i represents the wind pressure at the point i, P_α is the static pressure at reference height, ρ is air density, set as 1.25 $kg\ m^{-3}$, U_α is wind speed at the reference height, and the wind speed is 12.7 m/s at the top of CAARC building, 180 m.

Mean pressure coefficients on each surface of the CAARC standard tall building have been shown in Figure 5.

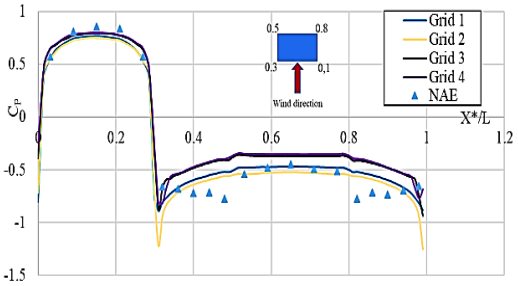

Figure 5: Sensitivity analysis of different grid sizes.

For the sensitivity analysis, the experimental data of the NAE university case for wind tunnel test on CAARC were used. To quantify the results, the mean absolute percentage error (MAPE), mean absolute deviation (MAD), and mean squared deviation (MSD) were determined using Eq. (3), Eq. (4) and Eq. (5) respectively.

$$MAPE = \frac{\sum_{t=1}^{n}\left|\frac{C_{pitunnel} - C_{piCFD}}{C_{pitunnel}}\right|}{n} \times 100\% \text{.....} \quad (3)$$

$$MAD = \frac{\sum_{t=1}^{n}|C_{pitunnel} - C_{piCFD}|}{n} \text{.....} \quad (4)$$

$$MSD = \frac{\sum_{t=1}^{n}|C_{pitunnel} - C_{piCFD}|^2}{n} \text{.....} \quad (5)$$

According to Table 1, numerical accuracy can meet the required standards when the grid resolution on the building surface is refined to 0.5 m.

Table1: Sensitivity of wind pressure coefficients to grid resolution

Error	Grid 1 (0.5m)	Grid 2 (1.0m)	Grid 3 (1.5m)	Grid 4 (2.0m)
MAPE	13.42	14.97	23.24	25.85
MAD	0.09	0.10	0.15	0.17
MSD	0.01	0.017	0.03	0.04

3.3 Selection of most reliable RANS turbulence model

The experimental data from wind tunnels were compared to each turbulent model independently. The distribution of C_{pi} obtained using different turbulence models; 0 equation model, 1 – equation $k-\varepsilon$ model, 2-equation Standard $k-\varepsilon$ model, 2 – equation $k-\omega$ model and 2 – equation $k-\omega\ SST$ model were compared with the experimental data. Figure 6 shows the results comparison for 2 $k-w\ SST$ model.

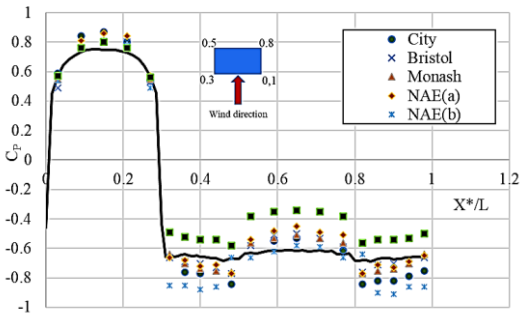

Figure 6 :2 k - w SST model

Table 2 shows three errors calculated using Eq. (3), Eq. (4), Eq. (5). According to those results, the 2 k – ω SST model shows minimum MAPD, MAD and MSD values.

Table 2: Comparison between numerical results and experimental results

Error	0 *eq*	1 *ke*	2 *ke*	2 $k-w$	2 $k-w$ *sst*
MAPE	14.10	15.01	14.97	19.40	11.88
MAD	0.08	0.10	0.10	0.13	0.07
MSD	0.01	0.01	0.02	0.03	0.01

3.4 Parametric study

For the parametric study the mesh size was chosen as 0.5m and the turbulence model as 2 $k-\omega\ SST$. As shown in Figure 7, 48 combinations were studied to identify their interfering effects. The responses: pressure distribution, interfering factor, base shear, and overturning moment are compared.

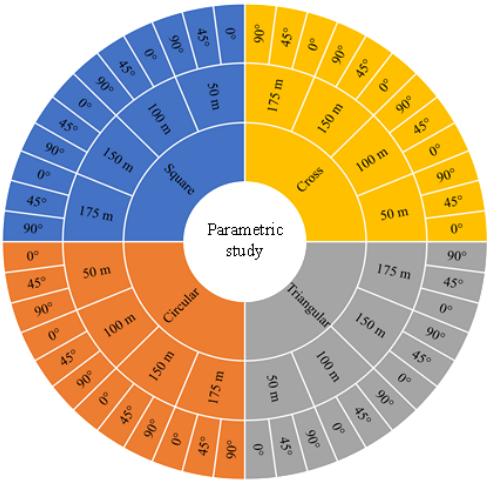

Figure 7: All combinations

4. Results and discussion

To identify the interfering effect of the upstream building, 3D modeling was carried out using Midas NFX, and the results are discussed in this section. The evaluation process involves analysing the responses on the principal building, while keeping one angle and height constant for different plan shapes. The shape that produces the highest interfering effect for that height and angle is identified as the critical shape. After that, a comparison is made between each angle for the critical shape. Finally, the critical angle for the selected shape and height is determined using the results obtained from the analysis.

4.1 Base moment and base shear comparison

The comparison of base moment for the 0-deg / 50m cases for all shapes is shown in Figure 8. Deviation was calculated based on the Eq. (6). The results indicate that the triangular shape has the maximum deviation, while the circular shape has the minimum deviation.

$$Deviation = \left|\frac{Isolated\ condition - |Interfering\ condition|}{Isolated\ condition}\right| \times 100\% \quad \ldots\ldots (6)$$

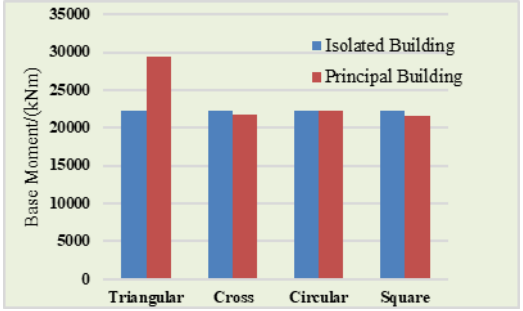

Figure 8: Base moment for 0-deg / 50m case

Next, the results were compared for the triangular shape case with different angles, as shown in Figure 9. In that, the maximum deviation is shown in 0-deg case and the minimum deviation is shown in 90-deg case.

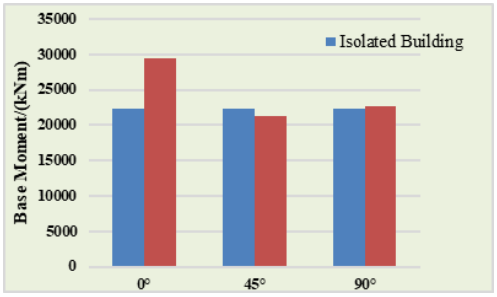

Figure 9: Base moment for triangular shape 50m case

Similarly, the base shear results indicate that the triangular shape has the maximum deviation, while the circular shape has the minimum deviation.

4.1 Pressure variation comparison

This study investigates the impact of interfering building plan shape on the principal building, specifically analysing the variation of mean Cp along height at the centreline of the windward face. Results are presented in Figure 10.

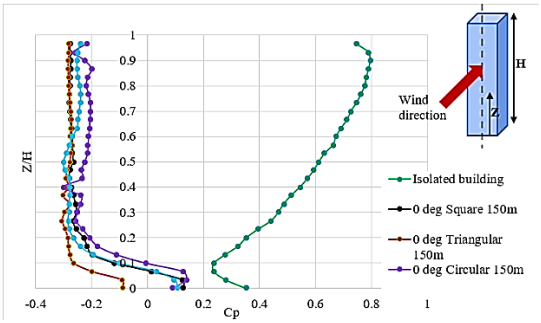

Figure 10: Cp variation with building height in windward face of principal building

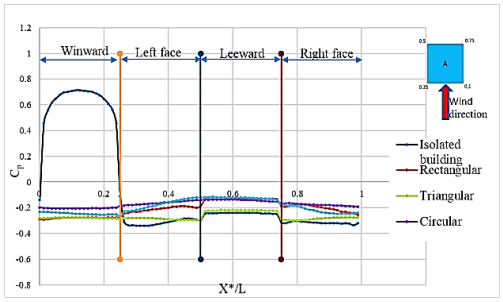

Figure 11: Pressure variation around the principal building at the 2/3 height for 0-deg / 150m cases

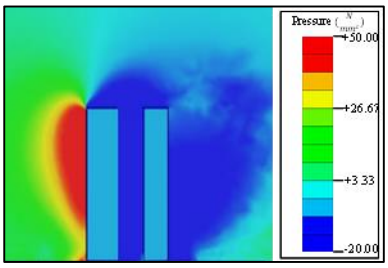

Figure 12: Sectional view of triangular shape 0-deg / 150m case

As shown in Figure 11 and Figure 12, the windward face is positive, and the leeward and sidewalls are negative for the isolate model. However, when a building interferes with an isolated model, the pressure coefficient behaviour changes dramatically.

5. Conclusions

Based on the results, the maximum increments of the base moment and base shear in the triangular 90-deg / 100m case and the triangular 90-deg/175m case were observed, and they were 151.75% and 31.30%, respectively. The results suggest that a safety factor for interfering effects should be considered in designing the building structures in the city area to ensure the stability of a building. And the maximum Cp variation in the triangular shape case was observed, and it was positive 0.8 to negative 0.3. The findings emphasized the significance of designing the cladding system's connection to both compression and tension forces. The results of the present study will be crucial in ensuring the stability and safety of the building structures when those buildings are going to develop in a dense building environment.

References

Melbourne W.H., 1980, Comparison of Measurements on The CAARC Standard tall Building Model in Simulated Model Wind Flows, Journal of Wind Engineering and Industrial Aerodynamics, 73-88.

Wang, Y., Huang, J., Liu, Y., & Li, Q. 2013. Investigating the effect of building shape on wind pressure distribution using CFD simulations. Journal of Wind Engineering and Industrial Aerodynamics, 120, 17-24.

Liu, Y., Huang, J., Wang, Y., & Li, Q. 2019. Influence of wind direction and building orientation on wind pressure distribution on building surfaces. Journal of Wind Engineering and Industrial Aerodynamics, 188, 18-25

Thermal Performance of Glass Facade Under Fire Loading: A Numerical Approach

Perera R.G.S.S., Ruwanmali J.H.A., Jayasinghe J.A.S.C.*

Department of Civil Engineering, University of Peradeniya, Sri Lanka

**supun0chamara@gmail.com*

Keywords: Finite element analysis, Glass facades, Insulated glass panel, Laminated glass panel, Thermal loads

1. Introduction

The requirement for non-structural elements has increased with the rise in high-rise buildings since recently. Non-load bearing walls are designed to withstand wind, seismic and fire loadings. The most popular non-load bearing walls are lightweight concrete precast sandwich wall panels, lightweight steel gauge framed wall panels, and curtain wall panels. When using combustible material for curtain walls, fire spreading risk is higher due to the large wall panel area. As a non-combustible material, glass is most suitable and widely used for curtain walls (Yuen *et al*., 2021). This study analyses the thermal performance of glass walls under fire loadings.

2. Literature review

New types of glazing are being used to enhance building aesthetics, but they can easily break during a fire, causing rapid enclosure fires. Wang *et al.*, 2017 conducted ten tests which were conducted on single coated, insulated, and laminated glazing to investigate their thermal performance and breakage. Based on their results, the air gap and fire side glass pane play a key role in thermal resistance in insulted glazing. In this study, numerical simulations were performed to investigate the heat transfer process through the glazing panels.

3. Methodology

Figure 1 shows general steps of the methodology of this study.

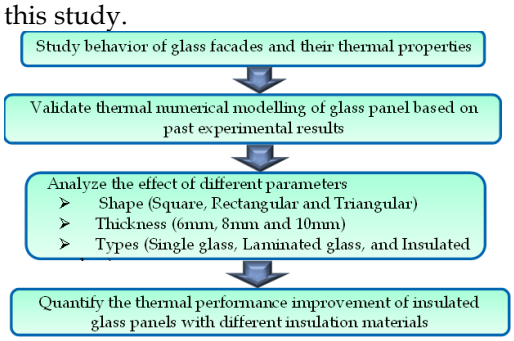

Figure 1: Flow chart of the methodology

3.1 Behaviour of glass facades

Studying glass behaviour is crucial for glass facades in modern buildings. Although, glass is a non-combustible material. But its brittleness may break and fallout very easily when subject to fire and it is highly vulnerable under mechanical loadings because of sudden failure. The fire performance of the glass is not easy to experimentally evaluate due to the susceptibility of the glass material properties to elevated temperature and the sensitivity of glass to thermal shock.

3.2 Numerical modeling and validation

Numerical simulation evaluated the thermal performance of glass facades under fire loading, using a validated model in *ABAQUS* software with past experimental data (Wang *et al.*,2017). Mainly, the thermal performance of a single glass panel was validated for temperature variation and breaking temperature. Laminated glass panels and insulated glass panels were investigated only for temperature variation. Figure 2 shows the geometric configuration of the different glass panels.

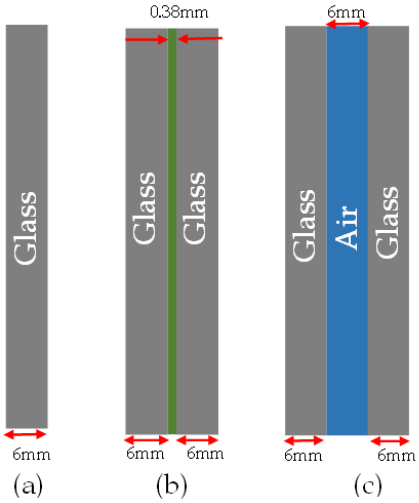

Figure 2: Geometric configuration of glass panels: (a) Single glass panel, (b) Laminated glass panel and (c) Insulated glass panel

Table 1 presents the material property data used to create three types of glass models.

Table 1: The material properties

Properties	Symbol	Value
Glass		
Density(kg/m^3)	ρ	2500
Modulus of elasticity (Pa)	E	7.3×10^{10}
Poisson ratio	υ	0.17
Thermal expansion coefficient ($1/K$)	β	8.46×10^{-6}
Reference temperature (K)	T_R	280
Specific heat capacity ($J/(kg.K)$)	C	820
Thermal conductivity ($W/(m.K)$)	K	0.94
Emissivity	ε	0.85
PVB		
Density (kg/m^3)	ρ_{PVB}	1070
Specific heat capacity ($J/(kg.K)$	c_{PVB}	1100
Thermal conductivity ($W/(m.K)$)	k_{PVB}	0.221
Air		
Density (kg/m^3)	ρ_{air}	1.16
Specific heat capacity ($J/(kg.K)$	c_{air}	1007
Thermal conductivity ($W/(m.K)$)	k_{air}	0.0263

3.3 Parametric study of glass panel

The temperature variation of a single glass panels was investigated by changing thickness, and the breaking temperature was investigated by changing shape. Thermal performance was analysed using square, rectangular, and triangular shapes and 6 mm, 8 mm, and 10 mm thicknesses under fixed boundary conditions. The temperature variation was investigated for laminated glass panels with varying polyvinyl butyral (PVB) film thicknesses 0.38mm, 0.76mm, 1.14mm, and 1.52mm. And also, temperature variation was evaluated for insulated glass panels with varying cavity gas thicknesses 8mm, 16mm, 24mm, and 32mm. Table 2 shows all parametric study models of glass panels.

Table 2: All models of parametric study

Glass type	PVB/Cavity thickness
Laminated	0.38mm
	0.76mm
	1.14mm
	1.52mm
Insulated	8mm
	16mm
	24mm
	32mm

Shape	Thickness	Investigated
Square	6mm	Temperature variation
Square	8mm	
Square	10mm	
Square	8mm	Crack behavior
Rectangular	8mm	
Triangular	8mm	

3.4 Improvements of the insulated glass with different insulation materials

Finally, the effect of cavity gas types on insulated glass thermal performance was studied by varying the gas type by using Air, Argon, and Krypton.

4. Results and discussion

4.1 Validation of thermal model

According to Figure 3, good agreement between experimental and numerical temperature variation results indicates the reliability of the single, laminated, and insulated glass panel models.

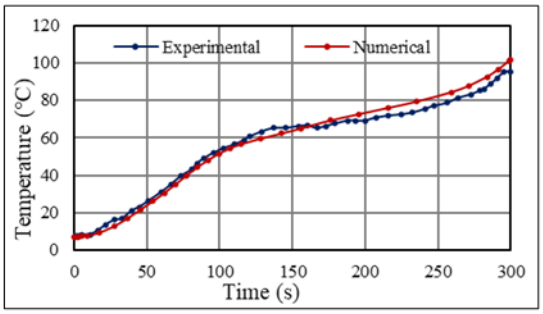

(a)

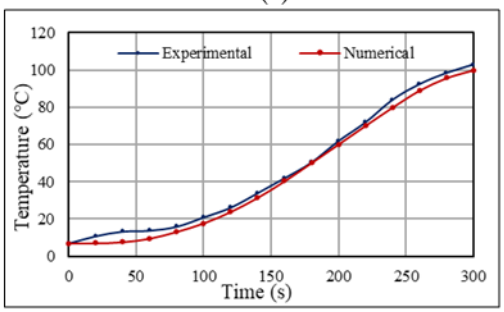

(b)

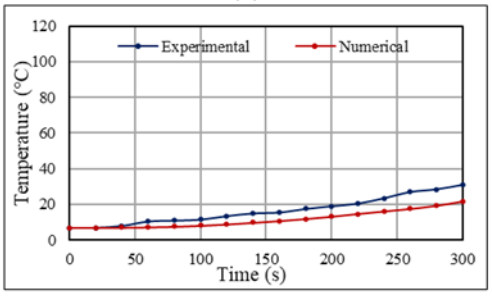

(c)

Figure 3: Comparison of temperature variation curves: (a) Single glass panel, (b) Laminated glass panel and (c) Insulated glass panel

The temperature variation results of the ambient side surface at 300s for the three types of glass models are shown in Figures 4 (a), (b) and (c).

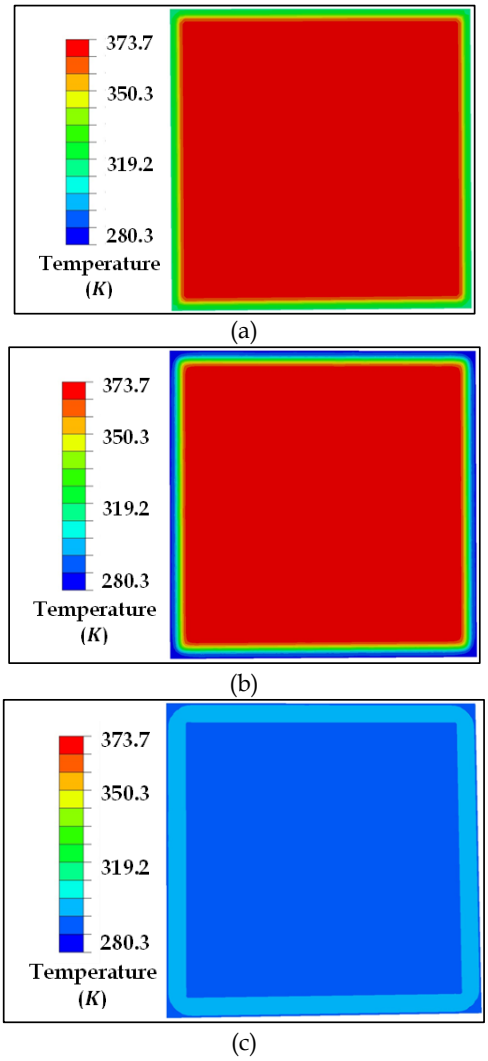

Figure 4: The variation of temperature on ambient side at 300s: (a) Single glass panel, (b) Laminated glass panel and (c) Insulated glass panel

The square-shaped single glass panel breaks at a maximum compressive principal stress of -35.9MPa as shown in Figure 5.

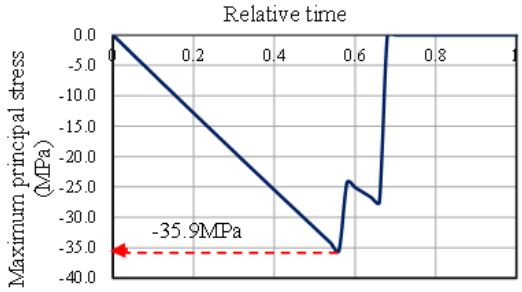

Figure 5: Comparison of maximum principal stress variation

Figure 6 shows that cracks initiate at four corners of the heat side of the square-shaped single-glass panel.

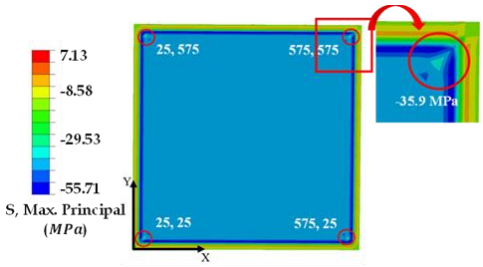

Figure 6: Crack initiate points of square-shaped single glass panel

4.2 Parametric Study

The temperature variation of the square-shaped single glass panel was investigated with varying glass thickness, as presented in Figure 7.

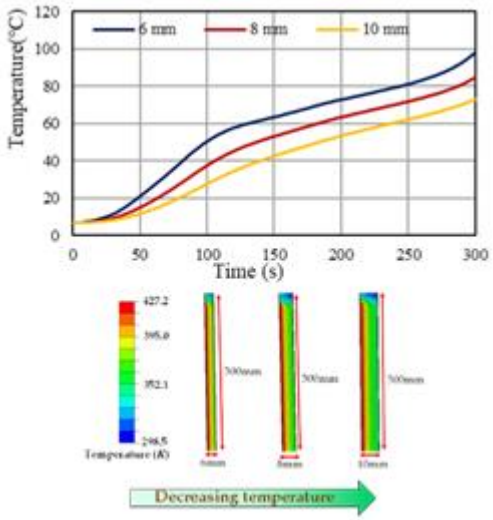

Figure 7: Comparison of glass thickness

According to the breaking behaviour results, it is clear that the worst shape for thermal performance is the rectangular shape. Observed temperature variation results from varying the PVB thickness of the laminated glass panel, as shown in Figure 8.

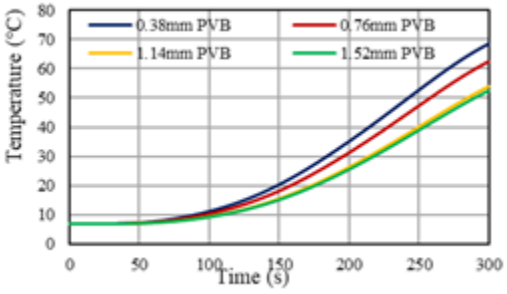

Figure 8: Comparison of PVB layer thickness

Figure 9 shows the temperature variation by varying the cavity thickness of the insulated glass panel. By comparing all the numerical results of the parametric study, the insulated

glass panel's thermal performance is better than the other two glass panels (see Figure 10).

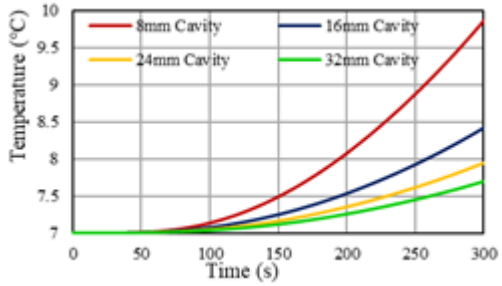

Figure 9: Comparison of cavity thickness

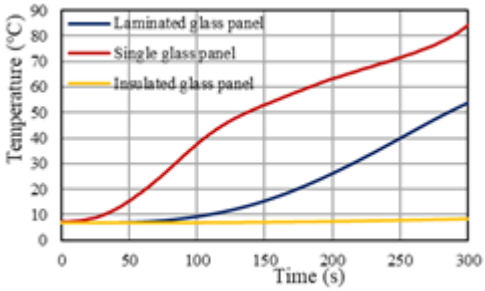

Figure 10: Comparison of different types of glass panels

4.3 Insulated glass panel with different insulation materials

The thermal performance of Krypton is better than that of the other two gases (Air and Argon), as shown in Figure 11.

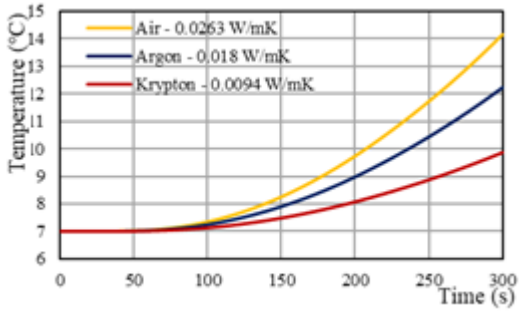

Figure 11: Comparison of different insulation materials

The variation of temperature patterns is slightly different from each model due to the variation of insulation material (see Figure 12).

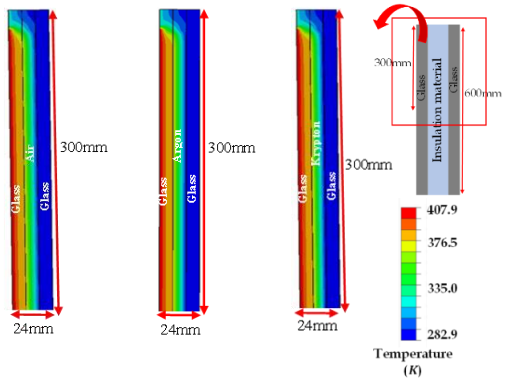

(a) (b) (c)

Figure 12: Comparison of the temperature variation for different insulation materials along thickness at 300s: (a) Air, (b) Argon and (c) Krypton

5. Conclusions

In this study, the temperature variation of single, laminated, and insulated glass panels was observed, as was the breaking behaviour of a single glass panel. Based on the results of the study, the following conclusions are made;

In single glass panels, surface temperature varies with thickness, while the crack-initiated temperature and time depend on the glass's shape. The temperature drop is around 13.5% when increasing the thickness by 2mm.

The laminated glass panel analysis proved that increasing the PVB layer thickness can further reduce temperature.

The ambient side temperature of insulated glass panel can be reduced by increasing the cavity thickness. The order of temperature increase rate on the ambient side is single glass > laminated glass > insulated glass.

Krypton is more effective insulation than Air and Argon for insulated glass panels.

References

Wang, Y., Wang, Q., Wen, J.X., Sun, J. and Liew, K.M., 2017. Investigation of thermal breakage and heat transfer in single, insulated, and laminated glazing under fire conditions. Applied Thermal Engineering, 125, pp.662-672.

Development of Earthquake Design Response Spectra for Sri Lanka Considering Short-Period and Long-Period Effects

Peiris N.S., Peiris B.R.D., Buddika H.A.D.S.*

Department of Civil Engineering, University of Peradeniya, Sri Lanka

**samithbuddika@eng.pdn.ac.lk*

Keywords: Seismic, Response spectrum, Ground motions

1. Introduction

Sri Lanka does not have proper guidelines for earthquake-resistant design of structures; their engineers are forced to adopt site-specific provisions from codes by foreign countries. This could lead to a knowledge gap and final results could change. Sri Lanka is located in the middle of the Indo-Australia tectonic plate which leads to less possibility of reaching earthquake due to tectonic plate fractural movements. However, due to the geological formation, there is a significant possibility of occurring short-period as well as long-period earthquakes around Sri Lanka. Therefore, it is required to analyse the effect of long-period and short-period ground motions for Sri Lanka. This study considers sets of ground motions that have long-period and short-period effects, then analysis and comparison were done in order to have a correct understanding of suitable response spectrum for Sri Lanka seismology for different earthquake possible conditions. Due to the seismological location of Sri Lanka, it is required to use far fault, non-pulse like long period and short period ground motions. Selected ground motions were soil Type A (Rock or other rock-like geological formation, including at most 5 meters of weaker material at the surface- Shear velocity > 800m/s) as per the Eurocode 8 soil classification. Based on the selected ground motion analysis, a comparison was done as described in the methodology, and based on the results conclusions were made.

2. Literature review

According to the available literature, the oldest known written account of an earthquake that struck Sri Lanka is found in a book that was published in Lisbon in 1616 and describes an incident that happened on April 14, 1615, not far from Colombo. There haven't been any other earthquakes of that size since. However, there were other earthquakes, including the ones in 1938 and 1940, which were felt throughout much of the island but did not result in any fatalities or material or serious damage. Very minor seismic activity (between 3 and 3.5 Richter scale) was observed in Sri Lanka in 1986.

There are two standard response spectra which are mentioned in the Senavirathna et al., (2020) paper and Venkatesan et al., (2017) paper both only up to 4 seconds time period. Because no long-term period ground motions occur around the island. So, there is no earthquake data to make the response spectrum more than 4 seconds. Using this response spectrum, it is possible to conduct response analysis for the structures which have a low natural period. To analyse high natural period structures required a long period response spectrum.

When it comes to available response spectra in the world Indian standard response spectra, Eurocode 8 specified response spectra for different magnitudes of the earthquake and soil condition, and Australian standard response spectra were much more dominant in analysing and developing response spectra for Sri Lankan conditions. Some spectra mentioned above include long-period effects.

Categorization of the earthquakes is important in order to have a proper understanding of how and what type of earthquakes have to be collected when analysing and developing response spectra for Sri Lanka considering short and long-period effects. The suitable types of ground motions are far fault, non-pulse like long and short period ground motions. The generating mechanism of long-period and short-period ground motion, the difference between far fault, near fault, pulse like and non-pulse like ground motions described in the Study on standard response spectrum parameters of special long-period ground movements paper and A seismological overview of long-period ground motion paper. Also ground motion classification based on soil condition and magnitude wise describe in the EN 1998-1: Eurocode 8: Design of structures for earthquake resistance.

3. Methodology

To achieve this objective, we extracted suitable types of ground motions that could occur in a country like Sri Lanka which has the properties of far fault, non-pulse like short and long period ground motions from PEER (Pacific Earthquake Engineering Research Centre) database. The extracted ground motions were then categorized into three sections, based on the magnitude, soil condition of the recorded station, and mean period of the ground motion. The first section included long-period ground motions with a magnitude greater than 5.5, the second section included short-period ground motions with a magnitude greater than 5.5 and the third section included short-period ground motions with a magnitude lesser than 5.5. All the ground motions that were selected in these three categories include only the soil type of rock. In order to separate ground motion based on soil condition Eurocode 8 specified ground motion separation criteria based on shear velocity used. Ground motions which has a mean period greater than 1.0 are considered as long period and other ground motions mean period lesser than 1.0 are considered short period ground motions.

After categorization, we developed mean and mean plus standard deviation response spectra for each category of ground motion. The response spectra provide a graphical representation of the maximum response of a structure to different ground motion intensities for a given period. The mean response spectra give the expected value of the response of a structure, while the mean plus standard deviation response spectra give an idea of the possible range of the response of a structure.

In order to have a detailed understanding of how response spectra behave in different earthquake types, we selected the best match ground motions for each category and plotted the respective response spectra. The best match ground motions were chosen based on the similarity in their seismic characteristics to those of Sri Lanka. The response spectra for each category showed different shapes and peak amplitudes, indicating the variation in seismic characteristics of different types of earthquakes.

Finally, in the analysis section, we compared the developed response spectra in each category with the standard design response spectra available in the world such as the Sri Lanka standard response spectra mentioned in Senavirathna et.al., (2020 paper, Venkatesan et.al., (2017) paper, Eurocode specified, Indian Standard and Australian Standard response spectra. The comparison revealed that the developed response spectra in each category were higher than the standard design response spectra for long-period ground motions. However, the developed response spectra for short-period ground motions were approximately in the range of the standard design response spectra.

4. Results

In this research far fault, non-pulse-like ground motions were further categorized based on the magnitude of the earthquake and the mean period of the ground motion. Mainly for magnitudes greater than or equal to 5.5 ground motions it was possible to collect long-period as well as short-period ground motions. For magnitudes less than 5.5 ground motions only short-period ground motions existed. In conclusion, we have separated collected ground motions into three categories magnitude greater than 5.5 long-period ground motions, magnitude greater than 5.5 short-period ground motions, and magnitude less than 5.5 short-period ground motions of soil type A, then compare respective response spectra with the already existing standard response spectra available in the world.

As the standard response spectra of Sri Lankan Senavirathna et.al., (2020) paper, Venkatesan et.al., (2017) paper, Indian Standard response spectrum for soil type – rock, Euro-code 8 response spectrum of magnitude greater than 5.5 for soil type - rock, Australian codes response spectrum for soil type rock were used. In addition to the standard response spectrum for each country mentioned previously two response spectra for records near to Himalayan and Andaman Islands were also mentioned in the comparison in order to take the idea of how the response spectra alike in the south Indian region with collected data from the PEER database.

4.1 Magnitude greater than 5.5, Long-period ground motion analysis

In this section mean and mean plus standard deviation response spectra of 16 long periods, far fault, and non-pulse-like ground motions with a magnitude greater than 5.5 were analysed. Out of 16 response spectra related to best match 7, 10, and all 16 ground motions were

analysed separately. Analysis results are shown in bellow figures.

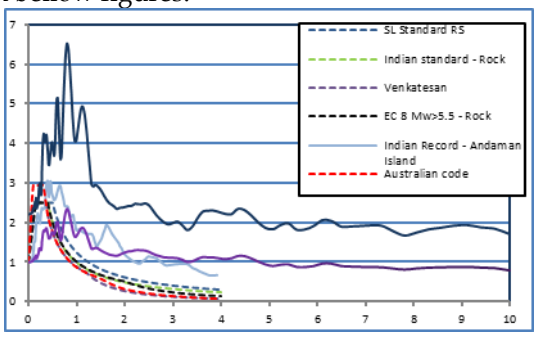

Figure 1: Response spectra comparison. Best match 7 out of 16 long-period ground motions magnitude greater than 5.5

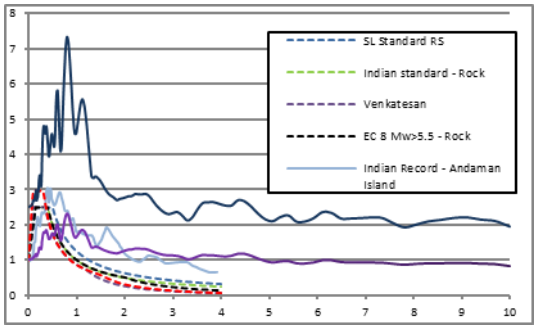

Figure 2: Response spectra comparison. Best match 10 out of 16 long-period ground motions magnitude greater than 5.5

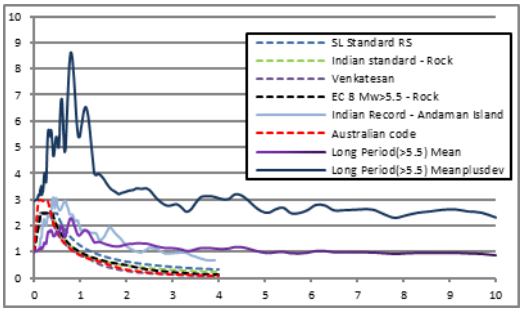

Figure 3: Response spectra comparison. All 16 long-period ground motions magnitude greater than 5.5

4.2 Magnitude greater than 5.5, short period ground motion analysis

In this section mean and mean plus standard deviation response spectra of 35 short periods, far fault, and non-pulse-like ground motions with magnitude greater than 5.5 were analysed. Out of 35 response spectra related to best match 7, 10, 20, and 30 ground motions were analysed separately. Analysis results are shown in bellow figures.

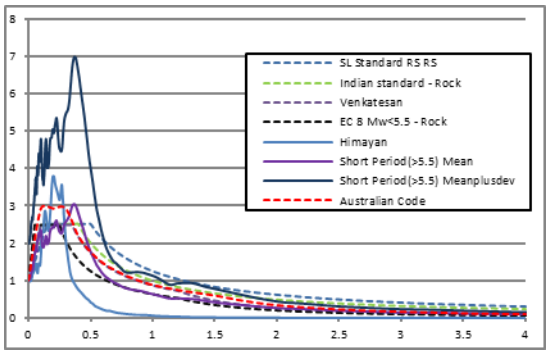

Figure 4: Response spectra comparison. Best match 10 out of 35 short-period ground motions magnitude greater than 5.5

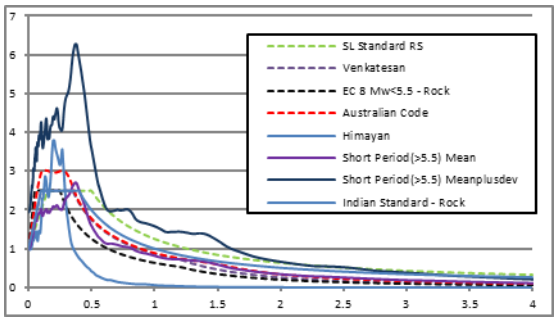

Figure 5: Response spectra comparison. Best match 20 out of 35 short-period ground motions magnitude greater than 5.5

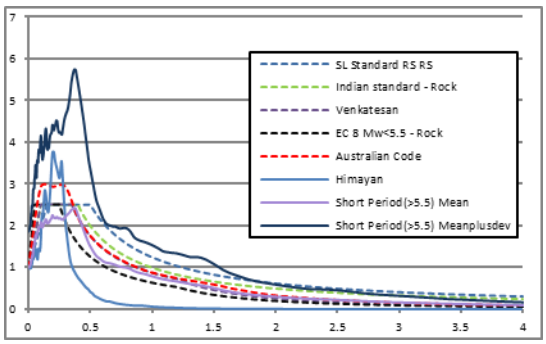

Figure 6: Response spectra comparison. Best match 30 out of 35 short-period ground motions magnitude greater than 5.5

4.3 Magnitude lesser than 5.5, short period ground motion analysis

In this section mean and mean plus standard deviation response spectra of 55 short periods, far fault, and non-pulse-like ground motions which a magnitude greater than 5.5 were analysed. Out of 55 response spectra related to best match 7, 10, 20, 30, and 50 ground motions were analysed separately. Analysis results are shown in the figures.

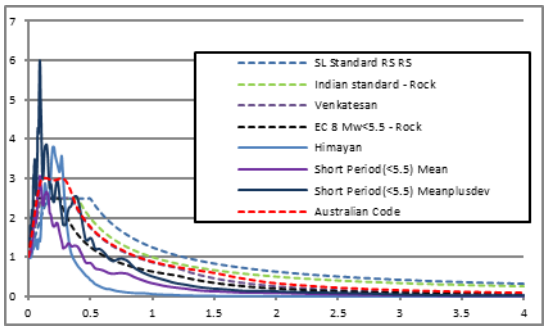

Figure 7: Response spectra comparison. Best match 7 out of 55 short-period ground motions magnitude lesser than 5.5

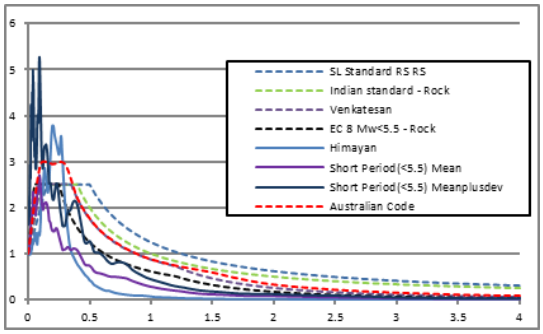

Figure 8: Response spectra comparison. Best match 10 out of 55 short-period ground motions magnitude lesser than 5.5

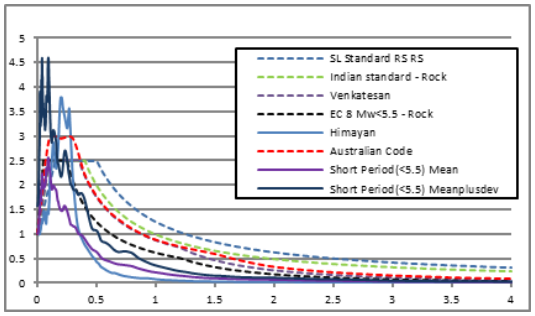

Figure 9: Response spectra comparison. Best match 20 out of 55 short-period ground motions magnitude lesser than 5.5

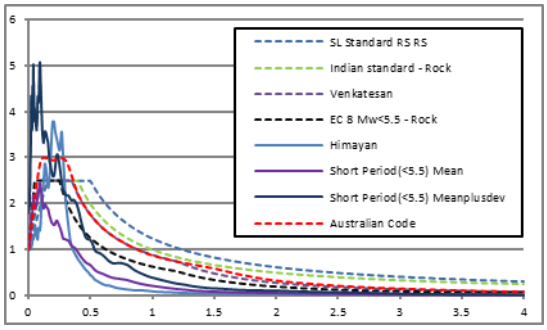

Figure 10: Response spectra comparison. Best match 30 out of 55 short-period ground motions magnitude lesser than 5.5

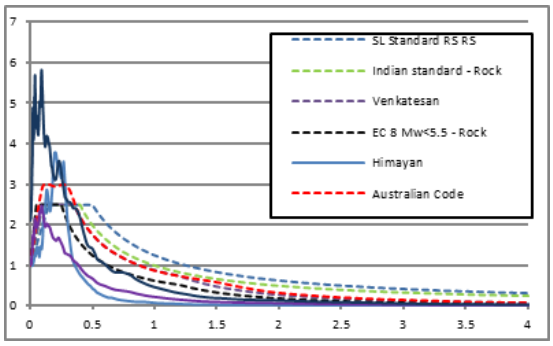

Figure 11: Response spectra comparison. Best match 50 out of 55 short-period ground motions magnitude lesser than 5.5

5. Conclusion

The developed response spectrum for ground motion category magnitudes greater than 5.5, long period and soil type rock has more dominant spectral acceleration values in high natural time periods. This spectrum does not match with any of the standard response spectra used to analyze and compare in this research. Therefore, this type of ground motions it is recommended to conduct response spectrum analysis by collecting suitable ground motions as mentioned in this research.

The developed response spectrum for ground motion category magnitudes greater than 5.5, short-period ground motions it was found that the mean spectrum closely follows Venkatesian et al. 2017 while the mean plus standard deviation closely follows the Seneviaratne et al. 2020

The developed response spectrum for ground motion category magnitudes lesser than 5.5 short-period ground motions, it was found that mean plus standard deviation closely followed the Eurocode 8 specified response spectrum for magnitude less than 5.5, soil type A and mean response spectrum was well below the standard response spectra.

References

Venkatesan, S., Lam, N., & De Silva, S. Design response spectra for Sri Lanka.

Seneviratne, H. N., Wijesundara, K. K., Perera, L. R. K., & Dissanayake, P. B. R. 2020. A macro seismic hazard zonation for Sri Lanka. Engineer, 37, 1.

Identification of Natural Frequency and Damping Ratio of Tall Builidngs in Sri Lanka Using Ambient Wind Vibration Data

Prabodya U.G.K.., Madusanga T.A., Buddika H.A.D.S.*

Department of Civil Engineering, University of Peradeniya, Sri Lanka

**samithbuddika@eng.pdn.ac.lk*

Keywords: Continuous wavelet transform, Damping ratio, Natural frequency, Tall buildings

1. Introduction

In Sri Lanka, tall building construction has been rapidly increasing, especially in urban areas. Tall buildings are significantly impacted by dynamic loads, particularly wind loads, which are predominant in Sri Lanka. When designing a tall building for wind, dynamic responses such as displacement, velocity, and acceleration of the building should be in habitability and safety region. In tall building design, natural frequency and damping ratio are vital for estimating dynamic responses and wind load. However, there is currently no specific empirical formula available in Sri Lanka to estimate these parameters, leaving engineers to rely on somewhat arbitrary selections based on their experience. Therefore, it is imperative to develop an empirical formula tailored to the Sri Lankan context. To address this need, the creation of a comprehensive database containing identified natural frequencies and damping ratios from existing buildings is essential.

Dynamic parameters such as natural frequency, damping ratio, and mode shapes define a structure's dynamic behaviour. Modal analysis is the preferred technique for extracting and quantifying these parameters in structural analysis. Modal analysis use acceleration or velocity data obtained during vibration test. There are two main modal analysis techniques such as experimental modal analysis (EMA) and operational modal analysis (OMA) (Ghalishooyan and Shooshtari, 2015). EMA is performed by artificially exciting the structure with a large size impact hammer/shaker. This technique uses both input excitation data and response measurement for the analysis. OMA is performed while the structure is in operation and uses ambient vibration data caused by environment excitation like wind, traffic, etc. OMA utilizes only measurable response data since the ambient excitation is unknown.

Ambient wind vibration data is utilized for dynamic parameter identification in in-situ tall buildings (Birtharia and Jain, 2015). Therefore, OMA techniques are used to identify dynamic parameters. Ambient wind vibrations, representing forced responses, are transformed into free vibrations via random decrement technique (RDT). Dynamic parameters are then identified using continuous wavelet transform (CWT) and Fast Fourier transform (FFT) on the free vibration modal response. Finally, a comparison is made between the identified natural frequencies and damping ratio values and those obtained from literature equations and FEM.

2. Literature review

This chapter highlights previous research findings and their influence on the current study's methodology, which uses RDT and CWT techniques for estimating building modal parameters.

2.1 Natural frequency

The natural frequency of a tall building is depending on its height, tip displacement (Tamura, 2012), and type of the building. The value can be acquired using an empirical equation provided in the literature.

Table 1: Methods to calculate natural period available in the literature

Code	Structural Type	Natural Period (s)
ASCE 7-10	RC moment frame	$T = 0.0670H^{0.9}$
	Other RC Building	$T = 0.043H$
Lagomarsino	RC	$T = 0.018H$
Eurocode I	RC	$T = 0.022H$
AS/NZS 1170 and Hong Kong design code	Steel and RC	$T = 0.022H$
Yukio Tamura	RC	$T = H/67$ (Habitability regime)

2.2 Damping

Damping dissipates vibration energy as heat or radiates it from the system. There are various physical causes of damping in buildings (AIJ 2000) such as internal friction damping, plasticity damping, external friction damping, radiation damping, external viscosity damping, aerodynamic damping, and others.

The damping ratio formula can be categorized into single-value and frequency and amplitude-dependent damping ratios.

Table 2: Values of structural damping ratios given by different codes

Method	Code	Structural damping ratio (%)
Single value damping ratio	Eurocode I	1.57
	AS/NZS 1170	0.5 – 1.0
	ASCE 7 - 10	2.0
Frequency and amplitude-dependent damping ratio	ISO 4354	1.2 – 2.0 (Height depend)
	AIJ 2000	$0.014f_i$ + 470(X/H) – 0.0018 (RC)
	AIJ 2000	$0.013f_i$ + 400(X/H) – 0.0029 (Steel)
	ESDU 83009	$0.0076f_i$ + 150(X/H) + 0.003
	Yoon	$0.0059f_i$ + 310(X/H) + 0.0039

3. Methodology

3.1 Work breakdown

The research work followed several main steps, as illustrated in the flowchart.

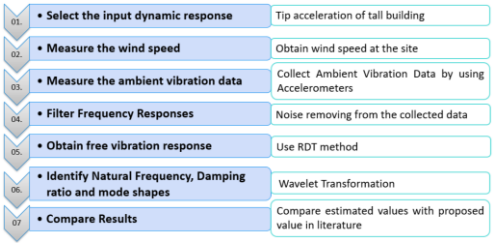

Figure 1: Research workflow

3.2 Data collection

Luna tower and twin peak buildings were selected for the case study of this project, they are located in Colombo, and building heights are 170m and 182m respectively. Acceleration was measured as dynamic response of the buildings under ambient wind vibration using accelerometers. Also, the wind speed at the top of the building was recorded at the time vibration data was measured. The measurement was taken at a rate of 200Hz and 500Hz within 30-40min duration.

3.3 Data processing

In this research, the Butterworth filter is used to remove noise (Liyana Kankanamge, 2016).

3.3.1 Random decrement technique

RDT is a well-established method to convert random responses to free decay responses. RDT decomposes acceleration response into free and force vibration component. The free vibration component can be obtained by a special averaging procedure of measurements which remove the random parts, leaving its deterministic part.

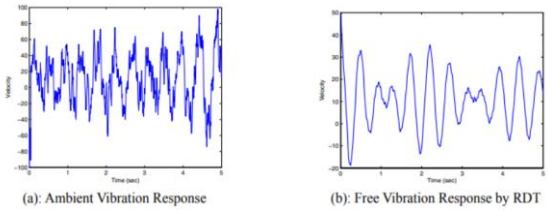

Figure 2: Example of free vibration response obtained from ambient vibration using RDT (M.R. Hemtaei and S.A. Anvar, 2008)

3.3.2 Continuous wavelet transformation

The general CWT formula used to decompose a function x(t) into frequency-time domain is given by the following equation,

$$CWT\{x(t)\}=W_x(\tau,s)=\frac{1}{\sqrt{s}}\int_{-\infty}^{+\infty} x(t)\psi^*\left(\frac{t-\tau}{s}\right)dt \quad .....(1)$$

The wavelet amplitude map is constructed using amplitude of wavelet coefficient, $|W(\tau,)|$. From the wavelet amplitude map, local maxima indicate the natural frequencies of the system. From the Wavelet amplitude map, the wavelet envelops $|W\ x\ (\tau,)|$ is extracted at natural frequencies. Then plot the wavelet envelope at the selected natural frequency in a natural algorithm scale. Damping ratio is estimated by taking the slope of that plot. A specialized

program developed in MATLAB, is used to do the above process.

4. Results

4.1 Natural frequency of the building

The building's natural frequency was estimated in two perpendicular directions using FFT and CWT techniques, as depicted in Figure 3.

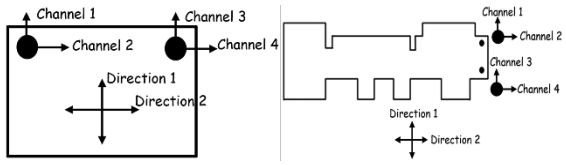

Figure 3: Arrangement of two accelerometers on the top floor of Twin peaks and Luna Towers

4.1.1 Twin peaks tower

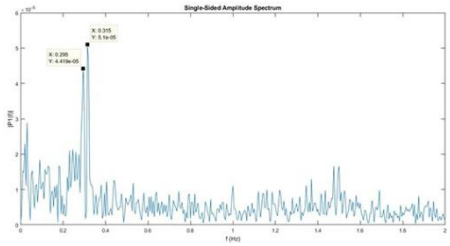

Figure 4: FFT for channel 1 in direction 1

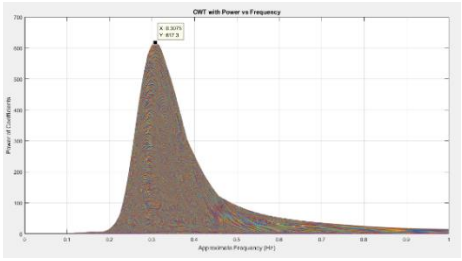

Figure 5: CWT power spectrum for channel 1 in direction 1

Table 3: Natural frequency comparison: FFT, CWT, FEM and empirical methods

Code	Natural Frequency (Hz)	
	Direction 1	Direction 2
KBC 2009	0.28	0.28
ASCE 7 - 10	0.14	0.14
Lagomarsino	0.30	0.30
Eurocode 1	0.25	0.25
Satake et al.	0.37	0.37
Yoon and Joo	0.29	0.29
Using FFT	0.30	0.29
Using CWT	0.31	0.30
Using FEM	0.18	0.19

4.1.2 Luna tower

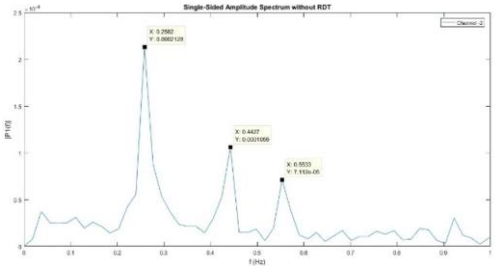

Figure 6: FFT for channel 2 in direction 2

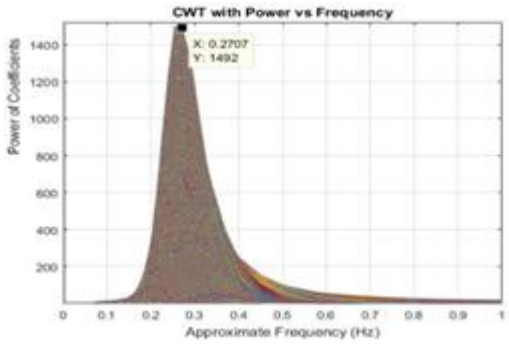

Figure 7: CWT power spectrum for channel 2 in Direction 2

Table 4: Comparison natural frequency of the building from FFT & CWT with empirical methods

Code	Natural Frequency (Hz)	
	Direction 1	Direction 2
KBC 2009	0.29	0.29
ASCE 7 - 10	0.15	0.15
Lagomarsino	0.32	0.32
Eurocode 1	0.27	0.27
Satake et al.	0.39	0.39
Yoon and Joo	0.31	0.31
Using FFT	0.26	0.26
Using CWT	0.25	0.27
Using FEM	0.16	0.24

4.2 Damping Ratio of the building

The building's damping ratio was determined through a CWT-based procedure using MATLAB. Figures illustrate 3D wavelet amplitude and tables presents the estimated damping ratio values for directions 1 and 2.

4.2.1 Twin peaks tower

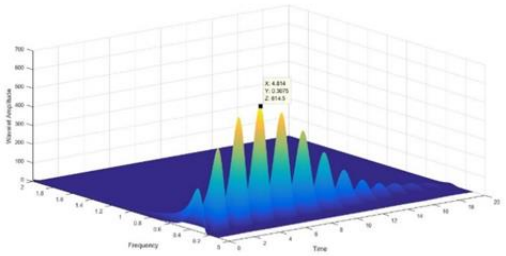

Figure 8: Wavelet amplitude map in direction 1

Table 5: Comparison of damping ratio values from CWT with empirical methods

Code	Damping ratio (%)	
	Direction 1	Direction 2
Eurocode 1	1.57	1.57
AS/NZS 1170	0.50	0.50
ASCE 7-10	2.00	2.00
ISO 4354	1.20	1.20
Lagomarsino	2.49	2.55
Using CWT	2.66	1.81

4.2.2 Luna tower

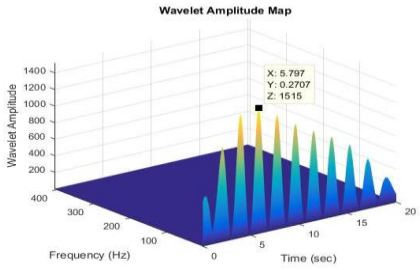

Figure 9: 3D wavelet amplitude in direction 2

Table 6: Comparison of damping ratio values from CWT with empirical methods

Code	Damping ratio (%)	
	Direction 1	Direction 2
Eurocode 1	1.57	1.57
AS/NZS 1170	0.50	0.50
ASCE 7-10	2.00	2.00
ISO 4354	1.20	1.20
Lagomarsino	2.99	2.79
Using CWT	2.23	1.67

5. Conclusions

Analysis of the Twin peak and Luna towers' average 1st mode natural frequencies in both direction 1 and direction 2, conducted through the FFT and CWT methods, revealed strikingly consistent results. In direction 1, FFT yielded natural frequencies of 0.30Hz for Twin peak and 0.26Hz for Luna, while CWT indicated values of 0.31Hz for Twin peak and 0.25Hz for Luna. In direction 2, FFT provided frequencies of 0.29Hz for Twin peak and 0.26Hz for Luna, and CWT yielded 0.30Hz for Twin peak and 0.27Hz for Luna. The agreement between the FFT and CWT methods reinforces the reliability of the results.
In a comparative analysis, the estimated results aligned well with empirical values from the literature, except for ASCE 7-10, which exhibited less agreement.

The estimated damping ratio values were 2.66%, 1.81% and 2.23%, 1.67% for Twin peak and Luna tower respectively but those values were not in good agreement with the values given in the literature.

Therefore, further applications of CWT based damping estimations method is recommended to find the damping ratio of tall buildings in Sri Lanka.

References

Yi, J., Zhang, J. and Li, Q., 2013. Dynamic characteristics and wind-induced responses of a super-tall building during typhoons. Journal of Wind Engineering and Industrial Aerodynamics, 121, pp.116-130.

Ghalishooyan, M. and Shooshtari, A., 2015, May. Operational modal analysis techniques and their theoretical and practical aspects: A comprehensive review and introduction. In 6th International Operatiional Modal Analysis Conference IOMAC 2015.

Wu, J.Y., 2001. Extracting damping ratios using wavelets (Doctoral dissertation, Massachusetts Institute of Technology).

Tamura, Y., 2013. Damping in Buildings and Estimation Techniques. Advanced Structural Wind Engineering, pp.347-376.

Tamura, Y., 2012. Amplitude dependency of damping in buildings and critical tip drift ratio. International Journal of High-Rise Buildings, 1(1), pp.1-13.

Liyana Kankanamge 2016. Application of Wavelet Transform in Structural Health Monitoring. Master's Theses

Birtharia, A. and Jain, S.K., 2015. Applications of ambient vibration testing: An overview. Int. Res. J. Eng. Technol, 2, pp.845-852.

WATER AND ENVIRONMENT

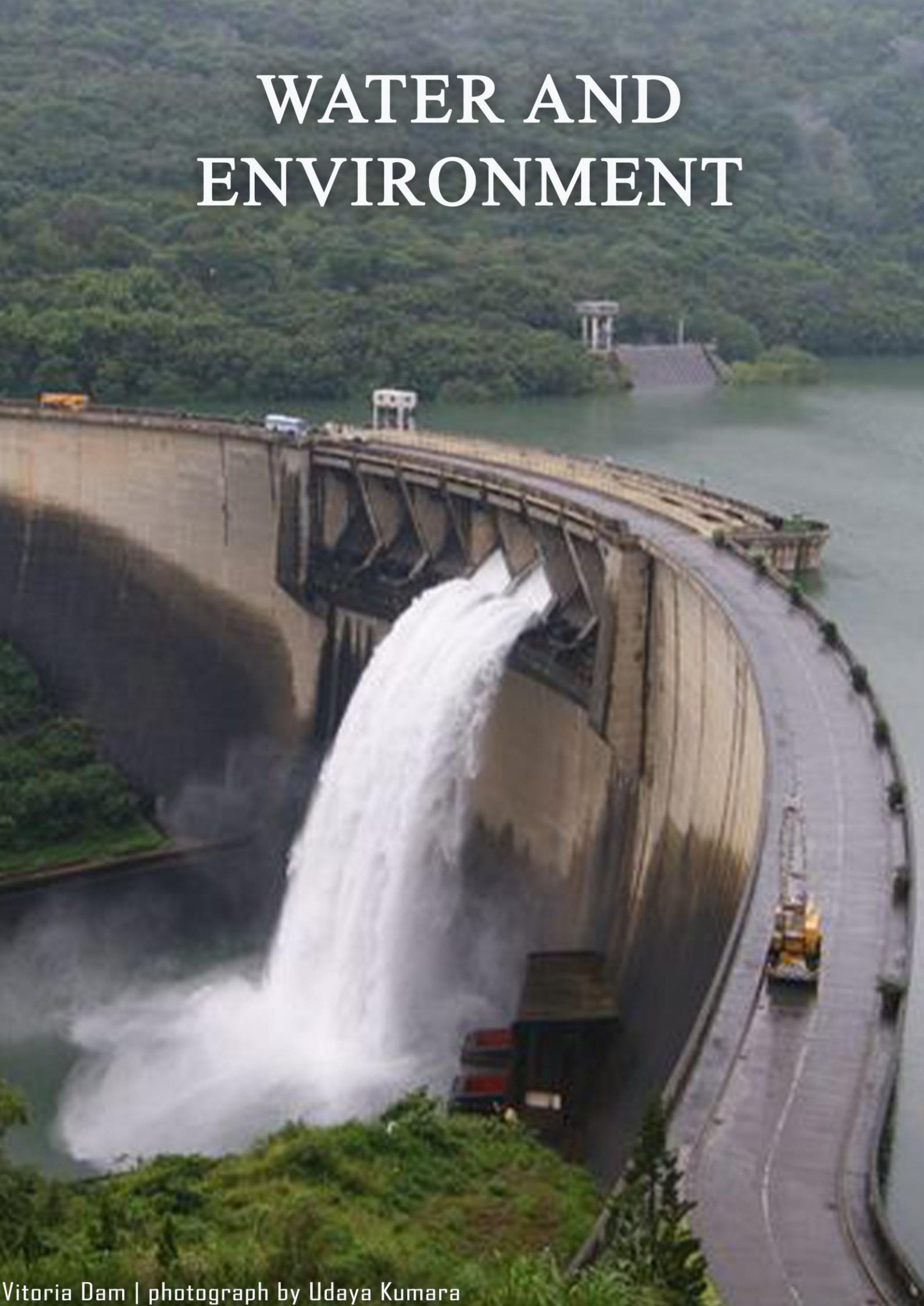

Vitoria Dam | photograph by Udaya Kumara

Spatial and Temporal Distributions of Droughts and Drought Characteristics in North-Western Province

Lakmal K.T.V.T., Silva L.R., Nandalal K.D.W.*

Department of Civil Engineering, University of Peradeniya, Sri Lanka

**kdwn@pdn.ac.lk*

Keywords: Drought, SPI value, Northwestern province, Temporal, Spatial

1. Introduction

In the past, the North-Western province has been susceptible to droughts, and the residents of this region continue to experience their effects now. Therefore, the purpose of this study is to inform the public about droughts and to encourage them to identify risk-reduction and adaptation strategies. In the North-Western province, this study examined the temporal and spatial distributions of droughts and their characteristics. For that Standard Precipitation Index (SPI) method and the Herbst method, to determine the durations of the droughts were used. Five rainfall gauging stations were chosen in each of the districts of Puttalam and Kurunegala to measure rainfall in order to calculate SPI values and use them to analyse droughts in the province. The research discovered patterns in the occurrence of droughts at those stations as well as how they differed spatially within the province. Rainfall data was collected at each of the stations monthly for the study's time frame of 1990 to 2019. For periods of a year, six months, three months, and one month, the SPI values were computed. The probability of a drought occurring was also estimated for each rainfall station, and the study's findings will help vulnerable communities in North-western Province understand, prepare for, and reduce their risk of a drought.

2. Literature review

The most common technique in use today for monitoring droughts is the Standard Precipitation Index. (Mishra and Desai 2005; Szalai and Szinell 2000) Hambantota was also severely hit by the 2001 drought in Sri Lanka, which had a negative impact on the dry and intermediate zones. In order to examine the usage of the SPI and appropriate SPI time scales, the SPI values were simulated with cumulative and average rainfall at Hambantota in 2001. After all, the study's findings made it very evident that the SPI technique worked best with timescales of three and six months. (Manesha and Vimukthini, 2015)

The Herbst method for identifying the onset and termination of droughts is explained in the research report. The onset test assumes that there was no drought before the available record and starts with inspecting the first month. If the difference is positive, it does not signify the start of a drought. The termination test is applied to the month following the first month with a positive difference after the start of the drought. If a termination condition is not satisfied, then two further tests are applied simultaneously. The first test involves adding all the differences from the first to the nth month of the test inclusive. The second test consists of ten sequential tests, comparing the actual precipitation. (Nandalal, 2018)

3. Methodology

The Meteorology Department of Sri Lanka provided the rainfall information used in this study. The data sample consists of monthly rainfall data collected over 30 years, from 1990 to 2019, at 10 rainfall gauging stations in Kurunegala and Puttalam districts. Data screening and missing data filling were then completed. For periods of a year, six months, and three months, the SPI values were computed.

3.1 Standard Precipitation Index method

Out of many rainfall indices, SPI is selected, because it only depends on precipitation data. SPI values are calculated for three months, six months, and one year for each station.

Calculation steps,

First, the data set's mean and standard deviation are calculated. Next, using equation (1) Shape

Parameter (β) and Scale Parameter (α) are calculated.

$$\beta = \frac{S^2}{\mu};\ \beta > 0 \qquad \alpha = \frac{\mu^2}{S^2};\ \alpha > 0 \quad (1)$$

Where S is the standard deviation and μ is the mean.

Then, Γ(α), gamma function value (2) is calculated, and using that the cumulative probability G(x) of an observed precipitation event is found. (3)

$$\Gamma(\alpha) = \int_0^\infty y^{\alpha-1} e^{-y} dy \quad (2)$$

$$G(x) = \frac{\int_0^x x^{\alpha-1} e^{-\frac{x}{\beta}} dx}{\beta^\alpha \Gamma(\alpha)} \quad ; \quad x > 0 \quad (3)$$

x is the amount of precipitation. Since gamma distribution is not defined for null values, H(x) is defined such that (4).

$$H(x) = q + (1-q)G(x); \quad (4)$$

q is the probability of zero values.

Finally, the cumulative probability H(x) is transformed to the standard normal random variable Z (SPI) with mean zero and standard deviation one.

$$SPI = Z = -\left(t - \frac{C_0 + C_1 t + C_2 t^2}{1 + d_1 t + d_2 t^2 + d_3 t^3}\right) \quad for\ 0 < H(x) < 0.5 \quad (5)$$

$$SPI = Z = +\left(t - \frac{C_0 + C_1 t + C_2 t^2}{1 + d_1 t + d_2 t^2 + d_3 t^3}\right) \quad for\ 0.5 < H(x) < 1 \quad (6)$$

Where,

$$t = \sqrt{\ln\left(\frac{1}{(H(x))^2}\right)} \quad for\ 0 < H(x) 0.5 \quad (7)$$

$$t = \sqrt{\ln\left(\frac{1}{(1.0 - H(x))^2}\right)} \quad for\ 0.5 < H(x) < 1 \quad (8)$$

And,

$c_0 = 2.515517$ $\quad c_1 = 0.802853$

$c_2 = 0.010328$ $\quad d_1 = 1.432788$

$d_2 = 0.189269$ $\quad d_3 = 0.001308$

According to the SPI value precipitation data can be categorized as given in Table 1

Table 1: Severity of droughts according to SPI values.

2.0	or	more	Extremely wet
1.5	to	1.99	Very wet
1.0	to	1.49	Moderately wet
-0.99	to	0.99	Near normal
-1.0	to	-1.49	Moderately dry
-1.5	to	-1.99	Severely dry
-2.0	or	less	Extremely dry

3.2 Herbst method

The Herbst method uses rainfall data to determine the occurrence and severity of a drought event. The method specifies the beginning and end of a drought event, depending on both the current month's rainfall and the prior month's rainfall. The sliding scale can be used to determine the beginning and end of a drought event. The monthly rainfall data of 10 stations is used to calculate the drought duration using the Herbst method.

Firstly, the monthly mean values (Pk) for each month are calculated. Then, using equation (9) a weightage is determined.

$$W_k = 0.1\left[1 + \frac{P_k}{\sum_{k=1}^{12} \frac{P_k}{12}}\right] \quad (9)$$

where Pk is the average precipitation for the considered month and Wk is the weighted average of the month. Next, the deficit of the previous month rainfall is calculated with respect to its monthly mean value as given in equation (10).

$$D_{i-1} = P_{i-1} - P_k \quad (10)$$

Where, D_{i-1} is the precipitation deficit of the previous month with respect to its monthly mean value and P_k is the mean precipitation for the previous month. Only months with deficits are considered for further calculations. Then effective rainfall for the month of consideration is calculates as in equation (11).

$$P_{e_i} = P_i + [D_{i-1} \times W_{i-1}] \quad (11)$$

Where, P_i is precipitation of the month of consideration and P_{ei} is the effective rainfall of the month of consideration. Next, a twelve-value sliding scale is prepared to compare with deficiencies and identify onset and termination periods of droughts. For this, monthly increment (MI) is calculated using equation (12).

$$MI = \frac{MAD - MMMR}{11} \quad (12)$$

Where, MAD is the mean annual deficiency of rainfall and MMMR is the maximum of mean monthly rainfalls. A sliding scale (SS) is then prepared using the equation (13).

$$SS = MMMR + (r-1)MI \quad (13)$$

Where, r is the order of the month from 1 to 12.

4. Results and discussion

4.1 Temporal variation of drought

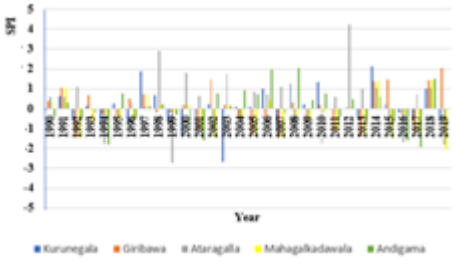

Figure 1: Annual SPI values for Kurunegala district

According to the results in Giribawa, it can be predicted that after 4 to 5 years there could be a chance to occur a drought event, and the probability of occurring it 23%. In Ataragalla also it can be concluded that after 8 years there is a possibility to have a drought year and the chance of a future year being a drought year is 27%.

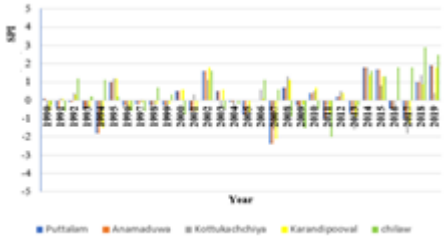

Figure 2: Annual SPI values for Puttalam district

Anamaduwa dominantly shows moderate drought conditions during these 30 years and in 1994 it experienced a severe drought year. A similar condition occurred in Karandipooval station and in 2007 it has experienced a severe drought condition. In Kottukachchiya dominantly shows very dry conditions and those were occurred in 2007, 2013, and 2017. In Chilaw one severe dry year was noticed and it was in 2011 and in Puttalam two very dry events occurred in 1994 and 2007.

4.2 Spatial variation of drought

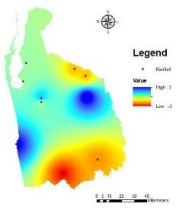

Figure 3: 2001 Annual SPI variation

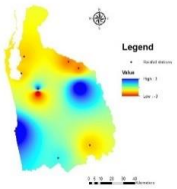

Figure 4: 2007 Annual SPI variation

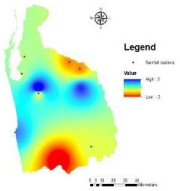

Figure 5: 2016 Annual SPI variation

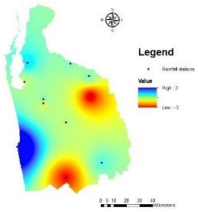

Figure 6: 2017 Annual SPI variation

Going from the south to the north of the province in 2001, the severity of the drought varied from an extreme drought state to a wet condition. However, the drought condition has already occurred when it goes to Giribawa and Mahagalkadawala areas. The province's northern region experienced severe drought conditions in 2007, particularly in Anamaduwa, Giribawa, and Mahagalkadawala. While it has seen wet weather when it has traveled to the southern half of the province, Kurunegala has once again got dry conditions. In 2016, there are severe drought conditions around Andigama and Ataragalla, and wet conditions have been reported further away from these stations. Similar to this, there were drought conditions in 2017 around Andigama, Mahagalkadawala, and Giribawa, but they have since disappeared.

4.3 Probability of drought occurrences

According to the annual SPI variation

Table 2 Probability of drought occurrences in Kurunegala district

Kurunegala	0.13
Giribawa	0.23
Ataragala	0.27
Mahagalkadawala	0.33
Andigama	0.17

According to Table 2 if it is considered annual SPI variation in Giribawa it has a 0.23 (nearly 1/4) probability to have a drought year. Which means it has a possibility to have a drought year once for four years.

Table 3 Probability of drought occurrences in Puttalam district

Anamaduwa	0.13
Chillaw	0.03
Karandipooval	0.13
Kottukachchiya	0.13
Puttalam	0.07

According to Table 3 if it is considered annual SPI variation in Anamaduwa it has a 0.13(nearly 1/10) probability to have a drought year, means it has a possibility to have a drought year once for ten years

4.4 Drought duration

The Herbst method was applied for the Kurunegala and Puttalam rainfall stations. The following periods were observed to be drought periods.

Kurunegala	2003 September -2004 May
	2011 October - 2012 June
	2016 August - 2016 November
Giribawa	2017 November – 2018 April

2018 November - 2019 June

Ataragalla 2009 October – 2010 March
2016 October – 2017 September

Mahagalkadawala
2016 October - 2017 February
Andigama 1990April – 1990 October
2001 October – 2002 March
2013 October – 2014 August
2016 July – 2017 March
Anamaduwa 2000 October – 2001 April
Chillaw 2000 October - 2001 January
2008 November -2009 October
2016 September – 2017 August
Kottukachchiya
1996 November -1997 May
2016 September – 2017 March
2017 October – 2018 May
Puttalam 2016 October – 2017 January

It shows that in many stations there have occurred drought periods in 2016 and 2017, which means those years can be considered dry years.

5. Conclusions

Anamaduwa and Kottukachchiya are a danger of experiencing a drought year after five years, and the probability of experiencing such a drought event is 13%, per the results of yearly SPI variation in the Puttalam district. In Karandipooval, the risk has a ten-year duration and a 13% chance of occurring. After ten years, Puttalam is also susceptible to a drought, which might be extremely severe.

According to the yearly SPI variation data for the Kurunegala district, Giribawa has a risk of experiencing a drought year after a period of four to five years and a 23% probability of doing so. These numbers are eight years and 27% for Ataragalla.

Different research on the island's droughts, the Disaster Management Center (DMC) report, states that the years 2001, 2007, 2016, and 2017 saw severe droughts across the whole island. When all of the study's findings are taken into consideration, practically all of the rainfall stations reveal drought conditions in each of the above-mentioned years. This indicates that the drought conditions that occurred each year caused these years to become dry years, and the DMC report further supports the study's correctness.

Additionally, more rainfall gauging stations in each district can be added for a much better analysis, and they can be chosen such that they have a good spatial variety. Drought analysis requires more than 30 years of data, and the 1-month scale of the SPI method makes it useless. Results from the Herbst technique and SPI values are frequently comparable. However, if the Herbst method indicates a drought duration, SPI values will indicate a drought condition throughout that duration. On the other hand, if SPI values indicate a drought condition during a certain period, the Herbst method may not have accurately recognized that period as a drought duration.

References

Alahakoon, N. and Edirisinghe, M. 2021. Spatial Variability of Rainfall Trends in Sri Lanka from 1989 to 2019 as an indication of climate change. J. International Journal of Geo Information 2021,10,84. pp. 1-18.

Drought Identification and Monitoring in Kurunegala District Using Standard Precipitation Index, Post Graduate Institute of Science, University of Peradeniya, Sri Lanka. (http://dlib.pdn.ac.lk/handle/123456789/1817)

Manesha, S., Vimukthini, S. and Premalal, K.H.M.S. 2015. Develop Drought Monitoring in Sri Lanka Using Standard Precipitation Index (SPI). J. Sri Lanka Journal of Meteorology. Vol. 1, pp. 64-71

Nandalal, K.D.W. 2018. Comparison of the Use of Herbst and SPI Methods in Identification of Hydrological Droughts.

Nianthi, K.W.G.R. 2012. Farmers' Responses to Drought: Dry Zone of Sri Lanka: (Case Study in Medirigiriya). J. Impact Factor 3.582 Case Studies Journal ISSN (2305-509X). Vol. 5, Issue 6, pp. 33-39.

Rajendram, K. 2021. Rainfall Variability and Drought in the Dry and Wet Zones of Sri Lanka. J. World Scientific News 160 (2021). pp. 172-189.

Rhee, J. and Carbone, G.J. 2010. Estimating Drought Conditions for Regions with Limited Precipitation Data. J. Journal of Applied Meteorology and Climatology. Vol. 50, pp. 548-559.

Silva, R.P.D, Ratnasiri, M.D. and Dayawansa, N.D.K. 2007. A Comparison Methods Used in Estimating Missing Rainfall Data. J. Journal of Agricultural Sciences. Vol. 3, pp. 101-108.

Improved Operation of Minipe Left Bank Canal Irrigation System

Silva U.H.M.S., Ranwala S., Nandalal K.D.W.*

Department of Civil Engineering, University of Peradeniya, Sri Lanka

**kdwn@pdn.ac.lk*

Keywords: HEC-HMS, CROPWAT, WEAP, Scenario, Operational pattern

1. Introduction

Due to the inadequacy of water supply, and inefficiency and inequity in irrigation water distribution, head-tail water disparity exists in Minipe left bank canal. To minimize the disparity the Minipe anicut is raised by 3.5 m. Though adequate water could be released, due to the misuse and mismanagement along the canal, irrigation water would not be distributed effectively. Therefore, it is important to improve the water distribution pattern in the Minipe left bank canal irrigation system. The current operational pattern is shown in Figure 1. The study is focused on developing an operational pattern for the Minipe left bank canal irrigation system to provide adequate water to the whole command area in both the Yala and Maha seasons using simulation models.

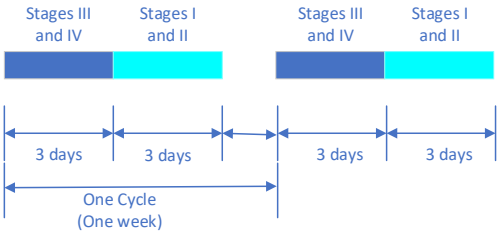

Figure 1: Existing operational pattern

2. Literature review

Sirimewan et al. (2019) mentioned that due to the population rise, the demand for irrigation water requirement has increased. The problems of irrigation water management in Sri Lanka have been found as issues of the efficiency of irrigation infrastructure and the equity of water distribution. Kumari et al. (2010) stated that crop diversification would lead to a reduction of water scarcity problems. Crop diversification is especially used during the Yala season because the water shortage is higher during that time. Hemaratne et al. (1991) proved that head-tail disparity exists in the Minipe Scheme. Tail- end farmers of the Minipe left bank canal suffer from water inadequacy. This leads to the destruction of the crops and poor economic status. More than one-third of the tailenders suffer from poverty. Kumari et al. (2010) pointed out that a high incidence of poverty can be seen at the tail end of the Minipe irrigation scheme, compared to their head and middle reaches. Though the economic aspect of water disparity in the Minipe left bank canal has been covered in past research, the water deficits have not been quantified. Due to the above research gap, it is necessary to quantify the water deficits and provide a solution to improve the operational pattern for the Minipe left bank canal irrigation scheme.

In Choudhari et al. (2014) HEC-HMS model was used to simulate a rainfall-runoff process. SCS curve number, SCS unit hydrograph, exponential recession, and Muskingum routing methods were used to compute runoff volume, peak runoff rate, base flow, and flow routing respectively. The research paper gave an insight into these methods. Shah et al. (2016) studied estimating crop water requirements and irrigation scheduling using CROPWAT software. For crop water requirements daily climatic data, rainfall data, soil data, and crop data were required. For the calculation of reference crop evapotranspiration Penman-Monteith equation was used. The study helped to understand the procedure for estimating crop water requirements in CROPWAT. Kirshanth and Sivakumar (2018) study gave insight into how to use WEAP models to simulate irrigation system operation and how to use different scenarios to develop an improved operational pattern for the Minipe left bank canal irrigation system.

3. Methodology

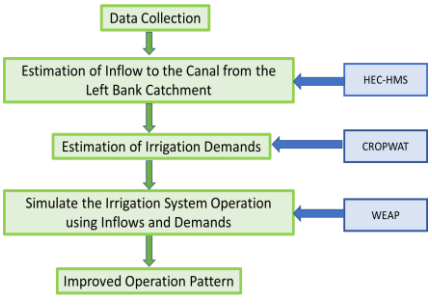

Figure 2: Overview of the methodology

3.2 Data collection

The rain gauge stations of Mapakadawewa, Aluthnuwara, Girandurukotte, and Hembarawa are used for daily rainfall data. Daily climatic data of Girandurukotte, Minipe anicut discharges, crop areas and crop periods, and sowing dates are the data collected for the study.

3.3 Estimation of inflows

The inflows to the Minipe left bank canal are estimated using rainfall data from the 2005-2020 period, using HEC-HMS software. First, the catchments are delineated using HEC-GeoHMS and ArcGIS software.

For estimation of inflows to the canal, a hydrological model in HEC-HMS software is used. The loss method considered is initial and constant method. The transform method is SCS Unit Hydrograph method, and the Base flow method is recession method. The initial loss, constant rate of loss, and percentage of impervious is taken as 8 mm, 1.6 mm/hr, and 1% respectively. Under the baseflow the initial type is taken as discharge per area, initial discharge is taken as 5 $m^3/s.km^2$, recession constant is taken to be 0.6, while a 0.4 ratio is taken for the ratio to peak threshold type.

The lag time of catchments is calculated using the Kirpich method.

$$t_c = kL^{0.77}S^{-0.385} \quad \text{.....(1)}$$

k = 0.0195
L= Channel flow length (m)
S = Main Channel Slope

To obtain the affecting area from the rain gauge stations, Thiessen polygons are drawn. According to these Thiessen polygons the rainfall data affecting the relevant sub-catchments, for relevant years 2005 to 2020 are chosen as input data to HEC-HMS software.

3.4 Estimation of irrigation demands

CROPWAT 8.0 model is used to estimate the irrigation water requirement for the command area of the Minipe left bank canal. Daily climatic data of Girandurukotte from 2015 to 2020 period are used. The rainfall data of Mapakadawewa are used for estimating crop water requirements in the command areas in Stage 1 and Stage 2. The rainfall data of Girandurukotte are used for estimating crop water requirements in the command areas in Stage 3 and Stage 4. The sowing dates are selected by referring to the seasonal summary reports (SSR). Soil data taken are reddish-brown soil. An irrigation efficiency of 60% is considered.

The crop water requirements are calculated for 100% paddy cultivation in both the Yala and Maha seasons. A cropping pattern of 70% paddy and 30% other field crops is introduced in the Yala season and crop water requirements are estimated. The other field crops considered are maize, green gram, and soya bean, 10% of each. Also, the crop water requirements are estimated by advancing the sowing date by two weeks.

3.5 Simulating the irrigation system operation

Using the calculated inflows to the canal and the irrigation water demands, the irrigation system is simulated for the 2015 to 2020 period, using WEAP software. For the 4 stages in the Minipe left bank canal scheme and their sections, 7 demand sites are introduced. Minipe left bank canal crosses Heen Ganga as an aqueduct. Therefore, Heen Ganga was neglected as an inflow. Hasalaka Oya is one of the main inflows to the canal. Minipe left bank canal crosses Hasalaka Oya as a level crossing. Therefore, it was identified as a reservoir in the WEAP model. Various scenarios are considered to improve the operational pattern. Operational patterns can be improved by reducing unmet demands. The existing operational pattern is considered in the model.

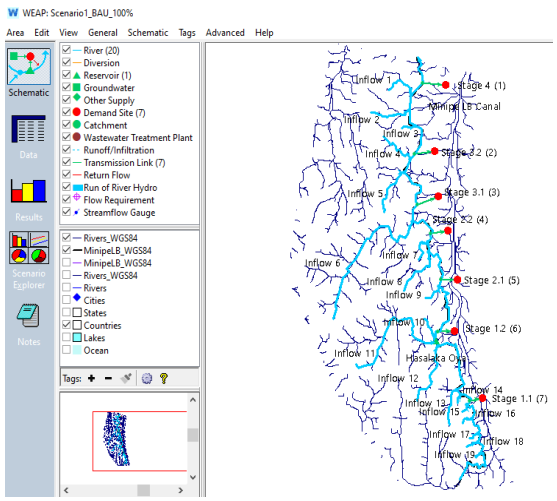

Figure 3: Schematic diagram in WEAP

Scenario 1 - Business as Usual (BAU) scenario. 100% paddy grown in Yala and Maha seasons.

Scenario 2 - 2 weeks planting date advanced. The planting date of both the Yala and Maha seasons advanced.

Scenario 3 - Changing the crop pattern in Yala to 70% paddy and 30% other field crops. Maha season cropping pattern as 100% paddy.

Scenario 4 - 2 weeks planting date advanced for 70% paddy and 30% other field crops.

Scenario 5 – Increasing Minipe anicut discharges by 15%, fulfilling Minipe left bank canal capacity constrain.

4. Results and discussion

4.1 Catchment delineation and HEC- HMS results

19 sub-catchments were identified by the catchment delineation. Including Heen Ganga and Hasalaka Oya. Since these streams are not gauged, there is no observed data to verify the accuracy of the results obtained. Therefore, the runoff coefficient was considered. The inflows calculated can be taken as accurate since the runoff coefficient of Mahaweli river is 30.9% according to the "Statistical Compendium on Natural Resources Management, Sri Lanka - 2000 - For Sustainable Development". The calculated rainfall runoff coefficients for the small catchments are slightly above it.

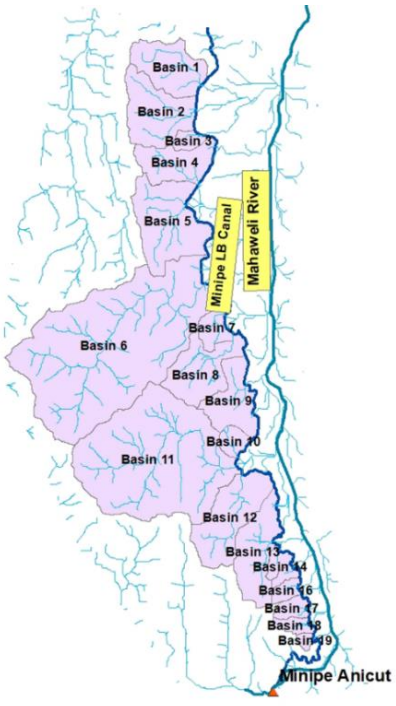

Figure 4: Sub-catchments of Minipe left bank canal

Table 1: Details of sub-catchments

Sub-Catchments	Area (km^2)	Lag time (min)	Rainfall/Runoff (%)
1	17.0	60	30.6
2	20.6	48	30.6
3	1.5	17	30.6
4	11.4	50	30.6
5	23.2	49	30.6
6	117.1	79	30.6
7	3.8	25	30.6
8	17.8	24	32.0
9	7.8	24	32.0
10	2.7	24	33.3
11	87.0	60	33.3
12	20.5	32	33.1
13	15.4	26	33.1
14	1.8	12	33.1
15	1.4	11	33.1
16	2.5	13	33.1
17	1.6	10	35.0
18	2.5	12	35.0
19	1.0	7	35.0

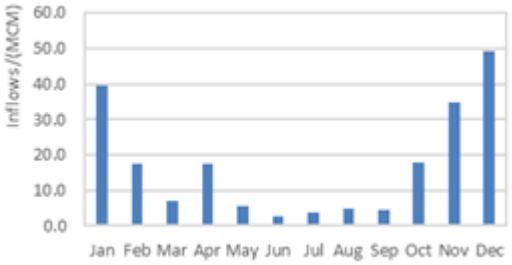

Figure 5: Monthly averages of the inflows to the canal.

4.2 CROPWAT results

The estimated Crop Water requirements (CWR) using rainfall data of Mapakadawewa (Mapa) and Girandurukotte (Gira) gauge stations for Maha seasons and Yala seasons are shown in Table 2 and Table 3 respectively.

Table 2: Crop water requirements in Maha seasons

Year	CWR/ (mm/season)			
	100% Paddy		Sowing date 2 weeks advanced	
	Mapa	Gira	Mapa	Gira
2015 -2016	333	347	280	277
2016 -2017	293	273	277	280
2017-2018	362	373	329	365
2018 -2019	374	401	321	389
2019 - 2020	319	306	297	283

Table 3: Crop water requirements in Yala seasons

Year	CWR/ (mm/season)					
	100% Paddy		70% Paddy		Sowing date 2 weeks advanced	
	Mapa	Gira	Mapa	Gira	Mapa	Gira
2015	674	678	563	560	576	621
2016	735	724	618	609	723	679
2017	708	703	592	584	740	704
2018	698	685	588	568	626	606
2019	752	575	580	464	701	528
2020	628	567	486	459	623	528

4.3 WEAP results

The results obtained for all the scenarios by WEAP modeling are shown in Figure 6 and Figure 7.

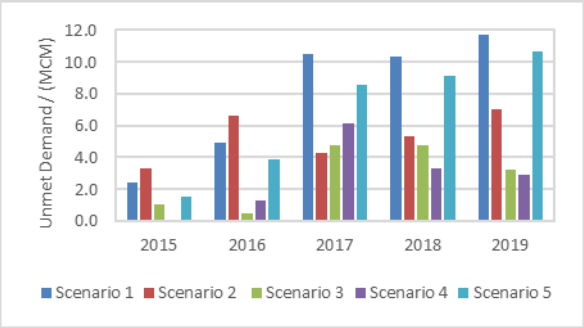

Figure 6: WEAP results for the Yala season

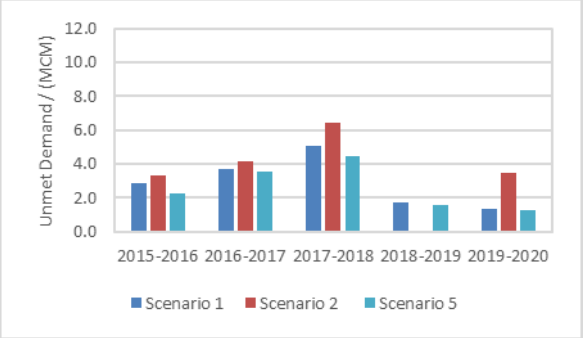

Figure 7: WEAP results for Maha season

The crop pattern of 70% paddy and 30% of OFCs were only introduced during the Yala season. Therefore, Scenario 3 and Scenario 4 were not considered for the Maha season.

5. Conclusions

From the results obtained in the Yala season by providing 70% of paddy and 30% of OFCs, the unmet demands have reduced by 64.2%.

By advancing the sowing date by 2 weeks in the BAU Scenario, the unmet demands have been reduced by 33.5% in the Yala season.

By advancing the sowing date by 2 weeks in the BAU Scenario, the unmet demands have increased by 18% in the Maha season. Therefore, advancing the sowing date by 2 weeks in the Maha season does not improve the operational pattern.

In Scenario 4, the reduction in unmet demands compared to the BAU Scenario is 66%. Therefore, by introducing 70% paddy and 30% OFCs and by advancing the sowing date by 2 weeks in the Yala season, the operational pattern has improved.

In Scenario 5, by increasing the Minipe anicut discharge by 15%, the unmet demands have been reduced by 15% in the Yala season and 11% in the Maha season.

References

Choudhari, K., Panigrahi, B. and Paul, J.C. 2014. Simulation of rainfall-runoff process using HEC-HMS model for Balijore Nala watershed, Odisha, India. International Journal of Geomatics and Geosciences, 5(2), p.253.

Kirshanth, L. and Sivakumar, S.S. 2018. Optimization of Water Resources in the Northern Province River Basins for Irrigation Schemes Used for Food Production in Sri Lanka. International Journal of Scientific & Engineering Research, Vol 9, Issue 7.

Kumari, B.A.P., Thiruchelvam, S., Dissanayake, K.M.H. and Lasantha, T. 2010. Crop diversification and income inequality in irrigation systems: The case of Minipe. Tropical Agricultural Research Vol. 21(3).

Shah, I.L., Suryanarayana, T.M.V. and Parekh, F.P. 2016. Estimation of Crop Water Requirement and Irrigation Scheduling using CROPWAT. ISH - Hydro International.

Sirimewan, D.C., Manjula, N.H.C., Samaraweera, A. and Mendis, A.P.K.D. 2019. Issues in sustainable water management of irrigation systems in Sri Lanka. 8th World Construction Symposium, Colombo, Sri Lanka.

Statistical Compendium on Natural Resources Management, Sri Lanka - 2000 - For Sustainable Development, published by the Planning Division, Ministry of Forestry & Environment, Sri Lanka in the year 2000.

Modeling Simulation of Electrochemical Cells for Water Treatment

Priyankara H.G.S.S.U., Rajapaksha T.R.E.A.H.D., Nanayakkara K.G.N.*

Department of Civil Engineering, University of Peradeniya, Sri Lanka

**nadeen@eng.pdn.ac.lk*

Keywords: Electrochemical oxidation, Electrocoagulation, Reaction Modeling, Optimization

1. Introduction

Electrochemical technologies are a promising alternative for the treatment of water and wastewater containing various types of pollutants. There are different electrochemical treatment methods that are used for water treatment to introduce new economically efficient solutions to water and wastewater treatment challenges. To evaluate the performance of electrochemical methods, reactor behaviour can be studied by varying physical parameters and operating conditions of the electrochemical reactors. Most of the literature are based on experimental studies to evaluate the reactor behaviour. Although computational modeling is an effective method for better understanding of reactors, scaling up of reactors, etc. it is lacking in literature. Therefore, this study focuses on developing computational models to understand the reaction behaviour of disinfection of *E. coli* and *E. faecalis* in ballast water using Electrochemical Oxidation (EO) and to optimize the reactor parameters used for simultaneous removal of Oil & Grease (O&G) and Chemical Oxygen Demand (COD) in service station wastewater using combined Electrocoagulation (EC) and Electrochemical Oxidation process.

2. Literature review

EC is a process that consists of creating a floc of metallic hydroxides within the effluent to be purified by electro-dissolution of soluble anodes (Pouet et al., 1995). EO is a very powerful method for breaking up even the most resistant organic compounds. EO can take place through two different mechanisms, i.e., direct oxidation and indirect oxidation (Anglada et al. 2009). Various parameters influence the efficiency of the electrochemical treatment process in removing pollutants from water and wastewater. The overall performance of treatment efficiency mainly depends on electrode material, design of electrodes, design of reactor, operating conditions, etc. (Anglada et al., 2009; Muddemann et al., 2019; Sillanpää et al., 2015). Many studies have been conducted in the past to evaluate the impact of the above-mentioned factors on pollutant removal efficiency and they have obtained the optimal conditions for the treatment process for the removal of relevant pollutants. Nanayakkara et al., (2012) designed, fabricated, optimized, and tested electrochemical disinfection reactor in laboratory and pilot scales to treat ballast water. Many experimental studies have done to study the hydrodynamic and reaction behaviour and to optimize the operating parameters of electrochemical reactors. But the use of the modeling approach for these studies is still under its initial stage in the research society. Monteil et al., (2020) carried experimental studies for the mineralization of Hydrochlorothiazide (HCT) using electrochemical advanced oxidation process. Based on the experimental results, a model for the mineralization of HCT solution was developed and simulated combining the mineralization kinetics with the hydrodynamics.

3. Methodology

Data sets to study the reaction behaviour were selected from a Ph.D. thesis for treatment of ballast water using electrochemical disinfection technology (Nanayakkara et al., 2010). The selected data sets were based on the disinfection efficiency of two major organisms: Escherichia coli (E. coli) and Enterococcus faecalis (E. faecalis) under different initial concentrations of bacteria using a lab scale reactor (Volume = 1.2 L, Length = 30 cm, Rectangular shaped) and a pilot scale reactor (with linear scaling factor of 80, compared to the laboratory scale reactor).

Data sets for the optimization study were selected from experimental research done previously by our research group on simultaneous removal of O&G and COD from service station wastewater. The experiments were conducted varying two major reactor cell parameters, current density, and duration of

electrolysis, for both O&G and COD removal studies. Related experimental data was used to optimize the two reactor parameters in order to achieve maximum removal efficiencies.

3.1 Reaction modeling study

Disinfection kinetics of microorganisms were developed considering the mass balance of the reactor. For the disinfection of *E. coli*, the reactor was considered to as a plug flow reactor and for the disinfection of *E. faecalis*, the reactor was considered to as a batch reactor. The reaction rate for the disinfection of microorganisms can be derived by,

$$r_A = - k\, C_A \cdot C_B^m \quad \text{.....(1)}$$

Where, C_A, C_B, and k are concentration of microorganisms, concentration of total chlorine without microorganisms in the electrolyte and reaction rate constant respectively.

The constant m was assumed to equal 1 due to pseudo first order kinetics for both lab scale and pilot scale reactors for both *E. coli* and *E. faecalis*. Based on the derived reaction rate equation, models for disinfection of microorganisms were developed under different initial bacterial concentrations for both lab scale and pilot scale reactors using Aquasim software (Version 2.1g). The values of k were estimated from the parameter estimation function and the final concentration profiles were obtained by performing simulations.

3.2 Optimization study

The experiment design was obtained from Minitab 19 software (central composite design). Based on the experimentally specified limits, the level of factors for optimization of reactor cell were obtained. According to the experimental results, model equations were developed for the removal efficiencies from the Minitab software and the optimum current density and electrolysis duration for the maximum removal of O&G and COD were obtained separately from the Python 3.11 software. The parameter optimization was done based on the Nelder-Mead method in Python software.

4. Results and discussion

4.1 Reaction modeling study

All the modelled concentration profiles for both *E. coli* and *E. faecalis* are well fitted with the experimental concentrations. At the initial stages of experiments, there are slight deviations between the modelled and experimental findings. Uncertainties of collecting samples at close time intervals and the assumptions made in developing the models may be the reasons for those variations. All the concentration profiles follow the same trend for the lab scale reactor for both *E. coli* and *E. faecalis*. For an example, figure 1 shows the final concentration profile of *E. coli* for the initial concentration of 10^5 CFU/mL.

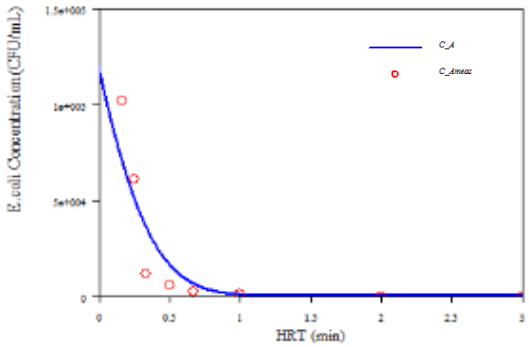

Figure 1: Final concentration profile of *E. coli* for 10^5 CFU/mL initial concentration

The modelled concentration profile of the pilot scale reactor for both *E. coli* and *E. faecalis* are not properly generated at the initial stage. For example, figure 2 shows the final concentration profile of *E. coli* for pilot scale reactor. Lack of data points within the initial stage and the effects due to the scaling up of the reactor can be suggested as the reasons for that observation.

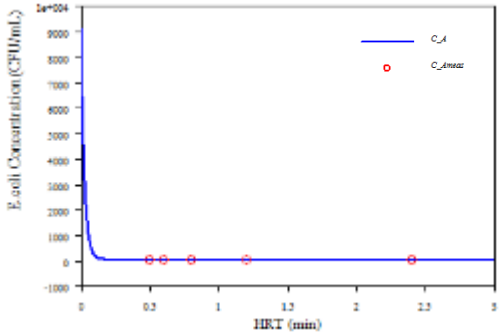

Figure 2: Final concentration profile of *E. coli* for pilot scale reactor (Initial concentration 9100 CFU/mL)

Kinetics of disinfection can be described using the reaction rate constants (k values). When the initial concentration increases, the value of k reduces for the lab scale reactor. The reasons can be the higher consumption of oxidants if the initial concentration of bacteria is high. It is clear that, the produced chlorine is consumed by

microorganisms and thus the demand for chlorine increased at higher initial concentrations. Therefore, a reduction in rate can be expected at higher initial concentrations. This result suggests that the initial concentration has a significant influence on the kinetics of inactivation. Table 1 and table 2 show the values of k for *E. coli* and *E. faecalis* respectively.

Table 8: Values of k for *E. coli*

Initial Concentration (CFU/mL)	**k (1/min).(L/mg)**
10^4 (Lab Scale)	24.6782
10^5 (Lab Scale)	8.4101
10^6 (Lab Scale)	2.4082
9100 (Pilot Scale)	23.9392

Table 9: Values of k for *E. faecalis*

Initial Concentration (CFU/100mL)	**k (1/h).(L/mg)**
810 (Lab Scale)	1.7161
910 (Lab Scale)	1.2798
2200 (Lab Scale)	0.3497
23000 (Pilot Scale)	32.0690

The values of k for pilot scale reactor are not following the trend of the lab scale reactor for both *E. coli* and *E. faecalis*. Scale up effect can be identified as the reason for that deviation. The influence of mass transport coefficient is prominent in scaling up of electrochemical reactors. The pilot scale reactor was linearly scaled up to 80 times of the lab scale reactor. Therefore, reduction of mass transport is expected at the pilot scale reactor.

4.2 Optimization study

The relationship between the efficiency of removing pollutants (O&G and COD) and electrolysis conditions obtained from the Minitab software. According to those mathematical relationships, the developed contour plots for O&G and COD are shown in figure 3 and figure 4, respectively.

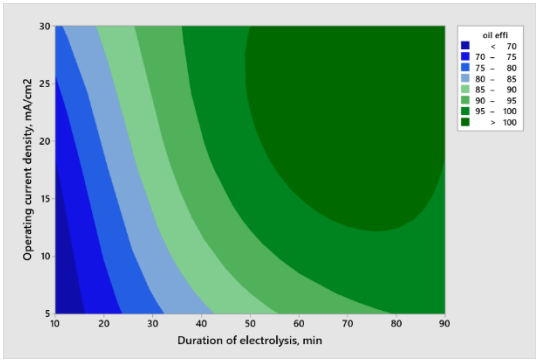

Figure 3: Contour plot for O&G removal efficiency vs. electrolysis duration and current density

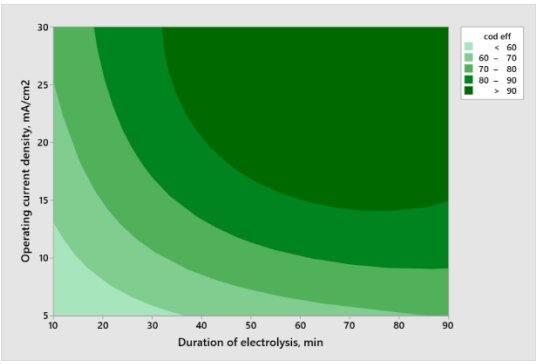

Figure 4: Contour plot for COD removal efficiency vs. electrolysis duration and current density

Concerning the obtained results from Python software, optimum current density and electrolysis duration are 29.598 mA/cm² and 70.111 min for the optimum removal of O&G through electrocoagulation process (removal efficiency of 100%). Similarly, the optimum current density and electrolysis duration are obtained as 28.167 mA/cm² and 74.150 min for the optimum removal of COD through electrocoagulation process (removal efficiency of 99.99%).

5. Conclusions

For development of reaction models, the Aquasim software has been used as the computational tool. Models were created for different initial concentrations of *E. coli* and *E. faecalis* for both lab scale reactor and pilot scale reactor. The reaction rate constants and final concentration profiles of microorganisms were obtained performing simulations. The modelled final concentration profiles followed the experimental findings. The reaction rate constants were reduced at higher initial concentrations for both *E. coli* and *E. faecalis* in

the lab scale reactor. The reaction rate constant of pilot scale reactor did not follow the trend indicating the scale up effect.

For the optimization study, Minitab 19 software was used to obtain the model equation for the removal efficiency of O&G and COD. Based on the obtained model equations, the optimum reactor parameters (Electrolysis duration and Current density) to achieve maximum removal efficiencies were found using Python 3.11 software. The optimized operating current density and duration were 29.598 mA/cm^2 and 70.111 min, respectively for the maximum removal of O&G through electrocoagulation. Similarly, the optimum current density and electrolysis duration were obtained as 28.167 mA/cm^2 and 74.150 min for the maximum removal of COD through electrochemical oxidation.

References

Anglada, Á., Urtiaga, A. and Ortiz, I. 2009, Contributions of electrochemical oxidation to waste-water treatment: fundamentals and review of applications. Journal of Chemical Technology and Biotechnology, 84: pp. 1747-1755

Monteil, H., Pechaud, Y., Oturan, N., Trellu, C. and Oturan, M., 2021. Pilot scale continuous reactor for water treatment by electrochemical advanced oxidation processes: Development of a new hydrodynamic/reactive combined model. Chemical Engineering Journal, 404, p.127048

Muddemann, T., Haupt, D., Sievers, M. and Kunz, U., 2019. Electrochemical Reactors for Wastewater Treatment. ChemBioEng Reviews, 6(5), pp.142-156.

Nanayakkara, K.G.N., Khorshed Alam, A., Zheng, Y. and Paul Chen, J., 2012. A low-energy intensive electrochemical system for the eradication of Escherichia coli from ballast water: Process development, disinfection chemistry, and kinetics modeling. Marine Pollution Bulletin, 64(6), pp.1238-1245.

Pouet, M. F., Grasmick, A. 1995, Urban wastewater treatment by electrocoagulation and flotation. (1995). Water Science and Technology, 31(3-4).

Sillanpää, M. 2015. Natural Organic Matter in Water Characterization and Treatment Methods. 1st ed. Waltham: IWA Publishing

Variability and Rainfall Trend Analysis in Urbanized Areas of Kandy District

De Silva P.R.T., Mendis E.M.T., Nanayakkara K.G.N.*

Department of Civil Engineering, University of Peradeniya, Sri Lanka

**nadeen@eng.pdn.ac.lk*

Keywords: Temporal rainfall variability, Rainfall trend, Coefficient of variation, Precipitation concentration index, Mann-Kendall test, Innovative trend analysis test

1. Introduction

Variability and rainfall trend analysis provides essential information for better water resource planning and management and for the development projects in urbanized areas. Literature reviews suggested limited variability, and trend studies were conducted in the Kandy district, providing necessary information for development projects. Therefore, the proposed research investigates the temporal rainfall variability and trend in the urbanized areas of Kandy district, using daily rainfall datasets of five rain gauge stations. Both annual and seasonal time scales were considered to get a more comprehensive understanding of temporal variation.

2. Literature review

Variability and trend of rainfall are regarded as the most significant aspect of the monsoon climate in Sri Lanka (Meegahakotuwa and Nianthi, 2018). Past studies identified four seasons (Nisansala et al., 2019) such as the Northeast Monsoon (NEM) from December to February, the South-West Monsoon (SWM) from May to September, the First Inter Monsoon (FIM) from March to April, and Second Inter-Monsoon (SIM) from October to November based on rainfall variations in Sri Lanka. Rainfall analysis provides essential information to decision-makers in areas such as water resource planning and management, development, disaster preparedness, and policy planning (Alahacoon and Edirisinghe, 2021).

2.1 Variability of rainfall

Variability of rainfall means the degree to which rainfall amounts vary through time. Variability analysis involves the use of Coefficient of Variation (CV), Precipitation Concentration Index (PCI). (Asfaw *et al.*,2018 and Rasel *et al.*,2016)

$$CV = \frac{\sigma}{\mu} * 100 \quad \text{.....(1)}$$

$$PCI_{annual} = \frac{\sum_{i=1}^{12} P_i^2}{\left(\sum_{i=1}^{12} P_i\right)^2} * 100 \quad \text{.....(2)}$$

$$PCI_{seasonal} = \frac{\sum_{i=1}^{12} P_i^2}{\left(\sum_{i=1}^{n} P_i\right)^2} * x * 100 \text{.....(3)}$$

Where x- seasonal months as a percentage of 12 months

2.2 Rainfall trend analysis method

Choosing the right statistical and graphical approaches among the many available is critical for obtaining reliable trend results (Saini et al., 2020). The MK test is an important nonparametric test which has high accuracy, repeatability, and flexibility (Rathnayake, 2019; Shahid, 2010).

$$S = \sum_{i=1}^{n-1} \sum_{j=i+1}^{n} sgn(X_j - X_i) \quad \text{.....(4)}$$

$$sgn(X_j - X_i) = \begin{cases} +1, > (X_j - X_i) \\ 0, = (X_j - X_i) \\ -1, < (X_j - X_i) \end{cases} \quad \text{.....(5)}$$

$$Var(S) = \frac{n(n-1)(2n+5) - \sum_{i=1}^{m} t_i(i)(t_i(i)-1)(2i+5)}{18} \quad (6)$$

$$Zc = \begin{cases} \frac{S-1}{\sqrt{Var(S)}}, & S > 0, \\ 0 & S = 0, \\ \frac{S+1}{\sqrt{Var(S)}}, & S < 0, \end{cases} \quad \text{.....(7)}$$

A positive Zc value indicates an upward trend, whereas a negative Zc value indicates a downward trend (Asfaw *et al.*,2018).

Sen presented an innovative graphical method for identifying positive and negative trends in climate data. This method is simple and

straightforward (Perera *et al.*, 2022 and Rathnayake 2019).

3. Methodology

This study focuses on heavily urbanized areas of the Kandy district for various reasons, such as population distribution, ongoing and proposed mega projects, data availability and the possibility of purchasing. Then, five rain gauges were selected covering the heavily populated area as Katugastota (1952-2020), Gannoruwa (1976-2020), King's Pavillion (1991-2020), Kundasale (1991-2020), and Hantana (2003-2020). Data were collected from Department of Meteorology and Mid Country Tea Research Institute, Hantana.

Missing rainfall data within a selected period was filled using Simple Arithmetic Mean (SAM) method. Seasonal and annual temporal variation were only represented graphically. Temporal variability of rainfall was carried out using Coefficient of Variation (CV) and Precipitation Concentration Index (PCI).
Seasonal and annual trend analysis were conducted using the MK test and the ITA test, which are widely used methods. Moreover, from the comparison of the trend methodologies, different trends results (increasing, decreasing, or trendless time series) have been identified.

4. Results and discussion

4.1 Variation of annual and seasonal rainfall

Table 1 shows the obtained average annual rainfall of five stations.

Table 1: Average annual rainfall

Station	Average Annual Rainfall (mm)
Katugastota	1868.6
Gannoruwa	1820.3
King's Pavillion	1991.0
Kundasale	1258.3
Hantana	1914.1

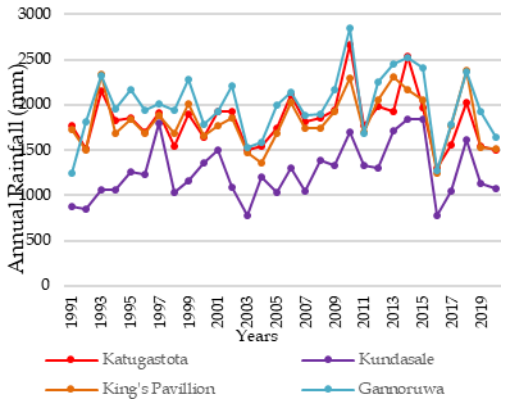

Figure 1: Annual rainfall variation

Figure 1 clearly shows the station vice temporal variation of the rainfall. Averagely all of these annual rainfalls show similar patterns with drops and rises. However, Kundasale had less annual rainfall compared to the other three stations while the other three stations had approximately the same annual rainfall for the period 1991-2020.

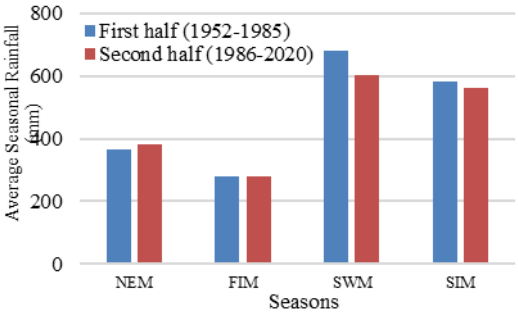

Figure 2: Average seasonal rainfall of Katugastota station for first half and second half of period (1952-2020)

The average seasonal rainfall of the period's first and second halves have some differences for the same station. Figure 2 shows rainfall changes obtained for two halves in Katugastota station.

4.2 Variability of rainfall

As shown in Table 2, the CV values for various time scales in all five stations generally show irregularity. Moreover, the analysis results indicate that PCI values are between 8-16 for all five stations.

Table 2: Statistical parameters of rainfall variability

Station	Series	CV (%)	PCI
Katugastota	Annual	Less	Moderate
	NEM	High	Moderate
	FIM	High	Moderate
	SWM	Moderate	Moderate
	SIM	High	Low
Gannoruwa	Annual	Less	Moderate
	NEM	High	Moderate
	FIM	High	Moderate
	SWM	High	Moderate
	SIM	High	Low
King's Pavillion	Annual	Less	Moderate
	NEM	High	Moderate
	FIM	High	Moderate
	SWM	High	Moderate
	SIM	High	Low
Kundasale	Annual	Moderate	Moderate
	NEM	High	Moderate
	FIM	High	Moderate
	SWM	High	Moderate
	SIM	High	Low
Hantana	Annual	Moderate	High
	NEM	High	Moderate
	FIM	High	Moderate
	SWM	High	Moderate
	SIM	High	Low

.

4.3 Rainfall trend analysis

The Figure 3 shows, Katugastota station has no possible trends in rainfall for the annual rainfall.

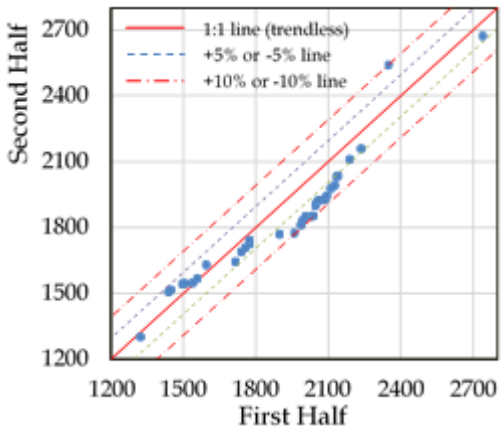

Figure 3: Results of ITA test of Katugastota station for annual time scale

According to Table 3, the negative and positive values of Z-statistics show downward and upward trends, respectively. Obtained annual and seasonal ITA test and MK test results for all other stations are presented in Table 4.

Table 3: Annual and seasonal Mann–Kendall results for Gannoruwa station

Time scale	Z	Interpretation
Annual	0.6750	Upward
NEM	1.0663	Upward
FIM	1.6532	Upward
SWM	-0.4011	Downward
SIM	-1.0858	Downward

As shown in Table 4, 80% match can be seen in Kundasale and Hantana. In Katugastota, Gannoruwa and King's Pavilion stations, some of time scale shows the incomparable trend results from the two methods.

Table 4: Summary of the comparison of MK test and ITA test

Station	Time Scale	MK test	ITA test
Katugastota	Annual	Downward	No Trend
	NEM	Downward	No Trend
	FIM	Downward	Downward
	SWM	Downward	Downward
	SIM	Downward	No Trend
Gannoruwa	Annual	Upward	No Trend
	NEM	Upward	Upward
	FIM	Upward	Upward
	SWM	Downward	No Trend
	SIM	Downward	Downward
King's Pavollion	Annual	Upward	Upward
	NEM	Downward	Upward
	FIM	Upward	Upward
	SWM	Downward	No Trend
	SIM	Upward	No Trend
Kundasale	Annual	Upward	Upward
	NEM	No Trend	Upward
	FIM	Upward	Upward
	SWM	Upward	Upward
	SIM	Upward	Upward
Hantana	Annual	Upward	Upward
	NEM	Downward	Downward
	FIM	Downward	Downward
	SWM	Upward	Upward
	SIM	Upward	Upward

5. Conclusions

When considering rainfall variability, annual rainfall shows less rainfall variability according to the obtained CV values for Katugastota, Gannoruwa and King's Pavillion. In each station, SIM has low precipitation concentration while other three seasons and annual rainfall shows moderate concentration according to the obtained PCI results. Two tests in rainfall trend analysis, statistical trend analysis, and graphical trend analysis results produced for five stations show that both tests produce comparable results for some seasons and contrasting trends for

other seasons. According to findings from a long-term trend analysis in the Gannoruwa station using two methods, the NEM and SIM seasons exhibit an upward trend and downward trend respectively in both, while the other two seasons and annual rainfall exhibit different trends in the two methods. According to findings from a long-term trend analysis in Gannoruwa station using two methods, the NEM and SIM seasons exhibit an upward trend and downward trend respectively in both, while the other two seasons and annual rainfall exhibit different trends in the two methods. In conclusion, Hantana and Kundasale have 80% and King's Pavillion have 40% comparable results in trend analysis. ITA test does not provide any numerical value of the trend. Therefore, if the trend is quantitatively important, at least a statistical trend analysis has to be carried out. This research develops a full picture of the recent rainfall over the urbanized area in Kandy district in both seasonal and annual distribution, which is important for planning and management of natural resources and development projects, hence, for future adaptation.

References

Alahacoon, N. and Edirisinghe, M., 2021. Spatial Variability of Rainfall Trends in Sri Lanka from 1989 to 2019 as an Indication of Climate Change. ISPRS International Journal of Geo-Information, 10(2), p.84.

Asfaw, A., Simane, B., Hassen, A. and Bantider, A., 2018. Variability and time series trend analysis of rainfall and temperature in northcentral Ethiopia: A case study in Woleka sub-basin. Weather and Climate Extremes, 19, pp.29-41.

Perera, A., Ranasinghe, T., Gunathilake, M. and Rathnayake, U., 2020. Comparison of Different Analyzing Techniques in Identifying Rainfall Trends for Colombo, Sri Lanka. Advances in Meteorology, 2020, pp.1-10.

Rasel, A.H., Islam, M. and Keramat, M., 2016. Analysis of annual and seasonal precipitation concentration index of north-western region of Bangladesh. In International conference on computer, communication, chemical, materials and electronic engineering (pp. 107-110).

Rathnayake, U., 2019. Comparison of Statistical Methods to Graphical Methods in Rainfall Trend Analysis: Case Studies from Tropical Catchments. Advances in Meteorology, (2019), pp.1-10.

Saini, A., Sahu, N., Kumar, P., Nayak, S., Duan, W., Avtar, R. and Behera, S., 2020. Advanced Rainfall Trend Analysis of 117 Years over West Coast Plain and Hill Agro-Climatic Region of India. Atmosphere, 11(11), p.1225.

Shahid, S., 2010. Rainfall variability and the trends of wet and dry periods in Bangladesh. International Journal of climatology, 30(15), pp.2299-2313.

Modeling of Pressure & Water Quality Variation in a Pipe Distribution Network

Chandrathilaka T.R.S.J., Jayawickrama R.M.C.D., Gunawardana W.C.T.K.*

Department of Civil Engineering, University of Peradeniya, Sri Lanka

**chandimag@pdn.ac.lk*

Keywords: Water quality modeling, Hydraulic modeling, EPAnet, Residual Chlorine, Turbidity

1. Introduction

Pressure deficiencies resulting from pipe leaks and bursts, deterioration of aging water pipes and elevation variations in a network is currently a main challenge in the operation of water distribution networks (WDNs). Water Quality is also important in WDNs. Mostafa (2013) says in his studies that, the loss of disinfection residual highly increases the risk of microbial contamination. So, it is critical to identify regions with low chlorine levels. Also, the turbidity is a measure of the cloudiness or haziness of a fluid caused by the presence of suspended particles can pose a health risk to consumers.

This research is based on the modeling and identification of pressure related and water quality parameter (residual chlorine level and turbidity) related issues in a WDN in Eriyagama area. EPANET computer software is uses to model and simulate the pressure and water quality parameter variation of Eriyagama WDN. So, the outcome of this research can be used to identify the pressure issues and water quality issues and possible to take remedial measures for those issues for relevant parties.

2. Literature review

There are many studies available regarding the hydraulic and water quality modeling. Alsaydalani (2019) have performed a study on extended-period simulations of hydraulic and water quality behaviour in WDNs using EPANET. The water flow in each pipe, the head at each node, and the water level in each tank are all tracked by EPANET. During a simulation period, it has been used to simulate the concentration of a chemical species and water age. Rossman (2000), in his study used a time Pattern to analyse an extended period of operation, which will cause demand at the nodes to vary periodically over a day. Also, water bills have been used to compute the water demand allocation to each node (junction) in the networks.

For the Kaliwates Sub-District, Widiarti et. Al., (2021) conducted research based on water quality modeling for the drinking water distribution network utilizing EPANET 2.0. The results of the modeling were obtained and compared to observed values. The pressure calibration values from the simulation results are compared to the pressure values from on-the-field observations with a correlation value of 0.928. According to the pressure calibration results, there is a high link between the simulation and on-the-field data, with a correlation value of 0.8-1.

Trussell (1998) says in his studies that, the major goal of maintaining a disinfectant residual is to maintain water quality throughout transit by avoiding pathogen regrowth as well as the inactivation of pathogens that may subsequently be introduced into the system. To model chemical species in a pipeline, EPANET requires reaction rate equations and decay or growth rate factors. Two processes are reported to be responsible for chlorine degradation. In distribution pipes, this is recognized as bulk decay and wall decay (Zin, 2021). Alsaydalani (2019) has conducted modeling research. The study says that the bulk decay and wall decay coefficients for chlorine can vary significantly, with the bulk decay coefficient varying with water quality and the wall decay coefficient varying with pipe material and condition. As a result, the pipe wall coefficient (Kw) can be connected to the pipe's age and material. The values for bulk fluid (Kb) and pipe walls (Kw) were estimated to be -0.1008 m/day and -0.20 m/day, respectively, based on previous research. Mostafa et al. (2013) assess the viability of using EPANET 2.0 as a measuring and controlling tool to estimate and predict chlorine concentration at various water network points by looking into how well it can simulate residual

chlorine decay through water networks while taking water-age analyses into account

3. Methodology

3.1 Site selection and data collection

For this study, the Eriyagama water distribution network in Kandy district was selected because, the pressure variation is high in that network as the area consist of different ground elevations. Basic EPANET model for Eriyagama water distribution network was taken from National Water Supply and Drainage Board (NWDB). The primary source of data for developing and upgrading the model in this study was the NWDB. The network details, water demands, were given by NWSDB. Also, field measurements of pressure and flow data, and measured water quality data were used for modeling.

3.2 Measurement for demand pattern

The demand pattern variation for extended period simulation was obtained using flow measurements using a bulk meter in the network at the inlet point (Uda-Eriyagama) for 24 hours. Then the demand multiplier values were obtained using those results.

3.3 Calibration of hydraulic model

Initially the field measurements of pressure and flow of the network were taken for hydraulic model calibration. Three manhole locations with fixed bulk meters in the network were selected for taking field measurements of pressure and flows. The flow measurements were taken using bulk meter readings and used to calculate the flow value for a particular time.

To calibrate the model, the EPANET 2.2 model of the network was converted and transferred to WaterGEM, and then used the WaterGEM's in built Darwin calibrator option to calibrate the model. In the calibration process, the Base demand values and the roughness coefficients were tuned. The pipe roughness coefficient was adjusted for values between 1-1.5 times the original value. The demands were adjusted between 0.8-1.4 times their original values and model was calibrated for best fit roughness coefficient and demands.

3.4 Identification of low- and high-pressure issue locations

The model was used to identify the low-pressure zones for current population. For further check and verification of low-pressure issues, a field survey was carried out. From model results, supply nodes below 20 psi (14.06 mH2O) pressure were considered survey to identify more possible low-pressure points in the network. Figure 1 shows the low pressures areas in blue colour.

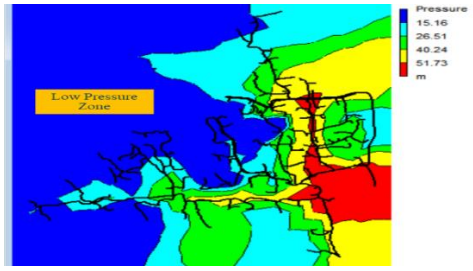

Figure 1: Contour plot of pressure

Modeling for demand in 2040 was done. Predicted future demand data of the Eriyagama network were used for nodal demand adjustments for year of 2040. All the current nodal base demands were multiplied by a factor of 1.11 to represent the year 2040. Then the model was run and nodal pressure below 20 psi were obtained.

Model was used to identify the high-pressure zones for current population. Supply nodes above 80 psi (56.25 mH2O) pressure were considered for survey to identify more possible High-pressure points in the network.

3.5 Water quality modeling

Initially for water quality modeling the calibrated EPANET model was used. The Model calibration was done using measured Residual Chlorine levels in different locations of the network. Those data were obtained from Sarasavi Uyana laboratory of NWSDB. Using the above data the model was calibrated. In the calibration process the Bulk reaction coefficient and the wall reaction coefficient were adjusted. The appropriate values for those coefficients to match measured values and model results are 0.2 mg/day and 0.18 mg/m^2/day respectively. Using the rest of data available from the water board, the model validation was done.

A field sampling and testing was carried out to identify the residual chlorine of the real network and to identify weather the test results tally with model out puts. Initially the identification of appropriate locations for water sample collection was done. For that, the EPANET model was run for residual chlorine variation and identified the nodes with chlorine

concentrations below 0.2 mg/l. Field sampling locations were identified using the above modeling results and the field samples were collected from housing connections in those places.

3.6 Field sampling and testing

The water samples were collected from sampling location and transported immediately. Then the Residual chlorine tests was done within less than one hour from collection. DPD (Diethyl Paraphenylene Diamine) colorimetric test kit were used for Chlorine test. Using Nephelometry the field samples were tested for turbidity.

3.7 Identification of pressure issues

The model was run to identify the low-pressure zones for current population and using those low-pressure areas, a field survey was carried out for further verification of adequate pressure to users. The supply nodes below 20psi (14.06 mmH2O) pressure were considered for survey. With future increased demands the pressures may be reduced. The remaining design life of the network of 20 years were considered. To simulate that mater, the model was run to simulate pressure variations in 2040, increasing the demand at each node and nodal pressure results were obtained. All the current nodal base demands were multiplied by a factor of 1.11 to represent the year 2040.This 1.11 value was defined based on population growth rate and new water supply connection trends.

Also the model was used to identify the high-pressure zones for current population. Supply nodes above 80 psi (56.25 mH2O) pressure were considered as high-pressure points in the network.

4. Results and discussion

4.1 Demand pattern

The demand multiplier values were obtained by dividing each flow rate by the average hourly flow rate. The obtained demand pattern is shown in Figure 2.

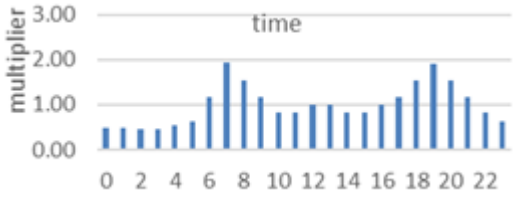

Figure 2: Demand pattern variation

4.2 Hydraulic calibration results

The overall fitness of the calibrated data is 0.877. The comparison of the fitness of the model result and measured values of pressure calibration can be seen in Figure 3.

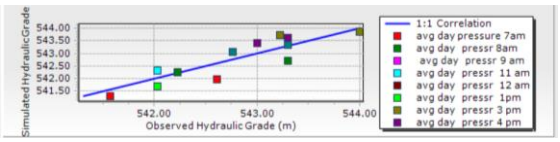

Figure 3: correlation between model result and measured values of pressure

4.3 Results for pressure issues

The model results of nodal pressures showed that the customers are having enough pressure at most of the time of the day. According to the field survey results, the water users of low-pressure zones were getting adequate pressure according to their opinion.

The model results of pressure were obtained for increased demand in the year of 2040. The nodal pressures at 7.00 A.M. (a demand peak) after the demand adjustments for future demand scenarios, the number of nodes below 20psi has increased to 55 nodes from 43 nodes with the increased demands in the year 2040 as shown in Figure 4.

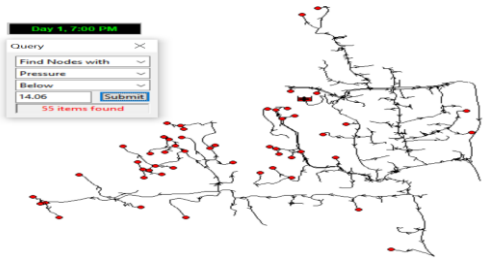

Figure 4: Pressure values for year 2040

But still, the pressure is adequate. No of nodes with zero pressure are about 10 at peak demand periods, even for the predicted future demand scenarios. That indicates the network has adequate pressure to get the required demand for almost all consumer units.

4.4 Residual Chlorine test results

Nodes below 0.2 mg/l of residual chlorine shown in Figure 5. The Chlorine test results of samples collected from selected sampling locations also showed that the chlorine levels are below 0.2 mg/l. Therefore, it can be seen that both the real network water quality and model run results shows inadequate chlorine levels at far ends.

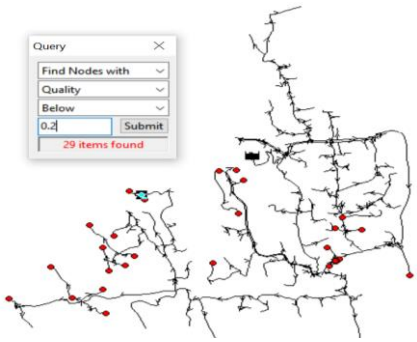

Figure 5: Nodes below 0.2 mg/l of residual chlorine

The lower concentrations of residual chlorine can be seen at the far ends of the distribution network. Currently NWSDB taking samples for water quality testing at random locations. Even though the test results show good chlorine concentrations at those locations, at the far ends the values are lower. The low chlorine concentration was critical at far ends, as seen both in the model and the field test results. So, it is recommended to follow a routine chlorine sampling at identified critical locations rather than currently measuring locations.

4.5 Turbidity measurement results

The modal turbidity simulation results showed that all the nodes are below the acceptable turbidity limit (2NTU). But the turbidity values of some of the field samples were with higher turbidity values. There may be lots of reasons for this increased turbidity values. The possible leakages through pipes and washing out of sediment partials at peak flows may be cause for turbidity issues. Further studies must be done regarding this matter.

5. Conclusions

According to model results of nodal pressures of extended period simulation, almost all the customers are having enough pressure at most of the time of the day. Even according to the field survey the customers are satisfied with the available pressure. With the increased future (2040) demands the water pressure at critical locations may further reduced. But it considerably with a lesser effect. So, the existing network can withstand expected future demands with minor improvements. Most of nodes areas consist of higher pressures which are higher than recommended pressure values.
Even though the NWSDB measured results show good chlorine concentrations at currently measuring locations, the chlorine concentration at the far ends are lower according to both in the model and the field test results. So, it is recommended to follow a routine chlorine sampling at identified critical locations rather than currently measuring locations. In most of the locations the turbidity level is acceptable. But according to the field sample tests Turbidity is higher than 2 NTU at some locations. Higher turbidity was associated with places where with the high demand values/more connections causing low pressure and that causing the suction due to low pressure. Further studies are required for turbidity based on suction phenomenon.

References

Alsaydalani, M.O.A., 2019. Simulation of pressure head and chlorine decay in a water distribution network: a case study. The Open Civil Engineering Journal, 13(1).

Widiarti, W.Y., Wahyuni, S., Wiyono, R.U.A., Hidayah, E., Halik, G. and Sisinggih, D., 2020. Evaluation of pipe network distribution system using EPANET 2.0 - a case study of the city of Jember. In IOP Conference Series: Earth and Environmental Science, Vol. 437012043.

Mostafa, N.G., Matta, M.E. and Halim, H.A., 2013. Simulation of chlorine decay in water distribution networks using EPANET–case study. Simulation, 3(13), pp.100-116.

Zin, N.N., Kazama, S., Takizawa, S., 2021. Network Model Analysis of Residual Chlorine to Reduce Disinfection Byproducts in Water Supply Systems in Yangon City, Myanmar. Water, 13, 2921.

Rossman, L.A., 2000. EPANET 2: user's manual

Trussell, R. R., 1998. An overview of disinfectant residuals in drinking water distribution systems. Wat. Suppl. 16(3/4), 1–15.

Machell, J., 2004. Water quality modeling in distribution networks, Doctoral dissertation, University of Sheffield, England

Modeling Storm Water Management Systems in Response to Different Rainfall and Land Use Patterns

Pramudika W.O.H., Ubhayaratna K.M.M., Gunawardana W.C.T.K.*

Department of Civil Engineering, University of Peradeniya, Sri Lanka

**chandimag@pdn.ac.lk*

Keywords: Storm water model, SWMM; Best Management Practices (BMPs), Urbanization, Urban runoff, Scenarios, Simulation

1. Introduction

The research project was focused on storm water management in urban areas to reduce the negative impacts of storm water runoff due to land development and rapid urbanization (Pathirana *et al,* 2020). The study was carried out in the Mulgampola sub-catchment of Kandy in Sri Lanka, which had been experiencing frequent flash floods for many years due to high-intensity rainfalls. The project aimed to identify suitable storm water management alternatives using Best Management Practices (BMPs) to reduce water quantity issues for urban areas (Hunt *et al,* 2009).

Figure 1: Study area

The objectives of the research were included identifying suitable storm water management options for the catchment to reduce the quantity of the storm water, developing hydraulic modeling for the selected catchment using SWMM software, and modeling the variation of runoff volume during different rainfall intensities. The study was covered both storm water runoff quantity, focusing on short-duration high-intensity rainfall events considering 6-hour rainfall with 30 min intervals and baseline return period is 10 years for quantity.

The research was analysed factors affecting surface runoff such as slope of the land, rainfall patterns, land use patterns, existing drainage infrastructure, destination of the storm water, available land area for placement of the storm water management systems (Harshani and Wijesekera, 2011). The study was also considered infiltration capacity of surfaces as it indirectly affects surface runoff.

2. Literature review

2.1 Storm water best management practices

This literature review focuses on the use of best management practices (BMPs) to mitigate the negative effects of storm water runoff in urban areas. The review highlights the need for BMPs to improve the ecological integrity of rivers and streams, reduce flooding and flash flooding, reduce sediment transport, and mitigate erosion (Khaniya *et al,* 2016). The review identifies several BMPs including green roofs, bio-retention cells, permeable pavements, rain barrels and cisterns, and vegetative swales. These BMPs use structural measures such as wetlands, ponds, swales, soak ways, infiltration trenches, roof storage systems, infiltration basins, bio-retention basins, vegetated filter strips, filter strips, and pervious pavements (Rossman, 2017). The review concludes that BMPs offer extensive environmental and societal benefits over conventional strategies, including improved air quality, CO2 sequestration, and thermal benefits from the reduction of the urban heat island effect, as well as benefits to society such as improved citizen health and aesthetic benefits (James *et al,* 2016).

2.2 SWMM for BMPs

The Storm Water Management Model (SWMM) is a rainfall-runoff model used to simulate the quantity and quality of runoff from urban areas. It can simulate different types of stormwater drainage systems and natural catchments. SWMM has been upgraded to include BMPs, which are represented by eight different types of sub-catchments (Rossman, 2010). SWMM uses a distributed discrete time model to simulate

runoff generated from each sub-catchment during a simulation period, using physical catchment characteristics, climate, land use, soil properties, and water quality as input parameters (Sha, 2017). SWMM's LID controls are represented by a combination of vertical layers with different properties.

3. Methodology

3.1 Study area

This research report focuses on the storm water-related quantity issues in the rapidly growing city of Kandy, Sri Lanka. The study area is located in the Mulgampola region, which is part of the Meda Ela catchment that discharges storm water into the Mahaweli River. The area experiences frequent flash floods due to land use changes induced by rapid urbanization, unauthorized construction, expansion of urban impervious area, and geographic and geologic characteristics of the region.

3.2 Data and data collection

Overall, this report provides a comprehensive overview of the data collection and analysis process for the SWMM modeling study of the Kandy area. The Table 3.1 shows the various SWMM parameters and data input origins.

Table 1: SWMM parameters and relevant data extractions

Type	SWMM Parameters	Data Sets
Sub-catchment	Spatial Location, Sub-catchment area, Average slope, Percentage of impervious area	Kandy 5418 GIS data set, 5m×5m resolution DEM, Google Earth's high-resolution satellite imagery, CAD survey Map
Conduit	Spatial Location, Cross section dimensions, Length	Kandy 5418 GIS data set, CAD survey Map, Field Survey data
Junctions	Spatial Location, Invert level elevations,	Kandy 5418 GIS data set, CAD survey Map, Field Survey data
Storm Water Outlet	Spatial Location, Invert level elevations,	Kandy 5418 GIS data set, CAD survey Map, Field Survey data
Rainfall	Time series data for precipitation	IDF curve data for Kandy Katugasthota 2019

3.3 SWMM model development

The Storm-water Management Model (SWMM) is a computer model used to simulate the movement of water through a watershed. It is a widely used hydrological model that can simulate the impact of various factors such as land use changes, urbanization, and the effectiveness of BMPs on reducing runoff.

In SWMM, a watershed is divided into sub-catchments which are areas of land that share similar characteristics such as slope, soil type, and land use. The mountain topography model was combined with the watershed and sub watershed data and transportation networks data produce the 19 sub catchment areas. Each sub-catchment is further divided into smaller units, including conduits, junctions, and outlets. The model uses information on these components to simulate the movement of water through the watershed, considering factors such as precipitation, evaporation, infiltration, runoff, and storage.

The SWMM model simulates the flow of water through conduits, channels, and the amount of water that is stored in catch basins and other storage units. It considers the impact of various factors on water movement, such as land use and the presence of roads. The model can predict the hydrological behaviour of a watershed under different conditions, making it a valuable tool for managing stormwater runoff.

Figure 2: The conceptualized storm-water drainage system, junctions, and the sub-catchments.

The precipitation data obtained for 5-year, 10 year and 25-year return periods from IDF

curves. Developed model was run only for 10-year return period, 6-hour storm and 30 min interval.

3.3 Design of model development scenarios

Table 2: Description of scenarios

Scenario	Remarks
Existing Condition (SC1)	S1 represent the existing state of the drainages. The hydrological environment in S1 was considered as the natural state in this research.
Only BR (SC2)	Bio retention capturing the runoff in corresponding sub catchment areas. Bio retentions were modelled via the SWMM with a surface soil storage and drain layers.
Only DP (SC3)	Detention pond collecting the runoff from critical sub catchment in the study area. The critical sub catchment was the sub catchment 1.
Only RB (SC4)	Rain barrel (RB) collecting the runoff from roofs, and it was planned to established to individual households and commercial buildings.
Combination BR + DP (SC5)	While bio retention (BR) pond collecting the runoff from corresponding sub catchment, the detention pond (DP) only collect runoff from critical sub catchment S1. Through this combination can be identified the effectiveness of the combined scenario.
Combination BR + RB (SC6)	Compare the effectiveness of runoff reduction, when used both BR and RB.
Combination DP + RB (SC7)	Compare the effectiveness of runoff reduction, when used both DP and RB.
Combination BR +DP +RB (SC8)	Compare the effectiveness of runoff reduction, when used BR, DP and RB.

4. Results and discussions

4.1 Calibration and validation

A numerical calibration method was used to calibrate a model due to the unavailability of measured values. The Rational formula was employed to determine the most appropriate parameters to enhance the model's accuracy and reliability. Three critical sub-catchments S1, S9 and S18 were chosen based on their significance to the overall system and impact on the accuracy of the model.

The SWMM model was validated using the Nash Sutcliffe efficiency as a goodness of fit test. The optimum statistical value occurs when the NSE is close to 1 (Chow et al.,2012). From this NSE equation obtained value for the critical sub catchments S1, S9 and S18 are 0.767, 0.874 and 0.796 respectively.

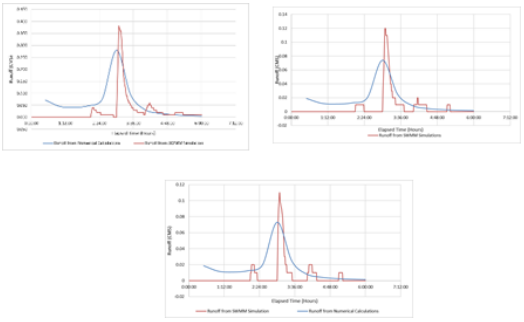

Figure 3: Numerical calculation and SWMM simulation results for sub catchment

4.2 Results

The study analyzed three different rainfall events with varying return periods to compare the runoff for an existing scenario. The maximum outflow volume occurred during a 25-year return period rainfall event. In the pre-development scenario, junction 12 was flooded, and sub catchments S1, S9, and S18 were found to be critical. Only the 10-year return period rainfall was considered in the developed scenarios.

Compared with SC1, peak runoff reduction rates for the SC2 to SC8 are 38.61%, 4.95%, 15.35%, 37.62%, 50%, 14.36% and 43.56%. According to this percentages largest peak runoff rate reduction happened in SC6. That is the combination of Bio Retention Pond and Rain Barrels for corresponding sub catchments. The percentage reduction rate of total flood volumes at scenario 2 to 8 are 63.59%, 10.6%, 31.52%, 75.27%, 84.24%, 41.30% and 100 %.

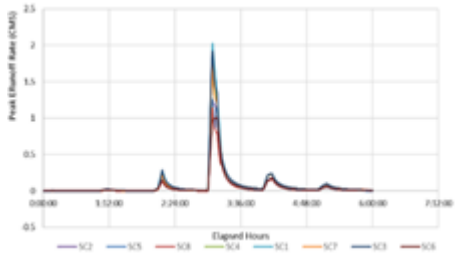

Figure 4: difference in the peak runoff rates under eight scenarios for the selected rain event.

4.2 Discussion

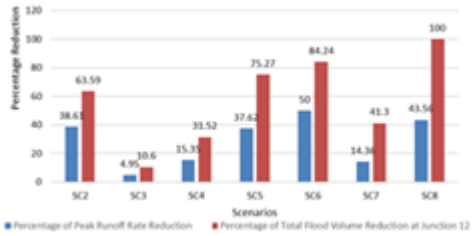

Figure 5: Percentage reduction of peak runoff rate and total flood volume compare with scenario one.

Seven BMP scenarios were evaluated based on peak runoff rate and total flood volume reduction rate and their percentage reductions are in the figure. According to that, Scenario 6 was found to be effective in reducing both types of flood risk, while scenario 8 showed considerable reduction in total flood volume. The combination of rain barrels and retention ponds was identified as the most suitable scenario for reducing both types of flood risk.

5. Conclusion

This study used SWMM modeling to address stormwater-related issues in a rapidly urbanizing area in Sri Lanka, identifying critical sub catchments and evaluating the effectiveness of different BMP scenarios for reducing flood risk. Due to the high population density in the selected area, we faced challenges in finding suitable locations to implement BMPs, resulting in a limited introduction of BMPs. The Rational formula was used to calculate the water runoff for three critical sub catchments: S1, S9, and S18. To assess the accuracy of the model, the Nash-Sutcliffe efficiency was used to compare the modeled results with the actual observed values. Scenario 6, which combined rain barrels and retention ponds, was found to be the most effective in reducing both peak runoff rate and total flood volume.

References

Platz, M., Simon, M. and Tryby, M., 2020. Testing of the storm water management model low impact development modules. JAWRA Journal of the American Water Resources Association, 56(2), pp.283-296.

Khaniya, B., Wanniarachchi, S.S. and Rathnayake, U.S., 2016. Sustainable stormwater management system: a conceptual design model for SLIIT, malabe campus, Sri Lanka. (Vol. 4, pp. 06-2016).

Pathirana, U.P.L.V., Peiris, M.T.O.V., Jayasinghe, A.B. and Mahanama, P.K.S., 2020. Assessment framework to select sustainable storm water management options for urban areas. Assessment, 7(02).

Harshani, H.M.D. and Wijesekera, N.T.S., 2011. Stormwater management modeling for ungauged watershed in Matara municipality. Engineer: Journal of the Institution of Engineers, Sri Lanka, 44(4).

Chow, M.F., Yusop, Z. and Toriman, M.E., 2012. Modeling runoff quantity and quality in tropical urban catchments using Storm Water Management Model. International Journal of Environmental Science and Technology, 9(4), pp.737-748.

Nandharathne, A.B.D.T. and Wijayaratna, T.M.N., 2015. Analysis of storm water drainage system at park road in Colombo using storm water management model (SWMM).

Experimental Investigation on Porous Concrete for Sustainable Drainage Systems

Niwunhella D.R.T., Kalpadeep D.N.S., Neluwala N.G.P.B.*

Department of Civil Engineering, University of Peradeniya, Sri Lanka

**pandukaneluwala@eng.pdn.ac.lk*

Keywords: Sustainable drainage systems, Porous concrete, Compressive strength, Infiltration rate

1. Introduction

The growing risk of floods in urban settings, resulting from intense and unpredictable rainfall, has become a significant concern due to the combined impact of urbanization and climate change. The lack of suitable drainage infrastructure exacerbates this issue. Sustainable Urban Drainage Systems (SUDS) offer a solution by addressing environmental concerns related to urban runoff and the damage caused by pollutants (Mbanaso, et.al, 2019). The improper disposal of construction waste has emerged as a global problem due to rapid urbanization, industrial expansion, and population growth (Roach, 2012).

While pavements, parking lots, and cover slabs have been successfully constructed using porous concrete, the exploration of different mix designs for porous concrete remains scarce. This study examines eight mix designs, four of which include changes in the weight of coarse aggregate sizes ranging from 12.5 to 25 mm. The remaining three mix designs incorporate fine aggregates, with varying percentages of fine aggregates (10%, 20%, and 30%). The objective of this research is to utilize recycled aggregates from construction waste to produce porous concrete slab panels, thereby investigating the compressive strength and infiltration rates of porous concrete for different aggregate gradation curves within the same mix design ratio.

2. Literature review

Numerous studies have explored the application of porous concrete in pavement designs, parking lots, and walking paths. Some research has focused on Sustainable Urban Drainage Systems (SUDS) and their role in drainage control.

2.1 Sustainable Urban Drainage Systems

Traditional sewer-based systems have been in use for 150 years to improve cleanliness and prevent urban flooding. Sustainable Urban Drainage Systems (SUDS) have emerged as alternative or supplementary methods to these conventional systems in the past four decades. 'Green' alternatives such as green roofs, rain gardens, infiltration trenches, swales, and dry and wet basins have been introduced as part of SUDS. Implementing SUDS systems leads to the evolution of drainage systems and enhances the quality of life for affected populations (Poleto, and Tassi, 2012).

2.2 Porous concrete drains and pavements

Porous concrete consists of coarse aggregate, Portland cement, and water, overlaying a stone aggregate reservoir, allowing for rapid water infiltration. This reservoir provides temporary storage as the runoff infiltrates into permeable soils below or drains out through an underdrain system. Porous concrete is employed in various applications that require permeability, noise absorption, or thermal insulation due to its high porosity. Porous asphalt and porous concrete pavements (Figure 1), are the most widely used and extensively studied porous pavement materials (Chandrappa, and Biligiri, 2016).

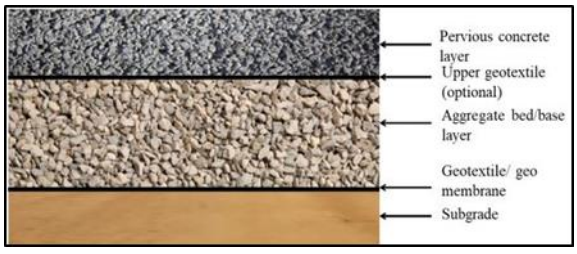

Figure 1: Cross section of the porous concrete pavement

2.3 Porous concrete properties

Porous concrete consists of a minimal number of fine particles, a precise proportion of water, and cement paste. The paste coats and bonds the mixture particles together, forming a network of highly porous interconnected voids that facilitate rapid water drainage. Increasing the cement content enhances the strength of the concrete.

Generally, porous concrete exhibits lower strength when recycled aggregates are used due to the larger void ratio. Recycled aggregate porous concrete has lower compressive strength compared to regular aggregate porous concrete. Clogging, which refers to a decrease in permeability, can occur in porous concrete and is caused by various physical, chemical, and biological mechanisms (Kia, et.al, 2017).

3. Methodology

There is a scarcity of studies in the existing literature that compare the infiltration rates of various coarse aggregate gradation curves in porous concrete. Additionally, the research on porous concrete made from recycled construction materials is limited. Therefore, in order to undertake our research, we had to develop a novel approach.

3.1 Material collection and preparation

Construction waste materials were collected from a construction site at the Faculty of Engineering on the university premises (Figure 2). The collected waste was broken and crushed to obtain the required aggregate particle sizes.

Figure 2: Construction waste collection

Sieve separation was performed to categorize the coarse aggregates into the following ranges: 4.75 - 9.5 mm, 9.5 - 12.5 mm, 12.5 - 19.5 mm, and 19.5 - 25 mm.

3.2 Porous concrete mix designs

Generally, the aggregate-cement ratios (A/C) range from 4 to 6 by mass, resulting in aggregate contents between 1300 kg/m3 and 1800 kg/m3. In the lab experiments, ACI Standard guidelines were followed. The target compressive strength for porous concrete was set at 15 MPa. The mix design ratio used was 1:4.3:0.3. The addition of water-reducing admixtures improved the workability and strength of the porous concrete. By incorporating recycled materials and admixtures, we were able to produce porous concrete with sufficient drainage capacity and strength. The mix design plan is presented in Table 1.

Table 1: Mix design plan

Mix Design No.	Description
1 – 4	Different 12.5 – 25 mm coarse aggregates % and no fine aggregates
5 – 7	10%, 20%, 30% fine aggregates and same coarse aggregate gradation curve
8	Construction wastes (10% fine aggregates & coarse gradation curve as Mix Design 2)

The first 7 mix designs focused on varying the aggregate gradation curves for normal coarse aggregates, with a mix design ratio corresponding to Grade 15. The initial 4 mix designs were conducted without fine aggregates, using different coarse aggregate gradation curves, primarily focusing on the 12.5 - 25 mm particle size range. The subsequent 3 mix designs included fine aggregates, with varying ratios of 10%, 20%, and 30% of the aggregate weight, while maintaining the same gradation curve for the coarse aggregates. The final mix design involved the use of construction waste materials.

3.3 Casting of porous concrete slab panels

Following the preparation of the porous concrete, infiltration testing and compressive strength testing were conducted for different mix designs. The laboratory tests adhered to the ASTM standard methods. To facilitate the testing, slab panels were cast from the porous concrete. The dimensions of the formwork for the slab panels were set at a length of 50 cm, width of 40 cm, and thickness of 8 cm.

The prepared formwork was placed on top of soil, and the slab panels were cast using the porous concrete. Casting was performed both with and without soil, and it was found that casting on soil was the most effective method, as it prevented grout accumulation at the bottom (Figure 3). During casting, compaction was

carried out as it proved to be effective in achieving desirable results.

Figure 3: Casted slab panel

3.4 Lab experiments and testing

The infiltration test followed the standard ASTM C1701 procedure. An infiltration ring with a diameter of 300 mm and a height of at least 5 cm was used for the test (Figure 4). The infiltration rate was calculated using Equation 1 provided in ASTM C1701.

$$I = (KM) \,/\, (D^2 * t) \quad \text{.....(1)}$$

where, K, M, D, t and I are conversion factor 126,870 $(in^3 s)/(lbs)$, mass of infiltrated water (lbs), inside diameter of infiltration ring(in), time to infiltrate water (sec) and infiltration rate (inches/hr) respectively.

Figure 4: ASTM C1701 standard infiltration test

Compressive strength analysis of the porous concrete was conducted according to the ASTM C39 standard testing method. Three cubes were cast for each test to obtain an average value. The curing process was carried out for 7 days and 28 days accordingly to ensure proper strength development.

4. Results and discussion

The results of the conducted mix designs were analysed and plotted in various ways to assess their impact.

4.1 Impact of aggregate size

In the first four mix designs, changes were made to the gradation curves of coarse aggregates, without adding fine aggregates. The infiltration rates corresponding to different 12.5 - 25 mm aggregate sizes are presented in Figure 5.

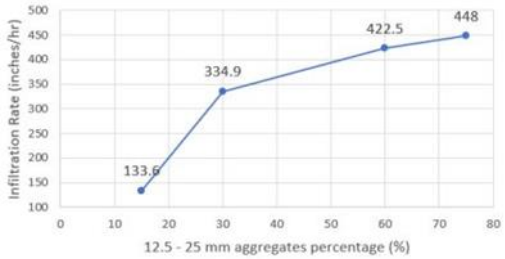

Figure 5: Infiltration rates for mix designs 1-4

It was observed that increasing the percentage of 12.5 - 25 mm coarse aggregates resulted in higher infiltration rates. Conversely, the compressive strength of the casted cubes after 7 days, as shown in Figure 6, decreased with an increase in the particle size of 12.5 - 25 mm coarse aggregates.

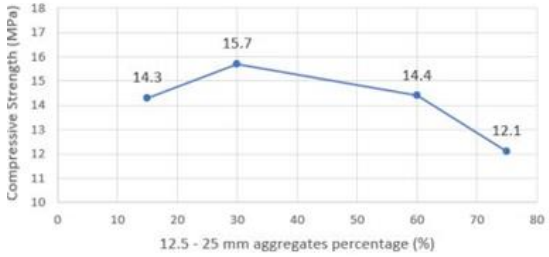

Figure 6: Compressive strength after 7 days

4.2 Impact of adding fine aggregates

In mix designs 5-7, different proportions of fine aggregates were added, using sand as the fine aggregate material. The percentages of fine aggregates were varied at 10%, 20%, and 30%. The coarse aggregates followed the same gradation curve as depicted in Figure 7.

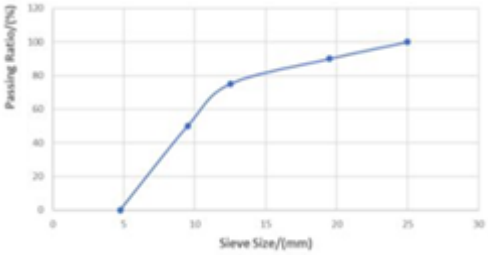

Figure 7: Coarse aggregates gradation curve

The infiltration rate values showed a decrease as the percentage of fine aggregates increased, as illustrated in Figure 8. This decrease can be attributed to the filling of voids by the fine particles, resulting in a reduction in porosity. However, the compressive strength values

exhibited an increase with higher percentages of fine aggregates.

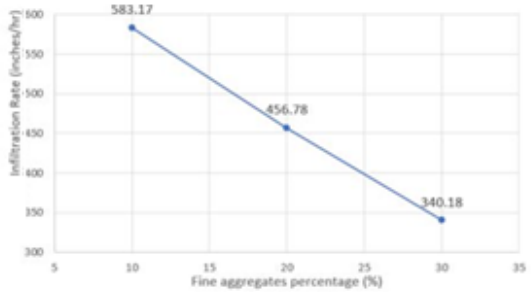

Figure 8: Infiltration rate values

4.3 Performance of porous concrete from construction wastes

In mix design 8, construction wastes were utilized as a replacement for normal coarse aggregates. Construction waste materials such as concrete, bricks, and wood were collected from a construction site. The average compressive strength value after 28 days was 16.28 MPa, and the infiltration rate value was measured at 1413.06 inches/hr.

4.4 Discussion

Replacing traditional concrete with porous concrete can be done for ideal spaces or actual locations such as parking lots, housing complexes, or footpaths can help mitigate overflowing drains and reduce runoff. Producing porous concrete from construction waste may offer an affordable and sustainable solution. The infiltrated water can be collected separately through perforated pipes or other appropriate methods. In heavily flooded urban areas, adding a layer of fine particles to the top surface of porous pavements can enhance the strength of road pavements. The findings of this research highlight the potential of porous concrete made from recycled aggregates as a viable solution for effective stormwater management in urban environments.

5. Conclusion

After conducting many lab experiments for different porous concrete mix designs following were the main conclusions.

The compaction increased the compressive strength of porous concrete. Average compressive strength values after 7 days for compacted cubes was 14.36 MPa and for non-compacted cubes was 4.19 MPa.

To increase the infiltration rate of slab panels, coarse aggregate particle sizes should be increased. When 12.5 – 25 mm coarse aggregates percentage increased from 15% to 75%, the infiltration rates increased gradually from 133.6 inches/hr to 448 inches/hr. But the 7-day compressive strength decreased from 14.3 MPa to 12.1 MPa.

When fine aggregates were introduced from 10% to 30%, the compressive strength increased from 16.5 MPa to 18.21 MPa and the infiltration rates decreased from 600 inches/hr to 320 inches/hr.

Construction wastes can be used to manufacture porous concrete. The average compressive strength value was 16.28 MPa after 28 days and the infiltration rate value was more than 1400 inches/hr averagely, which shows its potential to be used in urban flooding areas.

References

Mbanaso, F. U., Charlesworth, S. M., Coupe, S. J., Newman, A. P., & Nnadi, E. O. “Reuse of materials from a Sustainable Drainage System device: Health, Safety and Environment assessment for an end-of-life Pervious Pavement Structure”, 2019, pp. 1759–1770.

Roach, I., “Diverting lightweight C&D waste from landfill, Wastes Management”, 2001, pp.23-25.

Poleto, C., & Tassi, R. “Sustainable Urban Drainage Systems”. In M. S. Javaid (Ed.), Drainage Systems, 2012.

Chandrappa, A. K., & Biligiri, K. P. “Pervious concrete as a sustainable pavement material – Research findings and future prospects: A state-of-the-art review. Construction and Building Materials”, 2016, pp. 262–274.

Kia, A., Wong, H. S., & Cheeseman, C. R. “Clogging in permeable concrete: A review. Journal of Environmental Management”, 2017, pp. 221–233.

Numerical Weather Forecasting Capabilities During Rainfall Events

Jayasundara J.P.M.M., Prabashini W.A.P., Neluwala N.G.P.B.*

Department of Civil Engineering, University of Peradeniya, Sri Lanka

**pandukaneluwala@eng.pdn.ac.lk*

Keywords: Numerical weather forecasting, WRF, Physics schemes

1. Introduction

Weather forecasting is the application of current technology and science to predict the state of the atmosphere for a future time and a given location. Numerical weather prediction is a method of weather forecasting that uses mathematical models of the atmosphere and oceans to predict the weather based on current weather conditions. Several numerical methods have been utilized in recent studies to predict the weather in certain locations in Sri Lanka. Among them, the Weather Research and Forecasting (WRF) model was adopted by the majority of researchers, and they have gotten better outcomes with this model (Nandalal, et.al, 2012; Mafas, et.al, 2016). But, there is a shortage of studies that have reviewed the impact of individual parameterization options in WRF model for mountainous terrain such as the Kandy district.

The selected study area, Kandy District is situated in the Central Highland of Sri Lanka which has been identified as a district which is prone to landslides by Multi-hazard Disaster Mitigation Project. The annual and seasonal distribution of rainfall over Kandy District has considerable variations due to the complex topographical features and orographic barriers. Therefore, this study aims to develop a 24-hour weather forecasting model for Kandy by identifying the optimum microphysics parameterization scheme for the area.

2. Literature review

2.1 Weather research and forecast model (WRF)

General Circulations Models (GCMs) are used to simulate the global weather but, GCMs have low resolutions which require downscaling to regional level by regional climate models. There are two approaches to downscaling: dynamical and statistical. Statistical downscaling uses statistical relationships to predict local climate variables from large-scale variables. For dynamical downscaling, higher-resolution climate models called regional climate models (RCM) are used. There are several Regional Climate Models, among them WRF model is considered the latest and widely used mesoscale model which is used by both operational and research communities. Furthermore, the performance of the WRF model is reasonably better than that of MM5 (Pattanayak and Mohanty, 2008). and the accuracy of rainfall prediction in the Upper Mahaweli basin by WRF model is better compared to that of RegCM model (Mafas, et.al, 2016).

2.2 Physics schemes in the WRF model

The WRF model has multiple physics schemes namely microphysics scheme, cumulus scheme, boundary layer scheme, land surface scheme, and long/short wave radiation schemes that could be varied to fine-tune the model to suit its operating environment.

Microphysics scheme controls the simulation of the formation of cloud droplets, the formation of ice crystals, their growth, and their fallout as precipitation. The WRF model is armed with many options for microphysics schemes, namely, Kessler scheme, Lin et al scheme, WSM3 scheme (WRF Single Moment 3 class scheme), WSM5 scheme (WRF Single Moment 5 class scheme), WSM6 scheme (WRF Single Moment 6 class scheme), Thompson scheme, Ferrier scheme, and Morrison scheme.

3. Methodology

The simulation experiments in this study were conducted using the WRF model, version 4.0. The performance of the WRF model for the simulation of three rainfall events over Kandy district was attempted using four microphysics parameterization schemes WSM5, Ferrier, WSM6 and Lin et al.

WSM6 scheme has the lowest error in precipitation analysis (Chutia, et.al, 2019) and Ferrier microphysics performs well, due to the excessively high number of structures that this scheme produces (Cassola, et.al, 2015). In rainy season, WSM5 and in dry season, Lin yields the best performance for precipitation forecast

(Martí, 2022). Furthermore, the microphysics scheme of Purdue Lin (LIN) scheme produces the strongest cyclone (Maw, and Min, 2017).

To identify the optimum microphysics scheme, the selected microphysics options were changed while keeping other physics schemes at default options. The used default schemes are RRTM longwave radiation scheme, Dudhia shortwave radiation scheme, Kain-Fritsch cumulus scheme, Yonsei University planetary boundary layer scheme (YSU) and Noah land surface scheme. Though high-resolution yields more accurate simulations, particularly in regions that are topographically complex and exhibit heterogeneous land use (Giunta, et.al, 2019) it requires more powerful computers. Therefore, in this study, the WRF model was applied to Kandy district by employing one-way nested domains that consist of three domains of coarse to fine grid size of 27/9/3 km (1782 km × 1782 km, 594 km × 594 km, 189 km × 189 km).

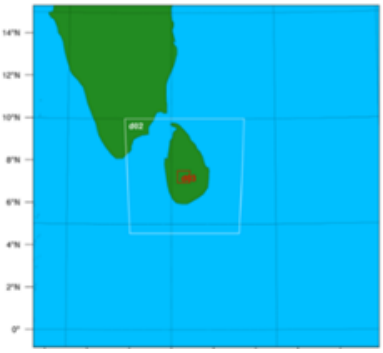

Figure 1: WRF domain configuration

The WRF model requires metrological and geographical data as input data for the simulations. This study used National Centers for Environmental Prediction NCEP FNL (Final) Operational Global Analysis data set for the boundary conditions, with Global Forecast System (GFS). These NCEP FNL (Final) operational global analysis data are on 1-degree by 1-degree grids prepared operationally every six hours.

In this study the performance of the WRF model was evaluated using three rainfall events having rainfall more than 50 mm/day in the North-East monsoon season (2019/11/28-2019/12/01, 2021/01/04-2021/01/07 and 2021/11/06-2021/11/09) over Kandy district.
For the comparison of model output fields with available 24-hour rainfall data, four rainfall stations operated by the Department of Meteorology: Katugasthota, Kundasale, Kandy kings pavilion, and Madulkelle were used.

In this study, verification of the results was applied to 24-hour precipitation accumulations for the 3 km domain, using frequency bias index (BIAS), root mean squared error (RMSE), mean absolute error (MAE), correlation coefficient and Total Model Performance. Total model performance is a combined index derived from MAE, RMSE, and slope that is used to quantify the overall performance. Consistency is seen from TMP values that tend to be small.

$$TMP = \frac{\frac{\text{MAE} + \text{RMSE} + \text{BIAS}}{\text{Yo, (mean)}} + (1 - \text{Corr}) + |1 - \text{Slope}|}{5}$$

Then the selected optimum microphysics scheme was used to forecast the rainfall that occurred on 2021/01/06 with a lead time of 24 hours.

4. Results and discussion

In this study, 24 hour accumulated rainfall data for the rain gauge stations over Kandy region was obtained using WRF model. As four microphysics schemes were considered for each selected four rainfall events, twelve model comparisons between the model's output and the observed daily rainfall data were performed to select the optimum microphysics scheme.

4.1 Identification of optimum physics scheme

4.1.1. 2021/01/04-2021/01/07 rainfall event

The averages of daily rainfall results for all four stations from each WRF microphysics scheme were compared with the averages of daily observation records from each station as shown Figure 2. This shows that WSM5 and WSM6 microphysics schemes have a closer agreement with the observed average data. Furthermore, all microphysics schemes were able to capture the occurrence of highest rainfall although they have underestimated the magnitude of it.

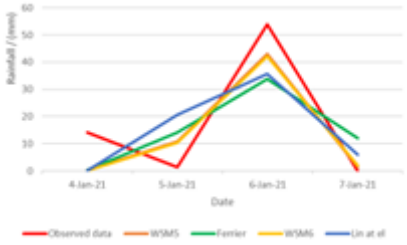

Figure 2: Comparison of WRF ARW model output data vs. average of observation station

Table 1 shows the statistical comparison between model output data and observed data for the 2021/01/04-2021/01/07 rainfall event.

Correlation and Total Model Performances (TMP) with bias, root means square error, slope, and mean absolute error were calculated to perform the statistical comparison. WSM5 microphysics scheme presents the optimum results with the lowest TMP value (0.5) for this event.

Table 1: Statistical comparison between model output data and observed data for the 2021/01/04-2021/01/07 rainfall event.

Microphysics Schemes	RMSE / (mm)	MAE / (mm)	BIAS / (mm)	Slope	Correlation coefficient	TMP
WSM5	17.75	13.74	-3.51	0.56	0.55	0.50
Ferrier	21.85	18.33	-2.23	0.48	0.58	0.74
WSM6	19.10	14.51	-3.68	0.55	0.48	0.54
Lin at el	18.76	16.35	-1.68	0.39	0.46	0.62

4.1.2. 2019/11/28-2019/12/01 rainfall event

Figure 3 shows the graphical distribution of modeled rainfall and observed rainfall as an average for the selected area. All four microphysics schemes were able to capture the occurrence of highest rainfall. However, they have underestimated the magnitude of it.

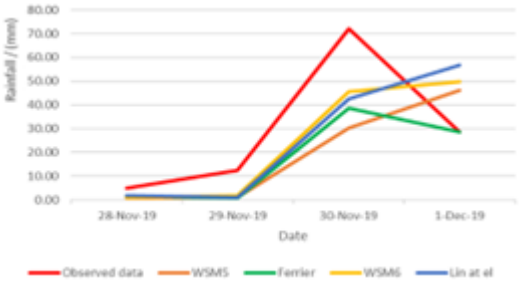

Figure 3: Comparison of WRF ARW model output data vs. average of observation stations

The estimated statistical evaluation parameters are displayed in Table 2. Here, Ferrier microphysics scheme presents the optimum results with the lowest TMP value (0.33).

Table 2: Statistical comparison between model output data and observed data for the rainfall event 2019/11/28-2019/12/01.

Microphysics Schemes	RMSE / (mm)	MAE / (mm)	BIAS / (mm)	Slope	Correlation coefficient	TMP
WSM5	30.02	22.24	-10.03	0.35	0.14	0.59
Ferrier	18.51	13.96	-12.17	0.48	0.58	0.33
WSM6	21.50	16.04	-4.89	0.60	0.44	0.41
Lin at el	27.84	19.00	-3.91	0.44	0.16	0.57

4.1.3. 2021/11/06-2021/11/09 rainfall event

Figure 4 shows the graphical distribution of modeled rainfall and observed rainfall as an average for the selected area. The Ferrier microphysics scheme has a closer agreement with the observed average data. Furthermore, all microphysics schemes were able to capture the occurrence of the highest rainfall although they have overestimated the magnitude of it.

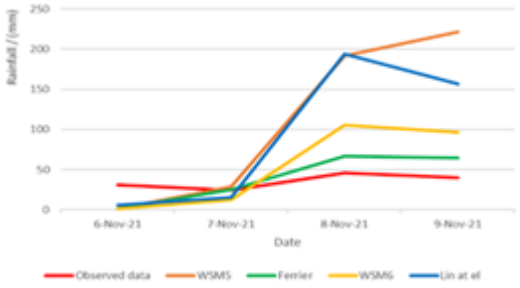

Figure 4: Comparison of WRF ARW model output data vs. observed data as an average over the area

The estimated statistical evaluation parameters are displayed in Table 3, and Ferrier microphysics scheme presents the optimum results with the lowest TMP value (0.53) for this event.

Table 3: Statistical comparison between model output data and observed data for the rainfall event 2021/11/06-2021/11/09.

Microphysics Schemes	RMSE / (mm)	MAE / (mm)	BIAS / (mm)	Slope	Correlation coefficient	TMP
WSM5	123.39	90.2	75.15	1.57	0.08	1.92
Ferrier	26.2	21.29	3.89	0.62	0.16	0.53
WSM6	35.95	36.31	19.66	0.98	0.17	0.76
Lin at el	134.76	102.61	86.32	3.25	0.34	2.46

According to the above simulations, it suggests that Ferrier microphysics scheme is the optimum microphysics scheme for Kandy district.

4.2 Forecasting

To evaluate the performance of the Ferrier microphysics scheme, which was gained as the optimum microphysics scheme, forecasting the precipitation was carried out. For 24 hours forecasting, input data obtained on 2021/01/05 was used to forecast the precipitation data for 2021/01/06. The comparison of forecasted rainfall data with observed rainfall data for 2021/01/06 for each rain gauging station is shown in figure 5.

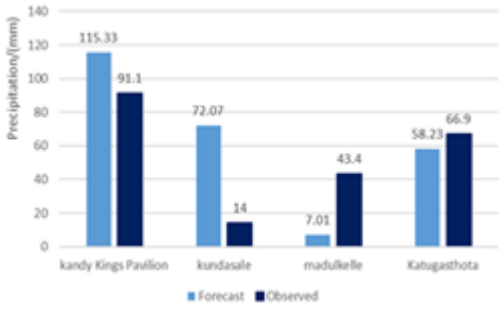

Figure 5: Comparison of forecasted rainfall with observed rainfall on 2021/01/06

By analyzing these graphs, it is evident that forecasted precipitation values for Kandy Kings Pavilion and Kundasale rain gauge stations are overestimated and forecasted precipitation values for Madulkelle and Katugasthota rain gauge stations are underestimated by the model.

5. Conclusions

Three rainfall events over the Kandy district were modeled with the WRF model using the WSM5, Ferrier, WSM6 and Lin et al microphysics Schemes.

According to the results, for event 2021/01/04–2021/01/07, WSM5 microphysics scheme and for events 2019/11/28–2019/12/01 and 2021/11/06-2021/11/09 Ferrier microphysics scheme predicted more accurate results with the lowest TMP values of 0.50, 0.33 and 0.53 respectively.

According to the above simulations, it suggests that the Ferrier microphysics scheme is the optimum microphysics scheme for the Kandy district.

According to the forecasting results, forecasting rainfall with the Ferrier microphysics scheme results in a random variation.

It is recommended that verifying the model for more events to accurately evaluate the model.

References

Nandalal, K., Sachindra, D. and Ratnayake, U., 2012. Application of WRF weather model to forecast precipitation in the Nilwala river basin. Engineer: Journal of the Institution of Engineers, Sri Lanka, 45(1), pp.51-67

Mafas, M., Muhammadh, K.M., Weerakoon, S.B. and Mutua, F., 2016, December. Comparative Study of WRF and REGCM Weather Predictions for the Upper Mahaweli River Basin. In Proceedings of the 7th International Conference on Sustainable Built Environment,

Pattanayak, S. and Mohanty, U.C., 2008. A comparative study on the performance of MM5 and WRF models in simulation of tropical cyclones over Indian seas. Current Science, pp.923-936.

Chutia, L., Pathak, B., Parottil, A. and Bhuyan, P.K., 2019. Impact of microphysics parameterizations and horizontal resolutions on simulation of "MORA" tropical cyclone over the Bay of Bengal using Numerical Weather Prediction Model. Meteorology and Atmospheric Physics, 131, pp.1483-1495.

Cassola, F., Ferrari, F. and Mazzino, A., 2015. Numerical simulations of Mediterranean heavy precipitation events with the WRF model: A verification exercise using different approaches. Atmospheric Research, 164, pp.210-225.

Martí, J., 2022. A sensitivy study of microphysics schemes of the wrf-arw model for low-level wind shear forecast in José Martí International Airport during convective storms. Revista Cubana de Meteorología, 28(3).

Maw, K. and Min, J., 2017. Impacts of microphysics schemes and topography on the prediction of the heavy rainfall in western Myanmar associated with tropical cyclone ROANU (2016). Advances in Meteorology, 2017.

Giunta, G., Salerno, R., Ceppi, A., Ercolani, G. and Mancini, M., 2019. Effects of model horizontal grid resolution on short-and medium-term daily temperature forecasts for energy consumption application in European cities. Advances in Meteorology, 2019.

Scale Effect on Rainfall-Runoff Modeling in Upper Kelani River Basin, Sri Lanka

Madhawa W.A.I., Madapatha M.K.D.K.C., De Silva M.M.G.T.*

Department of Civil Engineering, University of Peradeniya, Sri Lanka

**gouri@eng.pdn.ac.lk*

Keywords: Rainfall-Runoff Modeling, Scale Effect, HEC-HMS

1. Introduction

Rainfall-runoff Modeling is an important area of study in hydrological engineering, with two primary approaches: distributed Modeling and lumped Modeling. While distributed models are more accurate, lumped models are widely used due to their ease of use. This research paper aims to investigate the feasibility of improving the accuracy of a lumped hydrological model through subunits, in the Upper Kelani River Basin up to Hanwella, in Sri Lanka.

The study considered dividing the basin into multiple sub-basins to evaluate the scale effect on rainfall-runoff Modeling. Hydrologic Engineering Centre – Hydrologic Modeling System (HEC-HMS) Modeling software was used for this purpose and the sub-models inside were selected by referring to the previous studies conducted in the same study area.

The Kelani River basin was selected for the study because of the absence of prior efforts to analyze the scale effect in the upper Kelani River basin. Further, the Kelani River is very crucial to the high flood risks in downstream low-lying areas including the commercial capital of the country, and the significance of the river as a primary drinking water source in the Western Province, Sri Lanka. The findings of this study provide insights to improve flood risk management and water resource management in the region.

2. Study area

The upper Kelani River Basin, located in the central hills of Sri Lanka, is the focus of this study. The Kelani River is the fourth-longest river in Sri Lanka with a length of 145 km. It originates from the Sri Pada Mountain range and flows through Nuwara Eliya, Rathnapura, Kegalle, Gampaha and Colombo Districts, before discharging into the Indian Ocean. The basin area is approximately 2,230 km² which is bounded by 6°47'–7°05' North latitudes and 79°53' to 80°13' East longitudes.

The basin experiences an average annual rainfall of 3,718 millimetres, with rainfall levels varying between 500 to 5,000 millimetres depending on the season. Red Yellow Podzolic soil is the predominant soil type in the area, and rubber cultivations cover approximately one-third of the basin (33.5%). Tea cultivation is 11.8% and forests cover 10.2% of the basin while homesteads cover 24.6% of the land area. The land-use patterns have a significant impact on the hydrology and water quality of a basin and are therefore essential factors to be considered in any research related to hydrology and water quality. Figure 1 is the location of the study area in Sri Lanka.

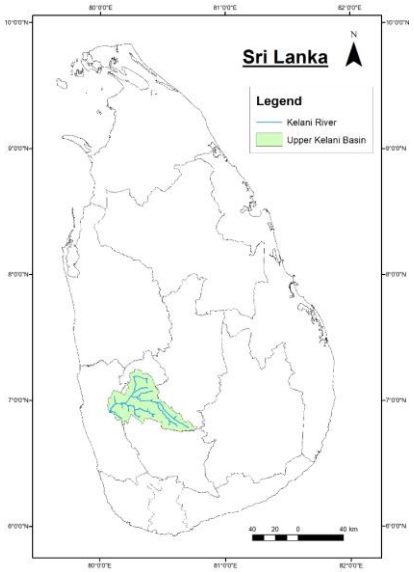

Figure 1: Upper Kelani River Basin

3. Literature review

Hydrological models are tools that use known inputs to predict unknown outputs. Lumped and distributed models are the two common types of hydrological models. Distributed models consider both spatial and temporal variations, while lumped models consider only temporal variations. Lumped models are commonly used in developing countries like Sri

Lanka, due to limited data availability, less time consumption, low computational power and the easiness of use (Brirhet & Benaabidate, 2016; Nandalal and Ratnayake 2010). HEC-HMS is a commonly used software because of its free availability, ability to consider the physical characteristics of the basin, and reasonable accuracy. There are three major components in the basin model of HEC-HMS namely, the loss component, transform component, and base flow component (Feldman Arlen D, 2000).
Good quality input is essential to have a good result from a model. Hence, before using rainfall records, it is important to check the continuity and consistency of the data. Simple Arithmetic Mean Method, Normal Ratio Method, and Double mass curve analysis can be used to estimate missing data and check the consistency. In order to distribute point rainfall data to the whole basin, the Arithmetic mean method, Thiessen Polygon method, IDW method, or Kringging method can be used (Subramanya K., 2008) .

Modeling software has a significant effect on the results of the scale. However, the technique used for sub-basin delineation according to the river network or based on other basin spatial characteristics such as slope and land use also can be contributed to the improvements of simulation results for lumped models in small river basins (Kanchanamala et al., 2016).

4. Methodology

Rainfall data from eight rainfall gauging stations were considered for this study. The locations of the rainfall gauging stations are presented in Figure 2. River flow data were taken from the flow gauge at Hanwella gauging station.

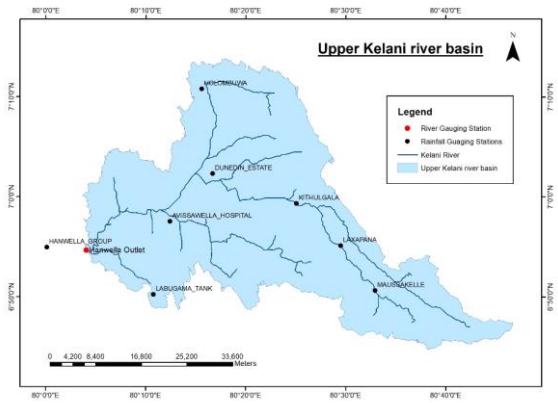

Figure 2: Rainfall gauge distribution over the Upper Kelani River basin

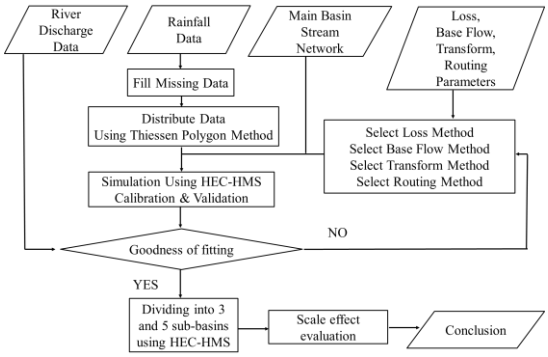

Figure 3: Workflow

Figure 3 is the workflow of this research. There are four main inputs; river discharge data, rainfall data, main basin stream network, and parameters related to HEC-HMS components. The rainfall data processing was in three main steps. First, missing data estimation was carried out, and then data consistency was checked using double mass curve analysis. Finally, the special data distribution was done using the Thiessen Polygon method.

Basin delineation was done using ArcMap 10.8 GIS software. Three basin models were considered in this study: (1) the whole basin as a single unit, (2) three sub-basins, and (3) five sub-basins. They were created based on the stream network as indicated in Figure 4.

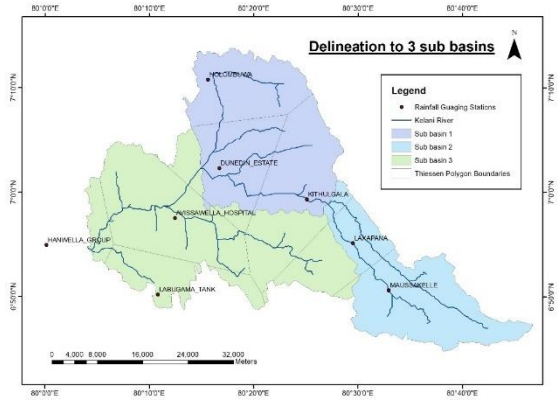

Figure 4: 3 sub-basins with Thiessen polygons

HEC HMS 4.10 was used for the model creation. Figure 5 shows the HEC-HMS-based model for the three sub-basins case. Similarly, rainfall-runoff models for the other two basins were also developed.

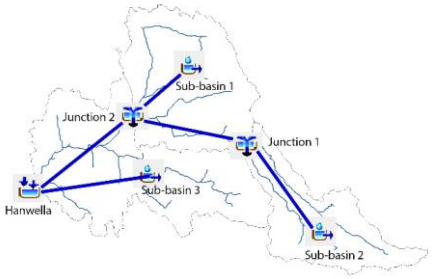

Figure 5: HEC- HMS model: 3 sub-basins

The soil moisture accounting method and the Clark unit hydrograph were used for the loss component, and for the transfer component evaluation respectively. The recession method and lag method were used as the base flow simulation and the routing respectively. These methods were selected by referring to the literature done in the same study area (De Silva et al., 2014; Gunathilake, 2019; Perera et al., 2021).

The parameters were optimized for this study, by starting from the parameter values found in the same literature. The parameters used in this study are given in Table 1.

Table 10: Model parameters

Parameter	Value
Loss - Soil moisture accounting method	
Soil (%)	70
Groundwater 1 (%)	45
Groundwater 2 (%)	80
Max infiltration (mm/hr)	55
Imperviousness (%)	40
Soil storage (mm)	200
Soil percolation (mm/hr)	75
GW 1 storage (mm)	1
GW 1 percolation (mm/hr)	60
GW 1 coefficient (h)	1.2
GW 2 storage (mm)	100
GW 2 percolation (mm/hr)	150
GW 2 coefficient (h)	1
Transform - Clark unit hydrograph method	
Time of concentration-Tc (h)	1
Storage coefficient- R (h)	28
Baseflow - Recession method	
Recession constant	40
Ratio to peak	0.7
Initial discharge (m3/s)	0.5
Routing - Lag method	
Lag time (min)	0.7Tc

The HEC-HMS software itself provides three parameters to assess the goodness of fit (RSR, Percentage Bias, and Nash-Sutcliffe Coefficient) between simulation results and observations in a basin model's outlet. These parameters were used to mathematically calibrate and validate the model and determine the degree of compatibility between the simulation results and the observations.

The goodness of fitting parameters obtained for the three cases, i.e., single basin case, 3 sub-basins case, and 5 sub-basins case, were compared to determine the scale effect on the rainfall-runoff Modeling in the upper Kelani River basin.

5. Analysis and results

The comparisons between the observed and simulated discharge were made through visual checks first. The visual checks were performed by comparing the plots of observed discharge and simulated discharge for each model combination. Examples of some fragments of plots for the run-off simulations of the whole basin and 3 sub-basins are presented in Figure 6, and Figure 7.

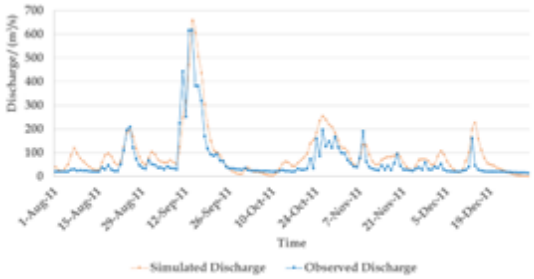

Figure 6: Simulated and observed discharges at Hanwella from Aug to Dec 2011 for single basin

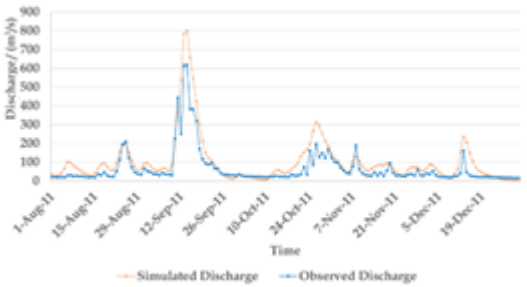

Figure 7: Simulated and observed discharges at Hanwella from Aug to Dec 2011 for 3 sub-basins

Then, a couple of statistical tests were carried out to ensure the accuracy of the model results. During the calibration stage (from 1998-2015), it was observed that the Nash-Sutcliffe coefficient for the 3 sub-basin simulation was slightly

higher than the single basin simulation. Similarly, the 5 sub-basins simulation showed an increase in the Nash-Sutcliffe coefficient compared to the 3 sub-basins simulation. Finally, the calibrated models were verified using data from the period 1990 to 1997. The results of the calibration and validation are presented in Table 2.

Table 2: Results for calibration and validation

Model	Nash-Sutcliffe	RSR	Percentage bias
Single Basin			
Calibration	0.74	0.5	2.80
Validation	0.79	0.5	-15.18
3 Sub-basins			
Calibration	0.75	0.5	8.48
Validation	0.79	0.5	-16.23
5 Sub-basins			
Calibration	0.79	0.5	-5.83
Validation	0.77	0.5	-22.40

Calibration and validation results of all the cases produced a good fitting with Nash Sutcliffe coefficients (0.65 to 0.75 is good while over 0.75 is ideal). The percentage bias is excellent in the range of ±10, good in the range of ±10 to ±15, and decent in the range of ±15 to ±25. RSR is at its best when it lies between 0 and 0.5.

6. Conclusions

The study aimed to investigate the effects of dividing a basin into sub-basins on the accuracy of runoff simulations. In order to achieve this, the upper Kelani River basin was first considered as a whole and then subdivided into three and five sub-basins. The results obtained for calibration indicated an improvement with regard to the Nash-Sutcliffe coefficient with the increase in the number of subbasins. However, the improvement was not significant, with values of 0.74, 0.75, and 0.79 for the whole basin, 3 sub-basin, and 5 sub-basin cases, respectively.

It is often easier to do a runoff simulation by considering the whole basin as a single unit. On the other hand, dividing the basin into sub-basins requires more time and effort. However, the results obtained from the sub-basin simulations were very close to those of the single-unit basin simulation. Consequently, for the upper Kelani River basin, it is suggested that considering the whole basin as a single unit is much more convenient and provides reliable results.

The study also analysed the bias values, and it was found that the single basin provided the best outcome compared to the other two simulations. Based on these findings, it can be concluded that the scale effect is not a crucial factor for accurate runoff Modeling in the upper Kelani River basin. However, the results could be improved by considering reservoir discharge data and increasing the number of rainfall gauges in future studies.

References

Brirhet, H., & Benaabidate, L. 2016. Comparison of Two Hydrological Models (Lumped and Distributed) Over A Pilot Area of The Issen Watershed in The Souss Basin, Morocco. European Scientific Journal, ESJ, 12(18), 347.

De Silva, M. M. G. T., Weerakoon, S. B., & Herath, S. 2014. Modeling of Event and Continuous Flow Hydrographs with HEC–HMS: Case Study in the Kelani River Basin, Sri Lanka. Journal of Hydrologic Engineering, 19(4), 800–806.

Feldman Arlen D. 2000. Hydrologic Modeling System HEC-HMS Technical Reference Manual.

Gunathilake, M. B. 2019. Application of HEC-HMS model to simulate long term streamflow in the Kelani River Basin, Sri Lanka Wavelet analysis View project.

Kanchanamala, D. P. H. M., Herath, H. M. H. K., & Nandalal, K. D. W. 2016. Impact of Catchment Scale on Rainfall-runoff Modeling: Kalu Ganga River Catchment upto Ratnapura.

Nandalal, H. K., & Ratnayake, U. R. 2010. Event Based Modeling of a Watershed Using HEC-HMS: Vol. XXXXIII (Issue 02).

Perera, D. W. V. M., Karunarathne, D. T. H. K., & de Silva M.M.G.T. 2021. Comparative Evaluation of the Spatial Distribution of Rainfall for Accurate Runoff Modeling; A Case Study in Upper Kelani River Basin. 190–197

Subramanya K. 2008. Engineering Hydrology (third edition).

Water Resource Management to Fulfill the Drinking and Irrigation Water Demand; A Case Study in Kegalle

Yasminda O.L., Abeysinghe A.A.T.S., De Silva M.M.G.T.*

Department of Civil Engineering, University of Peradeniya, Sri Lanka

**gouri@eng.pdn.ac.lk*

Keywords: Water resource management, Drinking water demand, Irrigation water demand, WEAP, CROPWAT

1. Introduction

1.1 Background

Rapid urbanization and development are causing severe problems of raw water extraction and related environmental and social impacts. Competition for the limited supply of freshwater has increased due to various demands of the exponentially increasing population and because of the increased pollution owing to anthropogenic activities. Further, water for agriculture is also becoming increasingly scarce in the light of growing water demands from different sectors. Hence, this study attempts to address the water demand in Kegalle district by increasing the water distribution coverage while assessing the distribution of water for irrigation requirements from the available surface water sources.

1.2 Study area

The Kegalle district is in the Sabaragamuwa Province with a land area of 1683 km^2 and Figure 1 shows the Kegalle in Sri Lanka map. It is composed of 11 divisional secretariat divisions. The most important fact related to this study is the pipe borne water coverage by National water supply and drainage board (NWSDB) in Kegalle district is only 23.6%. (Ministry of water supply,2016).

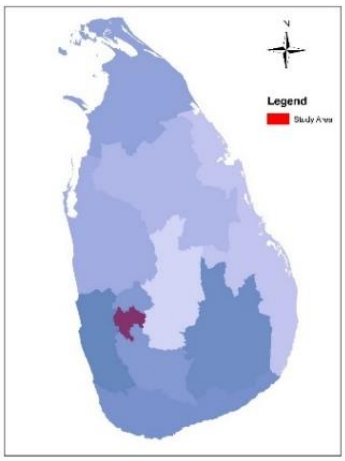

Figure 1: Study Area

Due to the large extent of the Kegalle district, the study area was confined to four divisional secretariat divisions namely; Ruwanwella, Dehiowita, Bulathkohupitiya, Yatiyantota. The selection was based on the number of streams flow through the area. Figure 2 shows the streams which flow through those divisional secretariat divisions.

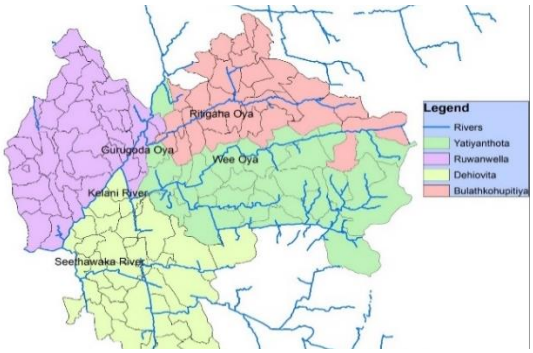

Figure 2: Streams that flow through four divisional secretariat divisions

2. Literature review

2.1 Pipe borne water

Sri Lanka, being a rich for water, has 40 percent pipe-borne water supply. Of which, 59.4 percent from dug wells, tube-wells, streams and springs, 10 percent from unsafe sources (Department of Census, 2012).

National water supply and Drainage board (NWS&DB) supplies pipe-borne water through 52,117 lines from water treatment plants to Kegalle District. Only 23.6 percent of residents have the access to pipe-borne water supply in Kegalle. (Consumer Manual,2016).

Due to the expansion of economic activities along with population growth, piped water consumption has increased over the years. For example, the total water consumption from piped water supplies increased from 120 million

cubic meters in 1994 to 382 million cubic meters in 2013 (Hussain et al., 2002; NWSDB, 2014).
Water scarcity prevails due to population increase and economic growth and standards of living improve, this is immediately reflected in the per capita use of water. (Gunatilaka A., 2008)

2.2 Water demand analysis using WEAP

The Water Evaluation and Planning (WEAP) system is an initiative of the Stockholm Environment Institute that provides a framework for water assessment and planning which can be used to represent current and future water conditions in each area depending on key assumptions (Levite et al. 2003). WEAP is a practical tool for water resources planning which incorporates not only water supply and demand issues, but also water quality and ecosystem preservation issues, by its integrated approach to simulate water systems and by its policy orientation (SEI, 2011).

2.3 Irrigation water requirement using CROPWAT

In Asia for instance, rice provides on average 32% of the total calorie uptake annually. Mainly because of a fast-growing population, demand for rice is expected to keep increasing in the coming decades. About 75% of the global rice volume is produced in the irrigated lowlands. Decreasing water availability for agriculture threatens the productivity of the irrigated rice ecosystem (Bouraima A-K, Zhang W H, Wei C F).

Estimate irrigation water requirement of rice using the Cropwat model. Cropwat is a FAO model for irrigation management designed by Smith which integrates data on climate, crop and soil to assess reference evapotranspiration (ETo), crop evapotranspiration (ETc) and irrigation water requirements. (Bouraima A-K, Zhang W H, Wei C F)

The reference evapotranspiration ETo was calculated by FAO Penman-Monteith method, using decision support software –CROPWAT 8.0 (Bouraima A-K, Zhang W H, Wei C F.)

3. Methodology

First, the water sources and study area were identified. Flow data from three-gauge stations, Glencource, Holombuwa, Kithulgala were collected over 22 years. Those flow data were collected from the Department of Irrigation. Then, the drinking water demand was analyzed. A population density map was created using the population data of Grama Niladhari Divisions in ArcGIS environment. Five population clusters were identified. When the clusters were created, the present coverage of NWSDB was excluded and the areas with the population density over 400capita/km^2 were considered. The best possible extracting point to each cluster was selected from the stream by considering the elevation of the extracting point, distance to the population cluster from the point.

Satisfaction of requirement in water demand of each cluster and the minimum flow from the extracting point were checked using WEAP. Population of a cluster, annual water consumption rate per person, population growth rate and the flow of extracting point were used as the inputs to WEAP. The water demand is assumed to increase according to the population. Under Reference Scenario, 0.9% population growth was considered for each cluster.

In this research only paddy was considered for the analysis of irrigation water demand. Irrigation clusters were created by considering the high paddy dense areas. Crop water requirement was calculated using CROPWAT software. Monthly rainfall data, climate data, crop data and soil data are the inputs to the CROPWAT. It was assumed that the irrigation techniques will not change substantially up to 2045. Annual irrigation area growth rate was taken as 0.9% for the irrigation water demand analysis and was calculated using CROPWAT.
Finally, the remaining flow and the irrigation water demand satisfaction were analyzed in WEAP software. Schematic diagram was created in WEAP. Extent of cluster and annual water consumption rate per hectare were used as inputs in WEAP.

4. Results and discussion

4.1 Drinking water demand analysis

Water demands were simulated for 23 years from 2022 to 2045 in WEAP. According to the reference scenario cluster C2, C3, C4 and C5 (Figure 3) water demands can fulfil by available water sources. hence, no unmet demands which refer to water shortage in these clusters from 2022 to 2045. However, in the cluster 1, supply requirement is 1.0 Mm^3 in 2022 whereas the supply is only 0.6 Mm^3. Hence, there is a

shortage of 0.4 Mm^3 in 2022. Further, the supply requirement in 2045 is 1.2 Mm^3 while the supply is only 0.6 Mm^3. Therefore, there is a shortage of 0.6 Mm^3 in 2045 as well. Unmet demands of population clusters were shown in Table 1 for the years 2022 and 2045. There was an increment in water demand with the time from 2022 to 2045. However, the unmet drinking water demand of cluster 1 may be fulfilled by changing the extracting point.

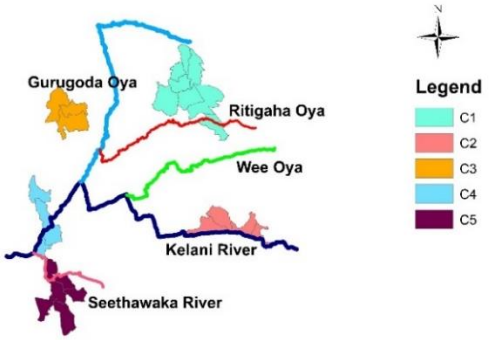

Figure 3: Population clusters

In WEAP, under High Growth (HG) scenario water demands increase more than the reference (RF) scenario because of high population growth rate whereas there is no significant change in the supply. So unmet demands of population clusters become higher. The increment of unmet demand was 0.49 Mm^3 from 2022 to 2045.

Table 1: Unmet demands of population clusters

Cluster	Unmet Demand ('000 m^3) (2022)	Unmet Demand ('000 m^3) (2045)
C1	371	599
C2	0	0
C3	0	0
C4	0	0
C5	0	0

4.2 Irrigation water demand analysis

Irrigation water requirement was calculated using CROPWAT. Water supply delivered and unmet demand were obtained by using WEAP.

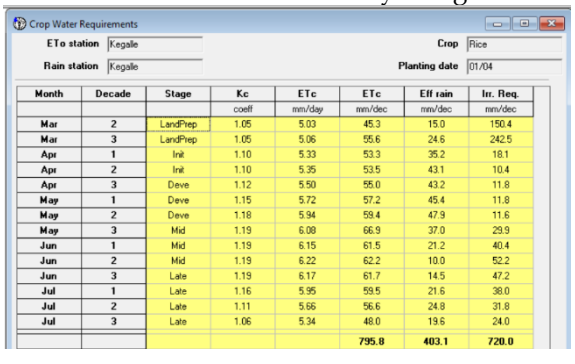

Figure 4: Irrigation water requirement

Figure 5 shows the irrigation clusters. No supply was delivered for Irrigation clusters I1 and I2 because of the limited flow in Ritigaha Oya and Gurugoda Oya.Delivered supplies are equal to the water demands in irrigation clusters I3 and I4. Hence, there is no unmet demand in I3 and I4. Irrigation requirement for 2022 is 1.9Mm^3 for irrigation cluster 5 while its supply is only 1.2 Mm^3. On the other hand, water requirement is 2.4 Mm^3 for 2045 while the supply is only 1.2Mm^3. Hence, the irrigation water requirement can be partially fulfilled for the cluster 5, throughout years. Taking Irrigation clusters as a unit and according to the RF scenario, the unmet demands which refer to the water shortage, may exceed from 4.6 million m^3 to 6.0 million m^3 in 2045.

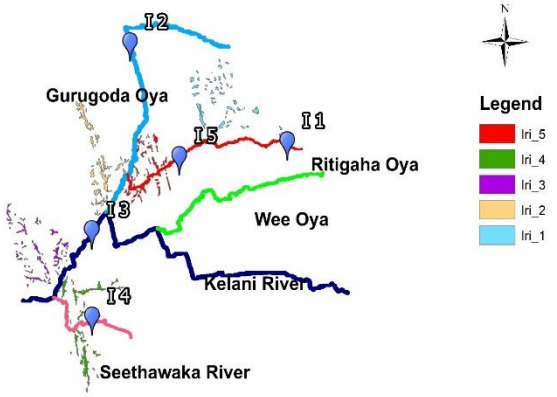

Figure 5: Irrigation clusters

Table 2: Unmet demands of irrigation clusters

Cluster	Unmet Demand (Mm^3) (2022)	Unmet Demand (Mm^3) (2045)
I1	1.8	2.2
I2	2.1	2.6
I3	0	0
I4	0	0
I5	0.7	1.2

5. Conclusions

Drinking water demand and irrigation water demand of four divisional secretariat divisions in Kegalle were analyzed. Water from Ritigaha Oya, Gurugoda Oya, Kelani River, and Seethawaka River were extracted. Five drinking water demand clusters and five irrigation water demand clusters were identified over the study area. Two scenarios are represented in WEAP, namely reference and high growth rate. The drinking water demand was calculated using

the WEAP model and all the clusters fulfilled their demand except cluster 1. This issue may be solved by changing the water extracting point accordingly. CROPWAT was used for calculating irrigation requirements and the WEAP model was used to assess the remaining water and fulfill irrigation requirements. For the irrigation water management two clusters which are clusters 3 and 4 fulfilled the irrigation water demand. Two Clusters, which are clusters number 1 and 2 did not even supply water for irrigation. So, the water extracting points need to be changed to that irrigation clusters where it can supply more water. Irrigation cluster number 5 was partially supplied. According to the results, none of these above-mentioned two Scenarios can be applied for the overall water shortage in Kegalle. Further, drinking and Irrigation water demands cannot be fulfilled for some selected clusters due to a lack of flow during the dry season in water resources.

References

Bouraima A-K, Zhang W H, Wei C F. 2015 Irrigation water requirements of rice using Cropwat model in Northern Benin. Int J Agric & Biol Eng, 8(2), pp.58－64.

Levite, H., Sally, H. and Cour, J. 2003 "Testing water demand management scenarios in a water-stressed basin in South Africa: Application of the WEAP model," Physics and Chemistry of the Earth, Parts A/B/C, 28(20-27), pp. 779–786.

Gunatilaka, A., 2008. Water security and related issues in Sri Lanka: the need for integrated water resource management (IWRM). Journal of the National Science Foundation of Sri Lanka, 36(0), p.3.

SEI, 2011. WEAP (Water Evaluation and Planning): User Guide for WEAP21. Stockholm Environment Institute, Boston USA.

Hussain, I., Thrikawala, S. and Barker, R. 2002 'Economic analysis of residential, commercial, and industrial uses of water in Sri Lanka', Water International, Vol. 27, No. 2, pp.183–193.

National Water Supply and Drainage Board (NWSDB) (2014) NWSDB Annual Report 2013, NWSDB, Colombo.

Sponsored By

TOKYO CEMENT GROUP

DEPARTMENT OF CIVIL ENGINEERING
FACULTY OF ENGINEERING
UNIVERSITY OF PERADENIYA
SRI LANKA

9 773021 673003